

Exhibit B.

Spectral phase transfer for indirect phase control of sub-20-fs deep UV pulses

Satoru Shimizu¹, Yasuo Nabekawa², Minoru Obara¹,
and Katsumi Midorikawa²

*1. Department of Electronics and Electrical Engineering, Keio University,
3-14-1 Hiyoshi, Kohoku, Yokohama-shi, Kanagawa 223-8522, Japan*

*2. RIKEN (The Institute of Physical and Chemical Research),
2-1 Hirosawa, Wako-shi, Saitama 351-0198, Japan
shimizu@ubara.elec.keio.ac.jp*

Abstract: We demonstrate the transfer of a shaped spectral phase in a pulse with a sub-20-fs pulse Fourier limit of a Ti:sapphire laser to that in a deep UV pulse at 256 nm in a sum-frequency-mixing process. The generated UV pulse maintains a sufficiently broad spectrum to form a sub-20-fs pulse due to broadband sum-frequency mixing with the group-delay-dispersion-matched scheme. The spectral phases of the deep UV pulse are measured with spectral phase interferometry for direct electric field reconstruction and compared with the phase applied to the Ti:sapphire laser pulse.

© 2005 Optical Society of America

OCIS codes: (140.3610) Lasers, ultraviolet; (320.7110) Ultrafast nonlinear optics; (320.5520) Pulse compression.

References and links

1. N. Dudovich, B. Dayan, S. M. Gallagher, and Y. Silberberg, "Transform-limited pulses are not optimal for resonant multiphoton transition," *Phys. Rev. Lett.* **86**, 47–50 (2001).
2. V. V. Lozovoy, I. Pastirk, and M. Dantus, "Multiphoton intrapulse interference IV. Ultrashort laser pulse spectral phase characterization and compensation," *Opt. Lett.* **29**, 775–777 (2004).
3. I. Pastirk, J. M. D. Cruz, K. A. Walowicz, V. V. Lozovoy, and M. Dantus, "Selective two-photon microscopy with shaped femtosecond pulses," *Opt. Express* **11**, 1695–1701 (2003). <http://www.opticsexpress.org/abstract.cfm?URI=OPEX-11-14-1695>.
4. A. M. Weiner, "Femtosecond pulse shaping using spatial light modulators," *Rev. Sci. Instrum.* **71**, 1929–1960 (2000).
5. F. Verluise, V. Laude, Z. Cheng, and C. S. P. Tournais, "Amplitude and phase control of ultrashort pulses by use of an acousto-optic programmable dispersive filter: pulse compression and shaping," *Opt. Lett.* **25**, 575–577 (2000).
6. M. Hacker, G. Stobrawa, R. Sauerbrey, T. Buckup, M. Motzkus, M. Wildenhain, and A. Gehner, "Micromirror SLM for femtosecond pulse shaping in the ultraviolet," *Appl. Phys. B* **76**, 711–714 (2003).
7. P. Baum, S. Lochbrunner, and E. Riedle, "Generation of tunable 7-fs ultraviolet pulses: achromatic phase matching and chirp management," *Appl. Phys. B* **79**, 1027–1032 (2004).
8. P. Baum, S. Lochbrunner, and E. Riedle, "Tunable sub-10-fs ultraviolet pulses generated by achromatic frequency doubling," *Opt. Lett.* **29**, 1686–1689 (2004).
9. M. Roth, M. Mehendale, A. Bartelt, and H. Rabitz, "Acousto-optical shaping of ultraviolet femtosecond pulses," *Appl. Phys. B* **80**, 441–444 (2005).
10. Y. Nabekawa and K. Midorikawa, "Broadband sum frequency mixing using noncollinear angularly dispersed geometry for indirect phase control of sub-20-femtosecond UV pulses," *Opt. Express* **11**, 324–338 (2003). <http://www.opticsexpress.org/abstract.cfm?URI=OPEX-11-4-324>.

11. C. Iaconis and I. A. Walmsley, "Self-referencing spectral interferometry for measuring ultrashort optical pulses," *IEEE J. Quantum Electron.* 35, 501–509 (1999).
12. H.-S. Tan, E. Schreiber, and W. S. Warren, "High-resolution indirect pulse shaping by parametric transfer," *Opt. Lett.* 27, 439–441 (2002).
13. T. Witte, K. L. Kompa, and M. Motzkus, "Femtosecond pulse shaping in the mid infrared by difference-frequency mixing," *Appl. Phys. B* 76, 467–471 (2003).
14. F. Eickemeyer, R. A. Kaindl, M. Woerner, T. Elsaesser, and A. M. Weiner, "Controlled shaping of ultrafast electric field transients in the mid-infrared spectral range," *Opt. Lett.* 25, 1472–1474 (2000).
15. M. Hacker, R. Netz, M. Roth, G. Stobrawa, T. Feurer, and R. Sauerbrey, "Frequency doubling of phase-modulated ultrashort laser pulses," *Appl. Phys. B* 73, 273–277 (2001).
16. M. Hacker, T. Feurer, R. Sauerbrey, T. Lucza, and G. Szabo, "Programmable femtosecond laser pulses in the ultraviolet," *J. Opt. Soc. Am. B* 18, 866–871 (2001).
17. H. Wang, and A. M. Weiner, "A femtosecond waveform transfer technique using type II second harmonic generation," *IEEE J. Quantum Electron.* 40, 937–945 (2004).
18. Y. Nabekawa and K. Midorikawa, "Group-delay-dispersion-matched sum-frequency mixing for the indirect phase control of deep ultraviolet pulses in the sub-20fs regime," *Appl. Phys. B* 78, 569–581 (2004).
19. G. Szabo and Z. Bor, "Frequency conversion of ultrashort pulses," *Appl. Phys. B* 58, 237–241 (1994).
20. V. D. Volosov, S. G. Karpenko, N. E. Kornienko, and V. L. Strizhevskii, "Method for compensating the phase matching dispersion in nonlinear optics," *Sov. J. Quantum Electron.* 4, 1090–1098 (1975).
21. O. E. Martinez, "Achromatic phase matching for second harmonic generation of femtosecond pulses," *IEEE J. Quantum Electron.* 25, 2464–2468 (1989).
22. T. Nakajima and K. Miyazaki, "Spectrally compensated third harmonic generation using angular dispersers," *Opt. Commun.* 163, 217–222 (1999).
23. I. Z. Kozma, P. Baum, S. Lochbrunner, and E. Riedle, "Widely tunable sub-30 fs ultraviolet pulses by chirped sum frequency mixing," *Opt. Express* 11, 3110–3115 (2003). <http://www.opticsexpress.org/abstract.cfm?URI=OPEX-11-23-3110>.
24. Y. Nabekawa, Y. Shimizu, and K. Midorikawa, "Sub-20-fs terawatt-class laser system with a mirrorless regenerative amplifier and an adaptive phase controller," *Opt. Lett.* 27, 1265–1267 (2002).
25. Y. Nabekawa and K. Midorikawa, "Broadband sum-frequency mixing for indirect phase control of UV pulses with a sub-20-fs TW-class Ti:sapphire laser system," in *Ultrafast Optics IV*, F. Krausz, G. Korn, P. Corkum, and I. A. Walmsley, eds., vol. IV, pp. 395–400 (Springer, New York, 2004).
26. Y. Nabekawa and K. Midorikawa, "High-order pulse front tilt caused by high-order angular dispersion," *Opt. Express* 11, 3365–3376 (2003). <http://www.opticsexpress.org/abstract.cfm?URI=OPEX-11-25-3365>.
27. K. Varjú, A. P. Kovács, G. Kurdi, and K. Ösvay, "High-precision measurement of angular dispersion in a CPA laser," *Appl. Phys. B [suppl.]* 74, S259–S263 (2002).
28. J.-K. Rhee, T. S. Sosnowski, T. B. Norris, J. A. Arns, and W. S. Colburn, "Chirped-pulse amplification of 85-fs pulses at 250 kHz with third-order dispersion compensation by use of holographic transmission gratings," *Opt. Lett.* 19, 1550–1552 (1994).
29. P. Baum, S. Lochbrunner, and E. Riedle, "Zero-additional-phase SPIDER: full characterization of visible and sub-20-fs ultraviolet pulses," *Opt. Lett.* 29, 210–212 (2004).
30. V. Bagnoud and F. Salin, "Influence of optical quality on chirped-pulse amplification: characterization of a 150-nm-bandwidth stretcher," *J. Opt. Soc. Am. B* 16, 188–193 (1999).

1. Introduction

Spectral phase control techniques have been widely used for the generation of shaped femtosecond pulses in order to investigate ultrafast coherent interactions in physical and chemical phenomena. A highly modulated spectral phase, which cannot be given by conventional dispersive media such as a prism pair, can be used for managing the quantum states of atoms or molecules. Dudovich *et al.*, for example, demonstrated that a π -flipped window in the spectral phase caused a constructive interference between the upper and lower parts of the spectral component across the resonant wavelength of the intermediate state for the two-photon resonant transition of the rubidium atom, resulting in the enhanced fluorescence of the two-photon transition [1]. Another example of a sinusoidal shape of the spectral phase is essential for the application of the method of multiphoton intrapulse interference scan [2] to the selective excitation of dye molecules [3].

Most of the experiments with spectral phase control, however, have been performed in the visible (VIS) or near-infrared (NIR) region, because instruments for phase control, such as a

liquid-crystal spatial light modulator (LC-SLM) [4] or an acoustooptic programmable dispersive filter (AOPDF) [5], are not transparent for other wavelength regions. Hacker *et al.* reported an exceptional research result at 400 nm using a micro electro mechanical system (MEMS) micromirror array [6]. It has also been reported that a state-of-the-art dispersion compensation technique with a deformable mirror yielded a pulse with a duration of 7 fs in the ultraviolet (UV) region [7, 8], and that the phase and the amplitude of the second harmonic of the Ti:sapphire laser can be controlled using an AOPDF made of fused silica in the violet~UV region [9], while the application of an arbitrarily shaped spectral phase to the broadband deep UV pulse has not been demonstrated.

Another approach to controlling the phase of the UV pulse is the indirect method. This is based on the fact that the spectral phase of the broadband input pulse can be transferred, in a three-wave mixing process with a nonlinear crystal, to that of the generated pulse if the other input pulse is monochromatic, as was described in Ref. [10]. This principle is routinely applied to generate sheared replica pulses in the measurement of the spectral interferometry of direct electric field reconstruction (SPIDER) [11]. Tan *et al.* reported the phase control of the mid-infrared pulse by utilizing a spectral phase transfer in an optical parametric amplification (OPA) process [12], and Witte *et al.* also demonstrated similar results in a difference-frequency-mixing (DFM) process [13]. These experiments for femtosecond mid-infrared pulses followed the earlier work by Eickemeyer *et al.* observing shaped electric field transients [14]. Hacker *et al.* demonstrated the phase transfer in second harmonic generation (SHG) [15], and also the generation of shaped UV pulses at 200 nm in the sum-frequency mixing (SFM) process [16]. Wang and Weiner confirmed that the amplitude of a second harmonic (SH) pulse in time domain was a directly scaled version of the shaped input pulse under the type II phase matching condition [17]. The advantage of this method is that we have no need for a special device for phase control corresponding to the special wavelength.

One of the issues in the generation of the ultrashort pulse in the deep UV region, other than that of spectral phase control, is the spectral narrowing due to the large amount of group delay (GD) mismatch in the nonlinear crystal between the generated deep UV pulse and the input VIS/NIR pulses. The SFM of the fundamental pulse and SH pulse in a BBO crystal under the type I phase-matching condition, for example, caused a delay of ~ 1 ps/mm from the fundamental pulse to the generated third harmonic pulse, resulting in the acceptable spectral width of the fundamental pulse being limited to only 2.3 nm-mm [18]. In order to compensate the phase mismatch for the frequency conversion using a nonlinear crystal, the method using angular dispersion has been proposed and demonstrated [19]. Volosov *et al.* [20] and Martinez *et al.* [21] increased the phase-matching bandwidth in SHG, and Nakajima and Miyazaki investigated the effectiveness of the use of angular dispersion for third harmonic generation (THG) [22]. To achieve efficient broadband frequency conversion, Kozma *et al.* optimized the generation of tunable sub-30-fs UV pulses by using chirped pulses in the SFM process [23].

In this paper, we present the experimental observation of phase transfer from a sub-20-fs laser pulse of a Ti:sapphire laser to a deep UV pulse in the SFM process. The issue of spectral narrowing due to GD mismatch has been solved by adopting a novel scheme of group-delay-dispersion (GDD)-matched SFM [18], and we obtained a sufficiently broad spectrum to form a sub-20-fs pulse at 256 nm wavelength. We observed fairly good agreement between applied phases with sinusoidal and stepwise shapes in an LC-SLM in the chirped pulse amplification (CPA) system of the Ti:sapphire laser and the measured phases in the generated deep UV pulses.

2. Experiment

We have already developed a sub-20-fs CPA system of a Ti:sapphire laser with a phase controller consisting of an LC-SLM and a conventional zero-dispersion stretcher [24]. As shown in

Fig. 1. we use a typical CPA system consisting of a mode-locked oscillator, an Offner stretcher,

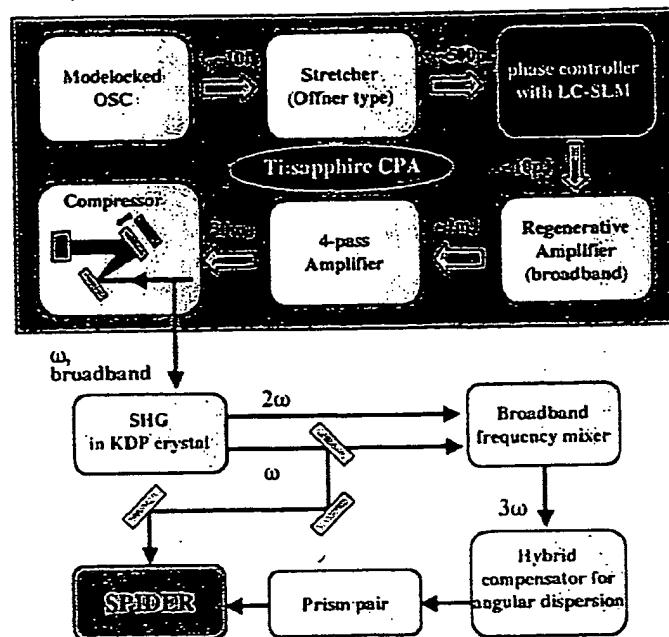


Fig. 1. Schematic diagram of experimental setup.

a regenerative amplifier, a four-pass amplifier, and a compressor. The phase controller with a LC-SLM is placed between the stretcher and the regenerative amplifier. In addition to the compensation of high-order dispersion in the amplified pulse from the CPA system, the additional phase modulations of sinusoidal and stepwise shapes of the pulse from this CPA system were previously demonstrated in Ref. [25].

An output pulse from the CPA system is given an appropriate chirp by adjusting the separation between the gratings of the pulse compressor so that the pulse duration of the Ti:sapphire laser should coincide with that of the quasi-monochromatic SH. The shorter edge of the spectrum is partially frequency doubled with a KDP crystal with a thickness of 8 mm in order to obtain the narrow-band quasi-monochromatic SH of sub-picosecond pulse duration due to a large GD mismatch, resulting in a wavelength of 376.5 nm with an energy of $\sim 100 \mu\text{J}$. The bandwidth of 2 THz is approximately equal to the resolution of the LC-SLM [25].

The generated SH and the residual fundamental are sent to the broadband sum-frequency mixer. The details of this broadband sum-frequency mixer are described in Ref. [18]. An appropriate angular dispersion of the fundamental pulse and the noncollinear geometry of the two input pulses in this broadband frequency mixer can eliminate the limitation of the spectral width under the GD- and GDD-matching conditions, resulting in a spectral width of $\sim 9.5 \text{ nm}$ centered at $\sim 256 \text{ nm}$ with an energy of $\sim 20 \mu\text{J}$. The angular dispersion of the generated UV pulse is compensated with the hybrid compensator using a prism of fused silica with an apex angle of 73° and a grating with a groove density of 1200 l/mm . The angular dispersion is reduced to $3/5$ with a telescope consisting of two concave mirrors with radii of curvature of 1.5 m and 2.5 m. Then the UV beam is collimated with the grating and the prism. The polarization of the UV pulse is rotated by 90 degrees with a quartz rotator, as shown in Fig. 2. These optics are

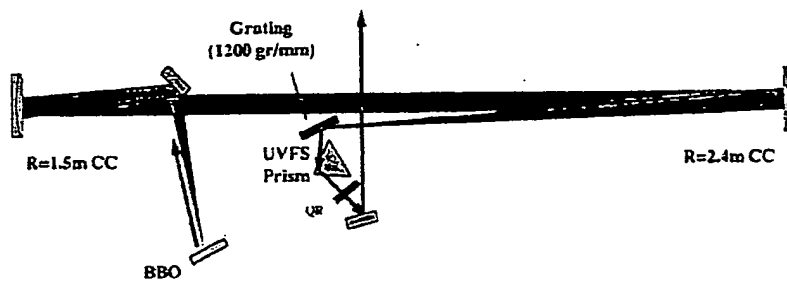


Fig. 2. Hybrid compensator for angular dispersion of generated UV pulse. QR: quartz rotator

configured on the basis of the results of the analysis of high-order angular dispersion described in Ref. [26].

The angular dispersion of output UV pulse from this hybrid compensator is measured by the method based on spectrally resolved interferometry proposed by Varjú *et al.* [27], as schematically shown in Fig. 3. Spatial fringes generated with the interferometer in Fig. 3, which cause the spatial inversion of the input pulse in one of the arms, include information on the direction of the pulse for each wavelength component, thus we can determine the angular dispersion by spectrally resolving the fringe.

The measured fringes and the angular dispersions are shown in Figs. 4 (a) and (b). The compensator with only a prism and a one-to-one telescope described in Ref. [18] exhibits the residual high-order angular dispersion, as is plotted by filled circles in Fig. 4(a), which was not resolved in the preliminary experiment [18]. The difference in angle for each wavelength component in the spectral range from 250 to 261 nm exceeds 5 mdeg. with the prism-only compensator, while it is within 1 mdeg. with the hybrid compensator of the prism and the grating, as is shown in Fig. 4(b). Due to the large Fresnel loss of the prism and the low diffraction ef-

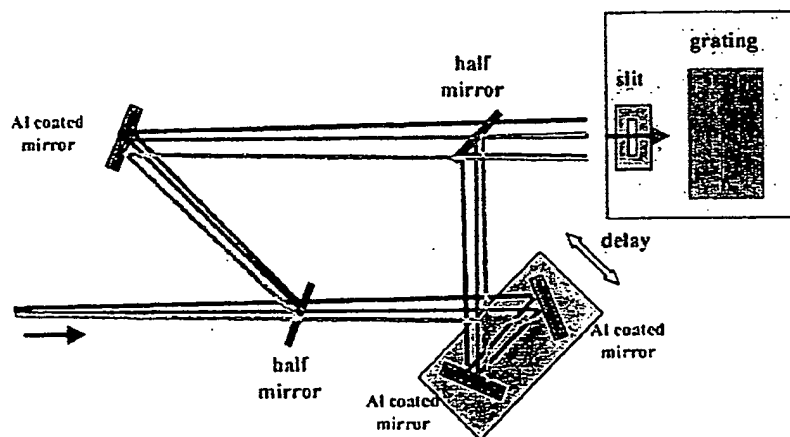


Fig. 3. Schematic of the interferometer for the measurement of the angular dispersion. Vertical fringes generated with this interferometer are spectrally resolved with a slit and a grating with a groove density of 2400 ℓ/mm and detected by a CCD camera.

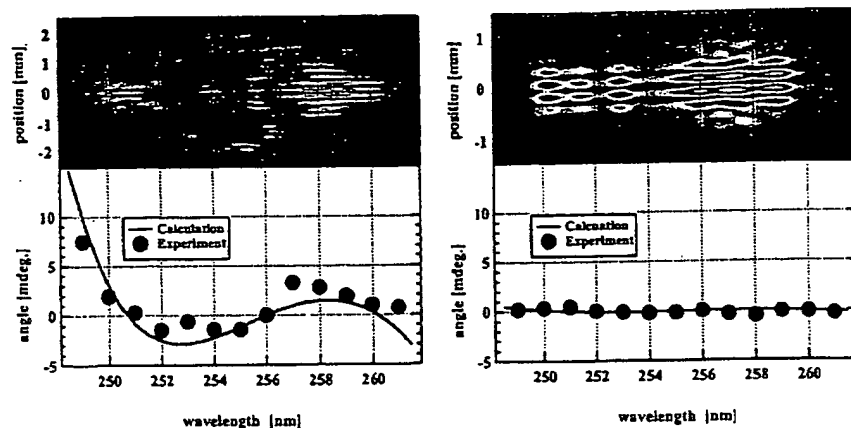


Fig. 4. Upper parts of both figures are the spectrally resolved figures for the measurement of the angular dispersion. (a) With the prism-only compensator. (b) With the hybrid compensator. Relative angles for the propagation directions in each spectral component resulting from these fringes are shown as filled circles in both figures. Solid curves are obtained from the ray-trace calculation described in ref. [26].

efficiency ($\sim 60\%$) of the Al-coated grating, the pulse energy is estimated to be a few μJ at the output of the hybrid compensator.

The pulse duration of the generated UV was expected to be a few ps due to the dispersions suffered from the extension of the grating separation in the CPA system, from the angular disperser in the broadband frequency mixer, and from the hybrid angular dispersion compensator. Thus, we measured the GDD in the generated deep UV pulse by the cross-correlation spectrally and temporally resolved down-conversion technique instead of the upconversion technique (STRUT) proposed by Rhee *et al.* [28], before utilizing the SPIDER apparatus. Note that the measured pulse duration with the SPIDER should be shorter than the delay between the two replica pulses needed for the SPIDER measurement.

Approximately half of the energy of the fundamental pulse was sent to a "recompressor", which consists of a pair of gratings with a groove density of 150 l/mm to compensate for the positive chirp given in the compressor in the CPA system, and then difference-frequency-mixed with the deep UV pulse. The spectrum of the generated DFM pulse was recorded at each delay between the fundamental and the deep UV pulse. We found that the duration of the deep UV pulse is $\sim 3\text{ ps}$ and determined that the GDD and the third-order dispersion (TOD) are $8.2 \times 10^{-27}\text{ [s}^2\text{]}$ and $2.4 \times 10^{-41}\text{ [s}^3\text{]}$, respectively, from the measured spectrogram shown in Fig. 5. A pair of prisms made of fused silica with a separation of 41.5 cm was utilized for removing most of the GDD. We obtained a pulse duration of 170 fs by adjusting the insertion of the prism pair such that the measured duration of the cross-correlation trace could be minimized.

The phase of the deep UV pulse behind the prism pair was measured with the SPIDER apparatus (Fig. 6). We used a Michelson interferometer to generate a pair of replicas of the UV pulse with a fixed delay of 1.227 ps . Two beam splitters, having the same thickness, generate two replicas of the UV pulse, resulting in the dispersions due to the transmission in these two beam splitters being the same. The zero-additional-phase (ZAP) SPIDER [29] does not need such an interferometer for the measured UV pulse. We did not, however, adopt the ZAP-SPIDER because the collinear geometry of the interferometer generates spectral fringes without adjusting the size of the beam waist on the slit of the spectrometer, and the energy of the UV pulse is

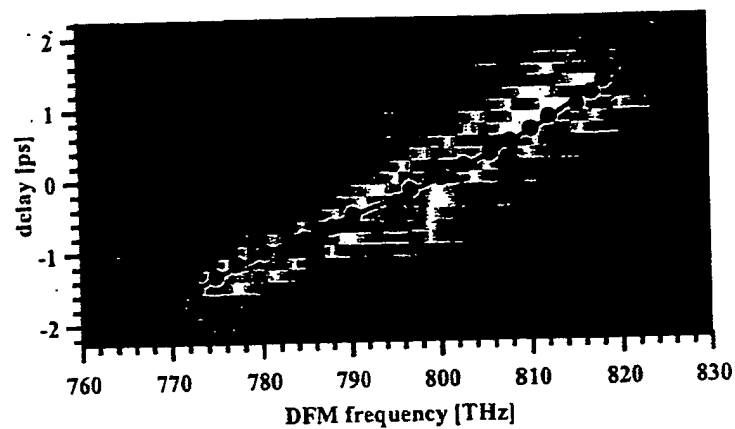


Fig. 5. Measured spectrogram of deep UV pulse without prism pair for compensation of chirp.

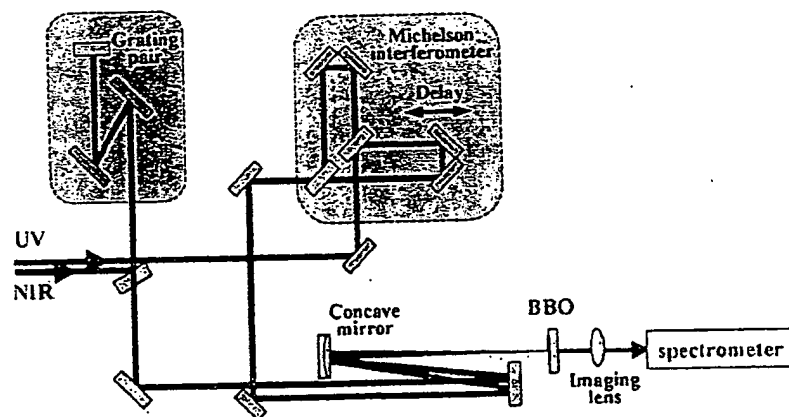


Fig. 6. SPIDER apparatus for measuring phase of UV pulse.

sufficiently high to generate the difference-frequency-mixed pulse behind the interferometer.

A pair of gratings with a groove density of 1200 ℓ/mm was used to generate a chirped NIR pulse from a portion of the fundamental pulse. Two replicas of the deep UV pulses were difference-frequency-mixed with the chirped NIR pulse in a BBO crystal with a thickness of 20 μm . The generated two pulses were spectrally sheared by 2 THz due to the high chirp of the NIR pulse and the delay between the replicas of the UV pulse. This pair of spectrally sheared and temporally delayed pulses was sent to a spectrometer (Ocean Optics Inc., HR2000), and the spectral interferogram was recorded. We extracted the information of the spectral phase with the inverse Fourier transform of this interferogram.

The GDD given by the grating pair in the SPIDER apparatus is $-1.1 \times 10^{-25} \text{ [s}^2\text{]}$, which is approximately ten times larger than that due to phase control with the LC-SLM ($9 \times 10^{-27} \text{ [s}^2\text{]}$), so that the change of the spectral shear of the two replica pulses with phase control can be estimated to be $\sim 10\%$ at most. Greater GDD of the grating pair would reduce this type of error.

The measured phase without phase control of the LC-SLM reveals an unexpected phase distortion (Fig. 7(a)) which might be caused by the roughness of the surface of the concave mirrors used in the broadband frequency mixer and the hybrid compensator. This type of phase

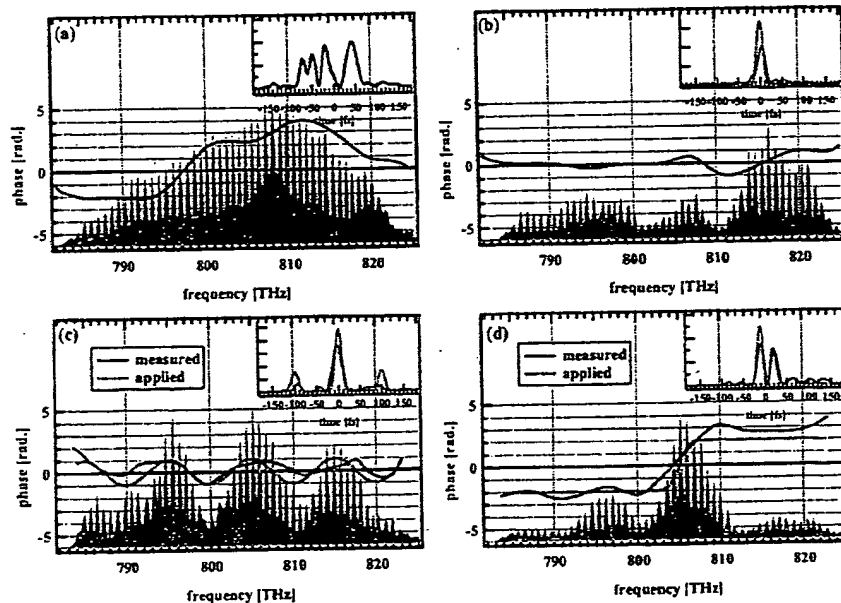


Fig. 7. Measured interferograms (hatched areas) and spectral phases (solid curves). The measured phases (a) without phase control and (b) with the inverse of the phase distortion applied. Applied phases (dashed curves) are given by the equations (c) $\phi = \cos\{2\pi(\nu - \nu_0)/\Delta\nu\}$ and (d) $\phi = \tanh\{(\nu - \nu'_0)/\Delta\nu'\}$, where $\nu_0 = 800 \text{ THz}$, $\Delta\nu = 10 \text{ THz}$, $\nu'_0 = 805 \text{ THz}$, and $\Delta\nu' = 1 \text{ THz}$. Temporal profiles calculated from the spectrum and the measured/applied phases are also shown as solid/dashed curves in the insets.

distortion induced by a stretcher for a CPA system was analyzed and measured by Bagnoud and Salin [30]. The Fourier transform of the measured spectrum and the phase with the distortion exhibits a modulated temporal profile over a $\sim 170 \text{ fs}$ duration, as shown in the inset of Fig.

7(a), which is consistent with the duration indicated by the cross-correlation measurement.

We applied the inverse of the phase distortion to the LC-SLM to cancel out the phase distortion, resulting in most of the distortion being eliminated (Fig. 7(b)), while the residual phase distortion adds subpeaks in the temporal profile to the main peak of the pulse with a duration of 20 fs, which is 11% longer than that of 18 fs calculated from the Fourier limit of the measured spectrum. The residual phase distortion may be due to the unexpected nonlinear effect in the SFM process, such as the cross phase modulation in the BBO crystal.

Because of the elimination of the phase distortion, we can expect further phase transfer from the fundamental pulse to the generated UV pulse by adding the shaped spectral phase to the inverse of the phase distortion. The results of the measured phases for a sinusoidal shape and a stepwise shape are shown as solid curves in Figs. 7(c) and (d), respectively. The dashed curves in these figures correspond to the applied phases. Although there are residual phase distortions in the measured phases, we can see fairly good agreement between the measured phases and the applied phases in both figures. Note that the addition of the spectral phase to the fundamental pulse has an influence on the power spectrum of the generated UV pulse. The interferograms with the SPIDER measurement, shown as hatched areas in Figs. 7(c) and (d), reflect the modulated intensity of the power spectrum. The phase-matching conditions in the SFM process might be slightly changed by the spectral phase control.

3. Summary

We demonstrated the transfer of the shaped spectral phase in a sub-20-fs pulse of a Ti:sapphire laser to that in a deep UV pulse at 256 nm. By indirect phase control via the SFM process, the spectral phases in the deep UV pulses are controlled by applying phase modulation to the LC-SLM in the CPA system. However, the correspondence between the applied and transferred phases should be improved to enable the practical application of these pulses.

This work was supported by the Ministry of Education, Culture, Sports, Science, and Technology (MEXT) through a Grant-in-Aid for Scientific Research for Young Scientists (A) No.16686006.

Single-pulse phase-control interferometric coherent anti-Stokes Raman scattering spectroscopy

Sang-Hyun Lim, Allison G. Caster, and Stephen R. Leone

Departments of Chemistry and Physics, University of California at Berkeley, Berkeley, California 94720, USA
and Lawrence Berkeley National Laboratory, Berkeley, California 94720, USA

(Received 19 April 2005; published 17 October 2005)

In coherent anti-Stokes Raman scattering (CARS) spectroscopy experiments, usually the amplitude of the signal is measured and the phase information is lost. With a polarization- and phase-controlled pulse shaping technique, the relative phase between the resonant and nonresonant CARS signals is controlled, and spectral interferometry is performed without an interferometer. Both the real and imaginary parts of the background-free resonant CARS spectrum are measured via spectral interferometry between the resonant and nonresonant signals from the same sample. The resonant signal is amplified significantly by homodyne mixing with the nonresonant signal as a local oscillator, greatly improving the detection limit.

DOI: 10.1103/PhysRevA.72.041803

PACS number(s): 42.65.Dr, 42.25.Hz, 78.47.+p, 82.53.Kp

Coherent anti-Stokes Raman scattering (CARS) spectroscopy has emerged as a promising microscopic technique for materials and biological imaging [1,2]. Optical molecular imaging is often limited by the necessary introduction of dyes or markers, which can perturb material structures or alter biological processes. Since CARS allows the identification of the desired molecules by their vibrational response, it circumvents the need for fluorescent labels [1,3,4].

In this letter, we demonstrate that it is possible to retrieve the imaginary part of the background-free resonant CARS spectrum *in situ* via spectral interferometry utilizing the nonresonant signal from the same sample as a local oscillator. We apply the polarization- and phase-control pulse shaping technique [5] to control the relative phase between the resonant and nonresonant CARS signals [6,7], but implement a double quadrature spectral interferometry (DQSI) method [8] utilizing the nonresonant signal as a local oscillator. Unlike previously reported interferometric CARS techniques [9,10], the interference between the two signals (the resonant and nonresonant CARS) is produced in the same sample, and the imaginary part of the resonant CARS spectrum is acquired directly. The technique not only extracts the imaginary part of the CARS signal, but also amplifies it significantly, allowing a further sensitivity improvement [9].

Most nonlinear spectroscopy experiments measure only the amplitude of a spectral response, and CARS is similar [11]. Figure 1(a) shows the square of the amplitude ($|L|^2$, the conventional CARS signal), and the imaginary ($\text{Im}[L]$) and real ($\text{Re}[L]$) parts of several Lorentzian lines (L) simulated for toluene [12].

$$L(\omega) = \sum_k \frac{A_k}{\omega - \Omega_k - i\Gamma_k} \quad (1)$$

where A_k , Ω_k , and Γ_k are the intensity, energy and linewidth of the vibrational mode k , respectively. The imaginary part of the vibrationally resonant third-order nonlinear susceptibility $\chi_{\text{res}}^{(3)}$ corresponds to the spontaneous Raman spectrum [9]. Although $|L|^2$ has a comparable spectral resolution to $\text{Im}[L]$, its spectral intensity distribution and the detailed peak shapes are different from $\text{Im}[L]$ [9].

It is desirable to measure $\text{Im}[L]$, which correlates directly with the wealth of vibrational Raman information available

[12,13]. Detecting $|L|^2$ has additional problems because of nonresonant signals, which dominate most condensed phase samples [1,3,14]. Since both the resonant and nonresonant signals are coherent, the two components interfere with each other, generating a modulated pattern in the measured CARS spectrum, which makes it difficult to use assignments from the known Raman spectrum directly [the interference pattern resembles the shape of $\text{Re}[L]$ shown in Fig. 1(a)] [1,14].

With single broad band pulse excitation, all possible combinations of wavelengths within the bandwidth can be used as pump, Stokes and probe pulses to generate the CARS signal [Fig. 1(b)]. The resonant and nonresonant CARS signals can be described by [6]

$$P_R(\omega) \propto \int_0^\infty d\Omega \frac{1}{(\Omega_R - \Omega) + i\Gamma_R} E(\omega - \Omega) A(\Omega) \quad (2)$$

$$P_{NR}(\omega) \propto \int_0^\infty d\Omega \frac{1}{\Omega} E(\omega - \Omega) A(\Omega) \quad (3)$$

$$\text{where } A(\Omega) = \int_0^\infty d\omega' E^*(\omega') E(\Omega + \omega'). \quad (4)$$

P_R and P_{NR} are the vibrationally resonant and the nonresonant polarizations, respectively, E is the laser field, and Ω_R and Γ_R represent the energy and the linewidth of the vibrational resonance, respectively. Note that P_{NR} is real and P_R is complex [6]. To obtain a multiplex CARS signal, it is necessary to separate a spectrally narrow probe pulse, and Silberberg and co-workers demonstrated this by applying phase- and polarization-control techniques [6,7]. If we assume that the linewidth of the probe [selected by the phase and polarization as shown in Fig. 2(a)] is spectrally much narrower than the linewidth of the vibrational peak (Γ_R), the resonant CARS component becomes

$$\begin{aligned} P_R(\omega) &\propto \int_0^\infty d\Omega \frac{1}{(\Omega_R - \Omega) + i\Gamma_R} E_{\text{pr}}(\omega - \Omega) A(\Omega) \\ &\approx \int_0^\infty d\Omega \frac{1}{(\Omega_R - \Omega) + i\Gamma_R} \\ &\quad \times \delta(\omega - \Omega - \omega_{\text{pr}}) \exp(i\phi_{\text{pr}}) A(\Omega) \end{aligned}$$

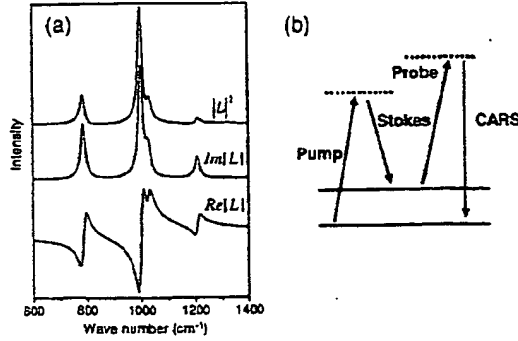


FIG. 1. (a) Simulation of a Lorentzian line shape function of toluene (resonances at 788, 1001, 1028, and 1210 cm^{-1}) with $\Gamma = 10 \text{ cm}^{-1}$ in Eq. (1). Note that the spontaneous Raman spectrum corresponds to $\text{Im}[L]$. (b) Energy level diagram of the CARS process.

$$\begin{aligned}
 &= [\exp(i\phi_{Pr})/(\Omega_R + \omega_{Pr} - \omega + i\Gamma_R)]A(\omega - \omega_{Pr}) \\
 &= L(\omega)\exp(i\phi_{Pr})A(\omega - \omega_{Pr}) \\
 &\text{if } E_{Pr}(\omega) \approx \delta(\omega - \omega_{Pr})\exp(i\phi_{Pr}) \quad (5)
 \end{aligned}$$

where L is the Lorentzian line shape function for CARS [the only difference from Eq. (1) is the relative resonance energy, i.e., $\Omega_R + \omega_R$ instead of Ω_L], δ is the delta function, ϕ_{Pr} is the relative phase of the probe with respect to the excitation part of the pulse [as shown in Fig. 2(a)], and ω_{Pr} is the frequency of the probe pulse.

The experimental scheme is shown in Fig. 2. Figure 2(a) shows the intensity, phase and polarization of the laser pulse controlled by the pulse shaper. Polarizations of the pump/Stokes and the probe pulses are along the x and y directions, respectively, as shown in Fig. 2(b). If we detect CARS signals along the $\pm 45^\circ$ polarization directions relative to the x axis [i and j directions in Fig. 2(b)], the CARS polarizations in the i and j polarization directions are

$$\begin{aligned}
 P_R^i &= (1/\sqrt{2})\exp(i\phi_{Pr})AL, \quad P_R^j = -(1/\sqrt{2})\exp(i\phi_{Pr})AL, \\
 P_{NR}^i &= P_{NR}^j = (1/\sqrt{2})P_{NR} \quad (6)
 \end{aligned}$$

The detected signals (S^i and S^j) become

$$\begin{aligned}
 S^i &= |\alpha_R P_R^i + \alpha_{NR} P_{NR}^i|^2 = \alpha_R^2 |P_R^i|^2 + \frac{1}{2}\alpha_{NR}^2 |P_{NR}|^2 \\
 &\quad + (1/\sqrt{2})\alpha_R \alpha_{NR} (P_R^i + P_R^{i*})P_{NR}, \\
 S^j &= |\alpha_R P_R^j + \alpha_{NR} P_{NR}^j|^2 = \alpha_R^2 |P_R^j|^2 + \frac{1}{2}\alpha_{NR}^2 |P_{NR}|^2 \\
 &\quad + (1/\sqrt{2})\alpha_R \alpha_{NR} (P_R^j + P_R^{j*})P_{NR} \quad (7)
 \end{aligned}$$

where α_{NR} and α_R are the intensity coefficients for the non-resonant and resonant CARS polarizations, respectively. Here we limit the consideration to randomly oriented samples. Since only a small portion of the laser spectrum is used as a probe (2 pixels out of 128 SLM pixels), we assume that P_{NR} is primarily parallel to the x axis (pump/Stokes direction). Combining Eqs. (6) and (7), we find that the difference, $S^i - S^j$, becomes

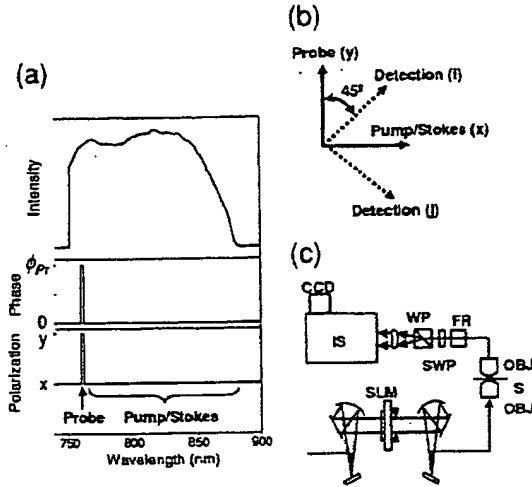


FIG. 2. (a) Intensity, phase and polarization of the phase- and polarization-controlled laser pulse used in the experiment. (b) Polarization directions of pump/Stokes, probe and CARS signal detection (i and j). (c) Experimental setup. SLM—dual liquid crystal spatial light modulator, OBJ—microscope objective, S—sample, FR—Fresnel rhomb (achromatic half wave plate), SWP—sharp-edge short wave pass filter, WP—Wollaston prism, IS—imaging spectrometer.

$$\begin{aligned}
 S^i - S^j &= \alpha_R \alpha_{NR} (P_{NR}/\sqrt{2})(P_R^i + P_R^{i*} - P_R^j - P_R^{j*}) \\
 &= \alpha_R \alpha_{NR} P_{NR} A \{ \exp(i\phi_{Pr})L + \exp(-i\phi_{Pr})L^* \} \\
 &= \alpha_R \alpha_{NR} P_{NR} A \{ e^{i\phi_{Pr}}(\text{Re}[L] + i\text{Im}[L]) + e^{-i\phi_{Pr}}(\text{Re}[L] \\
 &\quad - i\text{Im}[L]) \} \\
 &= 2\alpha_R \alpha_{NR} P_{NR} A (\text{Re}[L]\cos\phi_{Pr} - \text{Im}[L]\sin\phi_{Pr}) \quad (8)
 \end{aligned}$$

where $\text{Re}[L]$ and $\text{Im}[L]$ represent the real and imaginary parts of the Lorentzian line shape function, respectively. Equation (8) means that if we can detect S^i and S^j simultaneously, the real or imaginary parts of the resonant CARS signal (L) can be extracted simply by controlling the phase of the probe pulse [ϕ_{Pr} in Fig. 2(a)]. Since $S^i + S^j$ contains mostly nonresonant signals, we can extract the nonamplified resonant signal by the following normalized difference (D),

$$\begin{aligned}
 D &= (S^i - S^j)/\sqrt{S^i + S^j} \\
 &= \frac{2\alpha_R \alpha_{NR} P_{NR} A \text{Im}[L]}{\sqrt{\alpha_{NR}^2 P_{NR}^2 + 1/2(\alpha_R^2 |P_R^i|^2 + \alpha_R^2 |P_R^j|^2) + (\text{cross terms})}} \\
 &\approx 2\alpha_R A \text{Im}[L] \quad (9)
 \end{aligned}$$

In this way, we can detect only the resonant signals from samples that have different levels of nonresonant signals.

In the experimental setup [Fig. 2(c)], we control the phase and polarization of the laser pulse by an all-reflective 4f geometry pulse shaper with a dual 128 pixel liquid crystal spatial light modulator (LC-SLM, SLM-256, CRI) [5,7]. We compress the pulse at the sample position with a multiphoton intrapulse interference phase scan (MIIPS) [15]. To obtain an optimum CARS signal level, it is also necessary to compress

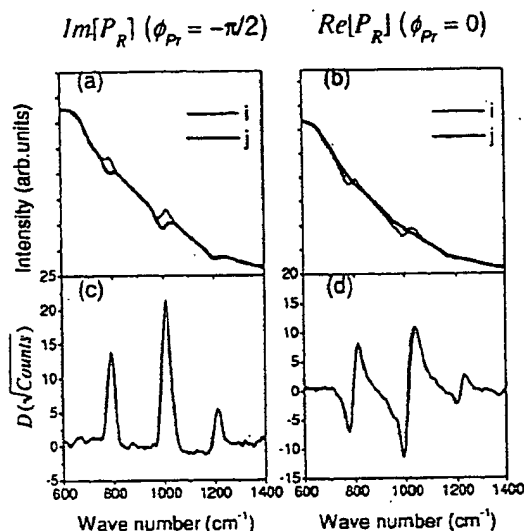


FIG. 3. DQSI-CARS of toluene: (a) and (b) The spectra in each polarization direction [i and j as in Fig. 2(b)] taken simultaneously in the imaging spectrometer. (c) and (d) the normalized difference spectra (D) according to Eq. (9). (a) and (c) are taken with $\phi_{\text{probe}} = -\pi/2$. (b) and (d) with $\phi_{\text{probe}} = 0$, respectively. Note that (c) and (d) correspond to the imaginary and real parts of the resonant CARS spectrum.

the higher order chirp, not just the quadratic phase modulation terms. Dispersion induced by most samples is negligible due to the short working distance ($280 \mu\text{m}$) of the microscope objective used in this experiment. After generating and collecting the CARS signal with microscope objectives (1.2 and 1.0 NA, respectively, infrared (IR) water immersion objectives, Olympus), the polarization is rotated by 45° with a Fresnel rhomb (achromatic half wave plate), and the i and j polarization signals are separated by a Wollaston prism. Directing the split beams (the i and j polarization signals) into an imaging spectrometer and onto a two dimensional CCD, we obtain both signal traces on every pulse [8,9,16]. The actual probe spectral linewidth in the experiment (30 cm^{-1} , corresponding to two pixels in the SLM) is wider than the Raman linewidth ($\sim 10 \text{ cm}^{-1}$), so Eq. (8) needs to be convoluted with the probe width. Note that we can simulate the experiment without the assumption of the narrow probe spectral width [Eq. (5)] by using the entire laser pulse spectrum in Eq. (2)–(4). However, we find that the general features are the same [16].

Figure 3 shows the experimental signal spectra along the i and j directions [Figs. 3(a) and 3(b)] and the normalized difference spectra according to Eq. (9) [Figs. 3(c) and 3(d)] with two different probe phases. As one would expect from Eq. (8), with $\phi_{\text{probe}} = -\pi/2$ the normalized difference signal (D) yields the imaginary part of the vibrational spectrum [Fig. 3(c)], and with $\phi_{\text{probe}} = 0$ the real part is obtained [Fig. 3(d)]. Note the similarity of Figs. 3(c) and 3(d) with the $\text{Im}[L]$ and $\text{Re}[L]$, respectively, shown in Fig. 1(a). As noted, the $\text{Im}[L]$ is what corresponds to the Raman signal [9].

Figure 4(a) shows the experimental DQSI-CARS spectra of several common lab solvents taken in a data acquisition

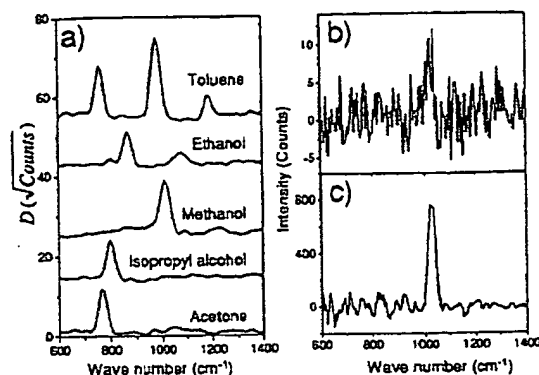


FIG. 4. (a) Experimental DQSI-CARS spectra of common lab solvents. The data are taken with the microscope setup in 10 ms experiment times. (b) and (c) Comparison of signal levels by the resonant-only CARS method and the homodyne-amplified DQSI-CARS method. (b) the phase- and polarization-controlled method according to Ref. [7]. (c) DQSI method under the same experimental conditions. The sample is 1 M KNO_3 solution in water and the experimental times are 10 ms. Note that this sample has ~ 40 times lower signal than toluene.

time of 10 ms. The measured average laser power is 40 mW just before the focusing microscope objective. The laser repetition rate is 90 MHz, and the estimated peak power is $\sim 2 \times 10^{13} \text{ W/cm}^2$ at the focus. A small drop of the sample is sandwiched between two microscope coverslips. The currently accessible CARS window is from 400 to 1500 cm^{-1} , although the signal decreases rapidly beyond 1200 cm^{-1} . The spectral resolution is around 35 cm^{-1} , which is a little broader than the two pixel width of the SLM (30 cm^{-1}) that defines the probe width [Fig. 2(a)].

Detecting the cross term, $P_{NR}(P_R^* + P_R)$ in Eq. (7), instead of $|P_R|^2$, has two other advantages for the interferometric retrieval of the complex spectral line shape function. First, P_R is amplified with the help of the much bigger P_{NR} , so-called homodyne amplification [6,17]. Second, the signal depends linearly on the sample concentration instead of quadratically [9]; a quadratic sample concentration dependence is the case for the normal CARS signal [1]. The linear concentration dependence is an important benefit, since it makes additional experimental improvements easier. For example, if one wishes to detect a sample at 10 times lower concentration, only 10 times better S/N is necessary, rather than 100.

Figures 4(b) and 4(c) demonstrate the homodyne amplification advantage that our DQSI-CARS technique provides. The sample is 1 M KNO_3 solution in water, which has a very weak CARS signal with a CCD exposure time of 10 ms. The same laser power as in Fig. 4(a) is used. We estimate the number of molecules in the excitation volume ($\sim 40 \text{ aL}$) is around 40 attomoles. Figure 4(b) shows a spectrum taken in a similar fashion to the phase- and polarization-controlled CARS method reported by Silberberg and co-workers [7]. In this technique, the nonresonant signal is blocked by a polarizer and only the resonant signal is measured. In Fig. 4(c), the spectrum is taken by the DQSI-CARS technique with

exactly the same experimental conditions (the same laser power and the same sample). Here we plot the difference between the signal traces ($S^i - S^j$) to directly compare the signal levels with the one in Fig. 4(b). As one can see in Figs. 4(b) and 4(c), the resonant signal is amplified by ~ 100 times. At the vibrational frequency of 1025 cm^{-1} , the S^i and S^j have signal intensities of $\sim 13\,000$ counts. This corresponds to a local oscillator of $\sim 110 \sqrt{\text{Counts}}$ and the amplification of the resonant signal matches well with the theoretical expectation. One disadvantage of our technique is that the signal is accompanied by shot noise originating from the nonresonant signals. With strong CARS-signal samples such as toluene, the signal-to-noise ratio (S/N) is slightly worse compared to Silberberg's original technique. However, for weak signal samples, our technique shows much better sensitivity as demonstrated in Figs. 4(b) and 4(c).

We also observed that the original phase- and polarization-controlled CARS method exhibits a problem with depolarization by the samples and optical components. Even if a small amount of the signal is depolarized, the resonant signal is dominated by the leakage of the nonresonant background, which can be bigger by orders of magnitude. The shot noise from this background will obscure the weak resonant signal. In our technique, the depolarization will also distort the vibrational peak shapes and change the base line level. Nevertheless, the noise level will be the same and make no change in the S/N ratio. So the DQSI-CARS method is more tolerant to sample depolarization.

One important question is how pure is the phase of the local oscillator and how it affects the interferometric modulations. Here the nonresonant and resonant signals generated by the pump/Stokes part of the pulse [Fig. 2(a)] serve as the local oscillator, which is the large broad component in Figs. 3(a) and 3(b). If the local oscillator contains a significant amount of a resonant signal generated from the pump/Stokes

part of the pulse, the interferometry will be contaminated by this sample-specific resonant signal. The relative ratio between P_R and P_{NR} at 788 and 1008 cm^{-1} , is approximately 10% for toluene [Fig. 3(a)]. $\alpha_{NR}/\alpha_R=500$ is required in Eqs. (7)–(9) to produce this amount of modulation. In most biological samples, this ratio will be significantly bigger by at least an order of magnitude because the resonant signal from the sample is small compared to the nonresonant signal from the solvent (water in most cases). From a numerical simulation with different values of α_{NR}/α_R , we find that even in the case of 10% modulation, the interferometry works reasonably well [16]. Even if the assumptions in Eq. (9) would break down in an extreme case, the result would be to distort the spectral shape, which would appear as a mixture of the imaginary and real parts, similar to previous multiplex CARS experiments [18]. Still, the position and amplitude of the vibrational peaks could be extracted by a numerical fitting process [18].

In conclusion, we demonstrate that it is possible to do full spectral interferometry with the resonant and nonresonant CARS signals generated from a single sample without a conventional interferometry setup. By combining the single pulse CARS and the DQSI techniques, we are able to retrieve the imaginary part of the resonant CARS spectra over the entire accessible multiplex CARS window. This novel technique connects the measured CARS spectrum directly to the Raman counterpart and also improves the signal sensitivity of multiplex CARS spectroscopy.

The authors gratefully acknowledge the Department of Energy (Contract No. DE-AC02-05CH11231) for the instrumentation used in this research and the National Science Foundation, Division of Materials Research, for support of personnel. A.G.C. acknowledges support from the National Science Foundation.

- [1] J. X. Cheng and X. S. Xie, *J. Phys. Chem. B* **108**, 827 (2004).
- [2] E. O. Potma, X. S. Xie, L. Muntean *et al.*, *J. Phys. Chem. B* **108**, 1296 (2004).
- [3] M. Muller and J. M. Schins, *J. Phys. Chem. B* **106**, 3715 (2002).
- [4] N. Dudovich, D. Oron, and Y. Silberberg, *Nature (London)* **418**, 523 (2002).
- [5] T. Brixner and G. Gerber, *Opt. Lett.* **26**, 557 (2001).
- [6] D. Oron, N. Dudovich, and Y. Silberberg, *Phys. Rev. Lett.* **89**, 273001 (2002).
- [7] D. Oron, N. Dudovich, and Y. Silberberg, *Phys. Rev. Lett.* **90**, 213902 (2003).
- [8] L. Lepetit, G. Cheriaux, and M. Joffe, *J. Opt. Soc. Am. B* **12**, 2467 (1995).
- [9] C. L. Evans, E. O. Potma, and X. S. Xie, *Opt. Lett.* **29**, 2923 (2004).
- [10] D. L. Marks, C. Vinegoni, J. S. Bredfeldt *et al.*, *Appl. Phys. Lett.* **85**, 5787 (2004).
- [11] M. D. Levenson and S. S. Kano, *Introduction to Nonlinear Spectroscopy* (Academic, San Diego, 1988).
- [12] F. R. Dollish, W. G. Fateley, and F. F. Bentley, *Characteristic Raman Frequencies of Organic Compounds* (Wiley, New York, 1974).
- [13] D. Lin-Vien, N. B. Colthup, W. G. Fateley *et al.*, *The Handbook of Infrared and Raman Characteristic Frequencies of Organic Molecules* (Academic, San Diego, 1991).
- [14] J. X. Cheng, A. Volkmer, L. D. Book *et al.*, *J. Phys. Chem. B* **106**, 8493 (2002).
- [15] V. V. Lozovoy, I. Pastirk, and M. Dantus, *Opt. Lett.* **29**, 775 (2004).
- [16] S.-H. Lim, A. G. Caster, and S. R. Leone (unpublished).
- [17] Some authors refer to this as a heterodyne amplification. In our terminology, homodyne and heterodyne are with respect to the frequencies of the signal and local oscillator. Here the signal and local oscillator have the same frequencies and we use "homodyne" instead of heterodyne.
- [18] G. W. H. Wurpel, J. M. Schins, and M. Muller, *J. Phys. Chem. B* **108**, 3400 (2004).

Switched Wave Packets: A Route to Nonperturbative Quantum Control

Jonathan G. Underwood,¹ Michael Spanner,^{1,2} Misha Yu. Ivanov,¹ Jeff Mottershead,¹
Benjamin J. Sussman,^{1,3} and Albert Stolow^{1,3,*}¹Steacie Institute for Molecular Sciences, National Research Council of Canada,
100 Sussex Drive, Ottawa, Ontario, Canada K1A 0R6²Department of Physics, University of Waterloo, Waterloo, Ontario, Canada N2L 3G1³Department of Physics, Queen's University, Kingston, Ontario, Canada K7L 3N6
(Received 19 February 2003; published 4 June 2003)

The dynamic Stark effect due to a strong nonresonant but nonionizing laser field provides a route to quantum control via the creation of novel superposition states. We consider the creation of a field-free "switched" wave packet through adiabatic turn-on and sudden turn-off of a strong dynamic Stark interaction. There are two limiting cases for such wave packets. The first is a Raman-type coupling, illustrated by the creation of field-free molecular axis alignment. An experimental demonstration is given. The second case is that of dipole-type coupling, illustrated by the creation of charge localization in an array of quantum wells.

DOI: 10.1103/PhysRevLett.90.223001

PACS numbers: 32.80.Qk, 42.50.Hz

The development of coherent laser sources and the control over optical phase implied has emerged as an important tool for the control of quantum processes. Brumer and Shapiro as well as Tannor and Rice developed coherent optical phase control schemes based on the quantum interference between two or more pathways to a degenerate target state [1]. Although these coherent control schemes are often based on a perturbative description in that the eigenstates of relevance are those of the field-free Hamiltonian, schemes using strong resonant or near-resonant laser fields have also been developed [2]. An alternative approach based on the nonlinear interaction of an adaptively shaped laser pulse using feedback-learning algorithms to optimize a chosen product was proposed by Rabitz [3]. This was most successfully demonstrated in the strong field fragmentation ionization of polyatomic molecules [4] and atomic ionization [5]. These schemes are nonperturbative in that the field-free Hamiltonian may not be pertinent, and they may take advantage of many processes including multiphoton resonances, dynamic Stark effects, propagation on multiple potential energy surfaces, and strong field ionization-fragmentation processes [6]. In nonionizing laser fields, strong shaped pulses have been used to control processes in condensed phases [7] and may take advantage of multiphoton resonances and intrapulse interferences [8] and dynamic Stark shifts. Although the underlying mechanisms are complex and difficult to elucidate, strong field shaped pulse feedback control has been as successful as coherent quantum interference control. Here we consider only to the dynamic Stark effect induced by nonresonant, nonionizing laser fields. By choice of laser frequency and intensity, complex competing processes might be eliminated.

As a first step to this nonperturbative control, we study experimentally and theoretically the creation of field-free

ground state superpositions via the adiabatic application of a strong nonresonant dynamic Stark coupling which is suddenly truncated, thus forming a wave packet. This "switched wave packet" will be very different in nature and composition than that created via resonant excitation or strong field ionization. We consider the interaction of a strong nonresonant laser field of the form $\mathbf{E}(t) = \hat{\mathbf{e}}\mathcal{E}(t)\cos(\omega t)$ with a quantum system, where $\hat{\mathbf{e}}$ is the direction of polarization of the electric field of frequency ω with a slowly varying envelope $\mathcal{E}(t)$. The Hamiltonian of the system in the presence of the laser field is then $H(t) = H_0 - \mathbf{d} \cdot \mathbf{E}(t)$, where H_0 is the field-free Hamiltonian and \mathbf{d} is the dipole moment of the system. The field-free eigenstates can often be separated into bands, as depicted in Fig. 1, representing the energy bands of a molecule, a set of quantum wells, a Stark or Zeeman manifold, or some other structure. If the optical frequency is greater than δ and smaller than Δ , the dynamics may be represented by an effective Hamiltonian where all other bands have been adiabatically eliminated. The equations of motion for the wave function $\Psi(t) = \sum_n a_n(t)e^{-iE_n t}|n\rangle$ expressed as a superposition of the initially populated band ($N = 0$) eigenstates are [9]

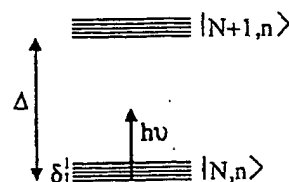


FIG. 1. A quantum system described by quantum numbers N and n . The laser frequency is chosen to be much larger than the intraband spacing δ (described by n) and much smaller than the interband spacing Δ (described by the N).

$$i\dot{a}_n(t) = \sum_m a_m(t) e^{i\omega_{nm}t} H_{nm}^{\text{eff}}(t), \quad (1)$$

where the leading terms of the effective Hamiltonian are

$$H^{\text{eff}}(t) = V^{\text{dipole}}(t) + V^{\text{Raman}}(t), \quad (2)$$

$$V_{nm}^{\text{dipole}}(t) = -\mathcal{E}(t) \cos(\omega t) \hat{\mathbf{e}} \cdot \mathbf{d}_{nm}, \quad (3)$$

$$V_{nm}^{\text{Raman}}(t) = -\frac{1}{4} |\mathcal{E}(t)|^2 \hat{\mathbf{e}}^* \cdot \boldsymbol{\alpha}_{nm}(\omega) \cdot \hat{\mathbf{e}}, \quad (4)$$

where $\mathbf{d}_{nm} = \mathbf{d}_{0n0m}$ is the transition dipole moment and

$$\boldsymbol{\alpha}_{nm}(\omega) = \sum_{N \neq 0} \sum_i \mathbf{d}_{0nN_i} \mathbf{d}_{N_i0m} \left[\frac{1}{\omega_{N_i} + \omega} + \frac{1}{\omega_{N_i} - \omega} \right] \quad (5)$$

In the situation where the intraband dipole moments are large, $V_{nm}^{\text{dipole}}(t)$ will dominate and the response follows the instantaneous electric field. Conversely, when the interband dipole moments are large, $V_{nm}^{\text{Raman}}(t)$ dominates and the response follows the electric field envelope $|\mathcal{E}(t)|^2$. These situations represent the two limiting cases for switched wave packets, and an example of each will be presented below.

When the interaction is turned on adiabatically [10], each eigenstate of the field-free Hamiltonian evolves into a single instantaneous eigenstate of the laser dressed system. The accumulated phase is given by the time integral of the instantaneous eigenenergy. Adiabatic behavior is achieved through sufficiently slow turn-on of the laser field and limiting the intensity to avoid crossing of the dressed states [11]. For the limiting case of a Raman dominated interaction, the application of the adiabatic approximation is clear and the relevant states and quasienergies are easily found from Eq. (4) [11]. For the case of a dipole dominated interaction, the Floquet states which explicitly include the fast electric field oscillations provide a useful description [12]. The adiabatic condition here refers to varying the envelope and carrier frequency slowly enough to avoid transferring population between the Floquet states. In either limiting case, a nonadiabatic change in the interaction leads to a superposition of dressed states and beats at frequencies corresponding to the differences between quasienergies of the dressed states [10]. This results in Rabi oscillations in the field-free state populations. A sudden truncation of the field will project the dressed state onto the field-free states forming a wave packet which subsequently evolves under the field-free Hamiltonian. The content of this wave packet will depend upon the nature of the strong interaction, the turn-on time τ_{on} , and the switching time τ_{sw} .

We first consider the limiting case of a switched wave packet in which the interaction is dominated by the Raman term, Eq. (4), an example being molecular rotors. An anisotropic linear molecule placed in a linearly polarized laser field experiences a potential of the form [13]

$$V(\theta, t) = -\frac{1}{4} (\alpha_{\parallel} - \alpha_{\perp}) |\mathcal{E}(t)|^2 \cos^2(\theta), \quad (6)$$

where θ is the angle between the laser polarization and the molecular axis, α_{\parallel} and α_{\perp} are the polarizability components parallel and perpendicular to the molecular axis, and the term in square brackets corresponds to the well depth $U(t)$. The Hamiltonian is then $H = BJ^2 + V(\theta, t)$, where J is the angular momentum operator and B is the molecular rotational constant. The aligned (pendular) molecule is described by a superposition of field-free rotational eigenstates $\psi(t) = \sum a_{JM} |JM\rangle$. Since $V(\theta, t)$ is independent of ϕ , the Hamiltonian is separable in θ and ϕ , implying conservation of M . We consider here a pulse shape of the form

$$|\mathcal{E}(t)|^2 = \begin{cases} \mathcal{E}_0^2 \sin^2\left(\frac{\pi t}{2\tau_{\text{on}}}\right), & t \leq \tau_{\text{on}}, \\ \mathcal{E}_0^2 \cos^2\left(\frac{\pi(t-\tau_{\text{on}})}{2\tau_{\text{sw}}}\right), & \tau_{\text{on}} < t \leq \tau_{\text{on}} + \tau_{\text{sw}}. \end{cases} \quad (7)$$

For each initial J , a single pendular state will be created if τ_{on} is long enough for adiabatic behavior. If τ_{on} is too short, the state created will be a superposition of pendular eigenstates and the wave packet will have additional time dependence to its alignment [13]. A switched rotational wave packet calculation is depicted in Fig. 2. A strong field pulse with $\tau_{\text{on}} = 15$ ps was used to create a switched wave packet in N_2 at 50 K. Alignment is measured by the expectation value of $\cos^2(\theta)$. At time t_{sw} , the pendular state is suddenly projected with $\tau_{\text{sw}} = 0.1$ ps onto the free rotor states, forming a field-free rotational wave packet. We present an experimental demonstration of a switched rotational wave packet. Briefly, a 1.064 μm laser pulse with τ_{on} of 125 ps and τ_{sw} of ~ 100 fs was generated using a plasma shutter method. A femtosecond Ti:Sa oscillator (80 fs, 800 nm) and a picosecond Nd:YAG oscillator (125 ps, 1.064 μm) were electronically synchronized with a timing jitter of ~ 1 ps. Both oscillator pulses were amplified at a repetition rate of 1 kHz. A two stage Ti:Sa amplifier system produced 2.5 mJ, 80 fs pulses. The

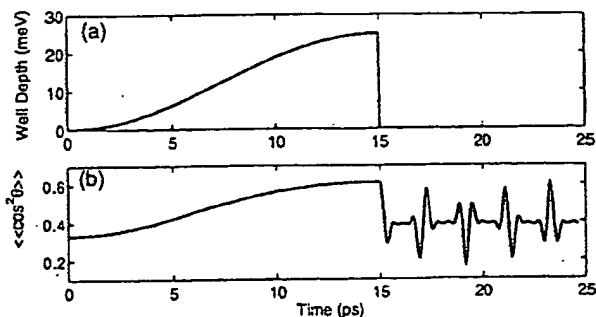


FIG. 2 Switched rotational wave packet in N_2 at 50 K. (a) The well depth, $U(t)$, created by a laser field with $\tau_{\text{on}} = 15$ ps and $\tau_{\text{sw}} = 0.1$ ps. (b) The time-dependent alignment of the ensemble showing wave packet revivals and field-free alignment.

picosecond amplifier was a diode pumped Nd:YVO₄ laser [14] producing 1 mJ, 125 ps pulses. The 1.064 μm beam was focused into an ethylene glycol jet with an intensity of $\sim 5 \times 10^{11} \text{ W cm}^{-2}$, below the threshold for breakdown. A fraction (600 μJ) of the 800 nm beam was focused to the same spot position and size in the jet with a peak intensity of $\sim 5 \times 10^{14} \text{ W cm}^{-2}$, well above the threshold for breakdown. The 800 nm triggered plasma acted as a shutter for the 1.064 μm pulse, truncating its transmission. In our case, the plasma was sustained by the intense 1.064 μm pulse. The transmitted 1.064 μm light had $\tau_{\text{on}} = 125 \text{ ps}$ and $\tau_{\text{sw}} \sim 100 \text{ fs}$, as seen in Fig. 3(a). Residual scattered 800 nm light copropagating with the 1.064 μm pulse was removed by dichroic beam splitters.

The 1.064 μm switching pulse was focused into a gas cell containing CO₂ (300 torr) with peak intensity of $\sim 10^{11} \text{ W cm}^{-2}$ corresponding to a well depth of $\sim 0.7 \text{ cm}^{-1}$. The alignment induced by the switching pulse was probed via optical Kerr effect (OKE) rotation of a copropagating weak 80 fs probe pulse, derived from the remainder of the 800 nm 80 fs pulse. Prior to the gas cell, this probe passed through a Glan-Taylor polarizer oriented at $+45^\circ$ clockwise with respect to the switching pulse. The 800 nm probe energy transmitted through a second crossed polarizer (-45°) was recorded as a function of time delay between the switching and probe pulses ($\Delta t = t_{\text{probe}} - t_{\text{sw}}$). The extinction ratio of the crossed polarizer pair was $< 10^{-6}$. The transmitted probe pulse was dispersed through a 0.4 m monochromator and detected with a photomultiplier tube.

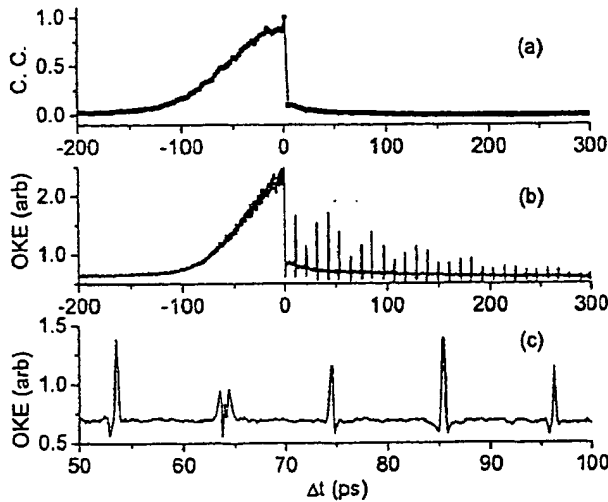


FIG. 3. Experimental demonstration of switched wave packets. (a) Cross correlation (C.C.) of the switching 1.064 μm laser pulse with an 80 fs, 800 nm pulse: $\tau_{\text{on}} = 125 \text{ ps}$, $\tau_{\text{sw}} = 110 \text{ fs}$. (b) Optical Kerr effect signal generated by the switching laser pulse from (a), focused ($f/30$) into 300 torr, 300 K CO₂ gas. (c) Expanded region from (b) showing rotational wave packet dynamics and field-free alignment in CO₂.

The OKE signal intensity is given by $I(\Delta t) = [(\cos^2 \theta) - \frac{1}{3} + C]^2$ [15]. The constant C describes the heterodyned signal contribution. Here the polarization rotation by the cell windows provided the local oscillator field for the heterodyne contribution. In Fig. 3(b), we plot the observed signal as a function of time delay between the switching and probe pulses. During their overlap, there is both an electronic and a nuclear component to the signal. After the switching of the 1.064 μm pulse, there is clear rotational revival structure and associated molecular axis alignment indicative of wave packet formation (we note, however, that, due to the room temperature of the gas sample, the macroscopic alignment is small). In this case, the revival structure decays in amplitude due to collisional decoherence. We note that the extension of the switched rotational wave packet method using elliptically polarized light provides a convenient route to field-free three-dimensional molecular alignment [16].

We next consider the limiting case of a switched wave packet in which the interaction with the laser field is dominated by the dipole interaction term, Eq. (3), an example being a coupled quantum well system. These systems respond to the instantaneous electric field and show dynamics dependent upon the carrier phase of the electric field relative to the envelope. Quantum well systems typically exhibit miniband widths much smaller than the interband separation. We therefore neglect the effects of interband transitions, and consider only the intraband dynamics. Within the tight binding (nearest neighbor) approximation, the Hamiltonian for a particle subject to a periodic potential is [17]

$$H_0 = \sum_{n=1}^N E_n |n\rangle \langle n| + \sum_{n=1}^{N-1} \Omega_n (|n\rangle \langle n+1| + |n+1\rangle \langle n|), \quad (8)$$

where N is the number of wells. This Hamiltonian is expressed in terms of the Wannier states $|n\rangle$ [18] with on-site energy E_n localized on the well n . Ω_n is the coupling between the n and $n+1$ wells. The interaction with a laser field polarized along the interwell direction is $H_I = -E(t)\mu = -edE(t) \sum_{n=1}^N n |n\rangle \langle n|$, where d is the well spacing. If the interaction is turned on adiabatically, each eigenstate of the field-free Hamiltonian will evolve into a single Floquet state. The quasienergy of the k th Floquet state is given by $\epsilon_k(t) = J_0[edE(t)/\omega]E_k$ [17]. The degeneracy at the zeros of the Bessel function means that the Wannier states $|n\rangle$ become eigenstates, electron tunneling is coherently suppressed, and dephasing of the Floquet states is inhibited [17]. This fact has previously been explored in relation to creating charge localization in such systems [19]. We show here that a switched wave packet generates time-dependent field-free charge localization. We expand the time-dependent wave function in terms of Wannier states, $\psi(t) = \sum_j a_j(t) |j\rangle$, and propagate numerically the equations of motion of the $a_j(t)$

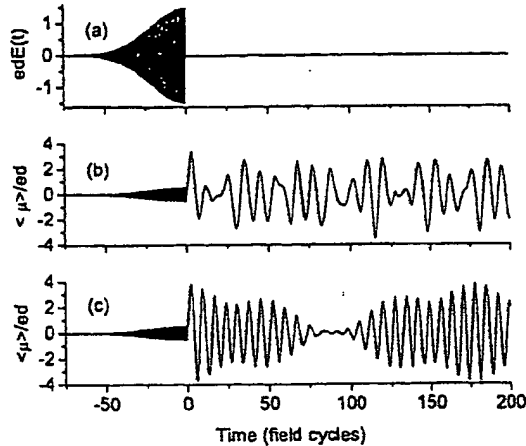


FIG. 4. Switched wave packets in a set of ten coupled quantum wells initially in the ground eigenstate. On-site energies are ϵ_j and $\Omega_j/\omega = 0.25$ for all wells. (a) Laser electric field $edE_0/\omega = 1.5$ with $\tau_{on} = 30$ cycles, $\tau_{sw} = 0.1$ cycles. (b) Induced dipole moment for carrier phase $\phi = 0.0$. (c) Induced dipole moment for carrier phase $\phi = \pi/4$.

coefficients. The crossing of the Floquet states restricts the value of $edE(t)/\omega$ to $\lesssim 2$ if adiabatic behavior is to be maintained. In Fig. 4, we show the creation of a switched wave packet in an array of ten wells with equal coupling strengths. The laser pulse, Fig. 4(a), has the form

$$E(t) = \mathcal{E}(t) \cos(\omega t + \phi),$$

$$\mathcal{E}(t) = \begin{cases} \mathcal{E}_0 e^{-t^2/\tau_{on}^2}, & t < 0, \\ \mathcal{E}_0 e^{-t^2/\tau_{sw}^2}, & t > 0, \end{cases} \quad (9)$$

where ϕ is the carrier phase of the electric field relative to the envelope. Since the Floquet states are $2\pi/\omega$ periodic, we require $\tau_{sw} \ll 2\pi/\omega$ to maintain the field induced superposition. In Figs. 4(b) and 4(c), we plot the induced dipole moment (charge localization) for two choices of the absolute carrier phase. During τ_{on} , we observe oscillations at the field frequency ω with only moderate localization as the tunneling splitting is reduced by the oscillating field. After τ_{sw} , the superposition evolves under the field-free Hamiltonian and strong time-dependent localization is observed, corresponding to induced charge oscillation in the wells. This localization is substantially larger than during the presence of the laser field and is seen to depend upon the carrier phase. This example is an illustration of a quantum control scenario requiring absolute carrier-envelope phase control [20].

In this Letter, we have explored the use of a strong dynamic Stark interaction with a quantum system for the creation of novel field-free superposition states. The evolution of these field-free switched wave packets contains information about the nature of the strong interaction as well as providing field-free localization. This nonresonant, nonperturbative, but nonionizing regime of inter-

action could provide new routes to the control of molecular dynamics via the time-dependent modification of an effective Hamiltonian. Control is exerted by reversibly modifying the propagator *during* propagation, as opposed to using only the field-free propagator or the multiple propagators implicit in strong field ionization.

*Electronic address: albert.stolow@nrc.ca

- [1] P. Brumer and M. Shapiro, *Annu. Rev. Phys. Chem.* **43**, 257 (1992), and references therein; R. J. Gordon and S. A. Rice, *Annu. Rev. Phys. Chem.* **48**, 601 (1997), and references therein.
- [2] K. Bergmann *et al.*, *Phys. Rev. Lett.* **70**, 1003 (1998); A. Shnitman *et al.*, *Phys. Rev. Lett.* **76**, 2887 (1996); M. N. Kobrak and S. A. Rice, *J. Chem. Phys.* **109**, 1 (1998).
- [3] R. S. Judson and H. Rabitz, *Phys. Rev. Lett.* **68**, 1500 (1992).
- [4] A. Assion *et al.*, *Science* **282**, 919 (1998); R. J. Levis *et al.*, *Science* **292**, 709 (2001).
- [5] M. Strehle and G. Gerber, *AIP Conf. Proc.* **525**, 295 (2000).
- [6] E. Constant *et al.*, *Phys. Rev. Lett.* **76**, 4140 (1996); *Molecules in Laser Fields*, edited by A. D. Bandrauk (Dekker, New York, 1994); H. Stapelfeldt *et al.*, *Phys. Rev. Lett.* **74**, 3780 (1995); M. Lezius *et al.*, *Phys. Rev. Lett.* **86**, 51 (2001).
- [7] T. Brixner *et al.*, *Nature (London)* **414**, 57 (2001); B. J. Pearson *et al.*, *Phys. Rev. A* **63**, 063412 (2001).
- [8] V. V. Lozovoy *et al.*, *J. Chem. Phys.* **118**, 3187 (2003).
- [9] B. W. Shore, *The Theory of Coherent Atomic Excitation* (Wiley, New York, 1990), Vols. I and II.
- [10] G. L. Peterson and C. D. Cantrell, *Phys. Rev. A* **31**, 807 (1985).
- [11] A. Messiah, *Quantum Mechanics* (Dover, New York, 1999).
- [12] K. Drese and M. Holthaus, *Eur. J. Phys. D* **5**, 119 (1999); H. P. Breuer *et al.*, *Z. Phys. D* **10**, 13 (1988).
- [13] C. H. Lin *et al.*, *Appl. Phys. Lett.* **10**, 397 (1971); J. P. Heritage *et al.*, *Phys. Rev. Lett.* **34**, 1299 (1975); B. A. Zon and B. G. Katsnel'son, *Sov. Phys. JETP* **42**, 595 (1976); B. Friedrich and D. Herschbach, *Phys. Rev. Lett.* **74**, 4623 (1995); J. J. Larsen *et al.*, *J. Chem. Phys.* **111**, 7774 (1999); J. Ortigoso *et al.*, *J. Chem. Phys.* **110**, 3870 (1999); T. Seideman, *J. Chem. Phys.* **115**, 5965 (2001); F. Rosca-Pruna and M. J. J. Vrakking, *Phys. Rev. Lett.* **87**, 153902 (2001).
- [14] J. E. Bernard and A. J. Alcock, *Opt. Lett.* **19**, 1861 (1994).
- [15] V. Renard *et al.*, *Phys. Rev. Lett.* **90**, 153601 (2003).
- [16] J. J. Larsen *et al.*, *Phys. Rev. Lett.* **85**, 2470 (2000).
- [17] M. Holthaus and D. W. Hone, *Philos. Mag. B* **74**, 105 (1996).
- [18] M. P. Marder, *Condensed Matter Physics* (Wiley, New York, 2000).
- [19] J. Karczmarek *et al.*, *Phys. Rev. A* **60**, R4225 (1999).
- [20] R. K. Shelton *et al.*, *Science* **293**, 6668 (2001).

Controlling ground-state rotational dynamics of molecules by shaped femtosecond laser pulses

M. Renard, E. Hertz,* B. Lavorel, and O. Faucher

Laboratoire de Physique de l'Université de Bourgogne, UMR CNRS 5027, Boîte Postale 47 870, 21 078 Dijon cedex, France

(Received 18 November 2003; published 8 April 2004)

We report controlled excitation of ground-state rotational wave packet by pulse-shaping technique. The experiment is conducted in nitrogen (N_2) at room temperature and atmospheric pressure. A femtosecond laser pulse produces rotational coherences in the vibronic ground state of N_2 through an impulsive Raman process. The laser pulse is tailored using a spatial light modulator producing spectral phase modulation. Periodic phase steps are applied in order to control the excitation of specific rotational Raman transitions. The outcome is the modification of the relative excitation between odd and even rotational states which allows the control of the symmetry and rephasing period of the wave packet.

DOI: 10.1103/PhysRevA.69.043401

PACS number(s): 33.80.Wz, 42.50.Ct, 34.50.Rk

I. INTRODUCTION

Investigations devoted to laser-controlled chemical reactions have stimulated considerable interest in the past decades. The basic idea consists of using laser parameters as control knobs in order to drive the outcome of photoexcitation into specific final states associated with the desired reaction products. Many control schemes relying on quantum interference effects have been developed to achieve this goal. The so-called "phase control" is based, for instance, on the coherent excitation of quantum systems by a bichromatic field inducing two phase-related pathways with a different number of photons [1,2]. The excitation can be controlled through the relative phase between the two frequencies. Apart from transition probability, autoionization rate [3], angular distribution of photoelectrons and photofragments [4], as well as ionization and dissociation branching ratio [5] have been thus manipulated. With the onset of the ultrashort laser technology, new possibilities have emerged in the field of coherent control. An approach proposed by Rabitz [6] consists in producing laser pulse shapes specifically designed to control the outcome of photoreactions. Primary works have been conducted with linearly chirped laser pulses but the potentiality of such control has been greatly expanded by the advances in terms of pulse-shaping techniques [7]. Nowadays, devices producing almost any arbitrary pulse shapes are available and a large amount of experiments using "pulse shapers" have been reported. The conjunction of such control technique with feedback loop algorithm is frequently exploited in order to determine optimum laser pulse shapes when the complexity of the underlying physics prevents any reliable predictions [8–13]. Pulse-shaping techniques [14–21] as well as other approaches [22–24] have been notably applied to exercise control of ground-state molecular dynamics. The latter features major interest related to the involvement of vibrational or rotational wave packets in a wide area of quantum dynamics. The temporal evolution of rotational wave packets (RWPs) gives, for instance, access to

structural information and allows diagnostics of molecular sample [25,26]. The production of a RWP with strong laser fields leads to macroscopic molecular alignment along the laser polarization [27–29]. Long-standing questions linked to orientational dependency of specific physical processes can be therefore settled by conducting analyses with aligned molecules [30]. Coherent rotational and vibrational molecular motions, impulsively [31–34] or adiabatically [35–38] excited, induce also a modulation of the refraction index well suited for temporal phase modulation. Such molecular phase modulation has been applied for spectral broadening and ultrashort optical pulse generation [31–40]. Relevance of this technique for optimization [41] of phase matching in harmonic generation has been considered too. In all these regards, investigations which aim at controlling rotational or vibrational dynamics feature appealing applications.

We demonstrate in this paper the control of rotational dynamics in the molecular vibronic ground state of N_2 . The RWP is produced by a phase-shaped femtosecond laser pulse via an impulsive stimulated Raman excitation. The detection of its temporal dynamics is based on the Raman induced polarization spectroscopy (RIPS) technique. The spectral phase modulation is imprinted to the excitation field using a spatial light modulator (SLM). We have opted for judicious periodic spectral phase steps, which takes advantage of the regular energy spacing between the Raman transition frequencies. We demonstrate selective excitation of specific rotational Raman transitions. The relative even and odd rotational states' contribution to the RWP is notably controlled and, therefore, the symmetry and revival period of the wave packet.

II. EXPERIMENTAL SETUP

An overview of the experimental setup is depicted in Fig. 1. The laser apparatus is based on a chirped pulse amplified Ti:sapphire femtosecond laser. The system operates at 20 Hz repetition rate and delivers pulses of 100 fs duration around 800 nm. The output beam is split in two parts to produce the pump and probe beams. The pump passes through a pulse shaper detailed below. The relative delay between pump and probe pulse is adjusted via a corner cube retroreflector

*Corresponding author.

Email address: edouard.hertz@u-bourgogne.fr

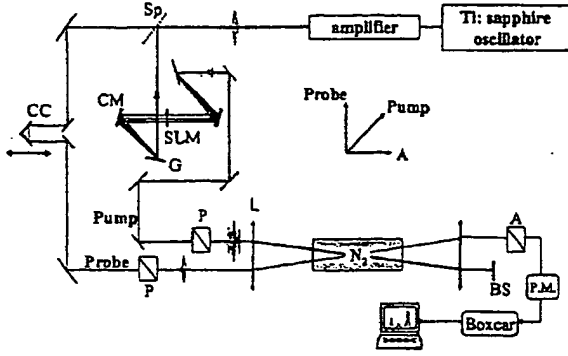


FIG. 1. Experimental setup. Sp, beam splitter; L, lens ($f = 175$ mm); CC, corner cube; CM, cylindrical mirror ($f = 200$ mm); G, gratings (1200 lines/mm); SLM, spatial light modulator (1×128 pixels); P, polarizer; A, analyzer; BS, beam stop; PM, photomultiplier. The relative field polarization of the pump, probe, and analyzer is depicted in the center of the figure.

mounted on a motorized linear stage. The relative polarization of the pump and probe beam is set at 45° with respect to each other via two polarizers. The two beams are then focused by a lens ($f = 175$ mm) and cross, at small angle ($\approx 5^\circ$), in a gas cell filled with N_2 under atmospheric pressure. Typical pump and probe energy are, respectively, $50 \mu\text{J}$ and $2 \mu\text{J}$. The intensity at the laser focus for the pump and probe beam is, respectively, $4 \text{ TW}/\text{cm}^2$ and $0.2 \text{ TW}/\text{cm}^2$. At the exit of the cell, the pump beam is blocked whereas the probe passes through an analyzer (A) polarized at 90° with respect to its initial polarization. The anisotropy of the sample induced by the pump interaction is thus detected through the depolarization of the probe with a photomultiplier. The signal, sampled by a boxcar, is stored in a personal computer.

The control of the wave packet is established by tailoring the pump pulse via a conventional 4f-pulse shaper [7]. A programmable spatial light modulator is placed in the Fourier plane of the pulse shaper composed of a pair of holographic gold coated gratings and cylindrical mirrors. The spectral phase modulation of the laser can be controlled by applying appropriate voltages to the pixels. The pixel spacing is $100 \mu\text{m}$ center to center and for some reasons explained later on; the frequency spatial distribution has been finely adjusted in order to reach the desired spectral sampling of $0.79 \times 10^{12} \text{ rad s}^{-1}/\text{pixel}$.

III. MODEL

As mentioned previously, the rotational wave packet is generated in the molecular vibronic ground state through an impulsive nonresonant Raman process. The laser coupling for a specific Raman transition of pulsation ω_j (with J the rotational quantum number) is proportional to

$$F(\omega_j) = \int_{-\infty}^{+\infty} E(\omega') E^*(\omega' - \omega_j) d\omega', \quad (1)$$

denoted hereafter "Raman field excitation." $E(\omega)$ refers to the spectral electric field. By developing the latter in terms of amplitude $\varepsilon(\omega)$ and phase $\phi(\omega)$,

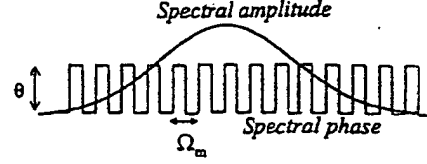


FIG. 2. Schematic representation of a periodic phase step modulation of the spectral laser phase.

$$E(\omega) = \varepsilon(\omega) \exp[i \phi(\omega)] \quad (2)$$

the factor $F(\omega_j)$ becomes

$$F(\omega_j) = \int_{-\infty}^{+\infty} \varepsilon(\omega') \varepsilon(\omega' - \omega_j) \exp[i \Delta \phi(\omega')] d\omega', \quad (3)$$

with

$$\Delta \phi(\omega') = \phi(\omega') - \phi(\omega' - \omega_j) \quad (4)$$

the phase difference between each pair of spectral components ($\omega', \omega' - \omega_j$) involved in the Raman excitation. According to Eq. (3), a control of both phase and amplitude of the Raman field excitation $F(\omega_j)$ is achieved by modifying the spectral laser phase. This effect, which results from quantum interference between excitation channels combining different laser frequencies, has been termed [42] "multiphoton intrapulse interference." When a periodic phase step of magnitude θ is imprinted on a symmetric spectral amplitude (Fig. 2), two specific values of the modulation period Ω_m are of a particular interest for selective excitation of Raman modes. If the Raman transition frequency ω_j is a multiple of Ω_m (i.e., $\omega_j = N\Omega_m$ with N integer), then the spectral phase difference $\Delta \phi(\omega') = 0$ independently of ω' . As a result, the excitation is similar to the one achieved with a Fourier-transform-limited pulse. Whereas if ω_j is a half-integer value of Ω_m [i.e., $\omega_j = (N + 1/2)\Omega_m$], the phase difference $\Delta \phi(\omega') = \pm \theta$ and the Raman field excitation is modulated by a $\cos(\theta)$ term. These results can be summarized as follows:

$$\omega_j = N\Omega_m \Rightarrow \Delta \phi(\omega') = 0, \quad \forall \omega' \Rightarrow F(\omega_j) = F_{\text{TLF}}(\omega_j), \quad (5a)$$

$$\omega_j = (N + 1/2)\Omega_m \Rightarrow \Delta \phi(\omega') = \pm \theta, \quad \forall \omega' \Rightarrow F(\omega_j) = F_{\text{TLF}}(\omega_j) \cos(\theta), \quad (5b)$$

where $F_{\text{TLF}}(\omega_j)$ denotes the Raman field excitation at ω_j with a Fourier-transform-limited pulse, i.e., $\theta = 0$. Thus, in the conditions described by Eq. (5b), the amplitude (and sign) of Raman excitations can be controlled at any desired level by adjusting the magnitude of the phase step θ .

When an ensemble of molecules is considered, the wave packet is built from the contribution of the whole set of populated rotational states excited within the laser bandwidth. The temporal evolution of the RWP induced by the phase-shaped femtosecond laser pulse is monitored through the time-resolved polarization technique RIPS. Periodic rephasing of the RWP induces an orientational anisotropy of the sample detected by measuring the polarization rotation of

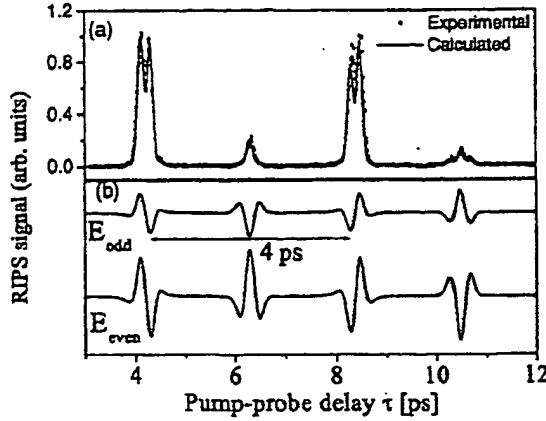


FIG. 3. (a) RIPS signal produced by an unshaped ($\theta=0$) pump pulse. (b) Contribution of odd and even rotational states to the overall signal (a). The latter is obtained by the sum squared of the odd and even contributions. The indicated arrow is used for the time-domain analysis (see text).

a time-delayed probe pulse. The signal corresponds thus to the time integral of the signal electric field squared detected through the analyzer (Fig. 1). An analytic expression of this signal as a function of the pump-probe delay τ can be written [43]:

$$I(\tau) \propto \int_{-\infty}^{+\infty} |E_{sig}(t)|^2 dt \propto \int_{-\infty}^{+\infty} \left| \Lambda(t-\tau) \text{Im} \left(\sum_j T_j F(\omega_j) \times \exp(-i\omega_j t - \gamma_j t) \right) \right|^2 dt, \quad (6)$$

in which E_{sig} is the signal field. Λ refers to the temporal profile of the probe envelope, T_j is a factor depending on molecular parameters, and γ_j stands for the Raman linewidth. It should be mentioned that the factor T_j depends on the rotational quantum number J and is proportional to the nuclear spin degeneracy factor g_J .

The signal produced in N_2 with a Fourier-transform-limited pulse ($\theta=0$) is depicted in Fig. 3(a) together with the calculated trace obtained from direct computation of Eq. (6). The observed alternation of small and large transients is specific to linear molecules with a center of symmetry and a nonzero nuclear spin. It results from the difference of spin degeneracy factor between rotational states of odd- and even- J values, respectively, equal to 3 and 6 in N_2 . This point is illustrated in Fig. 3(b), where the contribution to the theoretical signal of odd and even rotational states is plotted. It is shown that even rotational levels contribute to a signal field E_{even} two times larger than E_{odd} , the signal field produced by the odd distribution. As a result, the small transient recurrences observed in Fig. 3(a) arise from partial destructive interference between odd and even rotational distributions. With no alternation in the spin factor degeneracy, both odd and even rotational wave packet contributions would cancel each other out at these particular delays leading to a period of recurrence $T=1/(4Bc)=4.2$ ps (with $B=1.989$ cm $^{-1}$ the rotational constant). It should be noted that transients ob-

served in the signal RIPS reflect molecular alignment [28] occurring periodically subsequent to the interaction with the pump. In the present work, the extent of alignment is rather weak due to the low-field regime under which the experiment is conducted.

IV. RESULTS AND DISCUSSION

As detailed above, interference between odd and even rotational Raman modes plays a crucial role in the dynamics of the wave packet. In this respect, the controlled excitation of even rotational components, while the excitation of the odd ones remains unaffected as compared to the one produced with a Fourier-transform-limited pulse, reveals a number of attractive potentialities. This control is in principle achieved when all the even- J -value frequencies fulfilled the conditions of Eq. (5b), while the odd ones satisfy Eq. (5a). Unfortunately, such requirements cannot be strictly satisfied for all J . A satisfactory solution is to approach these criteria with the Raman transitions prevailing in the signal. With an unshaped laser pulse, the odd and even rotational levels having the prominent contribution in the RWP are $J=7$ and $J=8$, respectively. Therefore, the modulation period Ω_m should fulfill the following set of equations:

$$\omega_8 = (N + 1/2)\Omega_m, \quad (7a)$$

$$\omega_7 \equiv N\Omega_m. \quad (7b)$$

For a linear molecule in $^1\Sigma$ state, the pulsation of Raman transition is $\omega_J=4\pi Bc(2J+3)$ (disregarding the centrifugal distortion). For N_2 molecule, it leads to

$$\Omega_m = 16\pi Bc(19/18) = 3.16 \times 10^{12} \text{ rad/s}, \quad (8a)$$

$$N = 4. \quad (8b)$$

This spectral modulation does not satisfy Eqs. (5a) and (5b) for all odd- and even- J values, respectively. Nevertheless, it provides phase difference $\Delta\phi$ close to the ones defined in these equations as far as low ($J \leq 7$) and high ($J \geq 8$) J values are not concerned. The latter two correspond indeed to intermediate cases between Eqs. (5a) and (5b). The value of the modulation period $\Omega_m=3.16 \times 10^{12}$ rad/s is quite small with respect to the resolution of the 128 pixel modulator. When the spatially dispersed frequency spectrum matches the full aperture of the SLM, Ω_m covers an aperture equivalent to about 4 pixels. The frequency spatial distribution has been finely adjusted by tilting the grating angle in the shaper in order to reach the exact aperture of 4 pixels for Ω_m , corresponding to a spectral sampling of 0.79×10^{12} rad s $^{-1}$ /pixel. We emphasize that the above procedure could be avoided by using a modulator with a larger number of pixels.

Our primary goal is to manipulate the wave packet dynamics by controlling the relative excitation between odd and even rotational distributions. As already mentioned, the occurrence of small transient recurrences in Fig. 3(a) is caused by the difference of the spin degeneracy factor for odd and even rotational levels. With the same factor, these

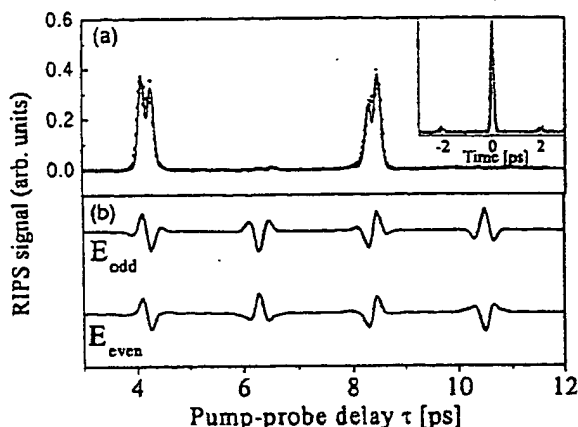


FIG. 4. (a) RIPS signal produced by a phase-shaped pump pulse [$\theta=1.18(\pi/3)$] with the inset showing intensity cross correlation associated with this modulation. (b) Even rotational state contribution (E_{even}) is reduced by a factor of 2 compared to an exciting Fourier-transform-limited pulse (see text).

two distributions would interfere destructively at these particular delays. We propose at first to use the periodical phase modulation to balance this effect. The spin factor degeneracy for states of even- J values is twice larger than for the odd ones, and thus their excitation should be attenuated by a factor 2 with respect to the odd ones. In the conditions defined by Eq. (8), we should be able to control the Raman excitation of even- J values, while leaving almost unchanged the excitation of the odd ones. By applying a spectral modulation of magnitude $\theta=\pi/3$, the excitation of even components is in principle modified by a factor $\cos(\pi/3)=1/2$ [Eq. (5b)]. Actually, a slight deviation from this value $\theta=\pi/3$ must be considered as a result of the approached solution found in Eq. (8). The correction factor, deduced empirically by numerical simulation, leads to an amplitude modulation of $\theta=1.18(\pi/3)$. The resulting RIPS trace obtained with such spectral modulation [Fig. 4(a)] exhibits the expected transient suppression for pump-probe delays $\tau=6.3$ and 10.5 ps. The bottom panel corroborates the achievement of the sought after effect since equivalent contribution for odd and even components is observed. Perfect destructive superposition occurs for $\tau=6.3$ and 10.5 ps, leading to the modification of revival period. By modulating the spectral phase with a periodic phase step, we demonstrate therefore the possibility of controlling the rephasing properties of a rotational wave packet. The electric-field excitation synthesized by such phase modulation consists of a pulse train as shown in inset by the intensity cross correlation (displaying the intensity squared). In the same spirit, it is possible to annihilate the excitation of even rotational components by using a value $\theta\equiv\pi/2$ [$\theta=1.11(\pi/2)$ precisely]. In this case, recurrences of equal amplitude are observed [Fig. 5(a)] with a half periodicity $T=1/(8Bc)=2.1$ ps. Figure 5(b) displays the sought after effect with a quasiexclusive excitation of odd rotational states. In the molecule N_2 , the odd rotational levels are antisymmetric with a negative parity, whereas even are symmetric with a positive parity. The prominent excitation of odd rotational components leads thus to the production of a wave

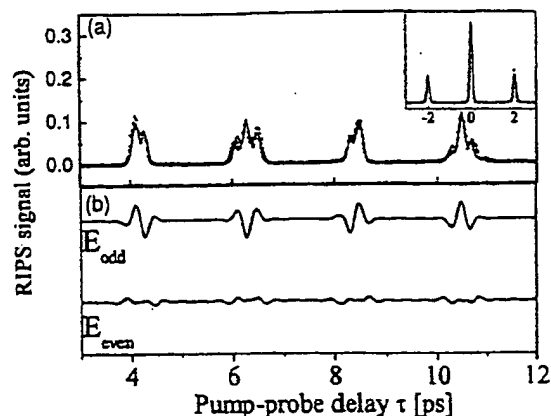


FIG. 5. (a) RIPS signal produced by a phase-shaped pump pulse [$\theta=1.11(\pi/2)$]. (b) Wave packet consists essentially of an odd rotational state contribution (see text).

packet with a specific parity and symmetry. This aspect could be considered in investigations implying wave packets of well-defined parity and/or symmetry such as, for instance, those devoted to parity violation in molecules [44].

The N_2 signal depicted in Fig. 3 exhibits another noticeable feature. The odd and even contributions turn out to be maximized for delays ($\tau=6.3$ and 10.5 ps) where they interfere destructively. At these particular delays, a maximum rephasing between all the even- J Raman modes on one hand, and all the odd- J Raman modes on the other hand, occurs but with a relative π -phase shift between them. It is therefore consistent to consider the possibility of rephasing these two sets of components. For this task, we have applied a modulation of magnitude $\theta=\pi$ inducing a π -phase shift between Raman transitions of opposite parities. The result, depicted in Fig. 6, displays effectively rephasing between odd and even components at proper delays. The magnitude of the signal as compared to Fig. 3(a) slightly decreases. This is caused by the nondominant Raman transitions whose frequencies do not fulfill the condition described in Eq. (5a) or (5b), as a result of the approximation carried out to deduce the final solution [Eq. (8)]. In other words, some pairs of photons

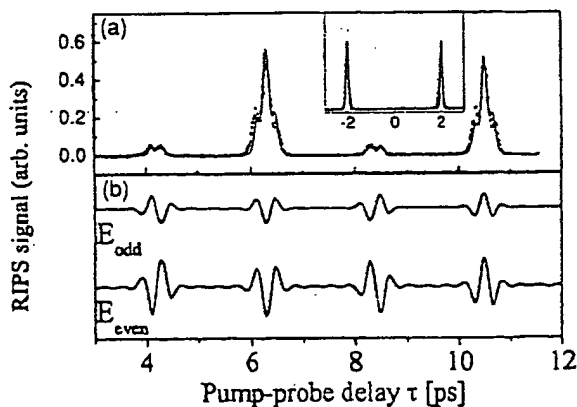


FIG. 6. (a) RIPS signal produced by a phase-shaped pump pulse ($\theta=\pi$). (b) Rephasing between odd and even rotational wave packet contribution at $\tau=6.3$ and 10.5 ps.

implied in each of these Raman transitions experience a phase difference $\Delta\phi(\omega')=0$, whereas others experience $\Delta\phi(\omega')=\pm\theta$. It should be noted, however, that the signal remains comparable with a pump pulse peak intensity reduced by a factor of about 2 [as suggested by the pulse train displayed in the cross correlation trace inserted in Fig. 6(a)]. Such spectral phase modulation features major interest for molecular alignment. Laser-induced molecular alignment is indeed intrinsically limited by the ionization process. A single pulse shaped into a train of pulses with lower energy but producing comparable alignment could be exploited in order to shift this expected limitation. This possibility will be investigated in a near future.

The frequency-domain interpretation can be supported by an analysis in the time domain [45,46]. Cross correlations inserted in Figs. 4–6 reveal that phase modulations considered in this work lead to trains of pulses, temporally shifted by $2\pi/\Omega_m$, whose relative amplitudes depend on the phase step magnitude θ . Each pulse is Fourier-transform limited and results therefore in signal fields E_{odd} and E_{even} , similar to those depicted in Fig. 3(b) ($\theta=0$), time delayed by $2\pi/\Omega_m$ with respect to each other. For instance, modulation with $\theta=\pi$ (Fig. 6) generates mainly two identical pulses, respectively, centered at $\tau=-2$ ps and $\tau=+2$ ps. The signal field E_{odd} , for the overall sequence represented in Fig. 6(b), corresponds hence to the superposition of E_{odd} ($\theta=0$, $\tau=-2$ ps) and E_{odd} ($\theta=0$, $\tau=+2$ ps) while E_{even} corresponds to the superposition of E_{even} ($\theta=0$, $\tau=-2$ ps) and E_{even} ($\theta=0$, $\tau=+2$ ps) [see the arrow indicated in Fig. 3(b)]. Similar analysis can be considered for the results presented in Figs. 4 and 5.

V. CONCLUSION

In this paper, the control of rotational dynamics by pulse-shaping technique is demonstrated. The wave packet is prepared by impulsive Raman excitation in the vibronic ground state of N_2 molecule. The excitation pulse is tailored by modulating the spectral phase with a spatial light modulator.

In contrast to investigations using feedback loop algorithm, we have opted for well-defined periodic phase function. The resulting manipulation of the wave packet as well as its dynamics is interpreted by means of a frequency-domain analysis. It is shown that precise control of the wave packet is possible even when using a 128 pixel modulator. The approach chosen to determine the appropriate modulation frequency of the periodic phase function is described in detail. The relative excitation between odd and even rotational components of the wave packet is controlled and thus its symmetry and rephasing properties. The production of a wave packet with a predominant antisymmetric contribution is reported. The relevance of the technique in the context of violation parity observation is mentioned. A spectral modulation which produces a rephasing of the wave packet in conjunction with a reduction of the laser pulse intensity is also investigated. It offers a valuable method for the optimization of dynamic alignment under strong field.

Manipulation of rotational coherences features also promising applications in the frame of optical diagnostics. Femto-second time-resolved spectroscopy techniques such as CARS or RIPS have been used [25,26] to determine temperature or concentration of molecules in gas phase. Thermometry measurements rely, for instance, on the fact that transient shapes are inherently temperature dependent. However, sensitivity of transient shapes is often effective only in a delimited range of temperature and tends to decrease at high temperature [47]. By specifically tailoring the pump pulse, it is possible to induce transient revivals with an enhanced sensitivity with respect to the temperature improving thus the accuracy of measurement. This should be considered as a continuation of the present work.

ACKNOWLEDGMENTS

The authors acknowledge financial support by the Conseil Régional de Bourgogne, by the CNRS, and by the ACI "photonique" from the French Ministry of Research. Stimulating discussions with R. Marquardt are acknowledged.

- [1] M. Shapiro, J. W. Hepburn, and P. Brumer, *Chem. Phys. Lett.* **149**, 451 (1988).
- [2] C. Chen, Y. Yin, and D. S. Elliot, *Phys. Rev. Lett.* **64**, 507 (1990).
- [3] D. Xenakis *et al.*, *J. Phys. B* **32**, 341 (1999).
- [4] B. Sheehy, B. Walker, and L. F. DiMauro, *Phys. Rev. Lett.* **74**, 4799 (1995).
- [5] L. Zhu *et al.*, *Science* **270**, 77 (1995).
- [6] A. P. Peirce, M. A. Dahleh, and H. Rabitz, *Phys. Rev. A* **37**, 4950 (1988).
- [7] A. M. Weiner, *Rev. Sci. Instrum.* **71**, 1929 (2000).
- [8] R. S. Judson and H. Rabitz, *Phys. Rev. Lett.* **68**, 1500 (1992).
- [9] C. J. Bardeen *et al.*, *Chem. Phys. Lett.* **280**, 151 (1997).
- [10] A. Assion *et al.*, *Science* **282**, 919 (1998).
- [11] T. Brixner *et al.*, *Nature (London)* **414**, 57 (2001).
- [12] R. J. Levis, G. M. Menkir, and H. Rabitz, *Science* **292**, 709 (2001).
- [13] R. Bartels *et al.*, *Nature (London)* **406**, 164 (2000).
- [14] T. C. Weinacht, J. L. White, and P. H. Bucksbaum, *J. Phys. Chem. A* **103**, 10 166 (1999).
- [15] T. C. Weinacht *et al.*, *Chem. Phys. Lett.* **344**, 333 (2001).
- [16] D. Zeidler *et al.*, *J. Chem. Phys.* **116**, 5231 (2002).
- [17] N. Dudovich, B. Oron, and Y. Silberberg, *Nature (London)* **418**, 512 (2002).
- [18] A. M. Weiner *et al.*, *Science* **247**, 1317 (1999).
- [19] J. G. Underwood *et al.*, *Phys. Rev. Lett.* **90**, 223001 (2003).
- [20] D. M. Villeneuve *et al.*, *Phys. Rev. Lett.* **85**, 542 (2000).
- [21] J. Karczmarek *et al.*, *Phys. Rev. Lett.* **82**, 3420 (1999).
- [22] D. J. Tannor and S. A. Rice, *J. Chem. Phys.* **83**, 5013 (1985).
- [23] I. Pinkas, G. Knopp, and Y. Prior, *J. Chem. Phys.* **115**, 236 (2001).
- [24] J. Faeder *et al.*, *J. Chem. Phys.* **115**, 8440 (2001).

- [25] T. Lang *et al.*, J. Chem. Phys. 115, 5418 (2001).
- [26] E. Hertz *et al.*, J. Chem. Phys. 113, 6629 (2000).
- [27] P. F. Rosca and M. J. J. Vrakking, Phys. Rev. Lett. 87, 153902 (2001).
- [28] V. Renard *et al.*, Phys. Rev. Lett. 90, 153601 (2003).
- [29] H. Stapelfeldt and T. Seideman, Rev. Mod. Phys. 75, 543 (2003).
- [30] I. V. Litvinyuk *et al.*, Phys. Rev. Lett. 90, 233003 (2003).
- [31] M. Wittmann, A. Nazarkin, and G. Korn, Phys. Rev. Lett. 84, 5508 (2000).
- [32] M. Wittmann, A. Nazarkin, and G. Korn, Opt. Lett. 26, 298 (2001).
- [33] N. Zhavoronkov and G. Korn, Phys. Rev. Lett. 88, 203901 (2002).
- [34] R. A. Bartels *et al.*, Phys. Rev. Lett. 88, 013903 (2002).
- [35] A. V. Sokolov *et al.*, Phys. Rev. Lett. 85, 562 (2000).
- [36] A. V. Sokolov, D. D. Yavuz, and S. E. Harris, Opt. Lett. 24, 557 (1999).
- [37] A. V. Sokolov, Opt. Lett. 24, 1248 (1999).
- [38] A. V. Sokolov *et al.*, Phys. Rev. Lett. 87, 033402 (2001).
- [39] V. Kalosha *et al.*, Phys. Rev. Lett. 88, 103901 (2002).
- [40] M. Spanner and M. Y. Ivanov, Opt. Lett. 28, 576 (2003).
- [41] R. A. Bartels *et al.*, Opt. Lett. 28, 346 (2003).
- [42] K. A. Walowicz *et al.*, J. Phys. Chem. A 106, 9369 (2002).
- [43] M. Morgen *et al.*, J. Chem. Phys. 102, 8780 (1995).
- [44] M. Quack, Angew. Chem., Int. Ed. 41, 4619 (2002).
- [45] E. Hertz *et al.*, Phys. Rev. A 61, 033816 (2000).
- [46] E. Hertz *et al.*, J. Chem. Phys. 113, 6132 (2000).
- [47] H. Tran *et al.*, J. Raman Spectrosc. 34, 994 (2003).

Molecular Fluorescence, Phosphorescence, and Chemiluminescence Spectrometry

Aleeta M. Powe,[†] Kristin A. Fletcher,[†] Nadia N. St. Luce,[†] Mark Lowry,[†] Sharon Neal,[‡] Matthew E. McCarroll,[§] Philip B. Oldham,^{||} Linda B. McGown,[⊥] and Isiah M. Warner^{*,†}

Department of Chemistry, Louisiana State University, Baton Rouge, Louisiana 70803, Department of Chemistry, University of Delaware, Newark, Delaware 19716, Department of Chemistry, Southern Illinois University, Carbondale, Illinois 62901, Department of Chemistry, Mississippi State University, Mississippi State, Mississippi 39762, and Department of Chemistry and Chemical Biology, Rensselaer Polytechnic Institute, Troy, New York 12180

Review Contents

Books, Reviews, and Chapters of General Interest	4614
General Instrumentation	4615
Laser-Based Techniques	4617
Sensors	4619
Sample Preparation, Quenching, and Related Phenomena	4619
Data Reduction	4620
Organized Media	4621
Low-Temperature Luminescence	4622
Total Luminescence and Synchronous Excitation Spectroscopies and Related Techniques	4622
Solid Surface Luminescence	4622
Luminescence in Chromatography, Electrophoresis, and Flow Systems	4623
Dynamic Luminescence Measurements	4624
Fluorescence Polarization, Molecular Dynamics, and Related Phenomena	4625
Chemiluminescence	4625
Near-Infrared Fluorescence	4625
Luminescence Techniques in Biological and Clinical Analysis	4626
Reagents and Probes	4628
Other Techniques and Applications	4629
Literature Cited	4630

This review covers the approximately two-year period since our last review (A1), roughly from January 2002 through December 2003. A computer search of *Chemical Abstracts* provided most of the references for this review. Coverage is limited to articles that describe new developments in the theory and practice of molecular luminescence for chemical analysis in the ultraviolet–visible and near-infrared region.

Citations may be duplicated between sections due to articles with contents that span several topics. However, in an effort to reduce the length of this review, we attempted to limit this kind of duplication. In general, citations are limited to journal articles and usually do not include patents, proceedings, reports, and dissertations.

We tried to focus on important advances of general interest and relevance to the field of analytical chemistry rather than

extensions of previous advances. This was done in an effort to continue our recent efforts to significantly reduce the length of this biannual review. In addition, we also expanded our description of individual citations for better clarification of content where necessary.

Although we are not able to provide extensive coverage of developments of relevance to broad areas such as chromatography and biological sciences, we tried to include major review articles and chapters relevant to these topics. If you feel that we omitted an important article published during the above referenced time period, please forward the reference to one of us and we will be certain to consider it for the next review.

BOOKS, REVIEWS, AND CHAPTERS OF GENERAL INTEREST

Bright and Munson described time-resolved fluorescence anisotropy along with fluorescence intensity decay in both time and frequency domains. They also reviewed instrumentation for the collection of single-photon counting and multifrequency phase modulation fluorescence (B1). A general review of molecular fluorescence, phosphorescence, and chemiluminescence was provided by Miyawa and Schilman (B2). Mann and Krull explained fundamentals of fluorescence polarization and described how it advanced protein analysis (B3). *Fluorescence Spectroscopy Imaging and Probes*, one of the Springer Series on Fluorescence, is a convenient resource providing reviews on a number of topics such as methods to investigate properties of membrane-bound proteins, the multiparameter detection of single fluorescent molecules immobilized in a thin polymer matrix, the use of metallic particles or surfaces to alter the rates and spatial distribution of fluorescence emission, and the development of fluorescence probes compatible with light-emitting diodes or diode lasers (B4).

Chemometric techniques coupled with advanced instrumental techniques can be applied to the analysis of unresolved multi-component systems. de Juan and Tauler reviewed the evolution of chemometric data analysis methods (B5). Celadi described traditional as well as newly developed chemometric and analysis methods as applied to spectroscopic and other multivariate data, paying special attention to instrument noise and situations where soft modeling would be more applicable (B6).

Fluorescence spectroscopy has often been employed to gain insight into analyte binding and dynamics. Santos and Castanho (B7) and Chattopadhyay (B8) discussed examples of fluorescence methods employed to study the dynamics of membrane proteins

* Corresponding author. E-mail: isiah.warner@chemgate.chem.lsu.edu.

[†] Louisiana State University.

[‡] University of Delaware.

[§] Southern Illinois University.

^{||} Mississippi State University.

[⊥] Rensselaer Polytechnic Institute.

and peptides, such as fluorescence lifetime, anisotropy, quenching, red-edge excitation shift, and energy transfer. Demchenko provided an excellent review of advances, applications, and progress in the field of red-edge effects (B9).

Single-molecule spectroscopy is becoming a powerful tool to study dynamics in complex microenvironments. Jung et al. summarized fundamental principles of single-molecule spectroscopy and focused on several related topics (B10). The analytical chemistry applications of single-molecule spectroscopy within fluid solutions, concentrating on the spectroscopy and detection of single fluorophores, was reviewed by Keller et al. (B11). In addition, Michalet et al. recounted the development of single-molecule fluorescence microscopy and spectroscopy (B12).

Temporal and spatial resolution of single or sparse molecules was achieved with fluorescence correlation spectroscopy (FCS). The number of reviews increased significantly, with FCS being applied to a variety of biological applications to determine local concentrations, diffusion coefficients in free solution and along cell or artificial membranes or surfaces, drug binding to proteins, and enzyme kinetics, as well as several other applications. Hess et al. provided an historical review of FCS including a discussion of the theoretical background and experimental setup, as well as examples of solution and cellular applications (B13). Krichevsky and Bonnet reviewed practical considerations for the design of an FCS instrument and experiment and compared this method to other spectroscopic techniques (B14). Hwang and Wohland related the theory of FCS and its applications for describing membranes and membrane-bound proteins (B15). The authors also compared FCS to fluorescence recovery after photobleaching, a method often used to measure diffusion in membranes.

The development of fluorescent protein technology, combined with imaging methods, allowed a greater understanding of the motion of proteins and protein interactions with components in living cells. Contag and Bachmann reviewed bioluminescence and fluorescence imaging methods, which enable in vivo measurements of gene expression in the former case and real time in vivo monitoring of several genetic regulatory processes in transgenic mice, gene transfer, and trafficking of immune cells in the latter (B16). Two-photon fluorescence tissue imaging was reviewed, and the spectroscopic properties of select endogenous fluorophores available with this technique were discussed (B17). The technique of fluorescence lifetime imaging microscopy was reviewed by the Lakowicz group, including a discussion of data analysis and select applications (B18).

Near-infrared (NIR) optical imaging, employing sensitive, enzyme-specific fluorescent beacons, can potentially be used for the early detection of many cancers as well as for monitoring patient therapy. Mahmood and Weissleder described a part of the associated biology, along with probe design considerations and hardware requirements for NIR imaging. They also provided examples of the in vivo NIR optical imaging of cathepsin and metalloproteinase (B19). Sevick-Muraca et al. reviewed common methods to illuminate and collect fluorescence from tissues, techniques for probe construction, and possible clinical applications (B20).

Chaudhury described fundamental principles of fluorescent molecules important in the development of optical biosensors (B21). The Lakowicz group reviewed different sensing methods

utilizing fluorescence spectroscopy and examined spectral properties of intrinsic and extrinsic fluorescence probes and their applicability toward biochemical systems (B22, B23). Rurack and Resch-Genger described the mechanisms, properties, and limitations of several methodologies to develop fluorescent molecular switches and sensors containing appropriate supramolecular and photophysical characteristics (B24). Quantum dots can be employed in biological assays to study noncovalent interactions between two or more molecules of biological interest. Sutherland reviewed recent advances in the use of quantum dots compared to traditional fluorescent probes (B25).

Fluorescence spectroscopy is a very useful technique to investigate molecular dynamics, molecular association, and microstructure within organized media. In addition, optical spectroscopy can be used to determine partition coefficients between bulk solution and organized assemblies. Miguel et al. reviewed the role of fluorescence to understand aggregation behavior within polymeric or surfactant solutions (B26). Also, Santos et al. described the determination of partition coefficients between aqueous and lipid phases, the advantages and limitations of spectroscopic versus separation techniques, and the differentiation between partitioning and binding behavior (B27).

The use of fluorescence in environmental analysis continues to be important. Hanrahan et al. described the utility of flow injection techniques coupled to molecular spectroscopic detectors to study environmental matrixes, and Patra reported recent developments in the analysis of polycyclic aromatic hydrocarbons (B28, B29). Lambert presented a review describing portable fluorescence-based detectors capable of measuring real-time oil concentrations (B30).

The application of fluorescence spectroscopy to food science was described by Dufour, and Marangoni reviewed the specific application of fluorescence anisotropy (B31, B32).

GENERAL INSTRUMENTATION

Several new and interesting fluorescence instruments were reported in the literature over the past two years. Many involved imaging technologies or fluorescence microscopy. Other areas where several instrumental advances were made are fluorescence detection in capillary electrophoresis (CE), DNA sequencing, microfluidic devices, and flow analysis. New and improved detectors and light sources also were described.

Laser microscopy techniques such as confocal laser scanning microscopes and new infrared laser scanning microscopes and their uses as sensitive tools for detecting biomolecules in their natural environment were reviewed. It was predicted that these techniques will be invaluable for clinical diagnostic studies and therapy soon (C1).

To deal with the rapid increase in the size of compound libraries and new targets emerging from the Human Genome Project, a joint venture between scientists and engineers from biotech and pharmaceutical industries helped develop two different ultrahigh-throughput screening systems based on confocal fluorescence analysis techniques. One instrument is a four-channel confocal fluorescence reader based on single-molecule detection methods with four parallel objectives, while the other instrument

is a confocal fluorescence imager based on pattern recognition (C2).

A review concentrating on the general design characteristics of the instrumentation discussed the advantages of lifetime-resolved imaging and the characteristics that distinguish imaging experiments from single-channel lifetime-resolved measurements. Lifetime-resolved imaging considerably extends the information derived from a fluorescence experiment. The authors reviewed the major issues concerning measurements and instrumentation, with the main purpose to provide the reader with an appreciation for the broad application of fluorescence lifetime-resolved measurements in imaging (C3). Other more detailed examples and instrumental designs also were reported, some of which are described below.

An inverted confocal microscope was adapted for the measurement of fluorescence emission dynamics (lifetime and fluorescence polarization anisotropy). Dynamic spectroscopic measurements were obtained with phase fluorometry based on a modulated linearly polarized laser beam fed to the epifluorescence port of the microscope. Characterization of the microscope showed results from microliter volumes comparable to those obtained in cuvettes (C4).

Techniques for determining the position of objects in space with resolution between that of fluorescence resonance energy transfer (FRET) and optical microscopy are of interest. Distances of ~ 10 nm can be measured using FRET, but the limit for optical resolution is the diffraction limit, which is several hundred nanometers. Calculation of the centroid of the images of individual fluorescent particles and molecules allows localization and tracking using optical microscopy but with a precision ~ 1 order of magnitude greater than the microscope resolution. An equation to describe localization precision allowing the assessment of the experimental apparatus was reported by Webb and co-workers (C5).

The design and characterization of a wide-field, time-domain fluorescence lifetime imaging microscope for picosecond time-resolved biological imaging was reported (C6). The system consists of a nitrogen-pumped tunable dye laser for UV-visible-NIR excitation, an epi-illuminated microscope with UV optics, and a time-gated intensified CCD camera with adjustable gate width for temporally resolved single-photon detection of fluorescence decays. The system displayed 1.4-mm spatial resolution, spectral tunability, and a large temporal dynamic range to image living human cells.

A compact time-correlated single-photon counting (TCSPC) microscope system for measuring fluorescence lifetimes less than 1 ns was described (C7). It is based on a pulsed violet laser diode mounted on an optical table above the microscope. The fluorescence emission is focused into a monochromator with a PMT detector. The compact, cool, and fast-pulsed laser diode is much more suitable for lifetime measurements than the traditional mode-locked lasers used in the past. The prototype instrument, validated using standard fluorophores, is compact (approximately 80×70 cm) and nearly fully computer controlled.

Another interesting modification to a conventional fluorescence microscope was reported. A total internal reflection microscope was equipped with a newly designed wedge prism allowing the imaging of the fluorescence spectrum of a single fluorescent

molecule by prism-based spectroscopy (C8). The instrument was used to obtain a spectral image of a single rhodamine red molecule attached to an essential light chain of myosin. Also, a spectral image of single-pair FRET between rhodamine red and Cy5 in a double-labeled myosin motor domain was reported. The method could become a useful tool for the investigation of dynamic processes of biomolecules at the single-molecule level.

Typically, gas discharge UV-visible lamps or lasers are used as light sources in detection schemes for CE. These sources are bulky, expensive, and difficult to couple into optical fibers. The lack of suitable light sources hindered the development of small-sized, high-throughput, cost-effective genomics instruments. The use of CE with laser-induced fluorescence excited by UV lasers in the range 200–300 nm was restricted by the available wavelengths and expense of the lasers. Sweedler and co-workers reported an instrument integrating a NeCu deep-UV laser operating at 248.6 nm with a single-channel CE system. Detection limits for serotonin and tryptophan were reported as 3.9×10^{-8} and 4.5×10^{-8} M, respectively (C9).

A capillary isoelectric focusing system with liquid core waveguide (LCW) laser-induced fluorescence whole column imaging detection was reported (C10). A Teflon AF 2400 capillary served as the separation channel and the axially illuminated LCW. The capillary has a refractive index between 1.29 and 1.31 compared to 1.33 for water, making total internal reflection very apparent. Use of the Teflon capillary eliminated the need for high refractive index additives such as glycerol, allowing the system more versatility. The system showed similar separation efficiency and peak capacity compared to a commercially available instrument with UV detection, but the sensitivity was enhanced by 3–5 orders of magnitude.

A CE laser-induced fluorescence instrument using an optical waveguide was described. The waveguide approach allowed for column excitation and detection with two-color discrimination (C11). Fluorescent dyes with two different wavelengths were simultaneously separated and detected to test the instrument design for applications in protein analyses.

A family of high-performance capillary DNA sequencing instruments based on a novel multicolor fluorescent detection technology was reported (C12). Two technological advances made this scheme possible: multilaser excitation of labeled fragments and "color-blind" single-photon detection of modulated fluorescence. The design and testing of several versions of an automated single-lane DNA sequencer as well as an approach to scaling the instrument up to multiple lanes was discussed.

Yeung and co-workers presented a novel high-performance quantitative assay for unamplified nucleic acids (C13). DNA molecules were labeled with YOYO-1, a fluorescent dye, and single DNA molecules imaged with a normal CCD camera (instead of an image-intensified CCD camera) as they migrated electrophoretically in a polymer solution. No chemical or biochemical amplification was required, and quantitation was achieved simply by counting the number of molecules over the measurement period. The technique was fast, sensitive, covered a wide dynamic range, and promised to be useful in the study of gene functions, disease, and clinical detection of mutant cells.

Fiber optics for fluorescence detection in a microfluidic device using a pair of optical fibers for shuttling laser light to the detection

zone and collecting the resulting emission for fluorescence analysis was reported. The dual-fiber detector produced sub-attomole detection limits with the entire detector, including laser source, electronics, and photon transducer, situated in a single box measuring 3 in. \times 10 in. \times 14 in. (C14).

Rigler and co-workers reported the parallel fluorescence detection of single biomolecules in microarrays (C15). Multifocal excitation was made possible through a 2×2 diffractive optical fan-out element, which produced uniform intensity in all four foci. Single biomolecule sensitivity was demonstrated in all four foci simultaneously. A modification gave a multifocal optical fluorescence correlation spectroscopy system for parallel flow analysis using a 4×1 fan-out array, with foci changeable from perpendicular or parallel to the flow direction (C16). Transport effects of diffusion as a function of flow and distance could be studied. Flows in all four foci could be simultaneously monitored when the array was perpendicular to the flow. Cross-correlation analysis could be performed by turning the microstructure, thereby having all four foci parallel to the direction of flow.

Shelby and Chiu described a technique for characterizing microfluidic flow profiles from slow laminar flow to fast near-turbulent flow. They used a photoactivated fluorophore, nanosecond-duration photolysis pulses from a nitrogen laser, and high-sensitivity single-molecule detection with Ar⁺ laser excitation. The measurement of flow speeds up to 47 m/s in a 33- μ m-wide straight channel, and the mapping of flow profiles in a 55- μ m-wide microchamber was reported (C17).

Also, new or improved detectors, light sources, and filters were reported. The feasibility of an array of single-photon detectors sensitive in the visible part of the spectrum was demonstrated. The first two-dimensional array (4×8) of single-photon avalanche diodes integrated in an industrial complementary metal oxide-semiconductor process was reported (C18). Benefits included low production costs, compactness, and the potential to easily modify the design to fit a specific application.

Hydrogenated amorphous silicon (a-Si:H) pin photodiodes were developed and characterized as fluorescence detectors for microfluidic analysis devices. First, a discrete photodiode was fabricated on a glass substrate and used to detect fluorescent dye standards using conventional confocal microscopy. Then a hybrid integrated detection system consisting of a half-ball lens, an optical interference filter with a pinhole, and an annular a-Si:H photodiode was developed and used in DNA fragment sizing and chiral analysis of glutamic acid. The detector exhibited high sensitivity at the emission wavelengths of commonly used fluorescent dyes and is readily microfabricated and integrated at low cost (C19).

The first complete range of compact picosecond to nanosecond excitation sources for fluorescence lifetime measurements based on laser diodes and LEDs were developed. They provide pulse durations shorter than 1 ns and repetition rates up to 80 MHz, making them candidates for TCSPC applications where short data acquisition time is crucial. Compact, inexpensive, and easy to use fluorescence lifetime spectrometers can be built using these sources (C20).

The availability of reliable, low-cost GaN-based semiconductor laser diode sources emitting at 404 nm made possible many new fluorescence-based measurements (C21). One application cited

is the characterization of the fluorescence behavior of gasoline samples.

Finally, acoustooptic tunable filters (AOTFs) play an increasingly important role in modern optical microscopy. When used with a laser light source in a confocal microscope, and when combined with a digital signal processor, up to six different wavelengths can be diffracted simultaneously, each at an individually controlled power level. This technology benefited techniques such as fluorescence recovery after photobleaching (FRAP) since the illumination can be controlled on a pixel-by-pixel basis while maintaining a high scan rate. It also enables bleaching of lines or irregular shapes (C22).

LASER-BASED TECHNIQUES

Applications of laser-based techniques such as multiphoton excitation, single-molecule detection and spectroscopy, fluorescence correlation spectroscopy (FCS), and laser scanning confocal microscopy have received a great deal of attention in recent years.

The use of multiphoton microscopy in the biosciences was reviewed (D1). It is said to be the best noninvasive means of fluorescence microscopy in tissue explants and living animals. Its use is increasing exponentially in part because of "smart" genetically encoded fluorescent indicators. Also, the risks and advantages of multiphoton microscopy in physiology have been discussed (D2). Multiphoton microscopy was introduced as a better alternative to traditional confocal microscopy due to its deep penetration depth, reduced photodamage, and lack of out-of-focus bleaching, as well as its a priori optical sectioning without the need for a confocal aperture. However, limitations such as photodamage and photobleaching in the focal plane can be worse than in single-photon microscopy; although, with low excitation intensity and special technical adaptations, photodamage can be avoided successfully.

Several reports of new dyes specifically designed for multiphoton excitation appeared in the literature. The first examples of heterocycle-based multibranch dyes with efficient two-photon absorption activity were reported (D3). Two coumarin-based two-photon-induced fluorescent molecules were synthesized and some structure-photophysical property relationships proposed. Remarkable enhancements in the fluorescence quantum yield and TPEF, two-photon excited fluorescence, activity were observed by replacing the anthryl group with an indolyl group in the terminal moiety of the coumarin-based π -conjugated framework (D4). Additionally, benzothiazole-based compounds with various π -electron donors were synthesized. All compounds exhibited high fluorescence quantum yields and strong two-photon-excited fluorescence. The measured TPEF cross section of one compound was reported to be ~ 6.1 times that of coumarin 307 (D5).

Several applications of multiphoton excitation were reported in the literature, but only a small number of these can be described in this review. Two interesting biological applications of multiphoton excitation in biological imaging were reported by Webb and co-workers. The two-photon excitation spectra of NAD(P)H, flavin adenine dinucleotide, and lipoamide dehydrogenase over the wavelength range of 720–1000 nm were measured and two-photon ratiometric redox fluorometry and microscopy developed for the investigation of mitochondrial metabolic states in isolated adult dog cardiomyocytes (D6). Two- and three-photon-excited intrinsic

fluorescence, combined with second harmonic generation by supramolecular structures, can produce images with the resolution and detail of standard histology without the need for exogenous stains. However, efficient application of multiphoton microscopy to intrinsic imaging requires knowledge of the nonlinear optical properties of specific cell and tissue components. Several intrinsic fluorophores and molecular assemblies were characterized and used in direct visualization of tissue morphology, cell metabolism, and disease states such as Alzheimer's disease and cancer (D7). Dittrich and Schwille used auto- and dual-beam cross-correlation FCS, using one- and two-photon excitation, to determine flow parameters, such as direction and viscosity, in microstructured channels. The authors reported dual-beam cross-correlation permits the separation of anisotropic and isotropic dynamics, and cross talk between two measurement volumes can be drastically reduced by using time-gated two-photon excitation operating in the dual-beam mode (D8).

A series of papers demonstrated that nonlinear optical processes can be controlled by modulating the phase of ultrafast laser pulses taking advantage of multiphoton, intrapulse interference (MII) (D9, D10). The MII method modulates the probabilities with which specific spectral components in the excitation pulse contribute to the two-photon absorption process. The spectral phase required to achieve maximum contrast in the excitation of probe molecules was determined, and a number of multiphoton excited images of different samples were presented (D11).

The feasibility of single-molecule DNA sequencing was reported. Fluorescently labeled nucleotides were detected during the cleavage of individual DNA fragments. Labeled bases flowing through the detection region were detected at the single-molecule level by laser-induced fluorescence. The digestion of a single strand of DNA by a single exonuclease was discernible (D12).

LeCaptain and Van Orden described other techniques that employ single-molecule fluorescence to resolve components in an electrophoretic experiment. These techniques have the potential for higher speed analysis, elimination of the sample plug injection step, and the ability to perform the analysis in shorter flow channels as compared to separations-based CE. Their CE/two-beam fluorescence cross-correlation spectroscopy technique was used to resolve the bound and unbound fractions of fluorescently labeled single-stranded DNA (ssDNA) in a ssDNA-protein complex as the analyte solution flowed continuously through a capillary (D13). Their technique was also used to discriminate molecules based upon the magnitudes and directions of their electrophoretic flow velocities. Sensitivity to molecular processes occurring on a millisecond time scale and the selectivity of the technique compared favorably to the corresponding properties of millisecond separations based on capillary zone electrophoresis techniques (D14).

Webb and co-workers used two-photon fluorescence resonance energy transfer and fluorescence correlation spectroscopy to examine Rous sarcoma virus Gag-Gag and membrane interactions in living cells (D15). Both techniques indicated there were strong interactions between Gag proteins in the cytoplasm. These methods have general applicability to *in vivo* studies of interactions involved in the formation of complex macromolecular structures.

Recent developments in single-molecule detection techniques led to a number of significant applications in biological research

including a dual-color cross-correlation technique for gene expression analysis (D16).

Several applications of laser scanning confocal microscopy were reported. The technique was employed for the determination of binding constants of receptor-ligand interactions in a microarray format (D17).

Laser scanning confocal microscopes are well equipped to photobleach user-defined regions, making them useful tools to perform FRAP experiments. A three-dimensional model was reported that describes the recovery process for a disk-shaped geometry photobleached by the scanning beam. The model allows quantification of FRAP experiments (D18). The ability of confocal microscopy to excite and detect fluorescence within a three-dimensional object with high local resolution allowed the investigation of protein adsorption to ion-exchange membranes. Proteins were labeled with different fluorescent dyes and observed using the confocal microscope after adsorption. The membrane structure itself was also visualized by coupling specific dyes. An image was created that allowed visualization of the membrane and the protein within its pore structure (D19).

Two reviews that focused on biological systems were published in the area of fluorescence correlation spectroscopy (D20, D21). Reports on FCS technology included discussions of two-photon photophysics (D22) and excitation saturation in two-photon FCS (D23), a method for time-resolved FCS (D24), methodology for fluorescence labeling, and high-throughput assay for analysis of protein interactions using fluorescence-cross-correlation technology (D25), improved data analysis approaches using *ab initio* modeling (D26) and detailed statistical treatment of standard deviation and bias (D27), experimental considerations such as artifacts in confocal FCS (D28), and effects of nonideal photodetection (D29). The Gratton group continued to develop the photon counting histogram (PCH) for analyzing FCS measurements. They reported the development of a method to minimize the impact of the fluorescence intensity drifts caused by matrix effects on PCH results (D30). Weiss et al. demonstrated that the mobility of particles, i.e., proteins in membranes as determined by FCS measurements, depended on the shape of the membrane and produces intensity fluctuations of fractal dimension (D31). They reported that inaccurate analysis of such data can lead to recovery of dynamic parameters that are overestimated by an order of magnitude. Several applications of FCS in fields other than biology were reported. Rigler discussed the importance for diagnostic analysis at the single-molecule level in an application that investigated the behavior of negatively charged single rhodamine-labeled molecules excited to fluorescence in confocal volume elements responding to oscillating voltage gradients between 1 and 15 kV/cm using FCS (D32).

There were several reports of applications of FCS in CE, including single-molecule FCS in electrophoretic mobility shift analysis (D33) and multicomponent analysis in CE using two intersecting excitation laser beams and a single detector (D34). A FCS oxygen sensor was described that has single-molecule detection sensitivity and is intrinsically calibrated (D35). A technique for measurement of diffusion coefficients without *a priori* knowledge of the geometry of the confocal volume was described that employs FCS of the confocal volume that is at the surface of a dielectric mirror (D36). Finally, a technique that

employs sequential intensity subtraction for isolation of only the bright aggregates in FCS imaging was demonstrated (D37).

SENSORS

Continued efforts are being invested into further enhancing technologies directed toward the development of viable sensors for biological or environmental applications. Genotoxicity tests available today have several shortcomings. Akyuz and co-workers provided evidence for a new concept of genotoxicity detection in living human cell cultures obtained by use of a newly developed assay, which is based on the quantification of fluorescent signals (E1). Two new twistophane macrocycles were synthesized; these compounds are made up of a cyclically conjugated dehydrobenzoannulene framework that incorporates 6,6'-connected-2,2'-bipyridine moieties for the purpose of coordinating metal ions (E2). An optical two-dimensional (2D) imaging biosensor was used to study real-time monitoring of lactate released from brain slices (E3). This biosensor is able to spatially differentiate lactate concentration variations with conventional optical microscopic spatial resolution. The 2D biosensor will enable the study of cellular communications and possibly other biological processes that require simultaneous temporal and spatial resolution.

An interesting study involved a homogeneous immunoassay for TNT and its analogues. This assay was developed using a microfabricated capillary electrophoresis chip (E4). The assay is based on the rapid electrophoretic separation of an equilibrated mixture of an anti-TNT antibody, fluorescein-labeled TNT, and unlabeled TNT or its analogue. New solvent-sensitive merocyanine dyes were also reported, which made possible the quantitation of protein activities such as conformational changes, ligand binding, or posttranslational modifications in individual living cells (E5). The dyes reported should be useful in the preparation of live cell biosensors for a diverse range of protein activities.

Sol-gel matrixes were shown to be relatively inert while preserving the spectroscopic properties and biological activity of the encapsulated proteins (E6). Horseradish peroxidase (HRP) is a hemoprotein widely used in the field of biosensors because of its high specificity for hydrogen peroxide. This study illustrated that the single tryptophan (Trp) fluorescence of HRP may be used to distinguish denaturation processes from leaching of the heme group, as well as to establish the extent of denaturation.

There are several papers that contain optical sensors utilizing fluorescence spectroscopy. A novel optical sensor for determining doxycycline based on the fluorescence quenching of *N*-allylcarbazole immobilized on a quartz glass plate surface by covalent bonding was described (E7). The sensor showed satisfactory virtues in reversibility, repeatability, selectivity, and sufficient lifetime resulting from its excellent optode membrane. The sensor can be used for the direct determination of doxycycline in pharmaceutical preparations and urine samples. von Bultzingslowen et al. developed an optical sensor for the measurement of carbon dioxide in modified atmosphere packaging applications (E8). It is based on the fluorescent pH indicator 1-hydroxypyrene-3,6,8-trisulfonate immobilized in a hydrophobic organically modified silica (ormosil) matrix.

The use of microfluidic devices as sensors is also presented in several papers. A novel approach for an integrated micro total analysis system based on a microfluidic on-chip device that

supports ultrasensitive confocal detection of fluorescent cells and particles, and subsequently allows for their precise sorting in the fluid phase with respect to spectroscopic properties such as brightness and color, was presented (E9). In another study, a novel microfabrication technique for the preparation of microfluidic cartridges for isoelectric focusing (IEF) by screen printing was demonstrated using small molecular markers and hemoglobins as model analytes to demonstrate IEF with whole-column detection in the cartridges (E10).

The development of novel sensors included a newly synthesized multichromophore chemosensor, *trans*-4-(*p*-*N,N*-dimethylaminostyryl)-*N*-vinylbenzylpyridinium chloride (E11). The influence of solvent viscosity on the rate constants of radiative and nonradiative deactivation processes of this compound in aqueous solutions was investigated. Novel chiral bisbinaphthyl compounds were synthesized for the enantioselective fluorescent recognition of mandelic acid (E12). The introduction of dendritic branches to the receptors significantly amplified the fluorescence signal of the receptor, thus increasing the sensitivity of the sensor in fluorescence recognition.

Wen-xu and Jian developed a novel method using a fiber-optic-based fluorescence chemical sensor for on-line continuous monitoring of a drug in animals (E13). The fiber-optic chemical sensor is potentially useful for monitoring blood concentrations of drugs and their metabolites in the biomedical field. A new intrinsically calibrated sensor technology represented by means of an O₂-FCS sensor was reported by Opitz and co-workers (E14). The O₂-FCS sensor was particularly suited for the quantitative determination of molecular oxygen within biological gases and fluids. The method utilizes FCS with the ultimate detection sensitivity of a single fluorescent molecule. This sensor is potentially useful for the screening of chiral catalysts for the asymmetric synthesis of α -hydroxycarboxylic acids. Maxwell et al. used colloidal gold nanocrystals to develop a new class of nanobiosensors that is able to recognize and detect specific DNA sequences and single-base mutations in a homogeneous format (E15).

SAMPLE PREPARATION, QUENCHING, AND RELATED PHENOMENA

Use of sample derivatization to facilitate fluorescence detection was reported. Aktas et al. demonstrated the derivatization of commercially available lisinopril tablets with 7-chloro-4-nitrobenzofuran (F1). In another study, pharmaceutical formulations of vigabatrin and gabapentin were derivatized with fluorecamine (F2). The authors extended the investigation to the *in vitro* determination of the two drugs in spiked human urine and observed no interference from commonly coadministered drugs.

The Warner research group employed steady-state quenching of 15 polymerized dipeptide surfactants to estimate aggregation numbers (F3). Compared with monomer aggregation numbers, the authors determined polymerization using γ radiation yielded molecular micelles with fewer repeat units. Aggregation numbers were also affected by the size of the N-terminal alkyl group.

Derivative spectroscopy and fluorescence quenching were used to determine liposome/aqueous-phase partition coefficients of nimesulide, an antiinflammatory drug, with egg phosphatidylcholine liposomes, a model cell membrane (F4). The quenching behavior of spectroscopic probes also allowed the authors to

conclude nimesulide is buried deep in multilamellar vesicles and large unilamellar vesicles. In a different study, the adsorption/desorption kinetics of rose bengal, distributed between a methanol/water solution and C_{18} derivatized porous-silica surface, were determined from the quenching by ferricyanide of the phosphorescence of rose bengal (F5).

The direct electron transfer between excited pyrene bound to a surface and a gold nanoparticle was reported for the first time by Ipe et al. (F6). Electron transfer can be used to probe changes in protein structure. The quenching by tryptophan of a neighboring fluorescent label, biimane, has been shown to be a novel technique for protein studies (F7). This method requires a low volume of protein and can significantly simplify labeling procedures. By observing fluorescence intensity, the motion of a single DNA nanomotor tagged with both a fluorophore and quencher can be observed in real time (F8).

Chiral recognition through spectroscopic techniques has been of interest for several years. Bolender et al. described methodologies necessary (theoretical as well as experimental) to determine the degree of chiral discrimination using steady-state fluorescence quenching (F9). The authors derived the Stern–Volmer equation containing a chiral recognition term for such a system.

The quenching of tryptophan residues within membrane-inserted polypeptides by acrylamide and 10-doxylnonadecane was studied by Caputo and London as a new technique to investigate the depth of tryptophan residues within these membranes (F10). Near the bilayer surface, acrylamide quenching of tryptophan dominates while 10-doxylnonadecane quenching is stronger for tryptophan deeply buried within the membrane. With this method, the authors were able to simultaneously detect polypeptides containing mixed populations of tryptophan residues that were both deeply inserted and shallow based on shifts in the fluorescence maximums induced by the two quenching agents.

Steady-state and time-resolved quenching techniques revealed the formation of a dark ground-state dye/tryptophan complex, where the fluorescent dyes investigated were rhodamine 6G and an oxazine derivative (F11). Molecular dynamics simulations combined with the fluorescence studies allowed the authors to determine a minimum "quenching distance" required for quenching to occur, which corresponded to van der Waals contact between fluorophore and quencher.

The application of fluorescence quenching techniques to study environmental samples continues to be important. Using synchronous fluorescence spectroscopy, Ghatak et al. determined conditional stability constants for the complexation of cobalt(II) with humic and fulvic acids in mangrove sediment (F12). Through fluorescence quenching experiments, the authors determined fulvic acid forms a more stable complex with cobalt(II) than does humic acid. The McGuffin research group employed the selective fluorescence quenching of polycyclic aromatic hydrocarbons (PAHs) to profile these persistent pollutants in environmental matrixes (F13). The authors determined the cause or source of these pollutants can accurately be confirmed with the method outlined. A method for the determination of trace nitrite in tap and lake water without the need for sample extraction was developed by Zhang et al. (F14). This group found the reaction of rhodamine 110 with nitrite under acidic conditions produces a new compound with lower fluorescence.

DATA REDUCTION

The application of fluorescence measurements to more complex, spatially heterogeneous samples continues to drive the development and employment of data reduction and analysis methods. One of the frontiers of this progression is the development of hyperspectral fluorescence imaging methods. Processing these information-rich data cubes can put severe demands on computer storage, retrieval, and processing systems, but the spectral dispersion of the fluorescence signal can have important analytical advantages. The groups of Haaland (Sandia National Labs) and Werner-Washburne (University of New Mexico) demonstrated the removal of glass fluorescence contaminating measurements on DNA microchips using alternating least-squares methodology (G1). Zarco-Tejada and co-workers inverted models based on radiative transfer theory to estimate chlorophyll and other measures of plant physiology from hyperspectral fluorescence images of forests (G2). More often, investigators reported working with three-way data sets constructed by stacking two-way data tables such as excitation–emission matrixes (EEMs, also called total luminescence spectra and fluorescence landscapes).

Investigators at the Laboratory of Chemo/Biosensing and Chemometrics at Hunan University published several papers describing modification and application of parallel factor analysis (PARAFAC) methods for simultaneous analysis of pharmaceutical mixtures (G3–G10). Frenich et al. compared the effectiveness of generalized rank annihilation (GRAM) and the trilinear decomposition (TLD) in resolving ternary mixtures of pesticides and found TLD produced superior results (G11). Hitzmann and co-workers used model estimates based on the three-way partial least-squares calibration of EEMs followed by process model optimization to monitor and characterize a bioprocess without acquiring measurements for model recalibration (G12). Arancibia and co-workers used several three-way methods including variants of GRAM and TLD to analyze the fluorescence collected from complex samples of antiinflammatories (G13) and piroxicam (G14).

Christensen and co-workers demonstrated the ability of PARAFAC methods to characterize the fluorescence of aging cheese and curing ham (G15, G16). Interestingly, only a few investigators reported using higher order measurements to fingerprint cancerous cells and tissues. There was no report of a true three-way analysis of spectra of malignant cells or tissue during the review period. Ramanujam and co-workers used PCA to reduce EEMs of breast cancer tissue followed by classification by a support vector machine algorithm to determine tissue malignancy (G17). They report specificity and sensitivity of 92 and 70%, respectively. Although Zheng and co-workers collected EEMs of bladder tumors, they classified the data very successfully using an algorithm that compared emission intensity ratios at a pair of wavelengths (G18). Chang et al. reported equipping a fluorescence microscope with filters "related to the diagnostically relevant principal components" in order to generate PCA score images of nasopharyngeal carcinoma lesions, which were expected to be more amenable to classification than fluorescence images (G19). Other work by Chang et al., using PCA-based methods to classify one-dimensional fluorescence spectra of nasopharyngeal carcinoma lesions, was more representative of the reports in which fluorescence was used in cancer diagnostics. Also, linear methods,

based on PCA and partial least squares were used by Dufour and co-workers in a number of papers to perform pattern recognition of spectra collected from food or bioprocesses, including dairy products (G20–G23), meat (G24), and bacteria (G25).

Reports of applications of nonlinear methods during this review period were limited in comparison to linear methods. Majumder et al. reported a unique approach to the classification of oral squamous cell carcinoma (G26). They compared a nonlinear classification scheme, the maximum representation and discrimination feature method, to a PCA-based algorithm and observed a substantial improvement in both sensitivity and specificity of the classification. Dolenko et al. described the determination of oil in coastal waters using artificial neural networks (ANNs) (G27). They reported successful determination of microgram per liter quantities of oil in the presence of very large fluorescence background signals. He and co-workers reported the development of an ANN method for quantifying oils and fuels in wastewater streams from coupled fluorescence and light scattering data (G28). Wolf and co-workers reported the development of an ANN method to monitor the activity of a biofilm reactor used to degrade industrial effluents (G29).

Analysis of fluorescence data reflecting molecular dynamics frequently presents special challenges. The Webb group at Cornell reported the development of an algorithm for tracking the motion of particles and molecules observed in fluorescence microscopy measurements (G30). Kalinin et al. reported a method for determining the distance between chromophores spanning a lipid bilayer in the presence of reversible energy migration from depolarization data (G31).

Barsegov and Mukamel reported a multitime correlation method for recovering lifetime as well as dynamic properties from photon arrival trajectories of single chromophores quenched by resonance energy-transfer acceptors at fluctuating distances (G32). Rosato and co-workers analyzed protein intensity decay data using a dipolar relaxation model that describes the lifetime as increasing exponentially after excitation (G33). Dolenko et al. used ANNs to determine the lifetime from intensity decay data (G34). Milstein et al. used a nonlinear, Bayesian optimization scheme to recover fluorescent indicator parameters, including lifetime, from frequency-domain optical diffusion tomography data (G35).

ORGANIZED MEDIA

Luminescence continues to play an important role in the development of analytical methods that utilize organized media as molecular scaffolding, the investigation of media/solute interactions, and the characterization of media. Organized media is a broad term that includes macrocycles or molecular assemblies that can sequester solutes in an environment that is distinct from the bulk solvent. A partial list of systems that meet this criterion includes cyclodextrins, surfactant micelles, lipid aggregates, polymer films, sol–gels, and nanoparticles. More than 250 articles describing luminescence phenomena in cyclodextrins appeared during the review period. Li and co-workers described the development of zinc and mercury sensitizers based on porphyrin/ β -cyclodextrin supramolecular complexes (H1, H2). They reported increased metalation and dual fluorescence of the porphyrin in the presence of zinc, which result in detection limits below 1 μ M. Warner and co-workers characterized the inclusion complex of

γ -cyclodextrin and 2,6-bis(4-methylphenyl)oxazole (H3). Articles describing the development of cyclodextrin-based sensors, which are quenched or emit upon binding a host molecule, also were reported. The work of Corradini et al., in which the design and synthesis of a cyclodextrin modified by a fluorophore and amino acid sidearm so that the fluorescence response was enantioselectively sensitive to the α -amino acid binding, is an interesting example of development in this area (H4).

More than 400 papers describing luminescence in micelles were reported. Characterizing solute interactions with micelles continues to be an important theme. The Warner group published a number of reports focused on understanding the factors influencing enantioselectivity in micelle/solute interactions in amino acid-based surfactant micelles (H5–H8). They have noted a substantial influence by counterions and alcohol modifiers on anolyte interactions with dipeptide polymer surfactants.

There is some evidence that interest in media formed by mixed amphiphiles is increasing. For example, Costa and co-workers used the photokinetics of a pyrene derivative to probe the dynamics of polymer-induced clusters of AOT reverse micelles (H9). Chakrabarty et al. used the fluorescence of a coumarin dye to characterize micelles prepared from mixtures of surfactants and bile salts. They found the solvation and rotational dynamics of the probe were slowed in the medium relative to pure water (H10).

Understanding the consequences of mixing amphiphiles was also an important theme in luminescence studies of lipid aggregates. For example, Veatch and Keller observed that dioleoylphosphatidylcholine (DOPC)/dipalmitoylphosphatidylcholine/cholesterol mixtures form two coexisting liquid phases: one rich in the unsaturated lipid (DOPC) and the other rich in the saturated lipid and cholesterol (H11). These studies are important to the investigation of the role of composition on the behavior of lipid rafts, liquid lipid microdomains that resist disruption by detergents and may play a role in stabilizing signaling proteins. Lipid mixtures can also lead to aggregates with unusual properties. The magnetic alignment of mixed short- and long-chain lipid aggregates (bicelles) has been known for many years. The formation and morphology of these thermotropic aggregates is a source of debate. Rowe and Neal used fluorescent tags to monitor the mixing of the short- and long-chain lipids as the temperature of bicelle suspensions was raised (H12). They observed substantial lipid mixing rather than phase separation of the long- and short-chain lipids at all temperatures and suggested that mixed aggregates coalesce to form alignable structures.

Other studies used fluorescence measurements to investigate sol–gels, thin films, and polymers. Harris and co-workers used total internal reflection (TIR) FCS (H13) and single-molecule fluorescence trajectories (H14) to study molecular transport in sol–gel films. TIR-FCS was used to measure mass transport rates through thin sol–gel films prepared by dip-coating porous silica particles onto microscope slides. The measured diffusivities were between 1 and 2 orders of magnitude slower than free diffusion and were related to the uniformity of the film. Single-molecule fluorescence tracking was used to examine diffusion in sol–gel films to identify spatial heterogeneity in different regions of the film. Fluorescence intensity profiles from single molecules were fit to a two-dimensional Gaussian function used to determine their position with subpixel resolution. Higgins and co-workers used

single-molecule probe measurements investigate the nanoscale environment of organically modified silicate thin films prepared with varying amounts of alkylated silanes (*H15*) and polymer thin films modified by hydration (*H16*). They were able to distinguish photochemical, rotational, and translational contributions to probe fluctuations and correlate them to changes in film structure. Vanden Bout and co-workers reported using single-molecule spectroscopy and near-field optical microscopy to investigate changes in nanoscale structure in various polymer films that accompany large-scale temperature-induced phase transitions (*H17–H19*).

Several reports document the progress that is being made in the development of nanoparticles for analytical (visualization/detection) and biomedical (drug delivery) applications. Ostafin et al. investigated the fluorescence properties of cascade blue inside silicate nanoparticles and observed higher emission intensity and resistance to pH-induced spectral shifts for fluorophores trapped inside the nanoparticles (*H20*). Chen and Rosenzweig reported the preparation of quantum dot (QD) doped stabilized micelles (*H21*). These micelles are easily visualized because they contain over 100 QDs and can be stabilized by hydrolysis of the surfactant organosilane head group. Lee and co-workers reported the development of polymeric nanoparticles composed of fatty acid/polymer conjugates (*H22*). Self-assembly of the conjugate in water produced a nanoparticle that has a hydrophobic core–hydrophilic shell structure. The leakage of encapsulated probes decreased with fatty acid chain length, but the micellization process (critical micelle concentration) exhibited an unusual dependence on the fatty acid chain length.

LOW-TEMPERATURE LUMINESCENCE

During the time period, a number of papers employed low-temperature luminescence analysis. Low-temperature single-molecule spectroscopy with time-gated detection was used to achieve real-time imaging of intramolecular energy transfer in rigid-rod conjugated polymers, allowing identification of homogeneously broadened, strongly polarized emission from individual chromophore units on a single chain (*I1*). Analysis of DNA–carcinogen adducts using a monoclonal antibody–gold biosensor chip with low-temperature laser-induced fluorescence detection was demonstrated (*I2*).

Numerous groups employed low-temperature procedures in analyzing molecular structure. Bourgeois et al. used low-temperature absorption and fluorescence to study crystals mounted in cryoloops with an off-line microspectrophotometer (*I3*). They found fluorescence microspectrophotometry can be used to investigate crystalline proteins containing chromophores, metal centers, or colored substrates if endogenous fluorophores are present in the macromolecule. The technique can be used to check the absence, presence, or redox-state of a fluorescent substrate or cofactor. Ogorodnikov et al. obtained unprecedented subnanosecond time resolution in low-temperature measurements of photoluminescence (PL) spectra of undoped potassium pentaborate crystals under selective photoexcitation (*I4*). Using this technique, the PL peaks associated with the intrinsic defects of the crystal lattice and the inhibition of electron excitations are detected. They further modified the method to study the complex dynamics of electronic excitations in potassium dihydrophosphate

crystals (*I5*). Novel data on the kinetics of the PL decay, time-resolved PL spectra, and time-resolved excitation PL spectra were acquired. In a separation investigation, Chen et al. described an original system containing nonaqueous capillary electrophoresis interfaced with ultralow-temperature separation and 77 K fluorescence detection (*I6*). The unique method can separate structurally similar molecules using a combination of low electrophoresis current and high voltage allowing for online spectral fingerprint identification. Bystol et al. demonstrated the utility of a cryogenic fiber-optic probe coupled to HPLC for the direct determination of benzo[a]pyrene without additional separation steps (*I7*).

TOTAL LUMINESCENCE AND SYNCHRONOUS EXCITATION SPECTROSCOPIES AND RELATED TECHNIQUES

Total luminescence, synchronous excitation, or other similar multiwavelength methods appeared in a number of unique analytical applications. General application areas not covered by this review include the environmental analysis of natural organic matter, as well as the environmental and clinical analysis of PAHs. Although these analyses are now relatively routine, reports of these applications continue to appear extensively in the literature. Recent developments in synchronous scanning fluorescence for multicomponent analysis were the subject of a major review by Patra and Mishra (*I1*).

Li et al. reported the use of synchronous excitation with total internal reflection fluorescence (TIRF) for the simultaneous analysis of multicomponents at solid/liquid interfaces (*I2*). Patra and Mishra described the technique of total synchronous fluorescence scanning (TSFS) which extends the typical two-dimensional synchronous scanning method to three dimensions by using a variety of possible wavelength intervals ($\Delta\lambda$) (*I3*). Although similar to a conventional EEM, the TSFS contour plot provides an alternative presentation for multicomponent spectra. The method of matrix isopotential synchronous fluorescence was used in combination with derivative techniques to detect analytes in samples with unknown background fluorescence without the necessity of a separation step (*I4*). The method was demonstrated with the detection of salicylamide in serum.

Wang et al. demonstrated the use of synchronous fluorescence with 4-aminophenol for the sensitive detection of protein (*I5*). They reported a detection limit for human serum albumin (HSA) of 80 ppb. Alternately, the same group also described the application of CdS nanoparticles with synchronous fluorescence for detection of protein (*I6*). In this case, they reported a detection limit of 21 ppb for HSA. A similar synchronous method using CdS nanoparticles was demonstrated for detection of DNA with detection limits as low as 10 ppb (*I7*). Dubayova et al. proposed the use of synchronous scanning fluorescence for routine clinical monitoring of urine samples as a convenient and sensitive screen for presymptomatic diagnosis of illness (*I8*).

SOLID SURFACE LUMINESCENCE

During this review period, articles pertaining to solid surface fluorescence dealt primarily with molecular interactions at solid surfaces. Shield and Harris reported a study examining molecular interactions on porous silica surfaces by phosphorescence quenching of probes immobilized on the silica surface (*K1*). Erythrosin B was used as a triplet-state probe with azulene as a quencher. In

the absence of oxygen, long-lived triplet-state phosphorescence enabled assessment of the rates of interfacial encounters and the dependence on local surface environment. Time-resolved luminescence measurements enabled the determination of the triplet-state lifetimes, which were used to construct Stern–Volmer plots under various conditions. It was found that diffusion of azulene through the silica pore network was efficient over a distance scale of ~ 0.5 μm , as probed by erythrosin quenching.

Several interesting papers were published that reported various aspects of single-molecule detection of DNA/RNA on surface-immobilized sensors. Piesert et al. reported a DNA hairpin sensor capable of detecting subpicomolar concentrations of DNA or RNA sequences (K2). The sensor is based on an approach analogous to that of molecular beacons, whereby the sensing response arises from changes in fluorophore–quencher distances following conformation changes upon hybridization with the target oligonucleotide. This system is unique in the utilization of the low oxidation potential of the DNA base guanosine. The guanosine base is used as a quencher through a photoinduced electron-transfer mechanism that occurs in the hairpin configuration.

Yao et al. reported results from a study of molecular beacon probe hybridization at the single-molecule level (K3). Fluorescence images of surface-immobilized DNA probes were obtained by using total internal reflection fluorescence microscopy, which allowed tracking of hybridization dynamics for individual probes. Of the individual probes that were tracked, 87.5% were reported to hybridize quickly and the remainder was found to react slowly. In a related study, Kim et al. examined conformational changes of single RNA molecules immobilized on a glass surface by FCS and FRET (K4). The dependence of opening and folding rates on Mg^{2+} and Na^+ was examined and was found to vary with changing salt conditions. The combined FCS and FRET approach is reported to be a powerful technique to examine conformational dynamics on a time scale of microseconds to seconds.

LUMINESCENCE IN CHROMATOGRAPHY, ELECTROPHORESIS, AND FLOW SYSTEMS

Numerous studies have been reported using chromatography with fluorescence detection. The general trend of the scientific community toward single-molecule analysis is also observed in papers published within this category. Several papers coming from Wirth's group were published detailing results from studies examining adsorption/desorption phenomena at solid surfaces of chromatographic relevance. It is known that analyte adsorption to silica surfaces in reversed-phase chromatography results in peak tailing and poor chromatographic performance, which is believed to be due to multiple adsorption sites. This effect is minimized by end capping and increasing the surface coverage of the stationary phase, but is not totally eliminated, and represents a fundamental limit to the resolution that can be achieved. To characterize this phenomenon, Wirth's group examined single-molecule dye adsorption on several chromatographically relevant surfaces. In 2002, Ludes and Wirth examined the specific adsorption of the cationic dye, 1,1'-diocetyldecyl-3,3,3',3'-tetramethylindocarbocyanine (DiI) at a solvent/ C_{18} - SiO_2 interface (L1). Using an inverted microscope equipped with a CCD camera for fluorescence imaging and confocal avalanche photodiode detection for single-molecule detection, the spatial heterogeneity of specific adsorption was examined. Three specific adsorption sites exist,

with desorption times ranging from 0.07 to 26 s. Another paper by the same group compared desorption behaviors of DiI onto fused silica and silica gel, both of which were coated with the same type of hydrocarbon monolayer (C_{18}) (L2). Similar desorption times were found for both substrates, indicating that the same types of absorption sites were found on fused silica and silica gel. A third article from the same group details the contributions of single-molecule spectroscopy to understanding the strong absorption phenomenon (L3). In this study, a combination of single-molecule spectroscopy, fluorescence correlation spectroscopy, fluorescence imaging, and atomic force microscopy were used to characterize the adsorption behavior of DiI. The strong absorption sites are isolated neutral silanols, and the absorption was found to be independent of pH down to pH 1.

In other work, Geng's group investigated a technique for the direct determination of solute molecules interacting with a C_{18} stationary phase under true separation conditions in capillary electrochromatography (CEC) (L4). In their method, the images of mobile-phase and stationary-phase packing were completely defined with laser scanning confocal fluorescence. This technique is also applicable to reversed-phase liquid chromatography and makes it possible to study the structure of the column, the quality of the stationary phase, and the mechanisms of separation.

Much work was conducted on PAHs. McGuffin's group thermodynamically and kinetically characterized six PAHs using reversed-phase liquid chromatography with laser-induced fluorescence detection (L5). Also, they employed fluorescence quenching, after separation with high-efficiency capillary liquid chromatography, to profile PAHs in environmental matrixes (L6). This technique can confirm the source or cause of an event with deleterious environmental impact, such as an oil spill, leak, or pollution from petroleum fuel production.

Research on DNA analysis continues. McGown's group used DNA oligonucleotides (DON) that form G-quartet structures as stationary phase in the separation of bovine milk proteins (L7). The open tubular CEC separation used DON that are covalently attached to the inner surface of a fused-silica capillary. In their method, the G-quartet-coated capillaries showed better resolution than either a naked capillary or one coated with DON that do not form a G-quartet structure.

Several researchers developed techniques based on microchip electrophoresis (μ -CE). Amirkhanian and Liu devised a multi-channel capillary-based electrophoresis (MCCE) system, based on multiplexed fluorescence detection, combined with a disposable separation cartridge for general analysis of DNA (L8). The instrument has solid-state light sources, multiple separation channels, and nonmoving detection microoptics, which provide for a robust CE machine. The innovative MCCE system will decrease the cost of DNA analysis and may be the preferred future instrument for molecular diagnostic applications and forensic DNA analysis. Beard and De Mello formulated a glass capillary microchip for the separation of biogenic amines using indirect fluorescence detection (L9). The decreased sample handling and speedy separations given by the coupling of indirect fluorescence detection with chip-based capillary electrophoresis yields a highly efficient technique for the analysis and detection of molecules not possessing a chromophore or fluorophore. In related research based on μ -CE, Dang et al. described a novel method for the swift

separation of complex oligosaccharides with light-emitting diode confocal fluorescence (L10). Under optimal conditions, 15 oligosaccharides were separated with superior electrophoretic efficiency within 45 s. An association of conventional CE and patterned fluorescence correlation spectroscopy was used by Sonehara et al. in developing a novel method to perform electrophoretic analysis independently of the original length of injected analyte plug (L11). In this process, the fluorescence emission of analyte molecules, migrating through a stationary interference pattern created by two intersecting excitation laser beams, was monitored. When the effective length is less than 1 cm, the authors' data predict their optimized technique is superior to conventional CE.

Recent work was conducted on the separation and detection of proteins and nucleic acids. A method was developed by Jackman and Schmerr for the evaluation of the performance of an antibody capture method using fluorescent peptides, capillary zone electrophoresis, and laser-induced fluorescence detection (L12). Berezovski et al. described a technique using low-affinity aptamers (synthetic DNA oligonucleotides) as probes in quantitative protein analysis (L13). The procedure is based upon nonequilibrium CE of the equilibrium mixture of a protein with its fluorescently labeled aptamer. The proposed method affords the use of aptamers for very sensitive affinity analysis of proteins, even when protein-aptamer complexes are unstable. McIntosh et al. reported using intercalating dyes as labels in DNA restriction fragment analysis by CE with frequency-domain fluorescence lifetime detection (L14). The dyes yield a broader range of lifetimes and better discrimination in multiplex detection.

Several flow injection systems with chemiluminescent detection were developed to determine various substances in air. A novel flow-through electrolytic cell was designed by Zheng and Zhang to measure sulfite, which was oxidized by in situ-generated Mn^{3+} (L15). The oxidized sulfite was then injected through the electrolytic cell to produce a strong chemiluminescence signal. Under optimal conditions, the emission intensity was linear with sulfite concentration and the detection limit was in the nanomolar range. Mihalatos and Calokerinos constructed a flow injection gas-phase chemiluminometer to monitor halogenated compounds that consume ozone upon UV radiation (L16). The quantification limits ranged from millimolar to nanomolar; however, the sensitivity of the instrument depended upon the ability of the compounds to destroy ozone.

A number of groups developed processes to determine pollutants in water. Yang et al. described a flow system for the determination of ammonium chloride based upon its oxidation with *N*-bromosuccinimide in alkaline media (L17). The system had a linear response to ammonium chloride in the 0.1–15 mM range. A simple and sensitive flow injection method for the detection of nitrate in water, described by Mikusa et al., is based on the online photolytic conversion of nitrate to nitrite in a quartz capillary (L18). Nakamura et al. investigated the reaction of Cl^- with bis(2,4,6-(trichlorophenyl)oxalate) in the presence of 9,10-diphenylanthracene in a methylcyanide/water medium (L19). This assay was used for the analysis of free Cl^- in tap water. A novel flow injection method was proposed for the determination of the disinfectant, 1,3-dichloro-5,5-dimethylhydantoin, by Rao et al. (L20). This

process, which had a detection limit of 10^{-8} nmol, was applied to detect trace amounts of disinfectant in swimming pools.

A few groups reported detection procedures pertinent to the pharmaceutical industry. Li et al. have found that adrenaline inhibits the electrochemiluminescence of $\text{Ru}(\text{bpy})_3^{2+}$ (L21). Based upon this finding they developed a method, with a detection limit in the nanomolar range, to determine adrenaline in pharmaceutical samples. A new, photochemically sensitized process for the detection of sparfloxacin (SPEX) in tablets and capsules was formulated by Sun et al. (L22). SPEX, when irradiated by UV radiation in acidic medium, undergoes a photochemical reaction. The photoproduct forms a complex with Tb_3 and sensitizes the chemiluminescent intensity of $\text{Ce}(\text{IV})\text{-SO}_3^{2-}$.

DYNAMIC LUMINESCENCE MEASUREMENTS

Several studies were described involving the use of dynamic fluorescence techniques in imaging, including a frequency-domain system for collecting spectrally resolved fluorescent lifetime images (M1), detection and identification of single mRNA molecules in living cells (M2), combination of time-correlated single-photon counting with near-field scanning optical microscopy to generate three-dimensional data sets, from which images of photons at particular time delays, images of fluorescence lifetime, or regions of interest fluorescence images can be extracted (M3), frequency-domain pH imaging of living cells (M4), resolution of two dye molecules that are less than 30 nm apart (M5), and measurement of the number of independent emitters in a detection volume, along with the fluorescence intensity, lifetime, and emission wavelength for trajectories and images of single molecules and multichromophoric systems (M6). Time-resolved spectral measurements were used to simultaneously resolve the fluorescence spectra and kinetics of fluorescence proteins and of zooxanthellae chlorophyll (M7). Stimulated emission depletion of two-photon excited states was combined with time-resolved detection for the study of molecular probe dynamics (M8). Time-resolved multiphoton excitation also was described for fluorescence imaging in studies of electric field-induced reorientation dynamics in polymer-dispersed liquid crystal films (M9).

Dynamic fluorescence lifetime methods were explored in CE and CEC. The application of fluorescence lifetime detection in DNA sequencing by capillary gel electrophoresis (CGE) and in microarrays was reviewed (M10). On-the-fly fluorescence lifetime detection was applied in CE for investigation of humic substances (M11); and novel acridone dyes and dye-labeled primers for use in four-decay DNA sequencing were studied (M12).

In other developments, lifetime and time-resolved techniques were used to investigate properties of liquids in nanometer-scale channels in a fused-silica microchip (M13), to study the effects of molecular organization in DNA oligomers (M14), to study relaxation of tryptophan and tyrosine in glycerol and in proteins (M15), to study the structural conformational transitions in copper proteins (M16), to investigate the effect of pressure on proteins and lipidic membranes (M17), and to analyze binding and determine the oligomeric state of a peroxisomal targeting signal receptor and an intraperoxisomal protein (M18).

The statistical basis and theoretical rationale for a photon-by-photon approach to probing single-molecule dynamics were

presented (M19, M20) and applied to the study of protein conformational dynamics (M21).

FLUORESCENCE POLARIZATION, MOLECULAR DYNAMICS, AND RELATED PHENOMENA

Several novel uses of fluorescence anisotropy were reported in the literature. The Lakowicz research group reported the differences in emission spectra, intensity decays, and anisotropy of 2,2'-dimethyl-*p*-terphenyl (DMT) for three- and four-photon excitation (N1). The authors observed no changes in emission spectra, intensity decay, or correlation times for the two methods of excitation; however, they reported a rather large intrinsic anisotropy of DMT, $r_0 = 0.70$, with four-photon excitation. The kinetics of the capture and release of a ligand by cell surface receptors was investigated using stopped-flow mixing technique and fluorescence anisotropy detection (N2). Using various fluorescence microplate readers coupled with polarization optics, Knight et al. were able to discriminate green fluorescent protein from autofluorescent interferences in genetically modified yeast cells (N3).

Select plant flavonols, such as quercetin, show advantageous therapeutic activities with low systemic toxicity but high potency. In aqueous solution, quercetin fluorescence is weak; however, when bound to HSA, the emission intensity increases and a new excited-state proton transfer (ESPT) emission band appears. Using fluorescence anisotropy, Sengupta and Sengupta noted the appearance of a third emitting species, a ground-state complex formed within the HSA environment (N4). The authors determined emissions from the ESPT and ground-state complex occur because quercetin binds to two distinct sites within HSA. The binding of camptothecins, potential anticancer agents, to HSA and cell membranes was investigated using fluorescence anisotropy (N5). Steady-state anisotropy was used to investigate the interactions of antibiotics of the polymyxins family with pyrene-labeled phospholipids (N6). Probes able to solubilize into different regions of the membrane provided insight into the effect of these antibiotics on lipid packing or phase transition.

Time-resolved fluorescence depolarization, with picosecond time resolution, of fluorescently labeled bacteriorhodopsin and bovine rhodopsin was employed to study loop conformational changes of the AB loop and EF loop of the former and the fourth cytoplasmic loop (helix VIII) of the latter (N7). Using functionally intact proteins, the authors determined two mechanisms of conformational changes. Mielke et al. fluorescently labeled bovine rhodopsin at cysteine residues located in cytoplasmic loops involved with signal transduction and activation (N8). The authors employed time-resolved fluorescence depolarization to investigate conformation changes and diffusion dynamics on the nanosecond time scale of these flexible loops.

Bell et al. applied the method of polarized fluorescence depletion (PFD) to investigate dynamic motions of rhodamine-labeled gizzard myosin regulatory light chain (RLC) exchanged into rabbit psoas muscle fibers (N9). PFD can increase the resolution of dynamics and orientational distributions determined from fluorescence polarization experiments. The authors suggest microsecond dynamic motions can account for the majority of disorder of the light-chain region during contraction.

Energy migration of two kinds of dendritic units, with 3- or 4-fold symmetry, was studied using ultrafast fluorescence anisotropy (N10).

The authors found the type of energy transfer depended upon the symmetry of the branching center. Using single-molecule fluorescence polarization of a sol-gel-encapsulated fluorophore, Viteri et al. correlated the mobility of a fluorophore with its photostability (N11).

CHEMILUMINESCENCE

Several groups developed procedures to evaluate sulfite and thus applied their methods to measure sulfur dioxide in air samples. Wang and He measured SO₂ in air by using triethanolamine as an absorbent material in a tris(2,2'-bipyridyl)ruthenium(II)-CO₃-SO₃-KClO₃ system (O1). In this system, the chlorate oxidized sulfite was used to detect the concentration of sulfite. A simple assay for alkaline phosphatase (ALP) using dihydroxyacetone phosphate or its ketal was developed by Kokado et al. (O2). The method, which was applied to the enzyme immunoassay of 17 β -estradiol using ALP as the label, was 4 times more sensitive than the colorimetric assay. Li et al. developed a novel plant tissue-based biosensor for dopamine detection (O3). The biosensor was used in vivo to monitor the variation of dopamine level in the blood of rabbit after dopamine administration. An excellent review on the use of micelles, reversed micelles, and microemulsions to improve the quality of chemiluminescent analyses was issued by Lin and Yamada (O4).

NEAR-INFRARED FLUORESCENCE

Developments reported in the area of NIR luminescence largely focused on DNA analysis and bioimaging. Several papers reported advances in oligonucleotide analysis based on the use of NIR luminescence. With the draft completion of the human genome, the ability to translate emerging disease-related genetic information into advances in health care will depend on efficient oligonucleotide analyses. Hammer et al. reported development of two new water-soluble NIR dyes which were conjugated to oligonucleotide primers (P1). The two porphyrazine dyes contain an isothiocyanate moiety capable of covalent linking to oligonucleotides. The two dyes differ in their degree of conjugation and exhibit absorption maximums at 683 and 755 nm. Another development in DNA analysis was reported by Wang et al. (P2). A microchip array was developed for the detection of low-abundant DNA mutations. The system is designed to analyze gene fragments that carry point mutations relevant to diagnosis of colorectal cancers. The significance of this development is demonstrated by the ability to detect 1 mutant DNA in 10 000 wild-type sequences.

Developments in the area of multiplex detection in CE and other formats include optimization of lifetime detection in the near-IR for DNA sequencing samples in CGE (P3). An interesting instrumental application was reported by Zhu et al., where the design and performance of a time-resolved NIR detector and its use in a two-color, two-lifetime DNA sequencing protocol are demonstrated (P4). Diode lasers provided excitation sources at 680 and 780 nm that were coupled and focused onto a capillary used for electrophoretic sorting of the DNA. The fluorescence is collected by the same objective, spectrally separated by a dichroic mirror and then focused onto separate single-photon avalanche photodiodes (SPADs). Two-channel fluorescence lifetimes were determined using time-correlated single-photon counting from the output of each SPAD. The system was evaluated by implementing

an automatic peak recognition algorithm. The authors report a base-calling accuracy of 95.1% over a read length of 650 base pairs. These developments offer promise toward the goal of higher throughput analysis by multiplexing on single capillaries.

Several papers and two reviews were published that focus on developing NIR luminescence for applications in medical imaging, exploiting the spectral window in which biological tissue is transparent. Also reported was a review of protease sensors for bioimaging (P5). The review focused on reported molecules that can be used to signal protease cleavage. Several reports focused on the development of new NIR probes and techniques for applications in optical imaging. Zaheer et al. reported the development of a new NIR fluorophore conjugate with retained bioactivity (P6). It is anticipated that the developed system will have application in the detection of human malignancies via fluorescence imaging of the conjugates with cancer specific ligands. Kircher et al. detailed the development of a system for measurement of in vivo enzyme activity by ratio imaging of dual-wavelength optical reporters (P7). The method is based on the use of two similar probes that differ in their degradability by the enzyme. The ratio of fluorescence from the two probes is used as a measure of the enzyme activity, and the magnetic properties of the probes allow magnetic resonance (MR) imaging of the probes. The development of magnetic nanoparticles for use in MR imaging as well as fluorescent signaling was reported by Josephson et al. (P8). The nanoparticles are prepared by conjugation of arginyl peptides, which can be activated by particular enzyme activity. This type of imaging probe can provide spatial information via MR imaging and chemical information by the NIR fluorescence. Jaffer et al. reported the development of a thrombin-activated, thrombin-sensitive probe that is capable of providing in vivo images of thrombin activity (P9). An 18-fold enhancement in fluorescence intensity was reported based on endogenous thrombin activity. Piszczek et al. also reported the development of new NIR fluorescent probes for use in bioimaging (P10). The probes are based on NIR-emitting lanthanides sensitized by a fluorescent chelator. The fluorescence of the probes using multiphoton excitation is demonstrated, and it is suggested that the probes are appropriate for tissue imaging, based on the wavelength of the fluorescence emission.

LUMINESCENCE TECHNIQUES IN BIOLOGICAL AND CLINICAL ANALYSIS

Numerous fluorescence-based techniques were described for biological analysis. Banerjee and Sarkar reported the influence of microenvironment on the spectral properties of long-acting nonsteroidal antiinflammatory drugs via steady-state fluorescence spectroscopy (Q1). Their results indicate how the microenvironments of these drugs control the nature of the predominant form in solution. Several researchers employed fluorescence methods to detect nitric oxide and its derivatives. Rodriguez and Feelisch developed a form of optical spectroscopy to identify and monitor, in real time, the modulation of NO concentration in vascular tissue (Q2). The technique is based on the ability of NO supplies to reversibly free NO when illuminated with light of certain wavelengths. This release can be detected as a photorelaxation of vascular smooth muscle. Dai et al. used a permselective cellulose acetate membrane with flow injection analysis and chemiluminescence detection to ascertain a derivative of NO, peroxynitrite

(ONOO⁻) (Q3). This technique makes monitoring ONOO⁻ in biological samples very easy.

A number of papers reported the study of skeletal muscle fibers by fluorescence methods. Kinesin, a molecular motor responsible for skeletal muscle movement, can make over 100 steps along the microtubule in 8-nm fractions. Rosenfeld et al. developed probes sensitive to motor-motor separation or microtubule binding to evaluate kinesin function (Q4). Their probes allow direct measurement of how quickly kinesin catches and releases the microtubule, which gives insight into its progressive movement. Shaw et al. found that the contraction of fast skeletal muscle fibers was specifically inhibited by the small organic molecule's, *N*-benzyl-*p*-toluenesulfonamide, suppression of phosphorus release (Q5). Matsunga et al. investigated a capillary-based unified system to measure expression of a specific gene directly from cells (Q6). Their confirmatory results set the foundation for future capillary electrophoresis or microchip instrumentation for automated, high-throughput gene expression analysis. Bright's group devised a novel two-photon phase-resolved fluorometer that can selectively monitor analyte emission spectra from optically difficult samples, such as urine, juices, and soft drinks, without sample pretreatment (Q7).

The use of luminescence spectroscopy to study biological membranes continues. Palmitoylphosphocholine (PPC) is a major lipid component of cellular membranes. Steady-state and time-resolved fluorescence was used by Metso et al. to study the structural dynamics of the principle phase transition of large unilamellar PPC vesicles (Q8). Their data show the possibility of an intermediate phase of a fluctuating lattice of gellike and fluidlike lipids, which, upon temperature increases, transforms into a disordered liquid phase. In another structural study, Asai studied the dispersal mechanism of retinol (vitamin A) into phospholipid using dynamic light scattering and fluorescence spectroscopy (Q9). He found only 3% of retinol was incorporated into the bilayer membranes and the excess vitamin A was stabilized as emulsion particles by the surface monolayer.

Two groups reported membrane interaction with antimicrobial or antibiotic analogues. Nisin is an antimicrobial peptide used as a food preservative in dairy products. In an effort to explain the mechanism of targeted pore formation, van Heusden et al. used site-directed tryptophan spectroscopy to detect the topology of nisin in lipid II, a cell wall precursor (Q10). Their results, which can have pharmaceutical applications, showed that lipid II altered the total orientation of nisin in membranes from parallel to perpendicular with respect to the membrane surface. Structural analogues of the antibiotic distamycin are potential candidates as gene modulators. Bhattacharya and Thomas investigated whether attaching fluorescent tags to these analogues changes their DNA binding affinity (Q11). Their data suggested that binding affinity is modified depending on the attachment point of the tag. These findings have implications for future design of fluorescent tags in molecular biology and medicine.

Numerous techniques using various forms of luminescent proteins for single-cell analysis were presented. Kunst et al. determined the flow profile of fluorescent particles inside a microcapillary using fluorescence fluctuations of a small molecule (Q12). With their method, they can describe the parameters of capillary flow experiments with fluorescent molecules, bacteria

and microspheres. New developments using luminescent quantum dots for spectroscopy and quantitative imaging of single cells were reported by Gao and Ne (Q13). The authors label both fixed and live cells with multicolor QDs and analyze single cells using fluorescence imaging and wavelength-resolved spectroscopy. Other researchers used correlation spectroscopy for detection. Knowles et al. report measuring the fluctuations of mitochondrial reticulum in osteosarcoma cells using Fourier imaging correlation spectroscopy (Q14). Their method allows a more complete description of mitochondrial dynamics than available by other means. Smith et al. used a bacteria species, which expresses green fluorescent protein (GFP), to determine the influence of different environmental pH conditions on GFP fluorescence (Q15). They found that GFP fluoresces best in neutral conditions and is unsuitable for environments above or below neutral.

Lakowicz's group developed numerous techniques with clinical applications. One creation is a glucose-sensing contact lens embedded with newly developed boronic acid containing fluorophores (Q16). Because tear glucose levels are usually 5–10 times lower than blood glucose levels, this approach may provide an alternative to invasive blood glucose monitoring. They further used boronic acid to develop fluorescent probes to analyze fluoride (Q17). Modification of the chemical structures of fluorescent probes to tailor their use in biological and biotechnological research was another development (Q18). Placing the fluorophores close to gold and silver metallic particles of various shapes and sizes changes the spectral properties of the fluorophore and allows the creation of uniquely specific characteristics. In a related study, Perez-Luna et al. developed a novel biosensor which is immobilized on a gold surface (Q19). Upon binding, a fluorophore experiences a reduction in fluorescence intensity and lifetime due to its close proximity to the metal surface. An increase in fluorescence is observed when the fluorophore dissociates from the surface-bound analyte and binds to free analyte in solution.

A number of other papers also contain reports of research with clinical applications. In a medical application, the potential of temporal and spectral fluorescence techniques for improving the surveillance of high-grade dysplasia in Barrett's esophagus was investigated (Q20). Fowler et al. studied the effects of formaldehyde treatment on the physical characteristics and monoclonal antibody (mAb) binding of pertussis toxin (PT) (Q21). Fluorescence data yielded evidence of progressive unfolding and reassociation of PT with mAb. Their evidence showed a helpful balance between protein stabilization and denaturation was attained by treatment with formaldehyde. Also, it demonstrated the importance of cross-linked species of PT for protection against whooping cough.

Research in the area of cardiovascular diseases was reported. For example, homocysteine is a marker for cardiac heart disease and imminent myocardial infarction. A simple fluorometric detection method for simultaneous determination of homocysteine thiolactone (HTL) and homocysteine (Hcy) in biological samples was described by Mukai et al. (Q22). In their method, the separation depends on isocratic ion-pairing and reversed-phase chromatography while the detection relies on Hcy reacting to form a stable fluorescent derivative. The sensitivity limit of the method is 200 fmol of HTL and 100 fmol for Hcy. Tomasevic et al.

incorporated a fluorescent lipid analogue to study the dynamics of the plasma membrane during hyperinsulinism (Q23). In the presence of insulin, two plasma membrane lipids and cholesterol were found to bind to hemoglobin. Their findings may be pertinent to cases of diabetes mellitus and hypoglycemia.

Recently, several studies involving RNA and DNA were published. Two groups developed methods to assay DNA or RNA catalysis. Mei et al. created and characterized a RNA-cleaving autocatalytic DNA molecule that synchronizes chemical catalysis with real-time fluorescence signaling (Q24). Their DNA enzyme cleaves chimeric RNA/DNA at the only RNA linkage, which is surrounded by a fluorophore–quencher pair. Also, their DNA enzyme has a stem–loop structure that can be conjugated to DNA aptamers to form deoxyribozyme biosensors. This unique structure easily connects chemical cleavage with fluorescence signaling. Based on the fluorescence quenching mechanism of molecular beacons, Rizzo et al. developed a sensitive method to assay RNase H enzymatic activity (Q25). The fluorescently labeled, single-stranded RNA–DNA substrate is held in proximity to the quencher by the RNA–DNA stem–loop structure. Once the substrate is cleaved, the fluorophore is disconnected from the quencher and fluorescence can be determined as a function of time.

Two groups concentrated on RNA translocation. Studer et al. introduced a new process for monitoring translocation of mRNA in the ribosome (Q26). In the method, the 3-end of a short mRNA was fluorescently labeled with pyrene. Thus, translocation of the mRNA by one codon resulted in a dramatic decrease in the fluorescence emission of pyrene, which can be utilized to directly monitor mRNA movement. Vijayanathan et al. used a molecular beacon approach to detect the association constant of RNA–DNA hybrid formation (Q27). This approach generated information that is useful to design oligonucleotides for antisense therapeutics. Soper's group described novel strategies for analyzing molecular signatures of disease states in real time. They used allele-specific primers to quickly detect point mutations in unamplified genomic DNA and discriminate between normal and mutant DNA in heterogeneous populations (Q28).

Three papers focused on RNA/DNA binding to drugs and proteins. The identification of a novel, potent inhibitor of DNA topoisomerase I was presented by Facompre et al. (Q29). This alkaloid displayed powerful cytotoxic activities against prostate cancer and multidrug-resistant tumor cell lines and is a key candidate for the formulation of topoisomerase I-targeted antitumor agents. Norfloxacin, an inhibitor of topoisomerase II, was found to bind similarly to double-stranded and supercoiled-DNA by Hwangbo et al. (Q30). Liu et al. investigated the interaction between DNA and dopamine and found that dopamine binds to DNA and can be used as an effective probe for a DNA assay (Q31). Zheng and Yeung described a novel approach to count single DNA molecules in low volumes using laser excitation (Q32). Their method can be applied to counting deformable molecules or nonspherical particles at extremely low concentrations.

Also, some work on fluorescent bacteria was reported. Kim and Gu successfully developed a high-throughput toxicity monitoring and classification biosensor system using four immobilized bioluminescent *Escherichia coli* strains (Q33). The bioluminescence of each strain increased in the presence of a particular kind

of damage, such as protein, DNA, membrane, or oxidative. In the method, the strains were immobilized in a 96-well plate and able to detect certain chemicals in water samples. The bioluminescence of the strains increased as a function of chemical concentration in a dose-dependent manner. The high-throughput capacity of these biosensors makes the detection of certain kinds of damaging agents in aqueous samples fast and easy.

REAGENTS AND PROBES

Recent advances in the fabrication of novel probes and reagents for the investigation into biological and medical technology are worthy of note. Techniques and applications such as fluorescence microscopy stemming from live animal multiphoton confocal microscopy to single-molecule fluorescence spectroscopy and imaging in living cells was utilized.

An easy and efficient approach to protein elucidation may be the recent development of molecular aptamers combined with fluorescence techniques. One report described the development of a fluorescent-based assay with synthetic DNA aptamers that can detect and distinguish molecular variants of proteins in biological samples in a high-throughput process (*R1*). This assay is applicable to proteins that are not naturally DNA binding. Li and co-workers, have pioneered a new protein probe, molecular aptamer beacon (MAB), for real-time protein recognition and quantitative analysis (*R2*). The unique properties of the MAB will enable the development of a class of protein probes for real-time protein tracing in living specimens and for efficient biomedical and diagnosis in homogeneous solutions.

A number of new dyes were reported for use in biological applications. One report included two new water-soluble porphyrane dyes containing an isothiocyanate function for covalent linking (*R3*). Both dyes were successfully conjugated to oligonucleotide primers, showing their potential for use in near-infrared-based DNA diagnostic applications. Another report detailed the use of novel intercalating dyes as labels in DNA restriction fragment analysis by capillary electrophoresis with frequency-domain fluorescence lifetime detection (*R4*). The dyes provided a wider range of lifetimes and better lifetime discrimination in multiplex detection.

By means of single-molecule measurements, the optical behavior of a dimer of tetramethylrhodamine-5-isothiocyanate was investigated (*R5*). The results demonstrated the capability of single-molecule techniques to provide detailed insight into the exciton dynamics in multichromophoric systems. This is a key point in understanding the behavior of relevant natural aggregates and, eventually, in allowing for a rational design of molecular photonic devices. Neuweiler et al. also described a single-molecule sensitive method to determine the rate of contact formation and dissociation between tryptophan and an oxazine derivative (MR121) on the basis of measurements of the photon distance distribution (*R6*).

Nanostructures that interface with biological systems recently received widespread attention in biology and medicine. In one study, semiconductor nanocrystals with narrow and tunable fluorescence were covalently linked to oligonucleotides and were able to retain the properties of both nanocrystals and DNA (*R7*). They found the possibility of directing fluorescent nanocrystals

toward specific biological targets and detecting them, combined with their superior photostability compared to organic dyes, opens the way to improved biolabeling experiments, such as gene mapping on a nanometer scale or multicolor microarray analysis. Another paper described the development of oligonucleotide-modified silica nanoparticles, which provided an efficient substrate for hybridization and can be used in the development of DNA biosensors and biochips (*R8*). Reproducibly synthesized cadmium selenide nanocrystals at high temperature in continuous-flow, chip-based microfluidic reactors that exhibit size distributions comparable to those of conventional macroscale syntheses, was investigated (*R9*). Their capability to precisely control the nanocrystal size demonstrated the ability to fine-tune physical properties and test wide ranges of conditions precisely and rapidly inside chip-based microreactors, enabling rational, cost-effective, and environmentally friendly development and production of novel nanostructures. Larson et al. investigated the use of semiconductor nanocrystals (quantum dots) as fluorescent labels for multiphoton microscopy, which affords multicolor imaging in demanding biological environments such as living tissue (*R10*). They characterized water-soluble cadmium-zinc sulfide quantum dots for multiphoton imaging in animals.

Numerous papers provided a description of fluorescent probe systems for various bioanalytical purposes. Spectroscopic and photophysical properties of two fluorescent probes for monosaccharides were presented (*R11*). A novel fluorescence probe FA, 2-(6-diethylaminobenzo[*b*]furan-2-yl)-3-hydroxychromone, was reported to have strong, highly specific, and stoichiometric binding to bovine serum albumin and exhibited a very characteristic two-band fluorescence spectrum (*R12*). The new probe was proposed for the study of the interaction of ligands and drugs of different nature with serum albumins. 4-(2-Pyren-1-ylvinyl)pyridine was investigated as a new fluorescent probe sensitive to micelles and phospholipid vesicles of different surface charge (*R13*). In a new application, laurdan was used as a fluorescent probe that detected changes in membrane-phase properties through its sensitivity to the polarity of its environment in the bilayer (*R14*). Variations in membrane water content cause shifts in the laurdan emission spectrum, which were quantified by calculating the generalized polarization.

The Tan group examined the use of molecular beacons as a new class of fluorogenic probes for multiple usages. They were utilized as fluorescent probes to report the presence of specific nucleic acids with high sensitivity and excellent specificity (*R15*) and as probes for both oligonucleotide and protein detection in complex solutions (*R16*). Also, the dynamics of DNA hybridization on a liquid/solid interface at the single-molecule level by using a hair-type molecular beacon DNA probe was monitored (*R17*). Their results illustrated the ability to obtain a better understanding of DNA hybridization processes using single-molecule techniques, which will improve biosensor and biochip development where surface-immobilized molecular beacon DNA probes provide unique advantages in signal transduction.

New strategies were developed by Wabuyele and co-workers for analyzing molecular signatures of disease states approaching real time using single pair fluorescence resonance energy transfer

to rapidly detect point mutations in amplified genomic DNA (R18).

OTHER TECHNIQUES AND APPLICATIONS

Room-temperature ionic liquids (ILs) gained prominence in the last several years as potential organic solvent replacements. Recently, several groups employed fluorescence techniques to characterize physicochemical properties of these novel solvents. The Pandey research group investigated the effects of water, ethanol, aqueous ethanol, and binary IL–IL mixtures on solvatochromic behavior of select probes when solubilized within 1-butyl-3-methylimidazolium hexafluorophosphate (bmimPF₆), a commonly investigated IL (S1–S4). This group determined physicochemical properties of bmimPF₆ could be successfully altered by the addition of cosolvents; however, the binary and ternary solvent systems studied display nonideal behavior depending upon the cosolvent or solvatochromic probe. The same research group investigated the fluorescence quenching of several PAHs by nitromethane within bmimPF₆ (S5). Nitromethane quenching selectivity was maintained in the IL, indicating the cation plays the dominant role in PAH solvation.

The solvation dynamics of several fluorophores solubilized within imidazolium-based ILs were investigated by Karmakar and Samanta (S6, S7). This group determined wavelength-dependent fluorescent decay for the probes studied and biphasic solvation dynamics consisting of a fast component attributed to the diffusional motion of the anion and a slower component resulting from the combined motion of the cation and anion. Chakrabarty et al. undertook an investigation of solvent relaxation within ILs and reported findings consistent with Karmakar and Samanta (S8). Both groups concluded solvation within ILs occurs much slower than within conventional solvents. The Maroncelli research group extended these investigations to include ammonium- and phosphonium-based ILs. They reported biphasic solvation dynamics within imidazolium-based ILs but observed solvation within ammonium- and phosphonium-based ILs to occur on a single time scale (S9, S10).

Investigations of energy, hydrogen, and electron-transfer reactions within bmimPF₆ were reported by Alvaro et al. (S11). The authors observed slow molecular diffusion and low oxygen solubility within this relatively high viscosity IL, as well as an increase in the lifetime of radical ions and the triplet excited state. Furthermore, a reduction of charge-transfer interactions was observed. Translational mobility of a probe, self-aggregation behavior of solutes, and thermal stability of proteins were also reported (S12, S13). To investigate the possibility for cellulose-catalyzed reactions within ILs, the Rogers' research group studied enzyme stability within 1-butyl-3-methylimidazolium chloride using fluorescence techniques (S14).

Several environmental applications of fluorescence techniques were reported. A measurement of fluorescence index of sediments from two alpine lakes in the Colorado Front Range adequately characterized changes in organic matter as a result of varying environmental conditions (S15). The characterization of crude petroleum oils (the concentration of aromatics and the American Petroleum Institute gravity) was successfully determined using fluorescence techniques (S16). The Eu³⁺–tetracycline–hydrogen peroxide complex allowed the accurate and precise determination

of hydrogen peroxide in river water (S17); furthermore, the use of time-resolved fluorescence measurements removed interferences from other fluorophores within river water. Using a cryogenic probe, Martin et al. employed time-resolved laser-induced phosphorimetry for the analysis of dioxins in complex mixtures containing other dioxin isomers, PAHs, polychlorinated biphenyls, and polychlorinated dibenzofurans (S18). Potential fluorescence and phosphorescence interferences were removed with the use of time resolution. Alimova et al. demonstrated the utility of fluorescence emission and excitation spectroscopy for the real-time detection of bacterial spores (S19).

Using DNA as a rigid support and fluorescent dyes as chromophores, a novel approach to the development of unidirectional photonic wires was presented by Heilemann et al. (S20). Time-resolved and steady-state techniques were used to show four dyes, each with different excitation energies and spaced ~3.4 nm apart, generating an energy cascade by fluorescence resonance energy transfer. The photonic wires presented were able to unidirectionally transfer energy over an approximate 10-nm distance with a spectral separation of about 250 nm, and an overall efficiency of photonic energy transfer of close to 0.60.

Researchers often attempted to correlate observable system parameters (e.g., the position of the absorption or emission maximums) with physicochemical properties of the system. Klymchenko and Demchenko developed an algorithm able to estimate the polarity, electronic polarizability, and hydrogen bond donor ability of the microenvironment of surrounding 3-hydroxy-flavone dyes from four spectroscopic parameters: the position of the absorption and emission maximums, the position of emission from the excited-state intramolecular proton-transfer product, and the ratio of intensity of the two emission bands (S21).

Duyvis et al. presented the application of fluorescence quenching studies to determine the level of riboflavin in beer, where the quenching of riboflavin fluorescence occurs as a result of the binding of riboflavin to the aporiboflavin binding protein. In this assay, the only sample pretreatment required was the dilution of the beer, and potential interferences from flavin mononucleotide and flavin adenine dinucleotide were avoided (S22).

Aleeta M. Powe received her B.S. in chemistry from the University of South Alabama, Mobile, AL, in 1990. She worked as a Special Volunteer at the Gerontology Research Center of the National Institute on Aging, National Institutes of Health, Baltimore, MD, as a researcher at Georgetown University Medical Center, and as a Chemical Information Specialist for the Food and Drug Administration before receiving her Ph.D. in analytical chemistry from American University in Washington, DC in 2002. She is currently a postdoctoral researcher under the direction of Professor Isiah M. Warner at Louisiana State University. Her research interests include investigating various aspects of atherosclerosis. She is especially interested in the interaction of cholesterol and cholesterol esters with different components within the plaque. She has been involved in research investigating binary and tertiary complexes of naphthalene derivatives via fluorescence.

Kristin A. Fletcher received her B.S. in mathematics and B.A. in chemistry (1995) and M.S. in analytical chemistry (1997) from the University of North Texas. She worked in the field of forensics before receiving her Ph.D. from New Mexico Institute of Mining and Technology under the supervision of Dr. Siddharth Pandey in 2004. She is currently a postdoctoral researcher in Dr. Isiah Warner's research group. Her research interests include the investigation of physicochemical properties of room-temperature ionic liquids and ionic liquid-based systems, capillary electrophoresis separations with ionic liquids as background electrolyte modifiers or stationary phase, and chiral recognition.

Nadia N. St. Luce received her B.S. in chemistry from the University of the Virgin Islands, U.S. VI, in 1999. She received her Ph.D. in organic chemistry from Louisiana State University (LSU), Baton Rouge, LA, in 2003. She is currently working as a postdoctoral researcher under the supervision of Dr. Isiah Warner at LSU. Dr. St. Luce's research interests include studying the properties of pH-sensitive dyes in different ionic liquids and the synthesis of a chiral fluorescent reagent for enantioselective recognition of D-amino acids.

Mark A. Lowry received his B.A. in chemistry from Central College in Pella, IA, in 1998. He then pursued graduate studies under the direction of Professor Lei Geng at the University of Iowa where he is a Ph.D. candidate in analytical chemistry. He is currently a research associate in Professor Isiah M. Warner's group in the Chemistry Department at Louisiana State University. His research interests include fluorescence instrumentation, imaging and image analysis, and techniques including single-molecule imaging/spectroscopy, and fluorescence correlation spectroscopy.

Sharon L. Neal received her B.S. in chemistry from Spelman College in 1980 and her Ph.D. in chemistry from Emory University in 1988. She joined the faculty at University of Delaware in 1998 where she currently holds the position of Associate Professor of Chemistry. She currently serves on the A-page Advisory Panel of Analytical Chemistry. Her current research interests include the development of multidimensional fluorescence methods for characterization of complex samples, development of chemometrics methods for analysis and interpretation of multidimensional fluorescence, characterization of biomembrane models, characterization of intrinsic protein fluorescence, photokinetic characterization of multiply emitting probes, drug or toxin/protein interactions, and drug or toxin/lipid interactions.

Matthew E. McCarroll is an Assistant Professor in the Department of Chemistry and Biochemistry at Southern Illinois University. He received his B.A. and B.S. degrees in chemistry and interdisciplinary studies from Appalachian State University in 1994. He pursued graduate studies at the University of Idaho under the direction of Professor Ray von Wandruszka, where he received his Ph.D. in 1998. He then spent two years as a postdoctoral associate under the direction of Professor Isiah M. Warner at Louisiana State University. In 2000, he joined the faculty at Southern Illinois University as an Assistant Professor. His research interests focus on the application of analytical chemistry to investigate complex chemical phenomena with an emphasis in the areas of molecular spectroscopy and organized media. These include studies of chiral and molecular recognition, the development of fluorescence sensors, and the development of new materials for chiral separations and analysis. Current efforts are primarily focused on the development of fluorescence anisotropy as a tool in the study of chiral recognition.

Philip B. Oldham is a Professor of Analytical Chemistry and currently serves as Dean of Arts & Sciences at Mississippi State University. He received his B.S. in chemistry from Freed-Hardeman University in Henderson, TN in 1980 and his Ph.D. in analytical chemistry from Texas A&M University in 1985. He spent a year following his graduate work as a Wellcome Research Fellow at Burroughs Wellcome Company, Research Triangle Park, NC, before joining the faculty at Mississippi State University in 1986. He currently serves on the editorial boards of the *Microchemical Journal* and the *International Journal of Bio-Chromatography*. Dr. Oldham's research interests include the development of techniques for the characterization of solute molecules resident in specific microenvironments, such as biological membranes, micelles, and/or surface films. The current technique of interest is total internal reflection fluorescence (TIRF) with electrochemical control of the sensor surface. Much of his efforts are currently being directed toward application of TIRF in the design and microfabrication of novel biosensor devices.

Linda Baine McGown is Professor and Chair of the Department of Chemistry and Chemical Biology at Rensselaer Polytechnic Institute. She received her B.S. in chemistry from the State University of New York at Buffalo in 1975 and her Ph.D. in chemistry from the University of Washington in 1979. She served as a predoctoral lecturer at Texas A&M University (1978–1979) and then as Assistant Professor of Chemistry at California State University, Long Beach (1979–1982). In 1982, she joined the Department of Chemistry at Oklahoma State University and was promoted to Associate Professor with tenure in 1985. She moved to Duke University in 1987 and left Duke to join the faculty at RPI in 2004. In 1994, she received the New York Section of the Society for Applied Spectroscopy Gold Medal. McGown's research interests include fluorescence lifetime techniques for chemical analysis, DNA aptamers for chemical separations and affinity MALDI-MS, characterization of humic substances, and novel organized media and biogels.

Isiah M. Warner is a Boyd Professor of the Louisiana State University (LSU) System and Philip W. West Professor of Analytical and Environmental Chemistry in the Department of Chemistry at LSU. He received his B.S. degree in chemistry from Southern University in Baton Rouge, LA, in 1968 and worked at Battelle Northwest in Richland, WA, for five years before pursuing his Ph.D. in 1973. He received his Ph.D. in analytical chemistry from the University of Washington in 1977 and served on the faculty of Texas A&M University for five years and on the faculty of Emory University for 10 years before joining the faculty of LSU in 1992. His research interests include fluorescence spectroscopy, studies in organized media, and separation science, with a focus on solving biomedical and environmental analytical problems.

LITERATURE CITED

- (A1) Agbaria, R. A.; Oldham, P. B.; McCarroll, M.; McGown, L. B.; Warner, I. M. *Anal. Chem.* 2002, 74 (16), 3952–3962.

BOOKS, REVIEWS, AND CHAPTERS OF GENERAL INTEREST

- (B1) Bright, F. V.; Munson, C. A. *Anal. Chim. Acta* 2003, 500, 71–104.
 (B2) Miyawa, J. H.; Schulman, S. G. *Drugs Pharm. Sci.* 2002, 117, 427–466.
 (B3) Mann, T. L.; Krull, U. J. *Analyst* 2003, 128, 313–317.
 (B4) Kraayenhof, R.; Visser, A. J. W. G.; Gerritsen, H. C., Eds. *Fluorescence Spectroscopy Imaging and Probes*, Springer Series on Fluorescence 2; Springer-Verlag: New York, 2002.
 (B5) de Juan, A.; Tauler, R. *Anal. Chim. Acta* 2003, 500, 195–210.
 (B6) Geladi, P. *Spectrochim. Acta, Part B* 2003, 58B, 767–782.
 (B7) Santos, N. C.; Castanho, M. *Trends Appl. Spectrosc.* 2002, 4, 113–125.
 (B8) Chattopadhyay, A. *Chem. Phys. Lipids* 2003, 122, 3–17.
 (B9) Demchenko, A. P. *Luminescence* 2002, 17, 19–42.
 (B10) Jung, Y.; Barkal, E.; Sübey, R. J. *Chem. Phys.* 2002, 117, 10980–10995.
 (B11) Keller, R. A.; Ambrose, W. P.; Arias, A. A.; Cai, H.; Emory, S. R.; Goodwin, P. M.; Jett, J. H. *Anal. Chem.* 2002, 74, 316A–324A.
 (B12) Michalet, X.; Kapanidis, A. N.; Laurence, T.; Pinaud, F.; Dooze, S.; Pflughoeft, M.; Weiss, S. *Annu. Rev. Biophys. Biomol. Struct.* 2003, 32, 161–182.
 (B13) Hess, S. T.; Huang, S.; Heikal, A. A.; Webb, W. W. *Biochemistry* 2002, 41, 697–705.
 (B14) Krichinsky, O.; Bonnet, G. *Rep. Prog. Phys.* 2002, 65, 251–297.
 (B15) Hwang, L. C.; Wohland, T. *Songklanakarin J. Sci. Technol.* 2002, 24, 1045–1058.
 (B16) Contag, C. H.; Bachmann, M. H. *Annu. Rev. Biomed.* 2002, 4, 235–60.
 (B17) Hsu, L.; Kim, K. H.; Dong, C. Y.; Kaplan, P.; Hanczewicz, T.; Buehler, C.; Berland, K. M.; Masters, B. R.; So, P. T. C. *Confocal Two-Photon Microsc.* 2002, 431–448.
 (B18) Herman, P.; Lin, H.-J.; Lakowicz, J. R. *Biomed. Photonics Handbook* 2003, 9/1–9/30.
 (B19) Mahmood, U.; Weissleder, R. *Mol. Cancer* 2003, May 2, 489–96.
 (B20) Sevcik-Muraca, E. M.; Houston, J. P.; Gurfinkel, M. *Curr. Opin. Chem. Biol.* 2002, 6, 642–650.
 (B21) Chaudhury, N. K. *Adv. Biosens.* 2003, 5, 37–62.
 (B22) Gryczynski, Z.; Gryczynski, I.; Lakowicz, J. R. *Methods Enzymol.* 2003, 360, 44–75.
 (B23) Tolosa, L.; Nowaczyk, K.; Lakowicz, J. In *An Introduction to Laser Spectroscopy*, 2nd ed.; Andrews, D. L., Demidov, A. A., Eds.; Kluwer Academic: New York, 2002; pp 139–170.
 (B24) Rurack, K.; Resch-Genger, U. *Chem. Soc. Rev.* 2002, Mar 31, 116–27.
 (B25) Sutherland, A. J. *Curr. Opin. Solid State Mater. Sci.* 2002, 6, 365–370.
 (B26) Miguel, M. d. G.; Burrows, H. D.; Lindman, B. *Prog. Colloid Polym. Sci.* 2002, 120, 13–22.
 (B27) Santos, N. C.; Prieto, M.; Castanho, M. A. R. B. *Biochim. Biophys. Acta* 2003, 1612, 123–135.
 (B28) Hanrahan, G.; Ussher, S.; Gledhill, M.; Achterberg, E. P.; Worsfold, P. J. *Trends Anal. Chem.* 2002, 21, 233–239.
 (B29) Patra, D. *Appl. Spectrosc. Rev.* 2003, 38, 155–185.
 (B30) Lambert, P. J. *Hazard. Mater.* 2003, 102, 39–55.
 (B31) Dufour, E. *Am. Lab.* 2002, 34, 50, 52–54, 56.
 (B32) Marangoni, A. G. *Phys. Prop. Lipids* 2002, 163–189.

GENERAL INSTRUMENTATION

- (C1) Halbhauer, K.-J.; König, K. *Anatomischer Anz.* 2003, 185, 1–20.
 (C2) Jaeger, S.; Garbow, N.; Kirsch, A.; Preckel, H.; Ganderberger, F. U.; Herrenknecht, K.; Ruediger, M.; Hutchinson, J. P.; Bingham, R. P.; Ramon, F.; Bardera, A.; Martin, J. J. *Biomol. Screening* 2003, 8, 648–659.
 (C3) Clegg, R. M.; Holub, O.; Gohlke, C. *Methods Enzymol.* 2003, 360, 509–542.
 (C4) Oldani, A.; Collini, M.; Chirico, G.; D'Alfonso, L.; Baldini, G.; Mazzei, F.; Barone, F.; Cellai, L.; Giordano, C.; Milani, M.; Pasinetti, A. *Proc. SPIE—Int. Soc. Opt. Eng.* 2003, 5139, 97–106.
 (C5) Thompson, R. E.; Larson, D. R.; Webb, W. W. *Biophys. J.* 2002, 82 (5), 2775–2783.
 (C6) Urayama, P.; Zhong, W.; Beamish, J. A.; Minn, F. K.; Sloboda, R. D.; Dragnev, K. H.; Dmitrovsky, E.; Mycek, M. A. *Appl. Phys. B: Lasers Opt.* 2003, 76, 483–496.
 (C7) Ryder, A. G.; Glynn, T. J.; Przyjalowski, M.; Szczupak, B. J. *Fluoresc.* 2002, 12, 177–180.
 (C8) Suzuki, Y.; Arakawa, H.; Maeda, M. *Anal. Sci.* 2003, 19, 111–115.
 (C9) Miao, H.; Rubakhin, S. S.; Sweedler, J. V. *Anal. Bioanal. Chem.* 2003, 377, 1007–1013.

- (C10) Liu, Z.; Pawliszyn, J. *Anal. Chem.* 2003, 75, 4887–4894.
 (C11) Iyer, S.; Stark, P.; Olivares, J. *J. Assoc. Lab. Autom.* 2003, 8, 41–45.
 (C12) Alaverdian, L.; Alaverdian, S.; Bilenko, O.; Bogdanov, I.; Filippova, E.; Gavrilov, D.; Gorbavitski, B.; Gouzman, M.; Gudkov, G.; Domratchev, S.; Kosobokova, O.; Lifshitz, N.; Luryl, S.; Ruskovoloshin, V.; Stepoukhovitch, A.; Tcherevishnick, M.; Tyshko, G.; Gorfinkel, V. *Electrophoresis* 2002, 23, 2804–2817.
 (C13) Anazawa, T.; Matsunaga, H.; Yeung, E. S. *Anal. Chem.* 2002, 74, 5033–5038.
 (C14) Qi, S. Z.; Liu, X. Z.; Ford, S.; Barrows, J.; Thomas, G.; Kelly, K.; McCandless, A.; Lian, K.; Goertel, J.; Soper, S. A. *Lab Chip* 2002, 2, 88–95.
 (C15) Blom, H.; Johansson, M.; Hedman, A. S.; Lundberg, L.; Hanning, A.; Hard, S.; Rigler, R. *Appl. Opt.* 2002, 41, 3336–3342.
 (C16) Blom, H.; Johansson, M.; Gosch, M.; Sigmundsson, T.; Holm, J.; Hard, S.; Rigler, R. *Appl. Opt.* 2002, 41, 6614–6620.
 (C17) Shelby, J. P.; Chiu, D. T. *Anal. Chem.* 2003, 75, 1387–1392.
 (C18) Rochas, A.; Gosch, M.; Serov, A.; Besse, P. A.; Popovic, R. S.; Lasser, T.; Rigler, R. *IEEE Photonics Technol. Lett.* 2003, 15, 963–965.
 (C19) Kamei, T.; Paegel, B. M.; Scherer, J. R.; Skelley, A. M.; Street, R. A.; Mathies, R. A. *Anal. Chem.* 2003, 75, 5300–5305.
 (C20) Wahl, M.; Ortmann, U.; Lauritsen, K.; Erdmann, R. *Proc. SPIE—Int. Soc. Opt. Eng.* 2002, 4648, 171–178.
 (C21) Yeo, T. L.; Ozanyan, K. B.; Hindle, F.; Poolton, N. R. J.; McCann, H. *Appl. Spectrosc.* 2002, 56, 846–851.
 (C22) Spring, K. R. *Laser Focus World* 2002, 38, 123, 125–126, 129.

LASER-BASED TECHNIQUES

- (D1) Zipfel, W. R.; Williams, R. M.; Webb, W. W. *Nat. Biotechnol.* 2003, 21, 1368–1376.
 (D2) Tauer, U. *Exp. Physiol.* 2002, 87, 709–714.
 (D3) Abbotto, A.; Beverina, L.; Bozio, R.; Facchetti, A.; Ferrante, C.; Paganì, G. A.; Pedron, D.; Signorini, R. *Chem. Commun. (Cambridge)* 2003, 2144–2145.
 (D4) Huang, Z.-L.; Li, N.; Sun, Y.-F.; Wang, H.-Z.; Song, H.-C.; Xu, Z.-L. *J. Mol. Struct.* 2003, 657, 343–350.
 (D5) Cao, D.-X.; Fang, Q.; Wang, D.; Liu, Z.-Q.; Xue, G.; Xu, G.-B.; Yu, W.-T. *Eur. J. Org. Chem.* 2003, 3628–3636.
 (D6) Huang, S. H.; Heikal, A. A.; Webb, W. W. *Biophys. J.* 2002, 82, 2811–2825.
 (D7) Zipfel, W. R.; Williams, R. M.; Christie, R.; Nikitin, A. Y.; Hyman, B. T.; Webb, W. W. *Proc. Natl. Acad. Sci. U.S.A.* 2003, 100, 7075–7080.
 (D8) Dittrich, P. S.; Schwillie, P. *Anal. Chem.* 2002, 74, 4472–4479.
 (D9) Walowicz, K. A.; Pastirk, I.; Lozovoy, V. V.; Dantus, M. *J. Phys. Chem. A* 2002, 106, 9369–9373.
 (D10) Lozovoy, V. V.; Pastirk, I.; Walowicz, K. A.; Dantus, M. *J. Chem. Phys.* 2003, 118, 3187–3196.
 (D11) Pastirk, I.; Dela Cruz, J. M.; Walowicz, K. A.; Lozovoy, V. V.; Dantus, M. *Opt. Express* 2003, 11, 1695–1701.
 (D12) Werner, J. H.; Cai, H.; Jett, J. H.; Reha-Krantz, L.; Keller, R. A.; Goodwin, P. M. *J. Biotechnol.* 2003, 102, 1–14.
 (D13) LeCaptain, D. J.; Van Orden, A. *Anal. Chem.* 2002, 74, 1171–1176.
 (D14) Fogarty, K.; Van Orden, A. *Anal. Chem.* 2003, 75, 6634–6641.
 (D15) Larson, D. R.; Ma, Y. M.; Vogt, V. M.; Webb, W. W. *J. Cell Biol.* 2003, 162, 1233–1244.
 (D16) Korn, K.; Gardellin, P.; Liao, B.; Amacker, M.; Bergstrom, A.; Bjorkman, H.; Camacho, A.; Dorhofer, S.; Dorre, K.; Ernstrom, J.; Ericson, T.; Favez, T.; Gosch, M.; Honegger, A.; Jaccoud, S.; Lapczynska, M.; Litborn, E.; Thyberg, P.; Winter, H.; Rigler, R. *Nucleic Acids Res.* 2003, 31, e89.
 (D17) Elbs, M.; Brock, R. *Anal. Chem.* 2003, 75, 4793–4800.
 (D18) Braeckmans, K.; Peeters, L.; Sanders, N. N.; De Smedt, S. C.; Dermeester, J. *Biophys. J.* 2003, 85, 2240–2252.
 (D19) Reichert, U.; Linden, T.; Belfort, G.; Kula, M. R.; Thommes, J. *J. Membr. Sci.* 2002, 199, 161–166.
 (D20) Brookhink, A. *Trends Opt. Photonics* 2002, 69, ThC1/1-ThC1/3 (*Laser Applications to Chemical and Environmental Analysis*).
 (D21) Haustein, E.; Schwillie, P. *Methods* 2003, 29, 153–166.
 (D22) Berland, K. M.; Shen, G. *Proc. SPIE—Int. Soc. Opt. Eng.* 2003, 4963, 1–12 (*Multiphoton Microscopy in the Biomedical Sciences III*).
 (D23) Berland, K.; Shen, G. *Appl. Opt.* 2003, 42, 5566–5576.
 (D24) Sonehara, T.; Kojima, K.; Irie, T. *Anal. Chem.* 2002, 74, 5121–5131.
 (D25) Doi, N.; Takashima, H.; Kinjo, M.; Sakata, K.; Kawahashi, Y.; Oishi, Y.; Oyama, R.; Miyamoto-Sato, E.; Sawasaki, T.; Endo, Y.; Yanagawa, H. *Genome Res.* 2002, 12, 487–492.
 (D26) Enderlein, J.; Bohmer, M. *Proc. SPIE—Int. Soc. Opt. Eng.* 2003, 4962, 27–37 (*Manipulation and Analysis of Biomolecules, Cells, and Tissues*).
 (D27) Saffarian, S.; Elson, E. L. *Biophys. J.* 2003, 84, 2030–2042.
 (D28) Hess, S. T.; Webb, W. W. *Biophys. J.* 2002, 83, 2300–2317.
 (D29) Hillesheim, L. N.; Mueller, J. D. *Biophys. J.* 2003, 85, 1948–1958.

- (D30) Chen, Y.; M. J. D.; Ruan, Q.; Gratton, E. *Biophys. J.* 2002, 82, 133–144.
 (D31) Weiss, M.; Hashimoto, H.; Nilsson, T. *Biophys. J.* 2003, 84, 4043–4052.
 (D32) Rigler, R. *Electrophoresis* 2002, 23, 805–808.
 (D33) LeCaptain, D. J.; Van Orden, A. *Trends Opt. Photonics* 2002, 69, ThA2/1-ThA2/3 (*Laser Applications to Chemical and Environmental Analysis*).
 (D34) Sonehara, T.; Irie, T. *Micro Total Analysis Systems* 2002, *Proceedings of the mTAS 2002 Symposium*, 6th, Nara, Japan, 2002; Vol. 1, pp 299–301.
 (D35) Opitz, N.; Rothwell, P. J.; Oeke, B.; Schwillie, P. *Sens. Actuators, B* 2003, B96, 460–467.
 (D36) Rigneault, H.; Lenne, P. F. *J. the Optical Society of America B: Optical Physics* 2003, 20, 2203–2214.
 (D37) Rocheleau, J. V.; Wiseman, P. W.; Petersen, N. O. *Biophys. J.* 2003, 84, 4011–4022.

SENSORS

- (E1) Akyuz, N.; Wiesmuller, L. *ALTEX: Alternativen Tierexp.* 2003, 20, 77–84.
 (E2) Baxter, P. N. W. *Chemistry—A European Journal* 2002, 8, 5250–5264.
 (E3) Qhobosheane, M.; Liu, X. J.; Cu, Y. R.; Wu, D. H.; Tan, W. H. *Appl. Spectrosc.* 2003, 57, 689–696.
 (E4) Bromberg, A.; Mathies, R. A. *Anal. Chem.* 2003, 75, 1188–1195.
 (E5) Tutchkline, A.; Kraynov, V.; Hahn, K. *J. Am. Chem. Soc.* 2003, 125, 4132–4145.
 (E6) Ferrer, M. L.; del Monte, F.; Mateo, C. R.; Gomez, J.; Levy, D. *J. Sol-Gel Science and Technology* 2003, 26, 1169–1172.
 (E7) Chen, L.-X.; Niu, C.-G.; Zeng, G.-M.; Huang, G.-H.; Shen, G.-L.; Yu, R.-Q. *Anal. Sci.* 2003, 19, 295–298.
 (E8) von Bultzingslowen, C.; McEvoy, A. K.; McDonagh, C.; Mac Craith, B. D.; Klimant, I.; Krause, C.; Wolfbeis, O. S. *Analyst* 2002, 127, 1478–1483.
 (E9) Dittrich, P. S.; Schwillie, P. *Anal. Chem.* 2003, 75, 5767–5774.
 (E10) Huang, T. M.; Erd, P.; Wu, X. Z.; Mikkelsen, S.; Pawliszyn, J. *Sens. Mater.* 2002, 14, 141–149.
 (E11) Mielniczak, A.; Wandelt, B.; Wysocki, S. *Materials Science* 2002, 20, 59–68.
 (E12) Xu, M.-H.; Lin, J.; Hu, Q.-S.; Pu, L. *J. Am. Chem. Soc.* 2002, 124, 14239–14246.
 (E13) Wen-xu, L.; Jian, C. *Anal. Chem.* 2003, 75, 1458–1462.
 (E14) Opitz, N.; Rothwell, P. J.; Oeke, B.; Schwillie, P. *Sens. Actuators, B* 2003, B96, 460–467.
 (E15) Maxwell, D. J.; Taylor, J. R.; Nie, S. *J. Am. Chem. Soc.* 2002, 124, 9606–9612.

SAMPLE PREPARATION, QUENCHING, AND RELATED PHENOMENA

- (F1) Aktas, E. S.; Ersoy, L.; Sagirli, O. *Farmaco* 2003, 58, 165–168 (*Societa Chimica Italiana: 1989*).
 (F2) Belal, F.; Abdine, H.; Al-Majed, A.; Khalil, N. Y. *J. Pharm. Biomed. Anal.* 2002, 27, 253–260.
 (F3) Billiot, F. H.; McCarroll, M.; Billiot, E. J.; Rugutt, J. K.; Morris, K.; Warner, I. M. *Langmuir* 2002, 18, 2993–2997.
 (F4) Ferreira, H.; Lucio, M.; de Castro, B.; Gameiro, P.; Lima, J. L. F. C.; Reis, S. *Anal. Bioanal. Chem.* 2003, 377, 293–298.
 (F5) Shield, S. R.; Harris, J. M. *Anal. Chem.* 2002, 74, 2248–2256.
 (F6) Ipe, B. I.; Thomas, K. G.; Barazzouk, S.; Hotchandani, S.; Kamat, P. V. *J. Phys. Chem. B* 2002, 106, 18–21.
 (F7) Mansoor, S. E.; McHaourab, H. S.; Farrrens, D. L. *Biochemistry* 2002, 41, 2475–2484.
 (F8) Li, J. W. J.; Tan, W. H. *Nano Lett.* 2002, 2, 315–318.
 (F9) Bolender, J. P.; Meyers, A.; Cordaro, J.; Ries, R. S. *Chirality* 2002, 14, 456–464.
 (F10) Caputo, G. A.; London, E. *Biochemistry* 2003, 42, 3265–3274.
 (F11) Valana, A. C.; Neuweiler, H.; Schulz, A.; Wolfrum, J.; Sauer, M.; Smith, J. C. *J. Am. Chem. Soc.* 2003, 125, 14564–14572.
 (F12) Ghatak, H.; Mukhopadhyay, S. K.; Biswas, H.; Sen, S.; Jana, T. K. *Indian J. Mar. Sci.* 2002, 31, 136–140.
 (F13) Howerton, S. B.; Goodpaster, J. V.; McGuffin, V. L. *Anal. Chim. Acta* 2002, 459, 61–73.
 (F14) Zhang, X.; Wang, H.; Fu, N.-N.; Zhang, H.-S. *Spectrochim. Acta, Part A* 2003, 59, 1667–1672.

DATA REDUCTION

- (G1) Martinez, M. J.; Aragon, A. D.; Rodriguez, A. L.; Weber, J. M.; Timlin, J. A.; Sinclair, M. B.; Haaland, D. M.; Werner-Washburne, M. *Nucleic Acids Res.* 2003, 31, e18/11–e18/18.
 (G2) Zarco-Tejada, P. J.; Miller, J. R.; Mohammed, G. H.; Noland, T. L.; Sampson, P. H. *J. Environ. Qual.* 2002, 31, 1433–1441.
 (G3) Cao, Y.-Z.; Mo, C.-Y.; Long, J.-G.; Chen, H.; Wu, H.-L.; Yu, R.-Q. *Anal. Sci.* 2002, 18, 333–336.
 (G4) Wu, H.-L.; Long, N.; Fang, Y.-F.; Mo, C.-Y.; Yu, R.-Q. *Fenxi Shiyanshi* 2002, 21, 44–47.
 (G5) Xie, H.-P.; Jiang, J.-H.; Shen, G.-L.; Yu, R.-Q. *Comp. Chem.* 2002, 26, 183–190.

- (G6) Lu, J.-Z.; Wu, H.-L.; Jiang, J.-H.; Gao, N.; Mo, C.-Y.; Yu, R.-Q. *Anal. Sci.* 2003, 19, 1037–1043.
- (G7) Xie, H.-P.; Chu, X.; Jiang, J.-H.; Cui, H.; Shen, G.-L.; Yu, R.-Q. *Spectrochim. Acta, Part A* 2003, 59, 743–749.
- (G8) Xie, H.-P.; Jiang, J.-H.; Long, N.; Shen, G.-L.; Wu, H.-L.; Yu, R.-Q. *Chemom. Intell. Lab. Syst.* 2003, 66, 101–115.
- (G9) Cao, Y.-Z.; Chen, H.; Wu, H.-L.; Yu, R.-Q. *Anal. Sci.* 2003, 19, 753–756.
- (G10) Chen, Z.-P.; Yu, R.-Q. *Anal. Chim. Acta* 2003, 487, 171–180.
- (G11) Frenich, A. G.; Zamora, D. P.; Galera, M. M.; Vidal, J. L. M. *Anal. Bioanal. Chem.* 2003, 375, 974–980.
- (G12) Solle, D.; Geissler, D.; Stark, E.; Scheper, T.; Hitzmann, B. *Bioinformatics* 2003, 19, 173–177.
- (G13) Arancibia, J. A.; Olivieri, A. C.; Escandar, G. M. *Anal. Bioanal. Chem.* 2002, 374, 451–459.
- (G14) Arancibia, J. A.; Escandar, G. M. *Talanta* 2003, 60, 1113–1121.
- (G15) Christensen, J.; Povlsen, V. T.; Sorensen, J. *J. Dairy Sci.* 2003, 86, 1101–1107.
- (G16) Moller, J. K. S.; Parolari, G.; Gabba, L.; Christensen, J.; Skibsted, L. H. *J. Agric. Food Chem.* 2003, 51, 1224–1230.
- (G17) Palmer, G. M.; Zhu, C.; Breslin, T. M.; Xu, F.; Gilchrist, K. W.; Ramanujam, N. *IEEE Trans. Biomed. Eng.* 2003, 50, 1233–1242.
- (G18) Zheng, W.; Lau, W.; Cheng, C.; Soo, K. C.; Olivo, M. *Int. J. Cancer* 2003, 104, 477–481.
- (G19) Chang, H.; Qu, J. Y.; Yuen, P.; Sham, J.; Kwong, D.; Wei, W. *J. Appl. Spectrosc.* 2002, 56, 1361–1367.
- (G20) Karoui, R.; Dufour, E. *Int. Dairy J.* 2003, 13, 973–985.
- (G21) Karoui, R.; Laguet, A.; Dufour, E. *Lait* 2003, 83, 251–264.
- (G22) Karoui, R.; Mazerolles, G.; Dufour, E. *Int. Dairy J.* 2003, 13, 607–620.
- (G23) Kulmyrzaev, A.; Dufour, E. *Lait* 2002, 82, 725–735.
- (G24) Dufour, E.; Frencia, J. P.; Kane, E. *Food Res. Int.* 2003, 36, 415–423.
- (G25) Leblanc, L.; Dufour, E. *FEMS Microbiol. Lett.* 2002, 211, 147–153.
- (G26) Majumder, S. K.; Ghosh, N.; Kataria, S.; Gupta, P. K. *Lasers Surg. Med.* 2003, 33, 48–56.
- (G27) Dolenko, T. A.; Fadeev, V. V.; Gerdova, I. V.; Dolenko, S. A.; Reuter, R. *Appl. Opt.* 2002, 41, 5155–5166.
- (G28) He, L. M.; Kear-Padilla, L. L.; Lieberman, S. H.; Andrews, J. M. *Anal. Chim. Acta* 2003, 478, 245–258.
- (G29) Wolf, G.; Almeida, J. S.; Crespo, J. G.; Reis, M. A. M. *Water Sci. Technol.* 2003, 47, 161–167.
- (G30) Thompson, R. E.; Larson, D. R.; Webb, W. W. *Biophys. J.* 2002, 82, 2775–2783.
- (G31) Kalinin, S. V.; Molotkovsky, J. G.; Johansson, L. B. A. *Spectrochim. Acta, Part A* 2002, 58A, 1087–1097.
- (G32) Barsgov, V.; Mukamel, S. *J. Chem. Phys.* 2002, 116, 9802–9810.
- (G33) Mei, G.; Di Venere, A.; De Matteis, F.; Rosato, N. *Arch. Biochem. Biophys.* 2003, 417, 159–164.
- (G34) Dolenko, S. A.; Dolenko, T. A.; Fadeev, V. V.; Gerdova, I. V.; Kompitsas, M. *Opt. Commun.* 2002, 213, 309–324.
- (G35) Milstein, A. B.; Oh, S.; Webb, K. J.; Bouman, C. A.; Zhang, Q.; Boas, D. A.; Millane, R. P. *Appl. Opt.* 2003, 42, 3081–3094.

ORGANIZED MEDIA

- (H1) Yang, R. H.; Li, K. A.; Wang, K. M.; Zhao, F. L.; Li, N.; Liu, F. *Anal. Chem.* 2003, 75, 612–621.
- (H2) Yang, R. H.; Li, K.; Wang, K. M.; Liu, F.; Li, N.; Zhao, F. L. *Anal. Chim. Acta* 2002, 469, 285–293.
- (H3) Yarabe, H. H.; Agbaria, R. A.; Rugutt, J. K.; McCarroll, M. E.; Gooden, R. A.; Werner, T. C.; Warner, I. M. *Appl. Spectrosc.* 2002, 56, 1048–1054.
- (H4) Corradini, R.; Paganuzzi, C.; Marchelli, R.; Pagliari, S.; Sforza, S.; Dossena, A.; Galaverna, G.; Duchateau, A. *Chirality* 2003, 15, S30–S39.
- (H5) Billiot, F. H.; McCarroll, M.; Billiot, E. J.; Rugutt, J. K.; Morris, K.; Warner, I. M. *Langmuir* 2002, 18, 2993–2997.
- (H6) Thibodeaux, S. J.; Billiot, E.; Warner, I. M. *J. Chromatogr., A* 2002, 966, 179–186.
- (H7) Tarus, J.; Shamsi, S. A.; Morris, K.; Agbaria, R. A.; Warner, I. M. *Langmuir* 2003, 19, 7173–7181.
- (H8) Tarus, J.; Agbaria, R. A.; Morris, K.; Billiot, F. H.; Williams, A. A.; Chatman, T.; Warner, I. M. *Electrophoresis* 2003, 24, 2499–2507.
- (H9) Paulo, P. M. R.; Lala, C. A. T.; Costa, S. M. B. *J. Phys. Chem. B* 2003, 107, 1097–1105.
- (H10) Chakrabarty, D.; Hazra, P.; Chakraborty, A.; Sarkar, N. *J. Phys. Chem. B* 2003, 107, 13643–13648.
- (H11) Veatch, S. L.; Keller, S. L. *Biophys. J.* 2003, 85, 3074–3083.
- (H12) Rowe, B. A.; Neal, S. L. *Langmuir* 2003, 19, 2039–2048.
- (H13) McCain, K. S.; Harris, J. M. *Anal. Chem.* 2003, 75, 3616–3624.
- (H14) McCain, K. S.; Hanley, D. C.; Harris, J. M. *Anal. Chem.* 2003, 75, 4351–4359.
- (H15) Higgins, D. A.; Collinson, M. M.; Saroja, G.; Bardo, A. M. *Chem. Mater.* 2002, 14, 3734–3744.
- (H16) Hou, Y. W.; Higgins, D. A. *J. Phys. Chem. B* 2002, 106, 10306–10315.

- (H17) Deschenes, L. A.; Vanden Bout, D. A. *J. Chem. Phys.* 2002, 116, 5850–5856.
- (H18) Deschenes, L. A.; Vanden Bout, D. A. *J. Phys. Chem. B* 2002, 106, 11438–11445.
- (H19) Teetsov, J.; Vanden Bout, D. A. *Langmuir* 2002, 18, 897–903.
- (H20) Ostafin, A. E.; Siegel, M.; Wang, Q.; Mizukami, H. *Microporous Mesoporous Mater.* 2003, 57, 47–55.
- (H21) Chen, Y. F.; Rosenzweig, Z. *Nano Lett.* 2002, 2, 1299–1302.
- (H22) Lee, J. H.; Jung, S. W.; Kim, I. S.; Jeong, Y. I.; Kim, Y. H.; Kim, S. H. *Int. J. Pharm.* 2003, 251, 23–32.

LOW-TEMPERATURE LUMINESCENCE

- (I1) Muller, J. G.; Lemmer, U.; Raschke, G.; Anni, M.; Scherf, U.; Lupton, J. M.; Feldmann, J. *Phys. Rev. Lett.* 2003, 91, 267403.
- (I2) Grubor, N. M.; Shinar, R.; Jankowiak, R.; Porter, M. D.; Small, G. J. *Biosens. Bioelectron.* 2004, 19, 547–556.
- (I3) Bourgeois, D.; Vermede, X.; Adam, V.; Fioravanti, E.; Ursby, T. *J. Appl. Crystallog.* 2002, 35, 319–326.
- (I4) Ogorodnikov, I. N.; Pustovarov, V. A.; Kirm, M.; Kruzhavov, A. V.; Isaenko, L. I. *Opt. Spectrosc.* 2002, 92, 702–709 (Translation of *Optika i Spektroskopiya*).
- (I5) Ogorodnikov, I. N.; Kirm, M.; Pustovarov, V. A.; Cheremnykh, V. S. *Opt. Spectrosc.* 2003, 95, 385–389 (Translation of *Optika i Spektroskopiya*).
- (I6) Chen, Y.-H.; Chung, Y.-L.; Lin, C.-H. *J. Chromatogr., A* 2002, 943, 287–294.
- (I7) Bystol, A. J.; Thorstenson, T.; Campiglia, A. D. *Environ. Sci. Technol.* 2002, 36, 4424–4429.

TOTAL LUMINESCENCE AND SYNCHRONOUS EXCITATION SPECTROSCOPES AND RELATED TECHNIQUES

- (J1) Patra, D.; Mishra, A. K. *Trends Anal. Chem.* 2002, 21, 787–798.
- (J2) Li, Y. Q.; Xu, J. J.; Wang, R. T.; Yu, L. J.; Li, Z. *Chin. Chem. Lett.* 2002, 13, 571–572.
- (J3) Patra, D.; Mishra, A. K. *Anal. Bioanal. Chem.* 2002, 373, 304–309.
- (J4) Murillo, P. J. A.; Alanon, M. A. *Talanta* 2002, 56, 557–564.
- (J5) Wang, L.-Y.; Wang, L.; Zhu, C.-Q.; Liu, J.; Li, L.; Yao, J. *Anal. Lett.* 2002, 35, 2259–2268.
- (J6) Wang, L.-Y.; Zhou, Y.-Y.; Wang, L.; Zhu, C.-Q.; Li, Y.-X.; Gao, F. *Anal. Chim. Acta* 2002, 466, 87–92.
- (J7) Wang, L.-Y.; Wang, L.; Gao, F.; Yu, Z.-Y.; Wu, Z.-M. *Analyst* 2002, 127, 977–980.
- (J8) Dubayova, K.; Kusnir, J.; Podracka, L. *J. Biochem. Biophys. Methods* 2003, 55, 111–119.

SOLID SURFACE LUMINESCENCE

- (K1) Shield, S. R.; Harris, J. M. *Langmuir* 2002, 18, 4307–4313.
- (K2) Piester, O.; Barsch, H.; Buschmann, V.; Heinlein, T.; Knemeyer, J. P.; Weston, K. D.; and Sauer, M. *Nano Lett.* 2003, 3, 979–982.
- (K3) Yao, G.; Fang, X. H.; Yokota, H.; Yanagida, T.; Tan, W. H. *Chem.-Eur. J.* 2003, 9, 5686–5692.
- (K4) Kim, H. D.; Nienhaus, G. U.; Ha, T.; Orr, J. W.; Williamson, J. R.; Chu, S. *Proc. Natl. Acad. Sci. U.S.A.* 2002, 99, 4284–4289.

LUMINESCENCE IN CHROMATOGRAPHY, ELECTROPHORESIS, AND FLOW SYSTEMS

- (L1) Ludes, M. D.; Wirth, M. J. *Anal. Chem.* 2002, 74, 386–393.
- (L2) Ludes, M. D.; Anthony, S. R.; Wirth, M. J. *Anal. Chem.* 2003, 75, 3073–3078.
- (L3) Wirth, M. J.; Swinton, D. J.; Ludes, M. D. *J. Phys. Chem. B* 2003, 107, 6258–6268.
- (L4) Lowry, M.; He, Y.; Geng, L. *Anal. Chem.* 2002, 74, 1811–8.
- (L5) Howerton, S. B.; McGuffin, V. L. *Anal. Chem.* 2003, 75, 3207–16.
- (L6) Howerton, S. B.; Goodpaster, J. V.; McGuffin, V. L. *Anal. Chim. Acta* 2002, 459, 1–73.
- (L7) Rehder-Silinski, M. A.; McGown, L. B. *J. Chromatogr., A* 2003, 1008, 233–245.
- (L8) Amirkhanian, V. D.; Liu, M.-S. *Proc. SPIE-Int. Soc. Opt. Eng.*, 2003, 4626, 238–246 (*Biomedical Nanotechnology Architectures and Applications*).
- (L9) Beard, N. P.; De Mello, A. J. *Electrophoresis* 2003, 23, 1722–1730.
- (L10) Dang, F.; Zhang, L.; Hagiwara, H.; Mishina, Y.; Baba, Y. *Electrophoresis* 2003, 24, 714–721.
- (L11) Sonohara, T.; Kojima, K.; Irie, T. *Anal. Chem.* 2003, 74, 5121–5131.
- (L12) Jackman, R.; Schmerr, M. J. *Electrophoresis* 2003, 24, 892–6.
- (L13) Berezhovski, M.; Nutiu, R.; Li, Y.; Krylov, S. N. *Anal. Chem.* 2003, 75, 1382–1386.
- (L14) McIntosh, S. L.; Deligeorgiev, T. G.; Gadjev, N. I.; McGown, L. B. *Electrophoresis* 2003, 23, 1473–1479.
- (L15) Zheng, X.; Zhang, Z. *Sens. Actuators, B* 2002, B84, 142–147.

- (L16) Mihalatos, A. M.; Calokerinos, A. *Anal. Chim. Acta* 2002, 451, 189–194.
 (L17) Yang, J.-d.; Huang, Y.-m.; Liu, S. *Xinan Shilan Daxue Xuebao, Ziran Kexueban* 2002, 27, 372–374.
 (L18) Mikuska, P.; Vecera, Z. *Anal. Chim. Acta* 2002, 474, 99–105.
 (L19) Nakamura, M. M.; Nina, C.; Jin-Ming, L.; Yamada, M. *Anal. Chim. Acta* 2003, 484, 101–109.
 (L20) Rao, Z.; Zhang, X.; Baeyens, W. R. G. *Talanta* 2002, 57, 993–998.
 (L21) Li, F.; Cui, H.; Lin, X.-Q. *Anal. Chim. Acta* 2002, 471, 187–194.
 (L22) Sun, C.; Zhao, H.; Yi, L.; Lu, Y. *Fenxi Huaxue* 2002, 30, 920–924.

DYNAMIC LUMINESCENCE MEASUREMENTS

- (M1) Hanley, Q. S.; Arndt-Jovin, D. J.; Jovin, T. M. *Appl. Spectrosc.* 2002, 56, 155–166.
 (M2) Knemeyer, J. P.; Herten, D. P.; Sauer, M. *Anal. Chem.* 2003, 75, 2147–2153.
 (M3) Kwak, E. S.; Vanden Bout, D. A. *Anal. Chim. Acta* 2003, 496, 259–266.
 (M4) Lin, H.; Herman, P.; Lakowicz, J. R. *Cytometry: J. Soc. Anal. Cytol.* 2003, 52A, 77–89.
 (M5) Heilemann, M.; Herten, D. P.; Heintzmann, R.; Cremer, C.; Muller, C.; Tinnefeld, P.; Weston, K. D.; Wolfrum, J.; Sauer, M. *Anal. Chem.* 2002, 74, 3511–3517.
 (M6) Weston, K. D.; Dyck, M.; Tinnefeld, P.; Muller, C.; Herten, D. P.; Sauer, M. *Anal. Chem.* 2002, 74, 5342–5349.
 (M7) Gilmore, A. M.; Larkum, A. W. D.; Salih, A.; Itoh, S.; Shibata, Y.; Bena, C.; Yamasaki, H.; Papina, M.; Van Woesik, R. *Photochem. Photobiol.* 2003, 77, 515–523.
 (M8) Bain, A. J.; Marsh, R. J.; Armoogum, D. A.; Mongin, O.; Porres, L.; Blanchard-Desce, M. *Biochem. Soc. Trans.* 2003, 31, 1047–1051.
 (M9) Higgins, D. A.; Luther, B. J. *Chem. Phys.* 2003, 119, 3935–3942.
 (M10) Hewitt, J. D.; McGown, L. B. *Appl. Spectrosc.* 2003, 57, 256–265.
 (M11) Lassiter, S. J.; Stryjewski, W. J.; Wang, Y.; Soper, S. A. *Spectroscopy* 2002, 17, 14.
 (M12) Mihindukulasuriya, S. H.; Morcone, T. K.; McGown, L. B. *Electrophoresis* 2003, 24, 20–25.
 (M13) Hibara, A.; Saito, T.; Kim, H. B.; Tokeshi, M.; Ooi, T.; Nakao, M.; Kitamori, T. *Anal. Chem.* 2002, 74, 6170–6176.
 (M14) Markovits, D.; Sharonov, A.; Onidas, D.; Gustavsson, T. *Chem. Phys. Chem.* 2003, 4, 303–305.
 (M15) Mei, G.; Di Venere, A.; Aggro, A. F.; De Matteis, F.; Rosato, N. *J. Fluoresc.* 2003, 13, 467–477.
 (M16) Mei, G.; Di Venere, A.; Nicolai, E.; Rosato, N.; Finazzi, A. A. *J. Fluoresc.* 2003, 13, 33–39.
 (M17) Tauc, P.; Mateo, C. R.; Brochon, J. C. *Biochim. Biophys. Acta* 2002, 1595(1–2), 103–115.
 (M18) Wang, D.; Visser, N. V.; Veenhuis, M.; van der Klei, I. J. *J. Biol. Chem.* 2003, 278, 43340–43345.
 (M19) Yang, H.; Xie, X. S. *Chem. Phys.* 2002, 284, 423–437.
 (M20) Yang, H.; Xie, X. S. *Chem. Phys.* 2002, 117, 10965–10979.
 (M21) Yang, H.; Luo, G. B.; Karnchanaphanurach, P.; Louie, T. M.; Rech, I.; Cova, S.; Xun, L. Y.; Xie, X. S. *Science* 2003, 302, 262–266.

FLUORESCENCE POLARIZATION, MOLECULAR DYNAMICS, AND RELATED PHENOMENA

- (N1) Gryczynski, I.; Piszczek, G.; Gryczynski, Z.; Lakowicz, J. R. *J. Phys. Chem. A* 2002, 106, 754–759.
 (N2) Wilkinson, J. C.; Beechem, J. M.; Staros, J. V. *J. Receptor Signal Transduction Res.* 2002, 22, 357–371.
 (N3) Knight, A. W.; Goddard, N. J.; Billinton, N.; Cahill, P. A.; Walsley, R. M. *J. Biochem. Biophys. Methods* 2002, 51, 165–177.
 (N4) Sengupta, B.; Sengupta, P. K. *Biopolymers* 2003, 72, 427–434.
 (N5) Kruszewski, S.; Burke, T. G. *Opt. Appl.* 2003, 32, 721–730.
 (N6) Clausell, A.; Pujol, M.; Alsina, M. A.; Cajal, Y. *Talanta* 2003, 60, 225–234.
 (N7) Alexiev, U.; Rimke, I.; Pohlmann, T. *J. Mol. Biol.* 2003, 328, 705–719.
 (N8) Mielke, T.; Alexiev, U.; Glasel, M.; Otto, H.; Heyn, M. P. *Biochemistry* 2002, 41, 7875–7884.
 (N9) Bell, M. G.; Dale, R. E.; van der Heide, U. A.; Goldman, Y. E. *Biophys. J.* 2002, 83, 1050–1073.
 (N10) Varnavski, O. P.; Ostrowski, J. C.; Sukhomlinova, L.; Twieg, R. J.; Bazan, G. C.; Goodson, T. III. *J. Am. Chem. Soc.* 2002, 124, 1736–1743.
 (N11) Viteri, C. R.; Gilliland, J. W.; Yip, W. T. *J. Am. Chem. Soc.* 2003, 125, 1980–1987.

CHEMILUMINESCENCE

- (O1) Wang, Y.; He, Z. *Fenxi Kexue Xuebao* 2002, 18, 453–456.
 (O2) Kokado, A.; Arakawa, H.; Maeda, M. *Luminescence* 2002, 17, 5–10.

- (O3) Li, B.; Zhang, J.; Jin, Y. *Biosens. Bioelectron.* 2002, 17, 585–589.
 (O4) Lin, J. M.; Yamada, M. *TrAC, Trends Anal. Chem.* 2003, 22, 99–107.

NEAR-INFRARED FLUORESCENCE

- (P1) Hammer, R. P.; Owens, C. V.; Hwang, S. H.; Sayes, C. M.; Soper, S. A. *Bioconjugate Chem.* 2002, 13, 1244–1252.
 (P2) Wang, Y.; Vaidya, B.; Farquar, H. D.; Stryjewski, W.; Hammer, R. P.; McCarley, R. L.; Soper, S. A.; Cheng, Y. W.; Barany, F. *Anal. Chem.* 2003, 75, 1130–1140.
 (P3) Lassiter, S. J.; Stryjewski, W.; Owens, C. V.; Flanagan, J. H.; Hammer, R. P.; Khan, S.; Soper, S. A. *Electrophoresis* 2002, 23, 1480–1489.
 (P4) Zhu, L.; Stryjewski, W.; Lassiter, S.; Soper, S. A. *Anal. Chem.* 2003, 75, 2280–2291.
 (P5) Funovics, M.; Weissleder, R.; Tung, C. H. *Anal. Bioanal. Chem.* 2003, 377, 956–963.
 (P6) Zaheer, A.; Wheat, T. E.; Frangioni, J. V. *Mol. Imaging* 2002, 1, 354–364.
 (P7) Kircher, M. F.; Josephson, L.; Weissleder, R. *Mol. Imaging* 2002, 1, 89–95.
 (P8) Josephson, L.; Kircher, M. F.; Mahmood, U.; Tang, Y.; Weissleder, R. *Bioconjugate Chem.* 2002, 13, 554–560.
 (P9) Jaffer, F. A.; Tung, C. H.; Gerszten, R. E.; Weissleder, R. *Arterioscler., Thromb., Vasc. Biol.* 2002, 22, 1929–1935.
 (P10) Piszczek, G.; Gryczynski, I.; Maliwal, B. P.; Lakowicz, J. R. *J. Fluoresc.* 2002, 12, 15–17.

LUMINESCENCE TECHNIQUES IN BIOLOGICAL AND CLINICAL ANALYSIS

- (Q1) Banerjee, R.; Sarkar, M. *J. Lumin.* 2002, 99, 255–263.
 (Q2) Rodriguez, J.; Feiltsch, M. *Proc. SPIE-Int. Soc. Opt. Eng.* 2003, 5068, 149–154 (*Optical Technologies in Biophysics and Medicine IV*).
 (Q3) Dai, K.; Vlessidis, A. G.; Evmiridis, N. P. *Talanta* 2003, 59, 55–65.
 (Q4) Rosenfeld, S. S.; Xing, J.; Jefferson, G. M.; Cheung, H. C.; King, P. H. *J. Biol. Chem.* 2002, 277, 36731–36739.
 (Q5) Shaw, M. A.; Ostap, E. M.; Goldman, Y. E. *Biochemistry* 2003, 42, 6128–6135.
 (Q6) Matsunaga, H.; Anazawa, T.; Yeung, E. S. *Electrophoresis* 2003, 24, 458–465.
 (Q7) Bukowski, E. J.; Bright, F. V. *Appl. Spectrosc.* 2002, 56, 1588–1592.
 (Q8) Metso, A. J.; Jutila, A.; Mattila, J. P.; Holopainen, J. M.; Kinnunen, P. K. *J. Phys. Chem. B* 2003, 107, 1251–1257.
 (Q9) Asai, Y. *Int. J. Pharm.* 2003, 253, 89–95.
 (Q10) van Heusden, H. E.; de Kruljff, B.; Breukink, E. *Biochemistry* 2002, 41, 12171–12178.
 (Q11) Bhattacharya, S.; Thomas, M. *J. Biomol. Struct. Dyn.* 2002, 19, 935–945.
 (Q12) Kunst, B. H.; Schots, A.; Visser, A. J. W. G. *Anal. Chem.* 2002, 74, 5350–5357.
 (Q13) Gao, X.; Nie, S. *Mater. Res. Soc. Symp. Proc.* 2003, 773, 69–76 (*Biomicroelectromechanical Systems (BioMEMS)*).
 (Q14) Knowles, M. K.; Guenza, M. G.; Capaldi, R. A.; Marcus, A. H. *Proc. Natl. Acad. Sci. U.S.A.* 2002, 99, 14772–14777.
 (Q15) Smith, C. B.; Anderson, J. E.; Fischer, R. L.; Webb, S. R. *Environ. Pollut. (Oxford)* 2002, 120, 517–520.
 (Q16) Badugu, R.; Lakowicz, J. R.; Geddes, C. D. *J. Fluoresc.* 2003, 13, 371–374.
 (Q17) DiCesare, N.; Lakowicz, J. R. *Anal. Biochem.* 2002, 301(1), 111–116.
 (Q18) Lakowicz, J. R.; Malicka, J.; Gryczynski, I.; Gryczynski, Z.; Geddes, C. D. *J. Phys. D* 2003, 36, R240–R249.
 (Q19) Perez-Luna, V. H.; Yang, S.; Rabinovich, E. M.; Buranda, T.; Sklar, L. A.; Hampton, P. D.; Lopez, G. P. *Biosens. Bioelectron.* 2002, 17, 71–78.
 (Q20) Pfeifer, T. J.; Palthankar, D. Y.; Poneris, J. M.; Schomacker, K. T.; Nishioka, N. S. *Lasers Surg. Med.* 2003, 32, 10–16.
 (Q21) Fowler, S.; Byron, O.; Jumel, K.; Xing, D.; Corbel, M. J.; Boigiano, B. *Vaccine* 2003, 21, 2678–2688.
 (Q22) Mukal, Y.; Togawa, T.; Suzuki, T.; Ohata, K.; Tanabe, S. *J. Chromatogr., B* 2002, 767, 263–268.
 (Q23) Tomasevic, N.; Nikolic, M.; Klappe, K.; Hoekstra, D.; Niketic, V. *J. Serb. Chem. Soc.* 2003, 68, 25–33.
 (Q24) Mei, S. H. J.; Liu, Z.; Brennan, J. D.; Li, Y. *J. Am. Chem. Soc.* 2003, 125, 412–420.
 (Q25) Rizzo, J.; Gifford, L. K.; Zhang, X.; Gewirtz, A. M.; Lu, P. *Mol. Cell. Probes* 2002, 16, 277–283.
 (Q26) Studer, S. M.; Feinberg, J. S.; Joseph, S. J. *Mol. Biol.* 2003, 327, 369–381.
 (Q27) Vijayanathan, V.; Thomas, T.; Sigal, L. H.; Thomas, T. J. *Antisense Nucleic Acid Drug Dev.* 2002, 12, 225–233.
 (Q28) Wabuyele, M. B.; Farquar, H.; Stryjewski, W.; Hammer, R. P.; Soper, S. A.; Cheng, Y. W.; Barany, F. *J. Am. Chem. Soc.* 2003, 125, 6937–6945.
 (Q29) Facompre, M.; Tardy, C.; Bal-Mahieu, C.; Colson, P.; Perez, C.; Manzanares, I.; Cuevas, C.; Bailly, C. *Cancer Res.* 2003, 63, 7392–7399.

- (Q30) Hwangbo, H. J.; Lee, Y. A.; Park, H.; Lee, Y. R.; Kim, J. M.; Yi, S. Y.; Kim, S. K. *Bull. Korean Chem. Soc.* 2003, 24, 579–582.
- (Q31) Liu, J.; Wang, Z. H.; Luo, G. A.; Li, Q. W.; Sun, H. W. *Anal. Sci.* 2002, 18, 751–755.
- (Q32) Zheng, J.; Yeung, E. S. *Aust. J. Chem.* 2003, 56, 149–153.
- (Q33) Kim, B. C.; Gu, M. B. *Biosens. Bioelectron.* 2003, 18, 1015–1021.

REAGENTS AND PROBES

- (R1) Fang, X. H.; Sen, A.; Vicens, M.; Tan, W. H. *ChemBioChem* 2003, 4, 829–834.
- (R2) Li, J. W. J.; Fang, X. H.; Tan, W. H. *Biochem. Biophys. Res. Commun.* 2002, 292, 31–40.
- (R3) Hammer, R. P.; Owens, C. V.; Hwang, S. H.; Sayes, C. M.; Soper, S. A. *Bioconjugate Chem.* 2002, 13, 1244–1252.
- (R4) McIntosh, S. L.; Deligeorgiev, T. G.; Gadjev, N. I.; McGown, L. B. *Electrophoresis* 2002, 23, 1473–1479.
- (R5) Hernandez, J.; van der Schaaf, M.; van Dijk, E.; Sauer, M.; Garcia-Parajo, M. F.; van Hulst, N. F. *J. Phys. Chem. A* 2003, 107, 43–52.
- (R6) Neuweiler, H.; Schulz, A.; Bohmer, M.; Enderlein, J.; Sauer, M. *J. Am. Chem. Soc.* 2003, 125, 5324–5330.
- (R7) Gerion, D.; Parak, W. J.; Williams, S. C.; Zanchet, D.; Micheel, C. M.; Alivisatos, A. P. *J. Am. Chem. Soc.* 2002, 124, 7070–7074.
- (R8) Hilliard, L. R.; Zhao, X. J.; Tan, W. H. *Anal. Chim. Acta* 2002, 470, 51–56.
- (R9) Chan, E. M.; Mathies, R. A.; Alivisatos, A. P. *Nano Lett.* 2003, 3, 199–201.
- (R10) Larson, D. R.; Zipfel, W. R.; Williams, R. M.; Clark, S. W.; Bruchez, M. P.; Wise, F. W.; Webb, W. W. *Science* 2003, 300, 1434–1436.
- (R11) DiCesare, N.; Adhikari, D. P.; Heynekamp, J. J.; Heagy, M. D.; Lakowicz, J. R. *J. Fluoresc.* 2002, 12, 147–154.
- (R12) Ercelen, S.; Klymchenko, A. S.; Demchenko, A. P. *FEBS Lett.* 2003, 538, 25–28.
- (R13) Singh, Y.; Gulyani, A.; Bhattacharya, S. *FEBS Lett.* 2003, 541, 132–136.
- (R14) Harris, F. M.; Best, K. B.; Bell, J. D. *Biochim. Biophys. Acta* 2002, 1565, 123–128.
- (R15) Fang, X. H.; Mi, Y. M.; Li, J. W. J.; Beck, T.; Schuster, S.; Tan, W. H. *Cell Biochem. Biophys.* 2002, 37, 71–81.
- (R16) Perlette, J.; Li, J. W.; Fang, X. H.; Schuster, S.; Lou, J.; Tan, W. H. *Rev. Anal. Chem.* 2002, 21, 1–14.
- (R17) Yao, G.; Fang, X. H.; Yokota, H.; Yanagida, T.; Tan, W. H. *Chem.-Eur. J.* 2003, 9, 5686–5692.
- (R18) Wabuyele, M.; Farquar, H.; Stryjewski, W.; Hammer, R. P.; Soper, S. A.; Cheng, Y. W.; Barany, F. *J. Am. Chem. Soc.* 2003, 125, 6937–6945.

OTHER TECHNIQUES AND APPLICATIONS

- (S1) Fletcher, K. A.; Pandey, S. *Appl. Spectrosc.* 2002, 56, 266–271.
- (S2) Fletcher, K. A.; Pandey, S. *Appl. Spectrosc.* 2002, 56, 1498–1503.
- (S3) Fletcher, K. A.; Pandey, S. *J. Phys. Chem. B* 2003, 107, 13532–13539.
- (S4) Fletcher, K. A.; Baker, S. N.; Baker, G. A.; Pandey, S. *New J. Chem.* 2003, 27, 1706.
- (S5) Fletcher, K. A.; Pandey, S.; Storey, I. K.; Hendricks, A. E.; Pandey, S. *Anal. Chim. Acta* 2002, 453, 89–96.
- (S6) Karmakar, R.; Samanta, A. *J. Phys. Chem. A* 2002, 106, 4447–4452.
- (S7) Karmakar, R.; Samanta, A. *J. Phys. Chem. A* 2003, 107, 7340–7346.
- (S8) Chakrabarty, D.; Hazra, P.; Chakraborty, A.; Seth, D.; Sarkar, N. *Chem. Phys. Lett.* 2003, 381, 697–704.
- (S9) Arzhantsev, S.; Ito, N.; Heitz, M.; Maroncelli, M. *Chem. Phys. Lett.* 2003, 381, 278–286.
- (S10) Ingram, J. A.; Moog, R. S.; Ito, N.; Biswas, R.; Maroncelli, M. *J. Phys. Chem. B* 2003, 107, 5926–5932.
- (S11) Alvaro, M.; Ferrer, B.; Garcia, H.; Narayana, M. *Chem. Phys. Lett.* 2002, 362, 435–440.
- (S12) Baker, G. A.; Baker, S. N.; McCleskey, T. M.; Werner, J. H. *ACS Symp. Ser.* 2003, 856, 212–224.
- (S13) Werner, J. H.; Baker, S. N.; Baker, G. A. *Analyst (Cambridge)* 2003, 128, 786–789.
- (S14) Turner, M. B.; Spear, S. K.; Huddleston, J. G.; Holbrey, J. D.; Rogers, R. D. *Green Chem.* 2003, 5, 443–447.
- (S15) Wolfe, A. P.; Kausal, S. S.; Fulton, J. R.; McKnight, D. *Environ. Sci. Technol.* 2002, 36, 3217–3223.
- (S16) Ryder, A. G. *Appl. Spectrosc.* 2002, 56, 107–116.
- (S17) Lei, W.; Duerkop, A.; Lin, Z.; Wu, M.; Wolfbeis, O. S. *Microchim. Acta* 2003, 143, 269–274.
- (S18) Martin, T. L.; Arruda, A. F.; Campiglia, A. D. *Appl. Spectrosc.* 2002, 56, 1354–1360.
- (S19) Allmova, A.; Katz, A.; Savage, H. E.; Shah, M.; Minko, G.; Will, D. V.; Rosen, R. B.; McCormick, S. A.; Alfano, R. R. *Appl. Opt.* 2003, 42, 4080–4087.
- (S20) Heilemann, M.; Buschmann, V.; Piester, O.; Tinnefeld, P.; Weston, K. D.; Sauer, M. *Proc. SPIE—Int. Soc. Opt. Eng.* 2003, 4962, 38–46.
- (S21) Klymchenko, A. S.; Demchenko, A. P. *Phys. Chem. Chem. Phys.* 2003, 5, 461–468.
- (S22) Duyvis, M. G.; Hilhorst, R.; Laane, C.; Evans, D. J.; Schmedding, D. J. M. *J. Agric. Food Chem.* 2002, 50, 1548–52.

AC040095D

Nonlinear magic: multiphoton microscopy in the biosciences

Warren R Zipfel, Rebecca M Williams & Watt W Webb

Multiphoton microscopy (MPM) has found a niche in the world of biological imaging as the best noninvasive means of fluorescence microscopy in tissue explants and living animals. Coupled with transgenic mouse models of disease and 'smart' genetically encoded fluorescent indicators, its use is now increasing exponentially. Properly applied, it is capable of measuring calcium transients 500 μm deep in a mouse brain, or quantifying blood flow by imaging shadows of blood cells as they race through capillaries. With the multitude of possibilities afforded by variations of nonlinear optics and localized photochemistry, it is possible to image collagen fibrils directly within tissue through nonlinear scattering, or release caged compounds in sub-femtoliter volumes.

MPM is a form of laser-scanning microscopy that uses localized 'nonlinear' excitation to excite fluorescence only within a thin raster-scanned plane and nowhere else. Since its first demonstration by our group over a decade ago¹, MPM has been applied to a variety of imaging tasks and has now become the technique of choice for fluorescence microscopy in thick tissue and in live animals. Neuroscientists have used it to measure calcium dynamics deep in brain slices^{2–11} and in live animals^{12–14} (reviewed in ref. 15), to study neuronal plasticity¹⁶ and to monitor neurodegenerative disease models in brain slices¹⁷ and in living mice^{18–21}. MPM has proved invaluable to cancer researchers for *in vivo* studies of angiogenesis^{22,23} and metastasis^{24,25}, to immunologists for investigating lymphocyte trafficking^{26–30} and to embryologists for visualizing a day in the life of a developing hamster embryo³¹. These types of applications define the most important niche for MPM—high-resolution imaging of physiology, morphology and cell-cell interactions in intact tissues or live animals.

Although two-photon excited fluorescence is usually the primary signal source in MPM, three-photon excited fluorescence^{32–37} and second-^{37–45} and third-harmonic generation (SHG, THG)^{46–48} can also be used for imaging. In fact, SHG imaging was one of the earliest forms of biological nonlinear microscopy, proposed⁴⁹ and demonstrated³⁸ decades ago. Notably, one of the most complex forms of nonlinear imaging, coherent anti-Stokes Raman scattering (CARS) microscopy, was developed even earlier⁵⁰. CARS microscopy derives contrast directly from Raman-active vibrational modes within molecules and requires two synchronized pulsed lasers operating at different wavelengths, rather than a single pulsed laser as in two- (or three)-photon and SHG and THG microscopy. Like SHG microscopy, CARS microscopy lay dormant for decades but has recently been markedly improved^{51,52} with the help of tunable, pulsed lasers in the infrared (IR) wavelength range.

Nonlinear excitation also has 'nonimaging' uses in biological research, such as the three-dimensional photolysis of caged molecules in femtoliter volumes^{16,53–56}, diffusion measurements by multiphoton fluorescence correlation spectroscopy (MP-FCS)^{57,58} and multiphoton fluorescence photobleaching recovery (MP-FPR or MP-FRAP)^{16,59–61}, and detecting bimolecular interactions using multiphoton two-color cross-correlation spectroscopy (MP-FCCS)⁶². Targeted, localized multiphoton excitation has also been used for transfection of single cells by opening a transient nanoscopic pore in the cell membrane with a parked femtosecond laser⁶³. Precise ablation and cutting is possible on the subcellular level. For example, a small region from a single chromosome from a fixed cell can be excised⁶⁴, opening the possibility of sub-chromosomal ablation in a living cell to study the effect of knocking out specific regions of a targeted chromosome.

Here, we review applications of MPM and provide a simplified, practical view of the optical, technological and photophysical aspects of this type of microscopy that may be foreign to biologists but is fundamental to an understanding of how best to apply this technology.

Moore's law of multiphoton microscopy

A search of publications referencing MPM (and its various synonyms) reveals several facts about the integration of this relatively new imaging technology into biological research. Publications involving MPM have increased exponentially over the past decade (Fig. 1) as femtosecond laser sources became robust and commercially available, and as the first commercial multiphoton microscopes were introduced in 1996 by BioRad Microscience (Hemel Hempstead, UK). About half of the total references have been consistently devoted to technique and instrumentation development rather than focused on specific biological questions. This is at least partly attributable to the unexplored potential of nonlinear optical processes for biological research (pointed out as early as 1978; ref. 49).

A survey of the instrumentation used in the studies employing MPM for biological research (255 out of 560 total references) indicates that 66% of these studies made use of laboratory-built systems, usually based

School of Applied and Engineering Physics, 212 Clark Hall, Cornell University, Ithaca, New York 14853, USA. Correspondence should be addressed to W.W.W. (www2@cornell.edu).

Published online 31 October 2002; doi:10.1038/nbt899



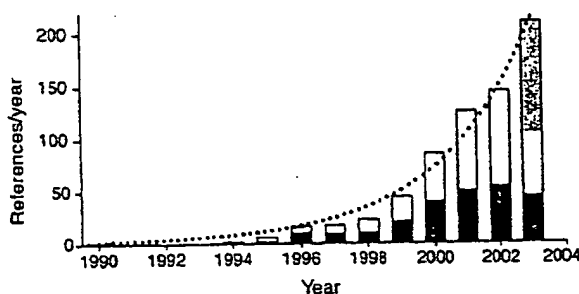


Figure 1 Publications employing, developing or reviewing MPM (from PubMed and ISI). Bar height (white and black) indicates the total number of references for the given year; black bars represent publications focusing on instrumentation development, the remainder being work in which MPM was used to help clarify a specific biological research goal. Gray bar is the estimated number based on twice the 2003 half-year total; dotted line is an exponential fit of the data.

on modified confocal microscopes. The remaining one-third employed commercial systems—27% from BioRad and 3.5% each from Zeiss (Oberkochen, Germany) and Leica (Wetzlar, Germany). Furthermore, the majority (~80%) of the publications are from a small number of research groups (~12) who have developed the required expertise to use the technique effectively. Taken together, these statistics indicate that MPM is still a specialized technology, used successfully by some, but apparently not yet at the level of routine use characteristic of conventional (single-photon) confocal microscopy.

Three-dimensionally localized excitation

Early in the development of quantum mechanics, it was shown theoretically by Maria Göppert-Mayer⁶⁵ that photons of lesser energy together can cause an excitation 'normally' produced by the absorption of a single photon of higher energy in a process called multiphoton or two-photon excitation. Two-photon microscopy, as normally practiced, uses the simplest version of her theoretical prediction: two photons of about equal energy (from the same laser) interact with a molecule, producing an excitation equivalent to the absorption of a single photon possessing twice the energy. If the excited molecule is fluorescent, it can emit a single photon of fluorescence as if it were excited by a single higher energy photon (Fig. 2). This event depends on the two photons both interacting with the molecule nearly simultaneously (~10⁻¹⁶ s), resulting in a quadratic dependence on the light intensity rather than the linear dependence of conventional fluorescence. Multiphoton processes such as two-photon excitation (TPE) are often termed 'nonlinear' because the rate at which they occur depends nonlinearly on the intensity. The intensity-squared dependence is the basis of the localized nature of two-photon excitation: doubling the intensity produces four times the fluorescence.

In MPM, as in conventional laser-scanning confocal microscopy, a laser is focused and raster-scanned across the sample. The image consists of a matrix of fluorescence intensity measurements made by digitizing the detector signal as the laser sweeps back and forth across the sample. TPE probabilities are extremely small, and focusing increases the local intensity at the focal point. Intensity (I) is the number of photons passing through a unit area per unit time (usually in photons cm⁻² s⁻¹), whereas power is energy per second (1 W = 1 J s⁻¹). Because intensity depends on the area, it is greater at the focus than a distance away, whereas the total power is the same everywhere along the beam. To calculate the intensity from measured laser power readings, 1 mW = $\lambda \times 5 \times 10^{12}$ photons s⁻¹ nm⁻¹ can be used (derived from $E = hc/\lambda$). For example, 1 mW at 960 nm is $\sim 5 \times 10^{15}$ photons s⁻¹.

Dividing this by the area of the beam in the focal plane (for high numerical aperture (NA) $\sim 10^{-9}$ cm²) gives an intensity at the focus of $\sim 5 \times 10^{24}$ photons cm⁻² s⁻¹. The intensity squared is 25×10^{48} photons² cm⁻⁴ s⁻², increasing the TPE probability in the focal plane by $\sim 10^7$ compared with the unfocused beam. Away from the focal plane, the TPE probability drops off rapidly so that no appreciable fluorescence is emitted (Fig. 2b), and intrinsic three-dimensional resolution is achieved.

Focusing alone is still not enough to make two-photon microscopy practical. For example, 1 mW of 960-nm light focused into 10 μ M fluorescein generates only $\sim 20,000$ fluorescence photons per second. Further reduced by a total collection efficiency of only a few percent, this intensity would be much less than one fluorescence photon per pixel on a typical laser-scanning microscope with a ~ 1 - μ s pixel dwell time. To generate enough TPE fluorescence for imaging, a pulsed laser is used to increase further the probability that two photons will simultaneously interact with a molecule, while still keeping the average power relatively low. A mode-locked titanium sapphire (Ti:S) laser—the most common laser used in MPM—produces ~ 80 million pulses per second, each with pulse duration of ~ 100 fs. With a pulsed laser, the two-photon fluorescence depends on the average squared intensity ($\langle I(t)^2 \rangle$) rather than the squared average intensity ($\langle I(t) \rangle^2$). The average intensity is equal to the number of pulses per second (R) times the integrated instantaneous intensity during a pulse, which yields^{36,66}

$$\langle I(t)^2 \rangle = g_p \langle I(t) \rangle^2 / (R\tau) \quad (1)$$

where g_p is a unitless factor that depends on the temporal laser pulse shape (0.66 for a Gaussian pulse shape), τ is the full-width half-maximum (FWHM) of the pulse and $\langle \rangle$ denotes the time-averaged value. For 100-fs pulses and $R = 80$ MHz, the TPE probability is increased by $g_p/R\tau = 10^5$, and 20,000 emitted photons becomes 2 billion photons per second with a mode-locked laser. This translates into around 100 photons per pixel in the imaginary multiphoton microscope just described.

Fluorescence excitation and two-photon action cross-sections

The two-photon cross-section (σ_{2p}) is a quantitative measure of the probability of a two-photon absorption. σ_{2p} has units of cm⁴ s, with 10^{-50} cm⁴ s called a Göppert-Mayer or 'GM'. Because it is difficult to measure σ_{2p} directly, the two-photon 'action' cross-section is usually measured; this is the product of the fluorescence quantum yield (ϕ_F) and the absolute two-photon absorption cross-section (σ_{2p})^{36,66,67}. Both the wavelength dependence and the absolute values of $\phi_F\sigma_{2p}$ are important

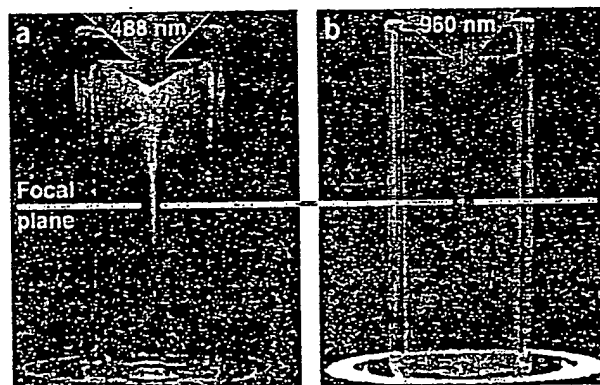


Figure 2 Localization of excitation by two-photon excitation. (a) Single-photon excitation of fluorescein by focused 488-nm light (0.16 NA). (b) Two-photon excitation using focused (0.16 NA) femtosecond pulses of 960-nm light.



in MPM. To determine an optimal TPE wavelength, doubling the maximum single-photon excitation wavelength is often a good approximation. However, many molecules exhibit obvious deviations from this rule because the selection rules for two-photon processes are different from single-photon selection rules. For symmetrical molecules, initial single-photon excited states are two-photon forbidden⁶⁸, and therefore fluorophores such as Rhodamine B⁶⁷ show a clear difference between their one- and two-photon absorption spectra, as shown in Figure 3a.

Intrinsic molecules such as NADH have extremely low action cross-sections ($<10^{-4}$ GM)^{36,37,69} yet have been successfully used with MPM imaging^{70–73}. The other extreme, CdSe-ZnS quantum dots, have cross-sections approaching 50,000 GM⁷⁴ and allow multiphoton imaging with a few microwatts of laser power. Most common fluorescent dyes have $\Phi_F\sigma_{2p}$ values in the range of 1–300 GM^{36,67}, although it is possible to design organic molecules specifically for high nonlinear absorption^{75–77}. Intrinsically fluorescent proteins, such as green fluorescent protein (GFP), have large action cross-sections (Fig. 3b and refs. 36, 78–81), and are particularly well suited for MPM in tissue explants and live animals^{24,82–88}.

Although relative two-photon excitation spectra (λ dependence)^{89,90} can be useful, it is often necessary to know $\Phi_F\sigma_{2p}(\lambda)$ explicitly when designing a particular MPM experiment. For example, cyan fluorescent protein (CFP) and yellow fluorescent protein (YFP) can be used for multiphoton fluorescence resonance energy transfer (MP-FRET)^{91–93} but also have potential for MP-FCCS⁶². For MP-FRET, CFP must be excited without exciting YFP; for MP-FCCS, by contrast, it is optimal to excite both proteins equally. The relative excitation spectra alone do not provide the needed information, and an absolute measure of the expected fluorescence from each species at a given wavelength is necessary. From Figure 3c, it is clear that MP-FRET is best carried out at 800 nm, whereas MP-FCCS would work best where the fluorescence from both species is about equal (~ 910 nm).

The optical and effective resolution of MPM

The optical resolution of a multiphoton microscope seems at first thought to be worse by a factor of 2 than a single-photon confocal microscope, because the illumination used is about twice the wavelength. However, this assessment is based on comparison to a hypothetical perfect confocal microscope that has an infinitely small pinhole⁹⁴. As the pinhole is opened, the resolution of a confocal microscope decreases and the resolution difference becomes less. In practice, the effective resolution achieved is a function of many complex factors, such as the absolute number of photons collected per pixel (pixel noise scales as the square root of the number of photons), and, in a confocal microscope, the fraction of true signal photons relative to scattered photons from outside the observation volume (that is, contrast). Because fluorescence only arises from the focus in MPM, when compared with confocal in scattering samples the effective resolution of the former often seems far superior^{95–97}.

Knowing the dimensions of the two-photon focal volume is useful, for example, to estimate the thickness of an optical section or to calculate the number of caged neurotransmitters one might expect to photolyse per laser pulse. The illumination point spread function, $\text{IPSF}(x, y, z)$, describes intensity everywhere in space near the focus, and in MPM only IPSF^2 is needed to define the true optical resolution⁹⁸ (assuming confocal detection is not used). IPSF^2 can be calculated (Fig. 4a) based on the work of Richards and Wolf⁹⁹, and fits of the lateral and axial intensity-squared profiles to a Gaussian function (Fig. 4b) yield expressions for estimating the diffraction-limited lateral (ω_{xy}) and axial (ω_z) $1/e$ radii of IPSF^2 (Fig. 4c). For NAs ≤ 0.7 , ω_{xy} is inversely proportional to NA; however, at higher NAs, this dependence deviates, and a better estimate

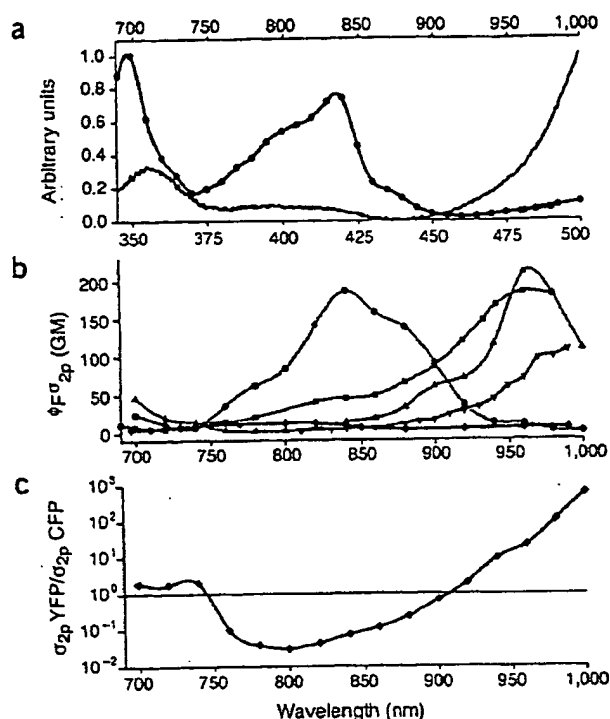


Figure 3 Two-photon action cross-sections. (a) Two-photon action spectrum of Rhodamine B (black) compared to the one-photon absorption spectrum (red). (b) Two-photon action spectra of five common fluorescent proteins (FPs): enhanced GFP (eGFP; green), CFP (cyan), YFP (yellow), *Discosoma* Red (dsRed; red) and wild type GFP (wtGFP; black). Note: our measurements of the FP cross-sections were normalized to the concentration of fluorescing protein as determined by FCS, and therefore our absolute values (but not line shape) for CFP and YFP differ from refs. 79 and 81. (c) Semilog plot of the cross-section ratio of YFP to CFP.

($\sim 1\%$ error) can be found by assuming a slight inverse power dependence of NA. Analogous to the nonparaxial derivations of ref. 100, an expression for ω_z of the two-photon focal volume can also be formulated (Fig. 4c). Conversions to the FWHM and $1/e^2$ radius (Fig. 4b) can be obtained by multiplication by $2\sqrt{\ln 2}$ and $\sqrt{2}$, respectively. The FWHM is a more common measure of optical resolution, whereas the $1/e^2$ radius is, for example, needed to recover diffusion coefficients from MP-FCS and MP-FPR measurements. Note that the objective lenses must be uniformly illuminated (overfilled) to achieve a diffraction-limited focus—a condition well approximated if, in practice, the $1/e$ beam diameter is no less than the diameter of the objective lens back aperture.

By approximating the IPSF^2 as a three-dimensional Gaussian volume, analytical integration over all space yields the TPE focal volume. This is not a volume with distinct walls but rather one based on averaging the TPE potential over all space. Integrating the three-dimensional Gaussian yields

$$V_{\text{TPE}} = \pi^{3/2} \omega_{xy}^2 \omega_z \quad (2)$$

where ω_{xy} and ω_z are calculated as in Figure 4c. Although these expressions provide a good estimate of the central lobe of IPSF^2 , they do not fully take the wings of IPSF^2 into account at regions far from the focus and the integrated Gaussian volume yields a value 68% of that obtained from numerical integration of the full vectorial approach of ref. 99. With



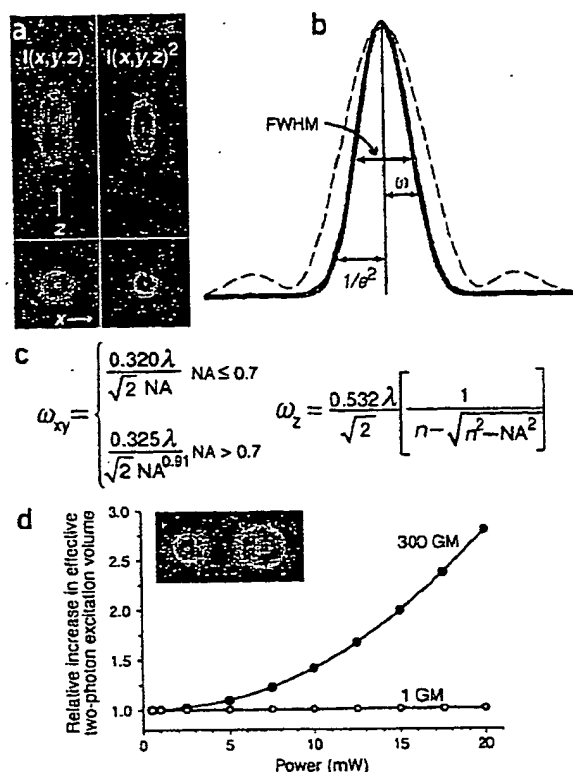


Figure 4 The two-photon excitation volume. (a) Axial and lateral views of IPSF and IPSF². Squaring the IPSF results in minimal wings relative to the center. (b) Axial profile (0,0,z) of IPSF (dashed red line) and IPSF²(0,0,z) (solid red). Dashed black line is a fit to a Gaussian function. (c) Equations for calculating the 1/e widths (ω) of the lateral (xy) and axial (z) intensity-squared profiles. (d) Excitation probability saturation of the TPE focal volume for a 1-GM and 300-GM fluorophore calculated at 1.2 NA for a 200-fs, 80-MHz source. Insert shows the lateral plane of the effective IPSF² at the focus for 1 GM (left) and 300 GM (right) at 20 mW.

this correction, equation (2) provides a good estimate of the TPE volume. For example, the effective TPE volume for a 1.2-NA lens at 900 nm is $(5.57) (0.175 \mu\text{m})^2 (0.451 \mu\text{m}) / 0.68 = 0.113 \mu\text{m}^3$ or ~100 attoliters.

In using a Gaussian approximation for the focal volume, it is assumed that the laser intensity is far from a level that would cause fluorophore excitation saturation. Assuming the lifetime of a fluorophore is less than the time between laser pulses, the TPE probability per laser pulse per fluorophore is $1 - \exp(-\alpha \sigma_{2p} P^2 \text{IPSF}^2(x,y,z) / (R^2 \tau))$, where P is the laser power and α is a conversion constant^{1,74}. Depending on the laser power and the value of σ_{2p} , this probability can saturate near the focal center (i.e., become 1.0), while continuing to increase in the wings of the focal volume, resulting in a marked deviation from the excitation volume predicted by equation (2). Figure 4d shows calculations carried out for molecules with cross-sections of 1 and 300 GM for laser powers up to 20 mW ($R = 80$ MHz and 1.2 NA), indicating that with a relatively high cross-section dye the optical resolution may begin to deviate from the optimal possible value. This effect was clearly seen with quantum dots⁷⁴, which have extremely high TPE cross sections. It also may become significant in cases where the peak laser intensity is unusually high, such as in applications of high-pulse power regenerative amplifier systems^{101,102} to increase imaging depth. Similar calculations carried out with $R = 200$ KHz for only 0.5 mW of power at the

focus yield an effective TPE volume 40 times larger than the nonsaturated focal volume.

Lasers and laser optics for MPM

The application of mode-locked Ti:S crystal-based lasers to MPM, first demonstrated in 1992 (ref. 103), was really the beginning of practical MPM. Before that, MPM involved femtosecond dye lasers, which were temperamental and required constant tweaking. Commercial Ti:S lasers from Spectra-Physics (Mountain View, CA, USA) and Coherent (Sunnyvale, CA), now with broadband optics permitting use of the full tunable range (~700 to 1,000 nm) without changing laser mirrors, have made MPM an accessible tool for biology. The recent introduction of computer-controlled, single-box Ti:S lasers from both companies continues this trend. Although other types of mode-locked lasers have been applied^{31,95,104,105}, Ti:S lasers are presently the most common and robust excitation sources for MPM.

The term 'mode-locked' refers to a laser operating with only a certain set of frequencies (modes) propagating in the laser cavity, with the phase between these modes locked so that there is destructive interference between the propagating frequencies everywhere in the cavity except at one point where the waves add constructively¹⁰⁶. This results in a single short pulse of light traveling in the cavity with the repetition rate dictated by the distance between the two cavity end mirrors and the speed of light (Fig. 5a,b). Femtosecond Ti:S lasers require a relatively large number of intracavity frequencies to achieve 100-fs pulses, and therefore the pulses have a significantly large spectral bandwidth. The laser spectrum is simpler to measure than the pulsewidth, so it is commonly monitored in a MPM system as an indication of proper mode-locking. The spectrum should be a symmetrical Gaussian shape (Fig. 5c) devoid of spikes that indicate an unwanted continuous-wave component (termed 'CW breakthrough'). The product of the pulsewidth and the spectral width (bandwidth) is called the time-bandwidth product (TBWP), which has a defined minimum value (the actual value depends on the temporal pulse shape). If the TBWP is equal to this minimum value, the pulses are 'transform-limited' and, assuming a Gaussian pulse shape, the temporal and spectral widths are related by $\tau = 0.44 \lambda_0^2 / c \lambda_{FWHM}$, where λ_0 is the peak of the spectrum (that is, 960 nm in Fig. 5c) and $c = 300$ nm/fs (speed of light). In a transform-limited pulse the wavelengths are randomized so any available color is equally probable anytime during the pulse. However, if this pulse passes through a dispersive material such as glass, it becomes 'chirped'; the longer wavelength components travel faster so the pulsewidth lengthens, but the spectrum remains unchanged. In the visible and near-IR region, all materials have positive dispersion (red leads blue), so that femtosecond pulses passing through optics are always 'positively chirped' and thus longer than they were directly out of the laser. Positive dispersion can be offset by adding negative dispersion before the beam travels through the optics. This is known as dispersion compensation, or pre-chirping, and has been applied to MPM^{107,108} but leads to an instrument that is more complicated to operate.

From equation (1) it can be shown that the increase in average power needed to maintain the same TPE with the longer pulse scales as the square root of the ratio of the chirped pulsewidth to the pulsewidth before the dispersive optics. For example, 2-fold increases in pulsewidth require 1.41-fold more laser power to achieve the same level of fluorescence. Pulse broadening resulting from dispersion can be estimated using

$$\tau_{\text{out}} = \tau_{\text{in}} (1 + 7.68(D/\tau_{\text{in}}^2)^2)^{1/2} \quad (3)$$

where D is the total dispersion in femtoseconds squared. A typical MPM system can have between 3,000 and 20,000 fs² of dispersion in

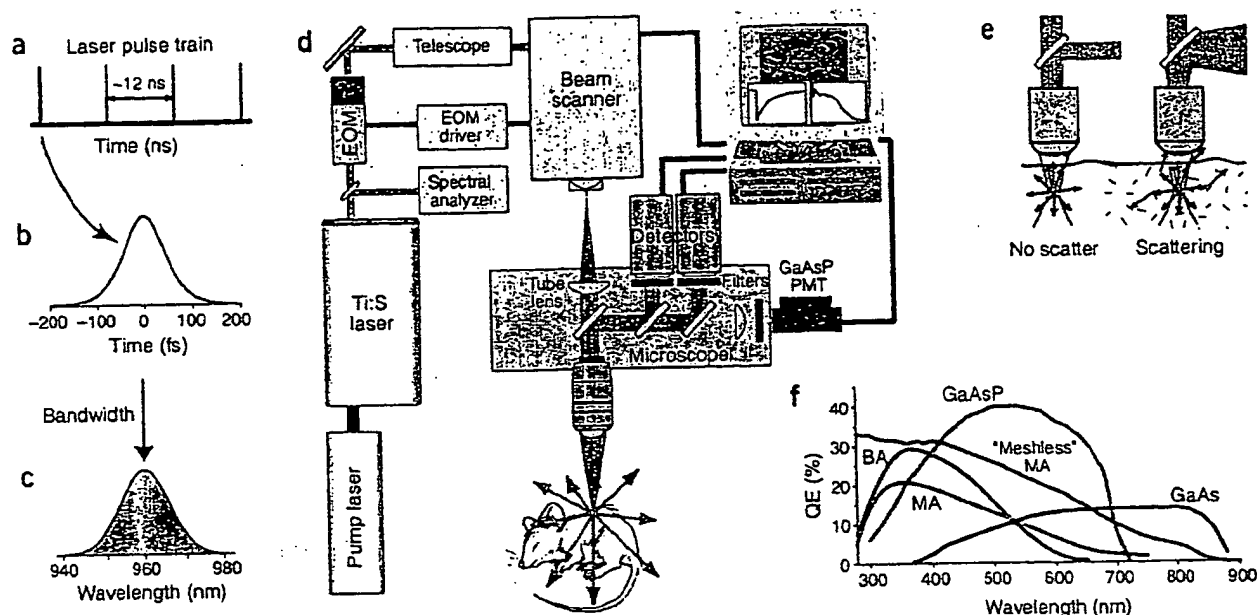


Figure 5 Components of a multiphoton microscope. (a) Pulse train from a laser mode-locked Ti:S at 80 MHz. (b) Pulses out of the laser typically have a FWHM duration of 100 fs and a spectral FWHM (c) of ~10 nm. (d) Schematic of a MPM system (see text). (e) Rays generated at the focus deep in a specimen may be scattered and enter the objective lens as skew rays, resulting in diverging epifluorescence. (f) Comparison of PMT photocathode efficiencies.

total, depending on the operating wavelength, objective lens used^{109–111} and other components such as beam modulators and beam-expanding lenses. Laser pulsewidths vary as well, typically ranging from 80 to 150 fs, depending on the manufacturer and wavelength. At 5,000 fs², this translates into pulsewidths of 190 and 177 fs, respectively, with both values being well within the range for efficient TPE. For a more dispersive system at 20,000 fs², the respective pulsewidths become 697 fs and 403 fs, requiring 50–80% more average power to have the same TPE efficiency as the ~180-fs pulses available at the focus of the less dispersive system.

The complete multiphoton microscope

Most multiphoton microscopes, including all commercial versions, essentially consist of a laser-scanning confocal adapted to reflect the near IR, a pulsed laser and a few required multiphoton peripherals. Figure 5d diagrams the components of a functional MPM system, similar to instruments reported in the literature^{112,113}.

Ti:S laser. A choice exists between a pair of two separate lasers (Nd:YVO₄ pump laser and Ti:S laser) or a 'single-box' version, which has both the pump laser and Ti:S oscillator in the same factory-sealed box. The two-laser combination presently has a broader tuning range than a single-box laser (as much as 690–1,020 nm compared with 720–920 nm) and the ability to stop mode-locking, which is sometimes useful to verify that the signal is actually due to two-photon fluorescence. Laser power available varies depending on the size of the pump laser, with 5 W pumped systems providing up to 1 W at the Ti:S peak wavelengths (~800 nm) and a few hundred milliwatts near the edges of the tuning curve (700 nm and 1,000 nm). Systems with a 10 W pump source produce ~50% more power across the wavelength range. For maximum flexibility and tuning range, the pump laser–Ti:S pair is as yet unsurpassed; however, simplicity of operation makes single-box lasers ideal for many situations, such as imaging facilities at which user friendliness is a priority.

Beam intensity control. There are several choices for controlling the laser intensity: a collection of neutral-density (ND) filters, a rotatable polarizer, an electro-optic modulator (EOM or Pockels cell) or an acousto-optic modulator (AOM). The two modulators have the ability to blank the beam during scanner turnaround and flyback; however, EOMs are typically less dispersive. For example, an EOM with a 50- to 80-mm-long KD*P crystal has between 2,000 and 4,000 fs² of dispersion, whereas an AOM made of TeO₂ can be 4-fold more dispersive¹¹⁴.

Beam telescope. A beam telescope can be used to adjust the size of the beam at the back aperture of the objective to be sure the lens is 'over-filled' for a diffraction-limited focus, or in some cases, underfilled for an axially extended focus. Note that in the position shown in Figure 5d, the range of useable beam diameters is ultimately limited by the size of the XY scanner mirrors, which may be only a few millimeters in diameter. With the availability of the new high-NA, low-magnification objectives, such as the Olympus 20 × 0.95 NA water immersion lens, which has a 17-mm back aperture, a better solution may be necessary. For example, beam expansion after the scanner is more optically complex to incorporate, but could better provide the range of beam sizes needed to optimize the focus.

Beam scanner. Of the various XY scanner designs available¹¹⁵, the most common is the nonresonant point scanner, which scans the focused beam across the specimen with an adjustable scan speed, permitting software 'zooming' (variable apparent magnification by scanning a smaller region, more slowly) and the important ability to rotate the scan axis. Resonant galvanometers capable of faster (video) scan rates^{116,117} can also be used, but these operate at only one frequency and cannot zoom, pan or rotate. Also useful is the ability to park the beam stably at any specified XY position, allowing point measurements such as MP-FCS⁵⁸ and MP-FPR measurements⁵⁹ using the same optics for both imaging and single-point measurements. This is critical for intracellular measurements⁶⁰ so that the measurement location is accurately known.

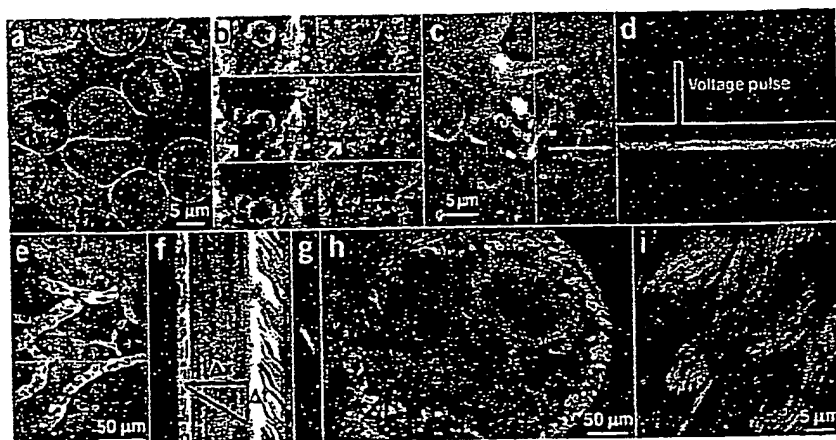


Figure 6 Applications showing various capabilities of MPM. (a) Simultaneous 780-nm excitation of three different fluorophores in RBL-2H3 cells labeled with 4',6-diamidino-2-phenylindole (DAPI) (DNA, blue pseudo color), PATMAN (plasma membrane, green) and tetramethylrhodamine (mitochondria, red). (b) Cell stimulation-induced granule-granule fusion¹⁴², as assessed by PATMAN membrane staining (gray scale and blue) and acridine orange-stained granules (green and red). (c) and (d) Calcium dynamics 300 μm deep into the neuropil of the lobster stomatogastric ganglion¹⁴³. (c) Processes of a 'PD' neuron filled with calcium green-1N. (d) A line scan shows that upon depolarization (pulse), in a dopamine-dependent manner, calcium enters through varicosities on the neurites, copyright 2000 (reprinted by permission of the Society for Neuroscience, ©2000) (e) Measuring blood flow in a vessel plexus under the intact tibial growth plate perichondrium in the mouse. Red blood cells appear as shadows within the fluorescence-containing blood vessels (methodology from ref. 144, and work carried out in collaboration with C. Farnum, Cornell University, and W. Horton, Shriners Hospital, Portland, Oregon). (f) The angle of the shadow traces in the line scan can be translated to the blood flow velocity. (g) Two-dimensional image autocorrelation is used to determine the average angle, in this case yielding an average blood flow of $\Delta x/\Delta t = 226 \mu\text{m s}^{-1}$. (h) Intrinsic emissions (yellow) detailing the tissue structure of a mouse's ovary can be imaged simultaneously with genetically incorporated GFPs. Ovarian surface epithelial cells were labeled by an intrabursal injection of virally incorporated eGFP. (Work done in collaboration with A. Flesken-Nikitin and A. Nikitin, Cornell University.) (i) Because collagen SHG is coherent, information about the specimen can be derived from the directionality of the SHG emission. In this 10-day-old rat tail tendon, immature fibril segments scatter backward (green), whereas mature fibrils scatter forward (red).

Detectors. The most efficient fluorescence collection scheme is obtained by the use of 'non-descanned' or direct detectors, because confocal detection is not needed with multiphoton excitation. Although it has been shown that a confocal aperture can improve the resolution of a two-photon microscope under certain conditions^{94,118}, for applications in which MPM is most advantageous (such as deep imaging in scattering specimens) a confocal pinhole will degrade performance because scattered emission photons will be rejected, even though they originated in the focal volume. In fact, highly scattered emissions may even be randomly divergent leaving the objective lens (Fig. 5e) and thus difficult to focus^{101,119}. For this reason, a particularly efficient detector design involves the use of a large-area photomultiplier tubes (PMT) close to the objective lens.

PMTs are the dominant detectors for both confocal and MPM because an imaging detector is not needed for point-scanning systems, and the high gain and absence of readout noise favors PMTs (pixel integration times are usually in the microsecond range). Charge-coupled detectors (CCDs) have not found widespread use in MPM, other than in situations requiring imaging detectors¹²⁰, but are rapidly improving with on-chip avalanche amplification to reduce the effect of readout noise. Avalanche photodiodes (APDs) have also been used in MPM and may be superior to conventional PMTs at extremely low fluorescence levels¹²¹.

A recent improvement in detectors for MPM are GaAsP photocathode PMTs (Hamamatsu H7422P), which offer high quantum efficiency

(QE) values in the important 400- to 650-nm range compared with PMTs using conventional photocathode materials (Fig. 5f). Peaking at ~42% QE, GaAsP detectors are close to the theoretical 50% maximum QE of a photocathode-based device, making them well suited for two-photon FCS, as well as multiphoton imaging. They also have a small transient-time spread (~150 ps) and a 1-ns output pulse, making them attractive for fluorescence lifetime imaging¹²². Two minor limitations are a relatively small active area of 5 mm diameter (this is, however, still much larger than an APD active area), making focusing optics a requirement, and a lower damage threshold than conventional photocathodes. Overall, they are a significant advancement in MPM detectors because higher detection efficiency can translate to lower excitation power and improved viability with live specimens. For wavelengths beyond 700 nm, GaAs PMTs can be used, in addition to enhanced 'meshless' multialkali PMTs (such as the Hamamatsu H7732-10), which have a relatively high QE, even above 650 nm (Fig. 5f).

Applications of MPM

The advantages of MPM, for the most part, arise from two basic attributes of the nonlinear excitation: localized excitation and the expanded wavelength accessibility of most fluorophores. The restriction of multiphoton excitation to the focal plane completely alleviates out-of-focus photobleaching and photodamage. All photons generated are signal; there is no background, so that emission collection can be both simple and efficient. The

lack of out-of-focus fluorescence, coupled with the use of IR light, explains the technique's successful use for fluorescence imaging in thick specimens. The second aspect, enhanced UV bands under TPE (Fig. 3a), simplifies multicolor imaging by allowing excitation of different fluorophores with the same laser, avoiding chromatic aberrations and providing a broad uninterrupted emission collection bandwidth.

Figure 6 shows a panorama of applications that highlight the strengths of MPM, including the simultaneous excitation of fluorophores whose emission spectra vary by hundreds of nanometers (Fig. 6a,b), deep imaging in live preparations (Fig. 6c,d) and live mice (Fig. 6e-h), as well as the use of intrinsic fluorophores and other nonlinear signals, such as SHG (Fig. 6h,i).

In addition to multiphoton fluorescence, an MPM system can easily be modified to collect light from nonlinear scattering processes, such as SHG. In harmonic generation, multiple photons simultaneously interact with non-centrosymmetrical structures without absorption, producing radiation at exactly half of the exciting wavelength (Fig. 7a). Because harmonic generation is a coherent process (scattered photons maintain phase information), the scattered beam must satisfy phase-matching constraints producing highly directed radiation rather than isotropic emission (Fig. 7b,c). SHG directionality is dependent on the distribution and directionality of the induced dipoles within the focal volume^{60,123}. SHG imaging is presently being investigated to image membrane potential sensing dyes with improved signal-to-

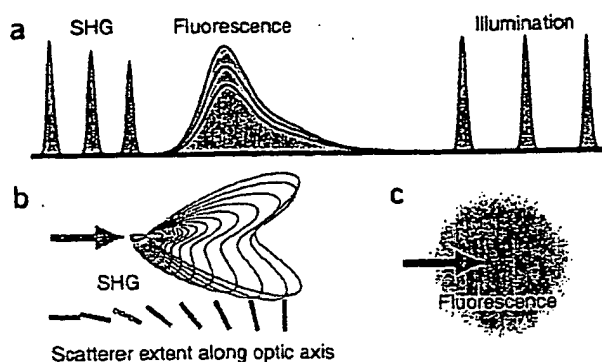


Figure 7 Two-photon fluorescence and SHG. (a) SHG is always at half the fundamental wavelength and tunes with laser, whereas fluorescence emission is unchanged, except in its magnitude as the laser tunes through the TPE absorption peak. (b,c) SHG is directional depending on the distribution and orientation of the nonlinear dipoles (b), whereas fluorescence is, in general, isotropically emitted (c).

noise^{39,124–126}, to visualize microtubule polarity^{42,44,127} and to obtain high-resolution images of unstained collagen structures in mouse models of disease^{24,37,127}.

Viability, photodamage and photobleaching

Although multiphoton excitation limits photodamage to the focal plane, the possibility of bleaching and damage within this region remains. Photodamage and decreased viability may be especially pronounced at the shorter Ti:S wavelengths where TPE of intrinsic tissue chromophores³⁷ is high. Clear enhancements in cellular viability with MPM over single-photon confocal microscopy are easiest to obtain at wavelengths >800 nm^{31,128}. It is generally thought that overall in the 700- to 1,000-nm range, single- and three-photon excitation damage is usually negligible, and photodamage in the focal plane is primarily due to two-photon processes¹²⁹, implying that pulsewidth is usually not a critical parameter in viability. This finding is contradicted by work that suggests highly nonlinear dependence of phototoxicity¹³⁰; however, the excitation doses (squared power \times dwell time) used in the work were nearly 1,000-fold higher than levels normally used in MPM. Probe photobleaching, like cellular photodamage, can only occur in the focal plane, but there is evidence that some molecules bleach more easily under TPE¹³¹ and may even show higher order (>2) photobleaching¹³².

Nonetheless, reduced damage outside of the focal volume can have tremendous advantages in optically thick specimens. The key to using MPM safely and successfully is not any different from that for any other form of microscopy; one must understand the effects and limits on the specific biological system under investigation, and always optimize to reduce the excitation intensity. In MPM, this means using efficient fluorescence detectors and blanking the laser while image data are not being acquired.

Conclusions and future areas of development

MPM is quickly becoming a standard tool for determining the molecular mechanisms of cell-based processes in basic biological research, tissue engineering and transgenic mouse models of disease and development. The number of publications focused on nonlinear microscopy development indicates that MPM has created its own field of research. Areas of development that hold particular promise range from fabrication of minimally dispersive objective lenses designed to optimize collection of scattered emissions, to the application of adaptive

optics^{133–135} to MPM for correcting aberrations of the point spread function.

As presently implemented, MPM can image hundreds of microns deep. We believe the ultimate depth limitation is not often a result of a lack of laser power but rather difficulty in collecting the generated fluorescence due to both absorption and scattering, which leads to collection losses (Fig. 5e), as well as reduced fluorescence due to degradation of the IPSP². A simple test for inadequate two-photon excitation is to measure the power dependence of the fluorescence deep within the specimen to test for saturation. If it scales as less than the power squared, saturation is occurring, indicating that more than sufficient excitation exists in the focal plane. In practice, we often find blurriness and a significant reduction in contrast in many specimens when the imaging depth is increased past several hundred microns, well before all signal is lost. Aberrations of IPSP² can be caused by either heterogeneity in the index of refraction in tissue or TPE focal volume saturation (see Fig. 4d). It may be possible to overcome the former difficulty by adaptive optics, in which the spatial phase of the beam is modified to pre-compensate for the path the rays take through the tissue. Curing the latter problem requires lower power, compensated by better detection.

Nonlinear optics, the 'magical' area of modern physics that helped spawn MPM, still has more to offer. Femtosecond lasers are being devised that can operate in the 1,000- to 1,300-nm range, just beyond that which a Ti:S laser can conveniently reach^{136,137}. This region is especially important for high-viability imaging of redder dyes and fluorescent proteins. Several groups are developing forms of multiphoton endoscopy^{138,139}, and new photonic crystal fibers now allow fiber delivery of 100-fs pulses through optical fibers with more than enough power for MPM and multiphoton endoscopy¹⁴⁰. Finally, the trick of modifying nonlinear optical responses by changing the phase of the spectral components that make up a femtosecond pulse—a field known as 'coherent control'—may make it possible to fine-tune multiphoton excitation¹⁴¹ to increase multiphoton absorption, reduce two-photon photobleaching or improve photo-uncaging efficiency.

Since its introduction a little over a decade ago, MPM has evolved from a photonic novelty to a tool for visualizing cellular and subcellular events within living tissue. As we focus on understanding the physiological and developmental consequences of the multitude of new genetic sequences uncovered, but not understood, MPM will surely continue to play an important part.

COMPETING INTERESTS STATEMENT

The authors declare competing financial interests (see the *Nature Biotechnology* website for details).

Published online at <http://www.nature.com/naturebiotechnology/>

1. Denk, W., Strickler, J.H. & Webb, W.W. Two-photon laser scanning fluorescence microscopy. *Science* **248**, 73–76 (1990).
2. Yuste, R. & Denk, W. Dendritic spines as basic functional units of neuronal integration. *Nature* **375**, 682–684 (1995).
3. Mainen, Z.F., Malinow, R. & Svoboda, K. Synaptic calcium transients in single spines indicate that NMDA receptors are not saturated. *Nature* **399**, 151–155 (1999).
4. Rose, C.R., Kovalchuk, Y., Eilers, J. & Konnerth, A. Two-photon Na^+ imaging in spines and fine dendrites of central neurons. *Pflügers Arch.* **439**, 201–207 (1999).
5. Tan, Y.P. & Llano, I. Modulation by K^+ channels of action potential-evoked intracellular Ca^{2+} concentration rises in rat cerebellar basket cell axons. *J. Physiol.* **520** Pt 1, 65–78 (1999).
6. Cox, C.L., Denk, W., Tank, D.W. & Svoboda, K. Action potentials reliably invade axonal arbors of rat neocortical neurons. *Proc. Natl. Acad. Sci. USA* **97**, 9724–9728 (2000).
7. Majewska, A., Tashiro, A. & Yuste, R. Regulation of spine calcium dynamics by rapid spine motility. *J. Neurosci.* **20**, 8262–8268 (2000).
8. Oertner, T.G. Functional imaging of single synapses in brain slices. *Exp. Physiol.* **87**, 733–736 (2002).
9. Frick, A., Magee, J., Koester, H.J., Migliore, M. & Johnston, D. Normalization of Ca^{2+} signals by small oblique dendrites of CA1 pyramidal neurons. *J. Neurosci.* **23**, 3243–3250 (2003).
10. Lendvai, B., Zelles, T., Rozsa, B. & Vizi, E.S. A vinca alkaloid enhances morphological

- dynamics of dendritic spines of neocortical layer 2/3 pyramidal cells. *Brain Res. Bull.* 59, 257-260 (2003).
11. Sabatini, B.L. & Svoboda, K. Analysis of calcium channels in single spines using optical fluctuation analysis. *Nature* 408, 589-593 (2000).
12. Svoboda, K., Denk, W., Kleinfeld, D. & Tank, D.W. *In vivo* dendritic calcium dynamics in neocortical pyramidal neurons. *Nature* 385, 161-165 (1997).
13. Helmchen, F., Svoboda, K., Denk, W. & Tank, D.W. *In vivo* dendritic calcium dynamics in deep-layer cortical pyramidal neurons. *Nat. Neurosci.* 2, 989-996 (1999).
14. Stosiek, C., Garaschuk, O., Holthoff, K. & Konnerth, A. *In vivo* two-photon calcium imaging of neuronal networks. *Proc. Natl. Acad. Sci. USA* 100, 7319-7324 (2003).
15. Helmchen, F. & Waters, J. Ca²⁺ imaging in the mammalian brain *in vivo*. *Eur. J. Pharmacol.* 447, 119-129 (2002).
16. Svoboda, K., Tank, D.W. & Denk, W. Direct measurement of coupling between dendritic spines and shafts. *Science* 272, 716-719 (1996).
17. Ladewig, T. *et al.* Spatial profiles of store-dependent calcium release in motoneurons of the nucleus hypoglossus from newborn mouse. *J. Physiol.* 547, 775-787 (2003).
18. Christie, R.H. *et al.* Growth arrest of individual senile plaques in a model of Alzheimer's disease observed by *in vivo* multiphoton microscopy. *J. Neurosci.* 21, 858-864 (2001).
19. Bacskai, B.J. *et al.* Non-Fc-mediated mechanisms are involved in clearance of amyloid-beta *in vivo* by immunotherapy. *J. Neurosci.* 22, 7873-7878 (2002).
20. D'Amore, J.D. *et al.* *In vivo* multiphoton imaging of a transgenic mouse model of Alzheimer disease reveals marked thioflavine-S-associated alterations in neurite trajectories. *J. Neuropathol. Exp. Neurol.* 62, 137-145 (2003).
21. Bacskai, B.J. *et al.* Imaging of amyloid-beta deposits in brains of living mice permits direct observation of clearance of plaques with immunotherapy. *Nat. Med.* 7, 369-372 (2001).
22. Brown, E.B. *et al.* *In vivo* measurement of gene expression, angiogenesis and physiological function in tumors using multiphoton laser scanning microscopy. *Nat. Med.* 7, 864-868 (2001).
23. McDonald, D.M. & Choyke, P.L. Imaging of angiogenesis: from microscope to clinic. *Nat. Med.* 9, 713-725 (2003).
24. Wang, W. *et al.* Single cell behavior in metastatic primary mammary tumors correlated with gene expression patterns revealed by molecular profiling. *Cancer Res.* 62, 6278-6288 (2002).
25. Wolf, K. *et al.* Compensation mechanism in tumor cell migration: mesenchymal-amoeboid transition after blocking of pericellular proteolysis. *J. Cell Biol.* 160, 267-277 (2003).
26. Cahalan, M.D., Parker, I., Wei, S.H. & Miller, M.J. Two-photon tissue imaging: seeing the immune system in a fresh light. *Nat. Rev. Immunol.* 2, 872-880 (2002).
27. Miller, M.J., Wei, S.H., Parker, I. & Cahalan, M.D. Two-photon imaging of lymphocyte motility and antigen response in intact lymph node. *Science* 296, 1869-1873 (2002).
28. Wei, S.H., Miller, M.J., Cahalan, M.D. & Parker, I. Two-photon imaging in intact lymphoid tissue. *Adv. Exp. Med. Biol.* 512, 203-208 (2002).
29. Miller, M.J., Wei, S.H., Cahalan, M.D. & Parker, I. Autonomous T cell trafficking examined *in vivo* with intravital two-photon microscopy. *Proc. Natl. Acad. Sci. USA* 100, 2604-2609 (2003).
30. Acuto, O. T cell-dendritic cell interaction *in vivo*: random encounters favor development of long-lasting ties. *Science* 300, 2828-2830 (2003).
31. Squinell, J.M., Wokosin, D.L., White, J.G. & Savister, B.D. Long-term two-photon fluorescence imaging of mammalian embryos without compromising viability. *Nat. Biotechnol.* 17, 763-767 (1999).
32. Gryczynski, I., Szymanski, H. & Lakowicz, J.R. On the possibility of calcium imaging using Indo-1 with three-photon excitation. *Photochem. Photobiol.* 62, 804-808 (1995).
33. Lakowicz, J.R. *et al.* Time-resolved fluorescence spectroscopy and imaging of DNA labeled with DAPI and Hoechst 33342 using three-photon excitation. *Biophys. J.* 72, 567-578 (1997).
34. Maiti, S., Shear, J.B., Williams, R.M., Zipfel, W.R. & Webb, W.W. Measuring serotonin distribution in live cells with three-photon excitation. *Science* 275, 530-532 (1997).
35. Williams, R.M., Shear, J.B., Zipfel, W.R., Maiti, S. & Webb, W.W. Mucosal mast cell secretion processes imaged using three-photon microscopy of 5-hydroxytryptamine autofluorescence. *Biophys. J.* 76, 1835-1846 (1999).
36. Xu, C., Zipfel, W., Shear, J.B., Williams, R.M. & Webb, W.W. Multiphoton fluorescence excitation: new spectral windows for biological nonlinear microscopy. *Proc. Natl. Acad. Sci. USA* 93, 10763-10768 (1996).
37. Zipfel, W.R. *et al.* Live tissue intrinsic emission microscopy using multiphoton-excited native fluorescence and second harmonic generation. *Proc. Natl. Acad. Sci. USA* 100, 7075-7080 (2003).
38. Freund, I. & Deutsch, M. 2nd-harmonic microscopy of biological tissue. *Opt. Lett.* 11, 94-96 (1986).
39. Campagnola, P.J., Clark, H.A., Mohler, W.A., Lewis, A. & Loew, L.M. Second-harmonic imaging microscopy of living cells. *J. Biomed. Opt.* 6, 277-286 (2001).
40. Mertz, J. & Moreaux, L. Second-harmonic generation by focused excitation of inhomogeneously distributed scatterers. *Opt. Commun.* 196, 325-330 (2001).
41. Moreaux, L., Sandre, O., Charpak, S., Blanchard-Desce, M. & Mertz, J. Coherent scattering in multi-harmonic light microscopy. *Biophys. J.* 80, 1568-1574 (2001).
42. Campagnola, P.J. *et al.* Three-dimensional high-resolution second-harmonic generation imaging of endogenous structural proteins in biological tissues. *Biophys. J.* 82, 493-508 (2002).
43. Campagnola, P.J., Mohler, W. & Millard, A.E. 3-dimensional high-resolution second harmonic generation imaging of endogenous structural proteins in biological tissues. *Biophys. J.* 82, 175a-175a (2002).
44. Dombeck, D.A. *et al.* Uniform polarity microtubule assemblies imaged in native brain tissue by second-harmonic generation microscopy. *Proc. Natl. Acad. Sci. USA* 100, 7081-7086 (2003).
45. Zoumi, A., Yeh, A. & Tromberg, B.J. Imaging cells and extracellular matrix *in vivo* by using second-harmonic generation and two-photon excited fluorescence. *Proc. Natl. Acad. Sci. USA* 99, 11014-11019 (2002).
46. Barad, Y., Eisenberg, H., Horowitz, M. & Silberberg, Y. Nonlinear scanning laser microscopy by third harmonic generation. *Appl. Phys. Lett.* 70, 922-924 (1997).
47. Muller, M., Squier, J., Wilson, K.R. & Brakenhoff, G.J. 3D microscopy of transparent objects using third-harmonic generation. *J. Microsc.* 191, 266-274 (1998).
48. Yelin, D., Oron, D., Korkotian, E., Segal, M. & Silberberg, Y. Third-harmonic microscopy with a titanium-sapphire laser. *Appl. Phys. B-Lasers* 67, S97-S101 (2002).
49. Sheppard, C.J.R. & Kompfner, R. Resonant scanning optical microscope. *Appl. Optics* 17, 2879-2882 (1978).
50. Duncan, M.D., Reintjes, J. & Manuccia, T.J. Scanning coherent anti-Stokes Raman microscope. *Opt. Lett.* 7, 350-352 (1982).
51. Zumbusch, A., Holtom, G.R. & Xie, X.S. Vibrational microscopy using coherent anti-Stokes Raman scattering (1999). *Phys. Rev. Lett.* 82, 4014-4017 (1999).
52. Muller, M., Squier, J., De Lange, C.A. & Brakenhoff, G.J. CARS microscopy with folded BoxCARS phasematching. *J. Microsc.* 197 (Pt 2), 150-158 (2000).
53. Piston, D.W., Summers, R.G., Knobel, S.M. & Morril, J.B. Characterization of involution during sea urchin gastrulation using two-photon excited photorelease and confocal microscopy. *Microsc. Microanal.* 4, 404-414 (1998).
54. Furuta, T. *et al.* Brominated 7-hydroxycoumarin-4-ylmethyls: photolabile protecting groups with biologically useful cross-sections for two photon photolysis. *Proc. Natl. Acad. Sci. USA* 96, 1193-1200 (1999).
55. Matsuzaki, M. *et al.* Dendritic spine geometry is critical for AMPA receptor expression in hippocampal CA1 pyramidal neurons. *Nat. Neurosci.* 4, 1086-1092 (2001).
56. Echevarria, W., Leite, M.F., Guerra, M.T., Zipfel, W.R. & Nathanson, M.H. Regulation of calcium signals in the nucleus by a nucleoplasmic reticulum. *Nat. Cell. Biol.* 5, 440-446 (2003).
57. Berland, K.M., So, P.T. & Gratton, E. Two-photon fluorescence correlation spectroscopy: method and application to the intracellular environment. *Biophys. J.* 68, 694-701 (1995).
58. Schille, P., Haupts, U., Maiti, S. & Webb, W.W. Molecular dynamics in living cells observed by fluorescence correlation spectroscopy with one- and two-photon excitation. *Biophys. J.* 77, 2251-2265 (1999).
59. Brown, E.B., Wu, E.S., Zipfel, W. & Webb, W.W. Measurement of molecular diffusion in solution by multiphoton fluorescence photobleaching recovery. *Biophys. J.* 77, 2837-2849 (1999).
60. Zipfel, W.R. & Webb, W.W. *In vivo* diffusion measurements using multiphoton-excited fluorescence photobleaching recovery (MPFPR) and fluorescence correlation spectroscopy (MPFCS) in *Methods in Cellular Imaging* (ed. Periasamy, A.) 345-376 (Oxford University Press, Oxford, UK, 2001).
61. Stroh, M., Zipfel, W.R., Williams, R.M., Webb, W.W. & Saitzman, W.M. Diffusion of nerve growth factor in rat striatum as determined by multiphoton microscopy. *Biophys. J.* 85, 581-588 (2003).
62. Heinze, K.G., Koltermann, A. & Schille, P. Simultaneous two-photon excitation of distinct labels for dual-color fluorescence cross correlation analysis. *Proc. Natl. Acad. Sci. USA* 97, 10377-10382 (2000).
63. Tirapuru, U.K. & König, K. Targeted transfection by femtosecond laser. *Nature* 418, 290-291 (2002).
64. König, K., Riemann, I. & Fritzsche, W. Nanodissection of human chromosomes with near-infrared femtosecond laser pulses. *Opt. Lett.* 26, 819-821 (2001).
65. Göpperl-Mayer, M. Über elementaraktuelle mit zwei quantensprüngen. *Ann. Phys.* 9, 273-294 (1931).
66. Xu, C. & Webb, W.W. Multiphoton excitation of molecular fluorophores and nonlinear laser microscopy in *Topics in Fluorescence Spectroscopy: Volume 5: Nonlinear and Two-Photon-Induced Fluorescence* (ed. Lakowicz, J.) 471-540 (Plenum Press, New York, 1997).
67. Xu, C. & Webb, W.W. Measurement of two-photon excitation cross sections of molecular fluorophores with data from 690 nm to 1050 nm. *J. Opt. Soc. Am. B* 13, 481-491 (1996).
68. Steinfield, J.I. *Molecules and Radiation*. (MIT Press, Cambridge, MA, 1989).
69. Huang, S., Heikal, A.A. & Webb, W.W. Two-photon fluorescence spectroscopy and microscopy of NAD(P)H and flavoprotein. *Biophys. J.* 82, 2811-2825 (2002).
70. Piston, D.W., Masters, B.R. & Webb, W.W. Three-dimensionally resolved NAD(P)H cellular metabolic redox imaging of the *in situ* cornea with two-photon excitation laser scanning microscopy. *J. Microsc.* 178 (Pt 1), 20-27 (1995).
71. Wong, B.J., Wallace, V., Coleno, M., Benton, H.P. & Tromberg, B.J. Two-photon excitation laser scanning microscopy of human, porcine, and rabbit nasal septal cartilage. *Tissue Eng.* 7, 599-606 (2001).
72. Noda, M. *et al.* Switch to anaerobic glucose metabolism with NADH accumulation in the beta-cell model of mitochondrial diabetes. Characteristics of betaHC9 cells deficient in mitochondrial DNA transcription. *J. Biol. Chem.* 277, 41817-41826 (2002).
73. Zhang, Q., Piston, D.W. & Goodman, R.H. Regulation of corepressor function by nuclear NADH. *Science* 295, 1895-1897 (2002).
74. Larson, D.R. *et al.* Water-soluble quantum dots for multiphoton fluorescence imaging *in vivo*. *Science* 300, 1434-1436 (2003).
75. Alibek, M. *et al.* Design of organic molecules with large two-photon absorption cross sections. *Science* 281, 1653-1656 (1998).
76. Wang, X.M. *et al.* Synthesis of new symmetrically substituted stilbenes with large multiphoton absorption cross section and strong two-photon-induced blue fluorescence. *Bull. Chem. Soc. Jpn* 74, 1977-1982 (2001).
77. Zhou, X. *et al.* One- and two-photon absorption properties of novel multi-branched molecules. *Phys. Chem. Chem. Phys.* 4, 4346-4352 (2002).





78. Heikal, A.A., Hess, S.T. & Webb, W.W. Multiphoton molecular spectroscopy and excited-state dynamics of enhanced green fluorescent protein (EGFP): acid-base specificity. *Chem. Phys.* 274, 37–55 (2001).
79. Blab, G.A., Lommerse, P.H.M., Cognet, L., Harms, G.S. & Schmidt, T. Two-photon excitation action cross-sections of the autofluorescent proteins. *Chem. Phys. Lett.* 350, 71–77 (2001).
80. Hanson, G.T. *et al.* Green fluorescent protein variants as ratiometric dual emission pH sensors. 1. Structural characterization and preliminary application. *Biochemistry* 41, 15477–15488 (2002).
81. Tsai, P.S. *et al.* All-optical histology using ultrashort laser pulses. *Neuron* 39, 27–41 (2003).
82. Mainen, Z.F. *et al.* Two-photon imaging in living brain slices. *Methods* 18, 231–239, (1999).
83. Shi, S.H. *et al.* Rapid spine delivery and redistribution of AMPA receptors after synaptic NMDA receptor activation. *Science* 284, 1811–1816 (1999).
84. D'Apuzzo, M., Mandolesi, G., Reis, G. & Schuman, E.M. Abundant GFP expression and LTP in hippocampal acute slices by *in vivo* injection of Sindbis virus. *J. Neurophysiol.* 86, 1037–1042 (2001).
85. Potter, S.M. *et al.* Structure and emergence of specific olfactory glomeruli in the mouse. *J. Neurosci.* 21, 9713–9723 (2001).
86. Strome, S. *et al.* Spindle dynamics and the role of gamma-tubulin in early *Caenorhabditis elegans* embryos. *Mol. Biol. Cell* 12, 1751–1764 (2001).
87. Ahmed, F. *et al.* GFP expression in the mammary gland for imaging of mammary tumor cells in transgenic mice. *Cancer Res.* 62, 7166–7169 (2002).
88. Lawson, N.D. & Weinstein, B.M. *In vivo* imaging of embryonic vascular development using transgenic zebrafish. *Dev. Biol.* 248, 307–318 (2002).
89. Bestvater, F. *et al.* Two-photon fluorescence absorption and emission spectra of dyes relevant for cell imaging. *J. Microsc.* 208, 108–115 (2002).
90. Dickinson, M.E., Simbuerger, E., Zimmermann, B., Waters, C.W. & Fraser, S.E. Multiphoton excitation spectra in biological samples. *J. Biomed. Opt.* 8, 329–338 (2003).
91. Periasamy, A. Fluorescence resonance energy transfer microscopy: a mini review. *J. Biomed. Opt.* 6, 287–291 (2001).
92. Majoul, I., Straub, M., Duden, R., Hell, S.W. & Soling, H.D. Fluorescence resonance energy transfer analysis of protein-protein interactions in single living cells by multifocal multiphoton microscopy. *J. Biotechnol.* 82, 267–277 (2002).
93. Bacskai, B.J., Skoch, J., Hickey, G.A., Allen, R. & Hyman, B.T. Fluorescence resonance energy transfer determinations using multiphoton fluorescence lifetime imaging microscopy to characterize amyloid-beta plaques. *J. Biomed. Opt.* 8, 368–375 (2003).
94. Gu, M. & Sheppard, C.J.R. Comparison of three-dimensional imaging properties between two-photon and single-photon fluorescence microscopy. *J. Microsc.* 177, 128–137 (1995).
95. Centonze, V.E. & White, J.G. Multiphoton excitation provides optical sections from deeper within scattering specimens than confocal imaging. *Biophys. J.* 75, 2015–2024 (1998).
96. Periasamy, A., Skoglund, P., Noakes, C. & Keller, R. An evaluation of two-photon excitation versus confocal and digital deconvolution fluorescence microscopy imaging in *Xenopus* morphogenesis. *Microsc. Res. Technol.* 47, 172–181 (1999).
97. Schilders, S.P. & Gu, M. Limiting factors on image quality in imaging through turbid media under single-photon and two-photon excitation. *Microsc. Microanal.* 6, 156–160 (2000).
98. Sheppard, C.J.R. & Gu, M. Image-formation in 2-photon fluorescence microscopy. *Optik* 86, 104–106 (1990).
99. Richards, B. & Wolf, E. Electromagnetic Diffraction in Optical Systems. 2. Structure of the Image Field in an Aplanatic System. *Proc. R. Soc. Lon. Ser. A* 253, 358–379 (1959).
100. Sheppard, C.J.R. & Matthews, H.J. Imaging in high-aperture optical systems. *J. Opt. Soc. Am. A* 4, 1354–1360 (1987).
101. Beaufort, E., Oheim, M. & Mertz, J. Ultra-deep two-photon fluorescence excitation in turbid media. *Opt. Commun.* 188, 25–29 (2001).
102. Theer, P., Hasan, M.T. & Denk, W. Two-photon imaging to a depth of 1000 microm in living brains by use of a Ti:Al₂O₃ regenerative amplifier. *Opt. Lett.* 28, 1022–1024 (2003).
103. Curley, P.F., Ferguson, A.I., White, J.G. & Amos, W.B. Application of a femtosecond self-sustaining mode-locked Ti:sapphire laser to the field of laser scanning confocal microscopy. *Opt. Quant. Electron.* 24, 851–859 (1992).
104. Hockberger, P.E. *et al.* Activation of flavin-containing oxidases underlies light-induced production of H₂O₂ in mammalian cells. *Proc. Natl. Acad. Sci. USA* 96, 6255–6260 (1999).
105. Wokosin, D.L., Squirell, J.M., Eliceiri, K.W. & White, J.G. Optical workstation with concurrent, independent multiphoton imaging and experimental laser microbeam capabilities. *Rev. Sci. Instrum.* 74, 193–201 (2003).
106. Hopkins, J. & Sibbett, W. Ultrashort lasers: big payoff in a flash. *Sci. Am.* 283, 73–79 (2000).
107. Soeller, C. & Cannell, M.B. Construction of a two-photon microscope and optimization of illumination pulse duration. *Phys. Rev. A* 43, 555–561 (1996).
108. Squier, J. & Muller, M. High resolution nonlinear microscopy: A review of sources and methods for achieving optimal imaging. *Rev. Sci. Instrum.* 72, 2855–2867 (2001).
109. Muller, D., Squier, J. & Brakenhoff, G.J. Measurement of femtosecond pulses in the focal point of a high-numerical-aperture lens by two-photon absorption. *Opt. Lett.* 20, 1038–1040 (1995).
110. Guild, J.B., Xu, C. & Webb, W.W. Measurement of group delay dispersion of high numerical aperture objective lenses using two-photon excited fluorescence. *Appl. Optics* 36, 397–401 (1997).
111. Muller, M., Squier, J., Wolleschensky, R., Simon, U. & Brakenhoff, G.J. Dispersion pre-compensation of 15 femtosecond optical pulses for high-numerical-aperture objectives. *J. Microsc.* 191, 141–150 (1998).
112. Majewska, A., Yiu, G. & Yuste, R. A custom-made two-photon microscope and deconvolution system. *Phys. Rev. Lett.* 441, 398–408 (2000).
113. Tsai, P.S. *et al.* Principles, design and construction of a two photon scanning microscope for *in vitro* and *in vivo* studies in *Methods for In Vivo Optical Imaging* (ed. Frostig, R.) 113–171 (CRC Press, Boca Raton, FL, 2002).
114. Iyer, V., Losavio, B.E. & Saggau, P. Compensation of spatial and temporal dispersion for acousto-optic multiphoton laser-scanning microscopy. *J. Biomed. Opt.* 8, 460–471 (2003).
115. Pawley, J.B. *Handbook of Biological Confocal Microscopy*, edn 2. (Plenum Press, New York, 1995).
116. Fan, G.Y. *et al.* Video-rate scanning two-photon excitation fluorescence microscopy and ratio imaging with cameleons. *Biophys. J.* 76, 2412–2420 (1999).
117. Nguyen, Q.T., Callamaras, N., Hsieh, C. & Parker, I. Construction of a two-photon microscope for video-rate Ca²⁺ imaging. *Cell Calcium* 30, 383–393 (2001).
118. Gauderon, R., Lukins, P.B. & Sheppard, C.J. Effect of a confocal pinhole in two-photon microscopy. *Microsc. Res. Technol.* 47, 210–214 (1999).
119. Oheim, M., Beaufort, E., Chaigneau, E., Mertz, J. & Charpak, S. Two-photon microscopy in brain tissue: parameters influencing the imaging depth. *J. Neurosci. Methods* 111, 29–37 (2001).
120. Egner, A., Jakobs, S. & Hell, S.W. Fast 100-nm resolution three-dimensional microscopy reveals structural plasticity of mitochondria in live yeast. *Proc. Natl. Acad. Sci. USA* 99, 3370–3375 (2002).
121. Tan, Y.P., Llano, I., Hopf, A., Wurriehausen, F. & Neher, E. Fast scanning and efficient photodetection in a simple two-photon microscope. *J. Neurosci. Methods* 92, 123–135 (1999).
122. Gratton, E., Breusegem, S., Sutin, J., Ruan, Q. & Barry, N. Fluorescence lifetime imaging for the two-photon microscope: time-domain and frequency-domain methods. *J. Biomed. Opt.* 8, 381–390 (2003).
123. Moreaux, L., Sandre, O. & Mertz, J. Membrane imaging by second-harmonic generation microscopy. *J. Opt. Soc. Am. B* 17, 1685–1694 (2000).
124. Peleg, G., Lewis, A., Linial, M. & Loew, L.M. Nonlinear optical measurement of membrane potential around single molecules at selected cellular sites. *Proc. Natl. Acad. Sci. USA* 96, 6700–6704 (1999).
125. Moreaux, L., Sandre, O., Blanchard-Desce, M. & Mertz, J. Membrane imaging by simultaneous second-harmonic generation and two-photon microscopy. *Opt. Lett.* 25, 320–322 (2000).
126. Millard, A.C., Jin, L., Lewis, A. & Loew, L.M. Direct measurement of the voltage sensitivity of second-harmonic generation from a membrane dye in patch-clamped cells. *Opt. Lett.* 28, 1221–1223 (2003).
127. Mohler, W., Millard, A.C. & Campagnola, P.J. Second harmonic generation imaging of endogenous structural proteins. *Methods* 29, 97–109 (2003).
128. König, K., So, P.T., Mantulin, W.W., Tromberg, B.J. & Gratton, E. Two-photon excited lifetime imaging of autofluorescence in cells during UVA and NIR photostress. *J. Microsc.* 183 (Pt 3), 197–204 (1996).
129. Koester, H.J., Baur, D., Uhl, R. & Hell, S.W. Ca²⁺ fluorescence imaging with pico- and femtosecond two-photon excitation: signal and photodamage. *Biophys. J.* 77, 2226–2236 (1999).
130. Hopf, A. & Neher, E. Highly nonlinear photodamage in two-photon fluorescence microscopy. *Biophys. J.* 80, 2029–2036 (2001).
131. Dittich, P.S. & Schulte, P. Photobleaching and stabilization of fluorophores used for single-molecule analysis with one- and two-photon excitation. *Appl. Phys. B: Lasers O* 73, 829–837 (2001).
132. Patterson, G.H. & Piston, D.W. Photobleaching in two-photon excitation microscopy. *Biophys. J.* 78, 2159–2162 (2000).
133. Neil, M.A. *et al.* Adaptive aberration correction in a two-photon microscope. *J. Microsc.* 200 (Pt 2), 105–108 (2000).
134. Booth, M.J., Neil, M.A. & Wilson, T. New modal wave-front sensor: application to adaptive confocal fluorescence microscopy and two-photon excitation fluorescence microscopy. *J. Opt. Soc. Am. A Opt. Image Sci. Vis.* 19, 2112–2120 (2002).
135. Marsh, P.N., Burns, D. & Girkin, J.M. Practical implementation of adaptive optics in multiphoton microscopy. *Opt. Express* 11, 1123–1130 (2003).
136. Brunner, F. *et al.* Diode-pumped femtosecond Yb:KGd(WO₄)₂ laser with 1.1-W average power. *Opt. Lett.* 25, 1119–1121 (2000).
137. Ilday, F.O., Lim, H., Buckley, J.R. & Wise, F.W. Practical all-fiber source of high-power, 120-fs pulses at 1 micron. *Opt. Lett.* 28, 1362–1364 (2003).
138. Jung, J.C. & Schnitzer, M.J. Multiphoton endoscopy. *Opt. Lett.* 28, 902–904 (2003).
139. Bird, D. & Gu, M. Two-photon fluorescence endoscopy with a micro-optic scanning head. *Opt. Lett.* 28, 1552–1554 (2003).
140. Ouzounov, D.G. *et al.* Delivery of nanjoule femtosecond pulses through large-core microstructured fibers. *Opt. Lett.* 27, 1513–1515 (2002).
141. Pastirk, I., Dela Cruz, J.M., Walowicz, K.A., Lazovoy, V.V. & Darius, M. Selective two-photon microscopy with shaped femtosecond pulses. *Opt. Express* 11, 1695–1701 (2003).
142. Williams, R.M. & Webb, W.W. Single granule pH cycling in antigen-induced mast cell secretion. *J. Cell Sci.* 113 (Pt 21), 3839–3850 (2000).
143. Kloppenburg, P., Zipfel, W.R., Webb, W.W. & Harris-Warrick, R.M. Highly localized Ca²⁺ accumulation revealed by multiphoton microscopy in an identified motoneuron and its modulation by dopamine. *J. Neurosci.* 20, 2523–2533 (2000).
144. Kleinfeld, D., Mitra, P.P., Helmchen, F. & Denk, W. Fluctuations and stimulus-induced changes in blood flow observed in individual capillaries in layers 2 through 4 of rat neocortex. *Proc. Natl. Acad. Sci. USA* 95, 15741–15746 (1998).

Control of Raman Lasing in the Nonimpulsive Regime

B. J. Pearson and P. H. Bucksbaum

FOCUS Center and Physics Department, University of Michigan, Ann Arbor, Michigan 48109-1120, USA
(Received 29 September 2003; published 18 June 2004)

We explore coherent control of stimulated Raman scattering in the nonimpulsive regime. Optical pulse shaping of the coherent pump field leads to control over the stimulated Raman output. A model of the control mechanism is investigated.

DOI: 10.1103/PhysRevLett.92.243003

PACS numbers: 33.80.-b, 42.50.-p

Since the advent of pulsed lasers, there has been extensive experimental and theoretical work on stimulated Raman scattering. More recently there has been a resurgence of interest in impulsive Raman scattering [1–4] due in part to the development of the field of learning coherent control [5–7], along with advances in ultrafast laser technology [8] and programmable pulse shaping [9,10]. In the impulsive regime, the laser bandwidth is large compared to the frequency of the Raman mode (typically a molecular vibration). In the time domain the pulse duration is short compared to the vibrational period, and one can shape the optical pulse to drive molecular mode(s) on resonance [11]. Alternatively, if the laser bandwidth contains photon pairs separated by the Stokes frequency, then the Raman gain can be seeded by the pump laser. Control of the Raman gain can be achieved by appropriately phasing colors in the pump pulse.

For the case of two-photon atomic absorption, this control mechanism has been described as the shaping of the nonlinear power spectrum of the driving field [12–14]. The idea has since been extended to multiphoton absorption in molecules [15,16], as well as vibrational Raman excitation in multimode molecular systems [11]. Here again analysis leads to an explanation of the control via the nonlinear power spectrum of the pump pulse.

In the nonimpulsive regime, the laser bandwidth is small compared to the frequency of the mode. Since there are no photon pairs separated by Stokes frequency in the pump pulse, the Stokes field must build up from spontaneous Raman scattering. This produces a Stokes field whose phase is random and cannot be controlled. Control may still be possible over the stimulated output spectrum or the final state populations in the presence of multiple Raman modes. Nonimpulsive control of the stimulated Raman spectrum in liquid methanol has been reported in experiments that used learning algorithms to discover the optimal driving field [17,18]. Here we demonstrate a possible mechanism for this control.

The details of our adaptive learning technique and laser system have been described previously [17]. In learning control experiments, the physical system is used to find the optimal driving field (pulse shapes) without prior knowledge of the Hamiltonian [5]. These solutions can be analyzed later to learn about the underlying

quantum dynamics. Briefly, our experiments use a shaped, ultrafast Ti:sapphire laser system as the excitation source. The laser pulses are shaped in an acousto-optic Fourier filter [10] interfaced with a computer. Our spectral bandwidth (4–5 THz) and pulse shaping characteristics provide temporal control over the pulses ranging from 100 fs to 5 ps in duration. Our adaptive learning algorithm determines the pulse shapes by optimizing a feedback signal derived from the Raman spectrum.

The system under investigation in these experiments is liquid phase methanol (CH_3OH). We focus on the two C-H stretch vibrational modes labeled *S* (2834 cm^{-1}) and *A* (2946 cm^{-1}) [19]. The experiments are performed in a 10 cm liquid cell, and the forward scattered Raman spectrum is collected and fed back to the algorithm. The learning algorithm is able to channel the gain into either of the two Raman modes. Although the algorithm finds a variety of pulse shapes that produce the desired effect, one class of solutions stands out. Figure 1 (inset) shows a representative pulse shape of this class of solutions in the

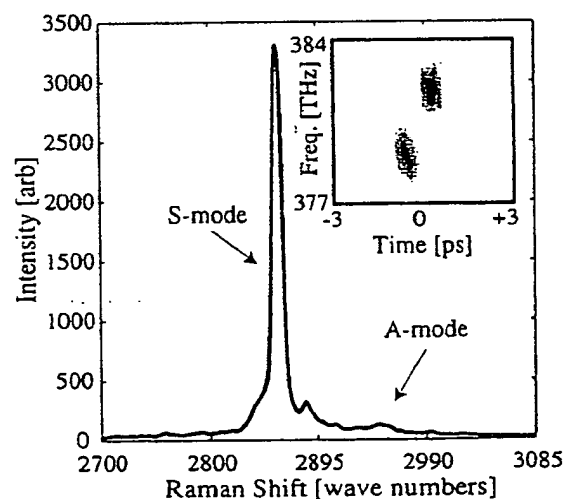


FIG. 1. Resulting Raman spectra obtained after optimization with the feedback algorithm. Inset shows a Husimi plot of the optimal "double-blob" pulse shape that led to *S*-mode excitation.

form of an optical Husimi distribution [20]. The Husimi plot is a two-dimensional convolution of the Wigner function [20–22] of the pulse shape that approximates the intensity distribution in both time and frequency. The optimal pulse shapes found by the algorithm consist of a pair of nearly transform-limited “blobs” that are separated by approximately 3.3 THz. This energy splitting matches the *S*-*A* mode spacing. Figure 1 shows the resulting Raman spectrum after excitation by the pulse shown in the inset of Fig. 1. The pulse produces strong selective excitation of the *S* vibrational mode.

These two-blob solutions suggest a quasi-impulsive model for the interaction, where the pump field directs the Raman gain through a coherent coupling between the two modes [17]. This coherence modulates the intensity envelope of the pulse. The modulation is apparent in the Wigner distribution, but has only a minimal effect on the Husimi distribution (Fig. 2).

In order to study the effect of the phase offset, we excite the molecules with the original pulse shape shown in Fig. 2. We then collect the stimulated Raman spectra as the phase offset between the two blobs is varied from 0 to π . Figure 3 shows the stimulated Raman output spectrum for several different phase offsets. As the offset is varied, the Raman gain oscillates between the two different Stokes modes. As is to be expected, this single parameter control is not as effective at mode selection as the full learning algorithm (see Fig. 1). Nevertheless, control is achieved by varying only the phase offset. Care was taken to adjust the laser intensity to avoid saturation of the Raman gain, since this leads to significant changes in the observed control.

A simple model that predicts the observed effect can be constructed by expanding on previous work on single mode Raman scattering. The theory governing stimulated Raman gain of a single active mode under excitation by an off-resonant pump pulse has been developed both semi-classically [23] and quantum mechanically [24,25]. In the

quantum case, the Stokes field in the nonimpulsive regime is generated by spontaneous fluctuations of the Raman polarizability. A number of approximations can be made to reveal the underlying physics. In the standard treatment, one assumes one-dimensional, plane-wave pulse propagation in the slowly varying envelope approximation (SVEA), and the calculation is performed in the transient regime where damping can be neglected. The pulse durations (0.1 to 1 ps) imply that the SVEA is valid. The assumption of transient scattering may be an oversimplification because the pulse lengths approach the decoherence times of the C-H vibrations [26]. With these simplifications, the interaction can be reduced to a set of coupled differential equations describing the propagation along \hat{z} of three fields inside the medium [27]:

$$\frac{\partial}{\partial x} \epsilon_L = -q \epsilon_S, \quad (1)$$

$$\frac{\partial}{\partial x} \epsilon_S = q^* \epsilon_L, \quad (2)$$

$$\frac{\partial}{\partial \tau} q = \frac{1}{4} \epsilon_L \epsilon_S^*. \quad (3)$$

In these equations, ϵ_L is the pump laser field, ϵ_S is the Stokes field, and q is the molecular polarizability. The independent variables $x \propto z$ and $\tau \propto (t - z/c)$ are the reduced space-time coordinates.

We have extended this treatment to include two vibrational Raman modes which, in addition to the original coupling to the same ground state, are Raman coupled to each other through two-photon transitions driven by the

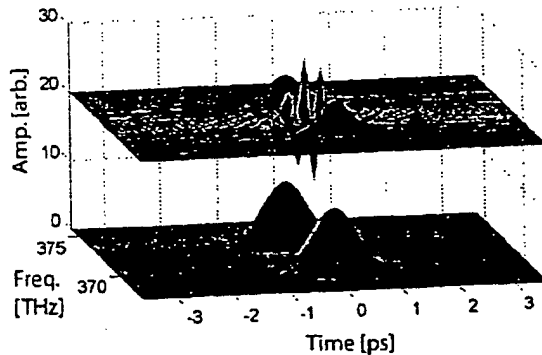


FIG. 2. Calculated Wigner plots for double-blob pulse used in the experiment when the phase offset between the blobs is equal to π . The lower plot is the Husimi distribution when the phase offset is zero.

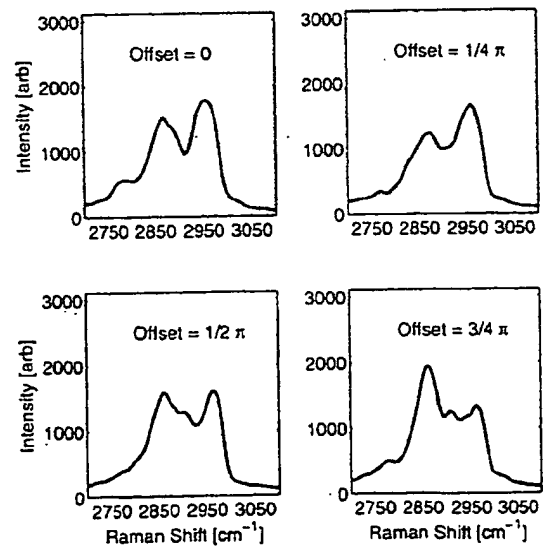


FIG. 3 (color online). Stimulated Stokes output as a function of the Raman shift from the central frequency of the pump pulse. The different panels show the output spectra for various phase offsets. The gain oscillates between the *S* and *A* modes.

applied pump field or the generated Stokes fields. The relevant energy levels are shown in Fig. 4, where $|e1\rangle$ and $|e2\rangle$ are the first excited levels of the two vibrational modes. Equations (4)–(9) are the modified equations governing the optical fields and molecular polarizabilities in the case of two modes,

$$\frac{\partial}{\partial x} \epsilon_L = -\epsilon_{S1} q_1 - \epsilon_{S2} q_2 - \frac{1}{4} \epsilon_L q_3 + \frac{1}{4} \epsilon_L q_3^*, \quad (4)$$

$$\frac{\partial}{\partial x} \epsilon_{S1} = \epsilon_L q_1^* + \frac{1}{4} \epsilon_{S2} q_3^*, \quad (5)$$

$$\frac{\partial}{\partial x} \epsilon_{S2} = \epsilon_L q_2^* - \frac{1}{4} \epsilon_{S1} q_3, \quad (6)$$

$$\begin{aligned} \frac{\partial}{\partial \tau} q_1 = & -\epsilon_L \epsilon_{S1}^* w_1 - i\alpha \epsilon_L \epsilon_L^* q_2 - i\epsilon_L \epsilon_{S2}^* q_3 \\ & - i\epsilon_{S2} \epsilon_{S1}^* q_2, \end{aligned} \quad (7)$$

$$\begin{aligned} \frac{\partial}{\partial \tau} q_2 = & -\epsilon_L \epsilon_{S2}^* w_2 + i\alpha \epsilon_L \epsilon_L^* q_1 - i\epsilon_L \epsilon_{S1}^* q_3 \\ & + i\epsilon_{S1} \epsilon_{S2}^* q_1, \end{aligned} \quad (8)$$

$$\begin{aligned} \frac{\partial}{\partial \tau} q_3 = & i\epsilon_{S2} \epsilon_L^* q_1 + i\epsilon_L \epsilon_{S1}^* q_2 - \epsilon_L \epsilon_L^* (w_1 - w_2) \\ & - \epsilon_{S2} \epsilon_{S1}^* (w_1 - w_2). \end{aligned} \quad (9)$$

In these equations, the q_i 's are the molecular coherences for the Raman-active transitions, the w_i 's represent the population inversion in each of the two modes, and α is a constant that describes the relative strength of the additional Raman coupling. Specifically, we include the quasi-impulsive pump-pump coupling, where the relative phase, ϕ_L , appears implicitly in the terms containing

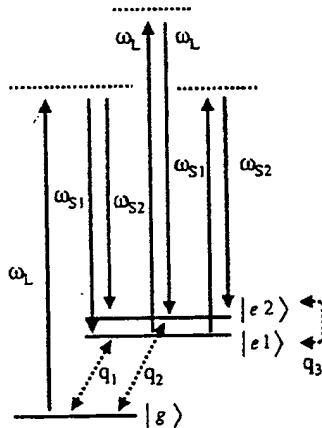


FIG. 4. Energy level diagram with two Raman-active vibrational modes. The three levels are Raman coupled by the pump (ω_L) and Stokes (ω_{S1} and ω_{S2}) fields. The interaction generates coherences between pairs of the three levels (q_1 , q_2 , and q_3). An additional interaction is included by allowing a two-photon Raman coupling between the two excited vibrational states driven by either the applied pump field or the generated Stokes fields.

$\epsilon_L \epsilon_L^*$. Finally, although substantial energy conversion between pump and Stokes fields is possible, the populations of the excited states in our experiments are always much less than the ground state, so terms in the calculation involving the off-diagonal coupling between the two excited states (q_3) may be suppressed.

In order to compare our model to the experimental results, we numerically integrate the set of coupled differential equations that describe the propagation of the fields inside the medium [see Eqs. (4)–(9)]. We set the amplitudes of the initial coherences (q_1 and q_2) to be small random numbers, which in turn determine the initial values of the Stokes phases ϕ_{S1} and ϕ_{S2} . The equations are integrated over an interaction region comparable to the experimental conditions. At the end of the interaction length we calculate the total energy contained in each of the Raman fields as we vary the phase offset ϕ_L in our model pump pulse.

We expect the initial phases of the Stokes fields to be random because they build up from spontaneous scattering. The stimulated Stokes field emerging from the methanol cell is clearly multimode, based on its angular divergence and far field appearance. When the excitation volume corresponds to a large value of the Fresnel number ($F = A/\lambda_S L$), such multiple spatial modes are excited, leading to a large number of independent stimulated Raman scattering processes in each laser shot [28,29].

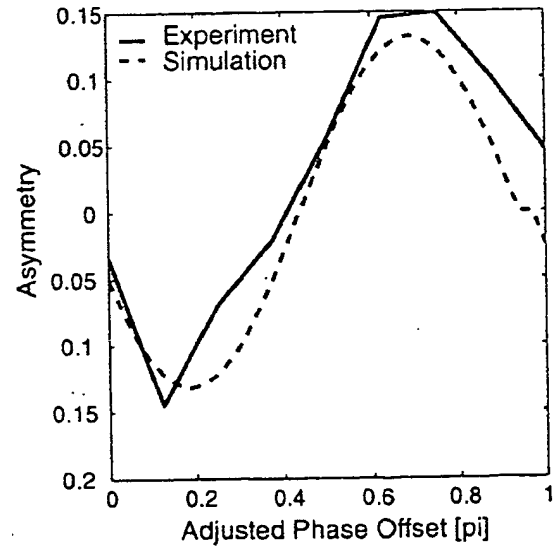


FIG. 5 (color online). Variation in mode excitation as a function of phase shift between the two spectral regions for both experiment (solid line) and simulation (dashed line). The vertical axis plots the difference in the mode excitation divided by the sum. The simulation results have been adjusted to the data using two parameters: the initial phase of the field and the coupling strength between the two excited states.

The high number of spatial modes implies multiple sets of initial phases for the two different Stokes frequencies on every laser pulse. Therefore we perform the integration over many trials of random initial amplitudes of the coherences q_1 and q_2 (using a white Gaussian noise about zero). The control comes from the $\epsilon_L \epsilon_L^*$ terms in the equations for the temporal derivatives of q_i . The physical picture is that the pump pulse drives the coherences q_i , which in turn drive the Stokes modes ϵ_{S1} and ϵ_{S2} . Changing the value of ϕ_L in the equations changes which mode receives a positive contribution and which receives a negative contribution. When the phase offset ϕ_L goes through $\pi/2$, the roles of the two modes switch.

We define the mode asymmetry as the ratio of the difference in energy between the two modes divided by the sum of the energy in the two modes. Although for a given initial pair (q_1, q_2) the mode asymmetry can take on any value between ± 1 , on average one of the modes is preferentially excited at each value of ϕ_L . Figure 5 shows the effect of mode switching for the results from both the experiment and simulation. The mode asymmetry is plotted along the vertical axis. We find that both the experiment and simulation show a variation in mode excitation with similar periods. The simulation results have been adjusted to the data using two parameters: the pump-pump Raman coupling strength (α) and the initial phase offset ϕ_L . The depth of modulation in the asymmetry increases as the Raman coupling strength increases (the plot shows the result with $\alpha = 7$). Changing the phase offset ϕ_L simply shifts the phase of the modulation. The phase offset in the experiment is unknown due to pulse propagation effects within the liquid. The mode control was relatively insensitive to the other parameters of the model, which were set to approximate experimental values of the Raman threshold.

In conclusion, we have demonstrated mode selection in stimulated Raman scattering in liquid methanol through control of the coherence of the pump laser. Control is possible even though the pump laser bandwidth is insufficient to seed the Stokes waves. Using our feedback control results as a starting point, we have constructed a simple model of the process that could explain the effect. The control in our model comes from the Raman coupling of the two excited modes by the pump laser.

We acknowledge Chitra Rangan, Paul Berman, and Bruce Shore for helpful discussions regarding the simulations. This work is supported by the National Science Foundation under Grant No. 9987916.

- [1] Y.-X. Yan, E. B. Gamble, Jr., and K. A. Nelson, *J. Chem. Phys.* **83**, 5391 (1985).

- [2] A. M. Weiner, D. E. Leaird, G. P. Wiederrecht, and K. A. Nelson, *Science* **247**, 1317 (1990).
 [3] A. Nazarkin and G. Korn, *Phys. Rev. A* **58**, R61 (1998).
 [4] R. A. Bartels, T. C. Weinacht, S. R. Leone, H. C. Kapteyn, and M. M. Murnane, *Phys. Rev. Lett.* **88**, 033001 (2002).
 [5] R. Judson and H. Rabitz, *Phys. Rev. Lett.* **68**, 1500 (1992).
 [6] W. S. Warren, H. Rabitz, and M. Dahleh, *Science* **259**, 1581 (1993).
 [7] H. Rabitz, R. de Vivie-Riedle, M. Motzkus, and K. Kompa, *Science* **288**, 824 (2000).
 [8] S. Backus, C. G. Durfee III, M. M. Murnane, and H. C. Kapteyn, *Rev. Sci. Instrum.* **69**, 1207 (1998).
 [9] M. M. Wefers and K. A. Nelson, *Opt. Lett.* **20**, 1047 (1995).
 [10] J. X. Tull, M. A. Dugan, and W. S. Warren, *Adv. Magn. Opt. Res.* **20**, 1 (1997).
 [11] T. C. Weinacht, R. Bartels, S. Backus, P. H. Bucksbaum, B. Pearson, J. M. Geremia, H. Rabitz, H. C. Kapteyn, and M. M. Murnane, *Chem. Phys. Lett.* **344**, 333 (2001).
 [12] D. Meshulach and Y. Silberberg, *Nature (London)* **396**, 239 (1998).
 [13] P. H. Bucksbaum, *Nature (London)* **396**, 217 (1998).
 [14] D. Meshulach and Y. Silberberg, *Phys. Rev. A* **60**, 1287 (1999).
 [15] K. A. Walowicz, I. Pastirk, V. V. Lozovoy, and M. Dantus, *J. Phys. Chem. A* **106**, 9369 (2002).
 [16] V. V. Lozovoy, I. Pastirk, K. A. Walowicz, and M. Dantus, *J. Chem. Phys.* **118**, 3187 (2003).
 [17] B. J. Pearson, J. L. White, T. C. Weinacht, and P. H. Bucksbaum, *Phys. Rev. A* **63**, 063412 (2001).
 [18] B. J. Pearson, D. S. Morris, T. C. Weinacht, and P. H. Bucksbaum, in *Femtochemistry and Femtobiology: Ultrafast Dynamics in Molecular Science*, edited by A. Douhal and J. Santamaria (World Scientific, Singapore, 2002), pp. 399–408.
 [19] T. Shimanouchi, *Tables of Molecular Vibrational Frequencies: Consolidated Vol. 1* (National Bureau of Standards, Washington, DC, 1972).
 [20] M. Hillery, R. F. O'Connell, M. O. Scully, and E. P. Wigner, *Phys. Rep.* **106**, 121 (1984).
 [21] L. Cohen, *Proc. IEEE* **77**, 941 (1989).
 [22] J. Paye, *IEEE J. Quantum Electron.* **28**, 2262 (1992).
 [23] R. L. Carman, F. Shimizu, C. S. Wang, and N. Bloembergen, *Phys. Rev. A* **2**, 60 (1970).
 [24] M. G. Raymer and J. Mostowski, *Phys. Rev. A* **24**, 1980 (1981).
 [25] M. G. Raymer and I. A. Walmsley, *Progress in Optics* (North-Holland, Amsterdam, 1990), Vol. XXVIII, pp. 181–270.
 [26] L. K. Iwaki and D. D. Dlott, *Chem. Phys. Lett.* **321**, 419 (2000).
 [27] M. Lewenstein, *Z. Phys. B* **56**, 69 (1984).
 [28] M. G. Raymer, I. A. Walmsley, J. Mostowski, and B. Sobolewska, *Phys. Rev. A* **32**, 332 (1985).
 [29] M. Scalora and J. W. Haus, *Opt. Commun.* **87**, 267 (1992).

Coherent control of the population transfer in complex solvated molecules at weak excitation. An experimental study

Valentyn I. Prokhorenko,^{a)} Andrea M. Nagy, and R. J. Dwayne Miller
*Department of Chemistry, University of Toronto, 80 Saint George Street, M5S3H6,
Toronto, Ontario, Canada*

(Received 12 November 2004; accepted 15 February 2005; published online 6 May 2005)

We performed a series of successful experiments for the optimization of the population transfer from the ground to the first excited state in a complex solvated molecule (rhodamine 101 in methanol) using shaped excitation pulses at very low intensities (1 absorbed photon per 100–500 molecules per pulse). We found that the population transfer can be controlled and significantly enhanced by applying excitation laser pulses with crafted pulse shapes. The optimal shape was found in feedback-controlled experiments using a genetic search algorithm. The temporal profile of the optimal excitation pulse corresponds to a comb of subpulses regularly spaced by ~ 150 fs, whereas its spectrum consists of a series of well-resolved peaks spaced apart by approximately 6.5 nm corresponding to a frequency of 220 cm^{-1} . This frequency matches very well with the frequency modulation of the population kinetics (period of ~ 150 fs), observed by excitation with a short (~ 20 fs) transform-limited laser pulse directly after excitation. In addition, an antioptimization experiment was performed under the same conditions. The difference in the population of the excited state for the optimal and antioptimal pulses reaches $\sim 30\%$ even at very weak excitation. The results of optimization are reproducible and have clear physical meaning. © 2005 American Institute of Physics. [DOI: 10.1063/1.1886750]

I. INTRODUCTION

During the past decade, coherent control of the light-driven chemical reactions and molecular processes has been successfully applied to different objects and under different conditions (e.g., see recent reviews^{1,2} and references therein). Appropriate shaping of the excitation laser pulse can significantly enhance the product yield by selective population of a particular state (a target) from which the photochemical reaction occurs.^{3–5} Based on the paradigm that the “molecule knows its own Hamiltonian much better than any of its observers,” a feedback-controlled learning procedure for experimentally solving the Schrödinger equation in real time was originally formulated and proposed by Judson and Rabitz.⁶ Using an evolutionary algorithm for the learning process combined with an appropriate pulse shaper,⁷ a stable optimal solution can be achieved without any preliminary knowledge about the system which is the subject for optimization. Intrinsic information about the subject of optimization can be further recovered by examining the time- and phase-profiles of the optimal pulse.

This approach has been applied to many molecules and molecular complexes in the gas phase and liquid phase,^{1,8–11} including also some natural biological systems^{12,13} as well. However, most experimental and theoretical investigations in this new “laser-optimizing” field of femtochemistry were and are still dedicated to the interactions with strong laser pulses,

where the saturation effects in the population of excited states^{14,15} and multiphoton processes¹⁶ play an essential and sometimes key role.

In contrast to coherent control applications in femtochemistry and related fields, in natural photoactive systems like photosynthetic units and light receptors, the light-driven reactions occur at very low intensities (sunshine) where only one photon per many molecules is absorbed per event. Therefore, it is important to establish whether or not it is possible to control target states under low excitation conditions. In this limit, the methodologies of coherent control of actinic light can be used to manipulate the light-harvesting efficiency or other examples such as the visual response to explore fundamental issues related to the roles of phase coherence and coherent information flow in the light-driven processes occurring in nature.

To answer this question, we took the simplest first step and investigated experimentally the possibility of controlling the population transfer (from the ground to the first excited electronic state) in complex solvated molecules at very low excitation, where only 1 of 100–500 molecules absorb a photon during the excitation cycle. It is quite clear that if we are able to control the $S_0 \rightarrow S_1$ population transfer under certain restrictions, we will also be able to explicitly use phase to control primary events in other photoactive systems as the excited state serves as the doorway state to all subsequent dynamical pathways. This concept can be readily extended to biological systems, for example, to gain control over the efficiency of energy transfer in photosynthetic antennae and as a consequence, the efficiency of the light harvesting in natural photosystems. Recent studies have shown some degree of

^{a)}Author to whom correspondence should be addressed. Electronic mail: prokh@lphys.chem.utoronto.ca

control in this regard.¹³ However, only the quenching of energy transfer was observed such that constructive interference was not established. In addition this study was conducted at relatively high excitation conditions. To our knowledge, the present study is the first experimental investigation of the coherent control of population transfer in molecules under weak excitation conditions.

The present paper is organized as follows. In the Experiment section we describe in detail our recently developed femtosecond laser spectrometer, combined with a pulse shaper, and experimental conditions. For performing the optimization experiments we have chosen the pump-probe technique which allows direct monitoring of the excited-state population at a given delay between the excitation and probe pulses. In addition, the wavelength- and time-resolved pump-probe spectra deliver valuable information about the population kinetics which is extremely important for understanding the physical processes responsible for the control of the population transfer efficiency. In Sec. III we describe and analyze our experimental observations. The core of this section is focused on the temporal-, spectral- and coherent properties of the excitation pulses obtained from optimization experiments (for both maximization and minimization scenarios). We specifically discuss the sensitivity of the population transfer to the phase information, contained in the optimal/antioptimal pulses, using results of suitable control experiments. Results of the bleaching experiments (power dependence of the bleaching induced with the different pulse shapes) indicate that the efficiency of population transfer in complex solvated molecules can be controlled at very low excitation, even at excitation levels as low as 1 excited state per 500 molecules. In addition, very unusual pump-probe kinetics obtained by excitation with the optimally shaped pulses is discussed. In Sec. IV we summarize our results and observations.

II. EXPERIMENT

The coherent control experiments have been carried out using a recently developed advanced femtosecond laser spectrometer combined with a laser-pulse shaper. The optical outline of the setup is shown schematically in Fig. 1. The details are as follows.

A. Laser system

A femtosecond laser source (FLS) which pumps the non-collinear optical parametric amplifier (NOPA) consists of a mode-locked erbium-doped fiber seed laser (Clark-MXR, USA), a stretcher, a home-built titanium-sapphire regenerative amplifier pumped by an in-house-developed frequency-doubled neodymium-doped yttrium lithium fluoride (Nd:YLF) *Q*-switched laser, and a compressor. The FLS delivers 140-fs laser pulses at 775 nm with a repetition rate of 1 kHz and an average power of 300 mW. This beam was used to pump a NOPA (Ref. 17) that was significantly improved in design with respect to the energetic and beam-pointing stability of the generated light. The NOPA produces femtosecond light pulses with a broad spectrum [65 nm full width at half maximum (FWHM)] centered at 575 nm, which

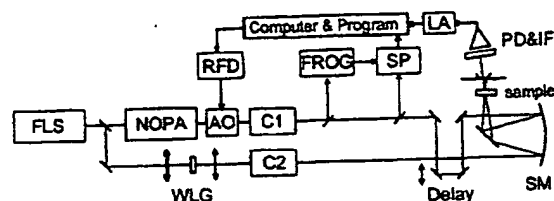


FIG. 1. Experimental setup for performing the pump-probe and coherent control experiments. Here FLS-femtosecond laser source (pulses at 775 nm having 140-fs duration with a repetition rate of 1 kHz), NOPA-tunable non-collinear optical parametric amplifier, AO-acousto-optic modulator driven by a programmable radio-frequency driver (RFD) (the pulse shaper), WLG-white-light generator, C1 and C2-pulse compressors, FROG-frequency-resolved optical gating setup [for details, see Fig. 2(a)], SP-spectrometer, SM-spherical mirror with a focal length of 15 cm, PD and IF-photodiode with interference filter (setup is shown in the configuration adapted for coherent control experiments) and, LA-lock-in amplifier synchronized to the AO.

can be compressed to a pulse duration of 10 fs. With an output power of 5 mW (technical efficiency of 15% with respect to the second harmonic of the incident beam) a short-term stability of 1.5% was achieved with a pump source instability of 1.2%, and the long-term stability was $\sim 2\%$ over a period of 3 h. High stability of the excitation beam is crucial for the successful implementation of coherent control experiments as the measurements typically take 1 h to perform. The measurement photodiodes were calibrated using a power meter (FieldMaster, Coherent, USA).

A small portion of the FLS beam was directed to the white light generator (WLG) consisting of a 2-mm-thick sapphire plate placed between focusing ($f=7$ cm) and collimating ($f=3$ cm) lenses. A spectral chirp of the white light was removed in the range of 520–650 nm after passing the compressor C2 (eight reflections between two chirped mirrors from R&D Laser Optics, Hungary). The spectral distribution of the generated white light was nearly flat in this spectral window. This light was used as a probe beam with a spectral density of ~ 20 pJ/nm at the sample. Compressing the white light significantly improves the resolution of pump-probe measurements and removes the artifacts which are usually present in transient absorption spectra measured with chirped probe pulses.¹⁸

B. Pump-probe and coherent control setup

Figure 1 shows the configuration of the pump-probe spectrometer adapted for performing the coherent control experiments. The excitation pulse shapes were controlled by changing both phase and amplitude distributions of the spectrum of a traveling pulse (generated from the NOPA) in an acousto-optic (AO) modulator (Dazzler, model 1.0/800, Fastlite, France), driven by a programmable radio-frequency driver (RFD). The large intrinsic dispersion introduced by the acousto-optic crystal (TeO_2) was compensated using a double-pass prism compressor C1 with the SF11 prisms separated by 35 cm. Effective control of the pulse shape by varying the amplitude and phase of the pulse spectrum (centered at 575 nm) was limited by the acousto-optic modulator to a 50-nm window.

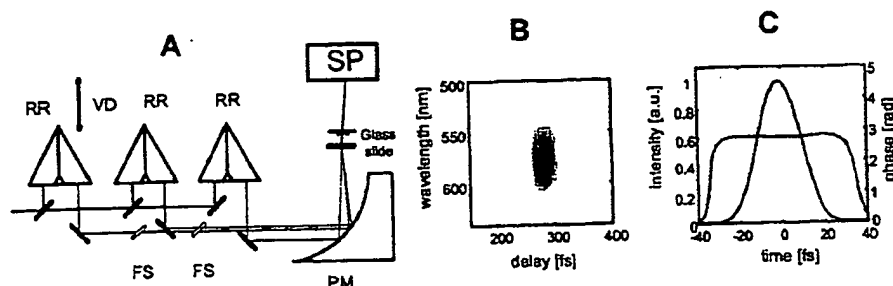


FIG. 2. (a) FROG setup used for the laser-pulse characterization: RR-hollow retroreflectors, VD-variable delay, FS-thin fused silica plates for chirp compensation of the beam splitters, PM-off-axis parabolic mirror (focal length of 5 cm), and SP-spectrometer. (b) FROG trace of transform-limited excitation pulses, passed through the acousto-optic modulator (see text for details). (c) Retrieved intensity and phase profiles (23 fs FWHM pulse duration).

Both pump and probe beams were focused into a 200- μm flow cell (glass windows with 100- μm thickness) by a spherical mirror (SM) with a focal length of 15 cm. The spot diameter was estimated to be 150 μm . The probe beam transmitted through the sample was filtered by an interference filter (IF) (centered at 580 nm; spectral width of 10 nm) and measured with a photodiode (PD) using a lock-in amplifier (model SRS830, Stanford Research Systems, USA). For modulation of the pump beam the same acousto-optic modulator was used with a specially designed electronic circuit (a commutator). The delay between the pump and probe pulses was controlled using a motorized translation stage with a resolution of 1 fs (Nanostep, model 17NST104, Melles Griot, USA). The spectra of the excitation pulses were measured using a spectrometer with a resolution of 1.3 nm (Sciencetech, model 9057, 300 /mm grating, Canada) with a fast photodiode array sensor (S3902, Hamamatsu, Japan). The spectral response of the spectrometer and sensor was calibrated using a halogen lamp with known spectral distribution. For performing pump-probe measurements, the probe beam after the sample was directed to the spectrometer, and the pump intensity was measured using a photodiode in combination with the lock-in amplifier. The number of spectra measured per second (20) was limited due to the relatively low sampling rate of the analog-to-digital converter (ADC) card (AT-MIO-16XE-50, National Instruments, USA). However, with an accumulation time of 1 s per delay step, the accuracy of the pump-probe measurements was about of 0.4 m-OD (optical density) ($\Delta A = 4 \times 10^{-4}$, where A is absorbance).

The instrument response function was measured as a cross correlation between the excitation and probe pulses using sum frequency generation in a 25- μm -thick BBO crystal, placed on the sample position. In the wavelength range of 520–640 nm, the FWHM of the cross correlation was 35–40 fs for an excitation pulse of 23-fs FWHM (see below), thus the duration of the probe pulse after the compressor C2 can be estimated to be ~ 30 fs.

C. Pulse characterization

For measurement and characterization of the temporal profiles of the tailored excitation pulses a frequency-resolved optical gating¹⁹ (FROG) technique has been applied. The optical layout of a home-built, compact, and portable FROG setup, based on the third-order nonlinear response, is shown

schematically in Fig. 2(a). For the nonlinear medium, a thin (100 μm) glass slide was used. The spectrum of the diffracted beam was measured using the same spectrometer and photodiode array sensor. The sensitivity of the FROG setup was measured to be 1.5 MW with a corresponding time resolution of ~ 5 fs. For reconstructing the intensity and phase profiles of the investigated laser pulses a commercial program, FROG 3.0 (Femtosoft Technologies, USA), was applied. Figure 2(b) displays a typical FROG trace of the transform-limited pulse, passed through the pulse shaper adjusted for a central wavelength of 575 nm (and 50-nm window). Figure 2(c) shows the retrieved intensity and phase profiles.

D. Sample and experimental conditions

For performing the experiments, we have chosen the xanthene dye rhodamine 101 as a model compound, dissolved in methanol (R101/MeOH). The R101 has nitrogen atoms rigidly linked to the xanthene skeleton. The rigid, planar, molecular structure favors an extremely high fluorescence quantum yield ($\approx 100\%$ for ethanol over a wide temperature range)²⁰ and a relatively long lifetime of the S_1 excited state; $T_1 = 5$ ns. In polar solvents like methanol, the carboxyl group (COOH) participates in the acid-base equilibrium (COO^- and H^+). Absorption and fluorescence spectra have been measured using a Perkin-Elmer UV/VIS spectrophotometer (model Lambda-2, Germany) and a Perkin-Elmer fluorimeter (model LS50B, UK), respectively. Corresponding spectra are plotted in Fig. 6. The optical density (absorbance) for the 200- μm cell was 0.6 at the absorption spectrum maximum (568 nm). All experiments have been carried out under “magic angle” conditions (54.7° between the pump and probe polarization vectors) at room temperature. The excitation energy was typically ~ 5 nJ corresponding to an excitation photon density of 8×10^{13} photons/ cm^2 /pulse. For a closed two-level system in the impulsive limit (the laser pulse is much shorter than the T_1 decay) the bleaching saturation energy²¹ is $E_{\text{sat}}(\lambda) = [\sigma_{01}(\lambda) + \sigma_{10}(\lambda)]^{-1}$,^{23,24} where σ_{01} and σ_{10} are the absorption and excited-state emission cross sections, respectively, and λ is the wavelength. The profiles of the absorption/emission cross sections correspond to absorption/emission spectra (see Fig. 6), and the magnitude of σ is related to the extinction coefficient ϵ as $\sigma_{01} = 3.86 \times 10^{-21} \epsilon$. For R101, $\epsilon = 9 \times 10^4 \text{ l mol}^{-1} \text{ cm}^{-1}$.²⁵ Assuming equal magnitudes for the absorption and emission transition dipole moments, we have

$E_{\text{sat}}(575) = 2.06 \times 10^{15} \text{ cm}^{-2}$, thus the excitation level used in these experiments is approximately 27 times lower than the characteristic saturation level. At these conditions only 1 molecule out of 100 absorbs a photon during the laser pulse. We can safely exclude any multiphoton process. The magnitude of induced bleaching $-\Delta A$ was typically in the range of 20–50 m-ODs (i.e., less than 10% of the initial absorbance). An excitation energy dependence was conducted in which the bleaching dependence was found to be linear with a correlation coefficient of $R=0.999$ up to $\Delta A=-100$ m-OD.

E. Software

For performing the various measurements (pump probe, pulse characterization, bleaching dependence, etc.) and coherent control experiments a set of programs was developed. These programs are based on the MATLAB shell, and corresponding hardware drivers have been developed using C-language and a low-level National Instruments data acquisition (DAQ) library. The efficiency of the MATLAB was particularly important in creating the programs for the coherent control experiments where a learning algorithm (usually a genetic search of the optimal pulse shape) should be incorporated into the program core. For this application a genetic algorithm toolbox, developed at the Department of Automatic Control and Systems Engineering, University of Sheffield (United Kingdom), was chosen.

F. Protocol of coherent control experiments

The feedback signal for the optimization search was the magnitude of bleaching (the target), measured using a delayed probe pulse at 580 nm. Initially the optimization starts from a set of pulses (initial population of 30–50 members) having randomly distributed amplitudes and phases in the wavelength space. For each pulse the magnitude of bleaching ΔA is measured sequentially. Due to the relatively large spectral width of the excitation pulses (50 nm) the measured signal ΔA is sensitive not only to the particular pulse shape but also to the spectral overlap of the pulse spectrum with the absorption spectrum of the sample. Therefore, in parallel to measuring the bleaching signal, the system measures simultaneously also the spectrum of the particular pulse. After overlapping this spectrum with the transmission spectrum of the sample, the energy of the excitation pulse absorbed in the sample is calculated as $E_{\text{abs}} \propto \int I(\lambda)[1 - T(\lambda)]d\lambda$, where $I(\lambda)$ is the spectral profile of the excitation pulse, and $T(\lambda) = 10^{-A(\lambda)}$ is the transmission of the sample. The measured magnitude of bleaching then is normalized to the absorbed energy E_{abs} , and a selection of pulses leading to the maximal normalized bleaching (or minimal normalized bleaching in experiments for minimization of the population transfer) occurs according to genetic rules. This normalizing removes the particular spectral dependence of the measured optimization signal and makes the selection process (and coherent control experiment) very robust and reproducible.

After the breeding of selected "individuals" (i.e., chromosome files corresponding to selected pulses) and applying mutation steps, the normalized bleaching is measured again for the offspring with subsequent reinsertion steps into the

current population. This loop is repeated for producing new generations until a convergence is achieved such that the measured bleaching for new generations remains constant within the accuracy of measurements (typically 0.5%–0.7% of the bleaching magnitude). A more detailed description of this algorithm can be found in documentation for the used genetic algorithm toolbox (available on the website <http://www.shef.ac.uk/gaipp/ga-toolbox/manual.pdf>).

In the reported experiments the control space was limited to 50 nm with a resolution of 2 nm for both phase and amplitude spectra, the amplitude resolution was 6 bits, and phase space was $[-2\pi, +2\pi]$. This gives a total chromosome length of 300 bits.

III. RESULTS AND DISCUSSION

A. Pump-probe kinetics in R101/MeOH by excitation with transform-limited pulses

In order to explore the detailed kinetics of the population transfer under impulsive excitation, we measured the differential absorption spectra $\Delta A(\lambda, \tau) = A^*(\lambda, \tau) - A_0(\lambda)$ in the 450–650-nm spectral window using a short, transform-limited excitation pulse [23 fs FWHM; see Figs. 2(a) and 2(b) for details] centered at 575 nm which corresponds to the absorption maximum of R101 in methanol. Figure 3(a) displays a three-dimensional (3D) plot of the population evolution $\Delta A(\lambda, \tau)$ during the first 2 ps after excitation. As can be seen, a prompt excitation leads to the appearance in the population kinetics of periodical oscillations which can be better seen in Fig. 3(b) (2D) (two-dimensional plot for the first 500-fs delay).

The phase of the oscillations shows a wavelength dependence which can be directly observed in Fig. 3(b) by comparing, e.g., traces at 580 and 600 nm. The period of the oscillations is ~ 150 fs and they decay within a characteristic decay time of ~ 900 fs [Fig. 4(a)]. The inset there shows the Fourier spectrum of the oscillations which have a central frequency of 214 cm^{-1} . Within the instrumental resolution of ~ 35 fs we can resolve vibrational modes up to $\sim 800 \text{ cm}^{-1}$; however, only oscillations around 214 cm^{-1} have been observed. During the first ~ 100 fs after excitation, the central position of the differential absorption spectrum (position of the maximal bleaching) moves rapidly to the red side of the spectrum [see Figs. 3(b) and 4(b)] with a characteristic speed of $2 \text{ nm}/10 \text{ fs}$ (standard deviation of $\pm 30\%$). This fast red-shift reflects the dynamic Stokes shift caused by solvation dynamics. In the recent study of Dao²⁶ a similar magnitude of the spectral diffusion ($1.3 \text{ nm}/10 \text{ fs}$) was found for the xanthene dyes (including R101/MeOH) using a two-color transient grating technique.

The appearance of oscillations (quantum beats) in pump-probe experiments reflects the contribution of the vibrational states excited by short pulses. This well-known effect has previously been explored both experimentally and theoretically (e.g., see Refs. 27 and 28). Very short laser pulses (as compared to the nuclear time scale) "kick" nuclear modes in a molecule and set off initially coherent oscillations of the corresponding vibrational states. Due to damping and vibrational dephasing, these oscillations disappear after ~ 1 ps in

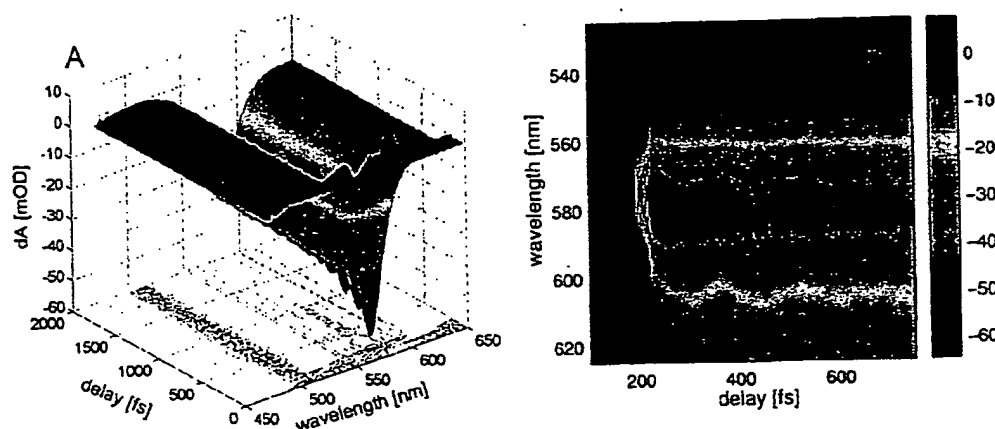


FIG. 3. (Color) (a) 3D plot of population kinetics in R101/MeOH excited by a 23-fs pulse. (b) 2D plot for the first 500-fs delay (zero delay between pump and probe pulses corresponds to 200 fs on this time base).

our case. The first events in the population kinetics are illustrated in Fig. 4(b), where the differential absorption spectra are plotted for different delays. Remarkably, the evolution of the spectrum is complete approximately 1.2 ps after excitation, after which time the shape of the spectrum remains unchanged (only the amplitude decreases with increasing delay due to a slow T_1 decay, i.e., population relaxation). Therefore, the coherent control experiments have been performed at longer delays (typically 5 ps after excitation), where we can safely assume full relaxation of the vibrational dynamics and exclude any contribution of the dephasing processes to the response.

B. Optimization of the population transfer

Our first optimization experiments were performed at a 2-ps delay after the "zero time point" (reported in Ref. 29); however, it was found that the optimal pulse is stretched over a time range of several hundreds femtoseconds. Thus, all following experiments were performed at longer delays, normally at 5 and 50 ps. Figure 5 shows a typical evolution of the population transfer optimization, monitored 5 ps after excitation. In these particular experiments, the bleaching

magnitude was maintained around 30–50 m-OD. The starting population was 30 members, and the probability of recombination was set to 0.7.

As can be seen, the maximization of the excited-state population saturates after 40–50 generations reaching a maximum value of bleaching ($-\Delta A$) which is approximately 20% higher in magnitude than the starting bleaching for the initial (randomly generated) population. Similarly, in the minimization experiment [Fig. 5(b)] the minimal value of the bleaching is approximately 30% lower than for the initial starting set of excitation pulses. Note that the bleaching magnitude corresponding to the initial population (the pulses having randomly distributed phases and amplitudes) was always slightly lower than by excitation using transform-limited pulses.

The spectrum of the optimal pulse [the "best of the best" from the experiment showed in Fig. 5(a)] consists of a series of well-distinguished peaks spaced apart by 6.5–7 nm [Fig. 6(a)]. For comparison, the absorption and emission spectra of R101/MeOH are also plotted. It should be pointed out that in all the performed optimization experiments (at 2-, 5-, and 50-ps delays, with different starting conditions and for different excitation levels; approximately 30 successful experi-

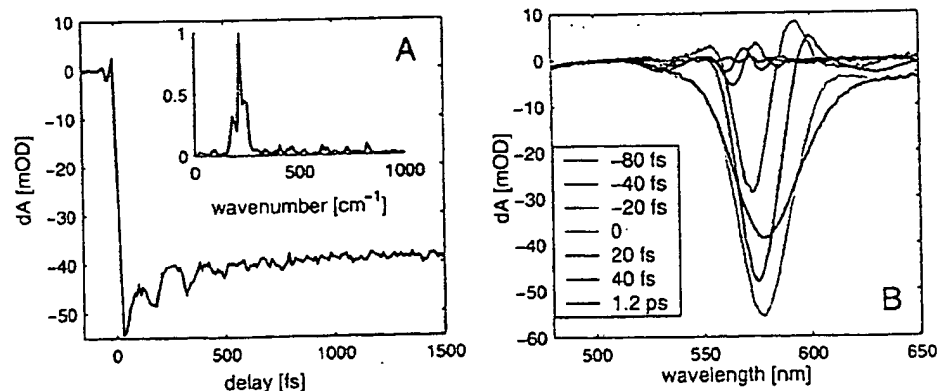


FIG. 4. (Color) (a) Population kinetics at 580 nm showing oscillations with a period of ~ 150 fs (inset: corresponding Fourier spectrum of residuals displays a component centered at 214 cm^{-1}). (b) Differential absorption spectra at different time delays as indicated.

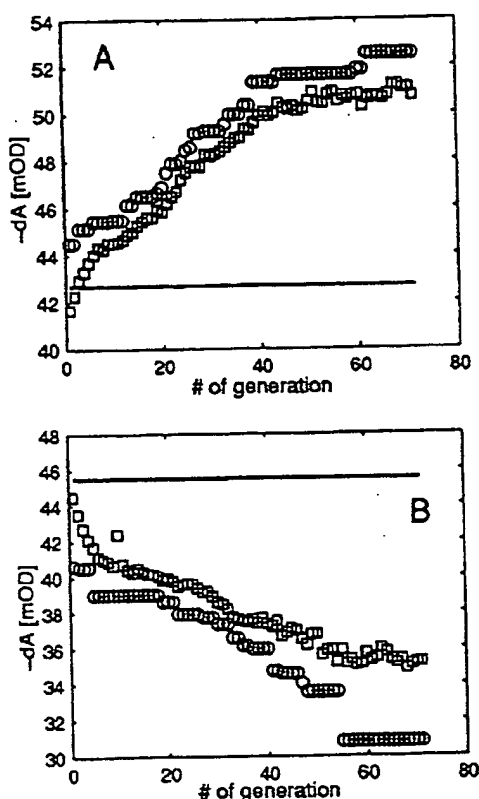


FIG. 5. Dynamics of the optimization of $S_0 \rightarrow S_1$ population transfer in R101/MeOH. (a) maximization experiment and (b) minimization experiment, where squares-average value (over the whole population), and circles-bleaching for the best (worst) pulses within the current population. The solid (straight) lines correspond to the bleaching amplitudes by excitation with transform-limited pulse.

ments) the spectra of the optimal pulses always display this distinct fine structure, whereas the absolute positions (as well as relative intensities of the peaks) vary within 1–1.5 nm. However, in all the spectra of the obtained optimal pulses the split between peaks was always 6.5–7 nm.

Remarkably the observed spectral spacing ($\sim 220 \text{ cm}^{-1}$ in the wave-number scale) corresponds exactly to the beating frequency of $\sim 150 \text{ fs}$ found in the population kinetics driven by a short and transform-limited pulse [Fig. 4(a)]. The FROG trace of the optimal pulse clearly displays this 150-fs modulation of the pulse envelope which can be considered as a comb of subpulses each with a duration of $\sim 40 \text{ fs}$, spaced apart by approximately 150 fs [Fig. 7(a)]. A similar feature was also found previously upon performing optimization experiments on the light-harvesting antenna complex LH2.¹³ In this work the target for optimization was the ratio between the intramolecular internal conversion (in carotenoids) and energy-transfer channels (from carotenoids to bacteriochlorophylls); however, despite the difference in optimization targets the determined optimal pulse was similarly modulated (several major subpulses spaced by 250 fs). Note that the results of this previous study are, generally speaking, rather negative than positive—the authors have only been able to demonstrate increasing of the internal conversion rate by ap-

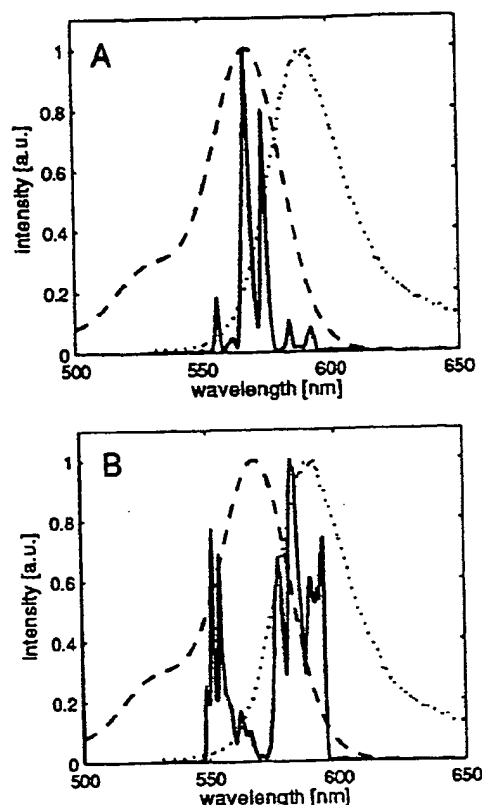


FIG. 6. Spectra of the optimal pulse (a) and anti optimal pulse (b) in comparison with absorption (dashed) and emission (dotted) spectra of R101/MeOH.

plying the tailored pulses, i.e., the suppression of the energy-transfer efficiency from carotenoids to bacteriochlorophylls.

The optimal pulse found in our experiment displays also a positive chirp which can be observed directly in the measured FROG trace [Fig. 7(a)]. In contrast to the optimal pulse, an anti-optimal excitation pulse which suppresses the efficiency of population transfer [the “worst of the worst” from the experiment showed in Fig. 5(b)] has a gap around the maximum of the absorption spectrum [Fig. 6(a)], where the core of the optimal pulse spectrum is located. The main spectral density of this anti-optimal pulse is overlapped with the emission spectrum, thus one can assume that such a pulse evokes a more efficient excited-state emission, reducing the population of the excited state. The time envelope of the anti-optimal pulse is also modulated with a period of $110 \pm 15 \text{ fs}$ [Fig. 7(c)] which is off resonance from the 150-fs oscillations in the population kinetics, and reflects in effect the spectral spacing between its red components (Fig. 6).

As can be seen directly from the FROG trace [Fig. 7(c)], the anti-optimal pulse has a strong but negative chirp that is favorable for effective population transfer from the excited state to the ground state. Note that such distribution of the spectral density for the anti-optimal pulse and the presence of the negative chirp have also been observed in all of the performed minimization experiments.

It should be pointed out that the software (FROG 3.0) used for retrieving temporal profiles of the pulses gives an ap-

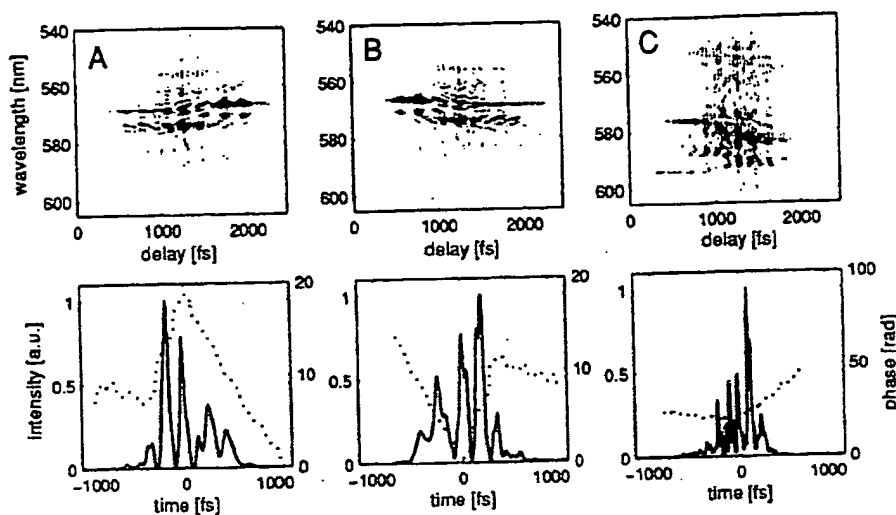


FIG. 7. Measured FROG traces (top) and retrieved intensity profiles (bottom, solid lines) with corresponding phases (bottom, dotted lines) for optimal pulse (a), optimal pulse but with a flipped phase (b) (see text for details), and (c) for anti-optimal pulse.

proximate solution by retrieving the pulse envelopes and phases from the experimental FROG traces if the pulse shapes are sufficiently complex. For example, in the experimental FROG traces, in addition to the well-resolved "slow" modulation with period of 110–150 fs, a fine modulation structure is also present (compare the top and bottom frames in Fig. 7). For the optimal pulse this regular modulation has a period of 60 ± 6 fs, whereas for the anti-optimal pulse the FROG trace is modulated by 43 ± 5 fs. For both pulses this fine modulation is more pronounced in the blue wavelength region. The physical meaning of this fine modulation is not completely clear at present.

The influence of linear chirp as well as its sign on the population dynamics was investigated and demonstrated¹⁴ for solvated dye molecules LD690 and LDS750. In this work, it was experimentally shown that the excited-state population is independent of the chirp at low excitation, while at high excitation energies strong chirp dependence has been observed. In a recent publication³⁰ the influence of the chirp sign on the transmission of the cyanine dye HDITC in ethanol was investigated. It was claimed (but not shown) that at very high excitations the transmission of the negatively chirped pulse that passed through the HDITC/ethanol is significantly higher than for the positively chirped pulse. The existence of a positive chirp in an excitation pulse leading to the enhancement of the fluorescence yield was also found previously³¹ by optimization of the excited-state population in the dye IR125. In this work the fluorescence signal was used as the feedback, thus only the population of excited state was actually controlled.³² At first glance, in the pump-probe experiments both the ground and excited-state populations contribute to the measured signal; however, the differential absorption spectrum for the closed two-level system (in our experiments we did not detect any excited-state absorption in R101/MeOH) is similarly proportional to the population of the excited state only. Indeed, the absorption coefficient of the excited two-level system can be given as

$$\alpha(\lambda, t) = \sigma_{01}(\lambda)n_0(t) - \sigma_{10}(\lambda)n_1(t),$$

where n_i are the populations of the electronic states S_0 and S_1 , whose sum is conserved so that $n_0(t) + n_1(t) = N \equiv \text{const}$. The absorption coefficient of a nonexcited (or fully relaxed) system corresponds to $\alpha_0(\lambda) = \sigma_{01}(\lambda)N$, thus the differential absorption spectrum is

$$\Delta A(\lambda, t) = d[\alpha(\lambda, t) - \alpha_0(\lambda)] \propto [\sigma_{01}(\lambda) + \sigma_{10}(\lambda)]n_1(t),$$

where d is the path length. Of course this simple representation, based on the Pauli master equations³³ (i.e., by taking into consideration only the diagonal elements of the density matrix), is applicable only for a system after complete relaxation/loss of coherence. By monitoring the pump-probe signal at very long delays, as compared to the characteristic dephasing time of the electronic transition and relaxation times of the vibrational states, this approximation is quite applicable. Thus, the results of the population transfer optimization using the pump-probe technique are comparable to those obtained by optimizing the fluorescence signal.

As it was shown previously (see, e.g., Refs. 14, 31, and 34), the positively chirped excitation pulse leads to enhancement of the excited-state population by minimizing the stimulated emission from the spectral components of the exciting pulse that "dumps" the population back to the ground state. By excitation with a negatively chirped pulse the "blue" components act first to transfer the population from the ground to the excited state, whereas the "red" delayed components transfer mainly the population to the ground state due to dynamic Stokes shift which reflects a downward movement of the population within the excited-state potential surface. However, this "pump-dump" scheme is suitable only at high-power excitation,¹⁴ where a molecule can cycle many times (at least twice) during the excitation, which is not the case for our experiments due to the very low excitation energy. Remarkably, in the optimization experiment of Bardeen *et al.*³¹ the most effective pulse which maximizes

the excited-state population regardless of the pulse energy (i.e., the optimal pulse) has been determined to be a high-power pulse.

As mentioned above, except for the positive/negative chirp, the optimal/antioptimal pulses display well-resolved substructures (subpulses) within an overall duration of ca. 550–600 fs FWHM. From the retrieved pulse profiles (Fig. 7, bottom) it follows that in the case of the optimal pulse, the change in phase from subpulse to subpulse is approximately $(1.5 \pm 0.2)\pi$, whereas for the antioptimal pulse this phase shift is significantly smaller $[(0.7 \pm 0.5)\pi]$. Taking this feature of the optimal pulse together with the positive chirp, we can assume that such a comb of subpulses “kicks” the underlying vibrational states periodically and resonantly keeping them in coherent conditions during ca. 600 fs, and thus effectively prevents the population from moving down along the excited-state potential surface. From this viewpoint the population transfer should be sensitive to (i) the phase information contained in an excitation pulse and (ii) to the dephasing time of the electronic transition.

C. Bleaching experiments with different excitation pulses

In order to explore the efficiency of population transfer at different excitation energies a series of bleaching experiments [i.e., dependence of bleaching on the excitation energy $\Delta A(E_{exc})$] was conducted using the same excitation pulse shapes obtained from the optimization experiments. Figure 8(a) shows the bleaching dependence measured using the optimal, transform-limited [shown in Figs. 2(b) and 2(c)], and antioptimal-shaped excitation pulses. In this experiment, the magnitude of bleaching was monitored at 580 nm (in correspondence with coherent control experiments; see the Experiment section) and 5 ps after zero delay. Figure 8(b) displays the same bleaching dependencies plotted versus actinic excitation energy which was calculated by taking into account the spectral overlap between absorption and excitation pulse spectra. As mentioned in the Experiment section, such normalization removes the particular spectral dependence of the bleaching and thus the absolute magnitude (or slope) of the measured bleaching can be objectively compared for different excitation pulses. Comparison of Figs. 8(a) and 8(b) clearly shows the importance of this normalization for performing the optimization experiments.

As can be seen, the induced bleaching of the R101/MeOH depends linearly on the excitation energy in the measured range, independent of the pulse shape. The difference in ΔA (i.e., in the population of the excited state) is very significant—the optimal pulse transfers the population with 30% higher efficiency compared to the antioptimal pulse. Moreover, for the optimal pulse the population transfer efficiency is approximately 10% higher than the transform-limited pulse. Note that the differential absorption spectra, measured at 5-ps delay, have identical shapes (except for the amplitudes) independent of the excitation pulse profiles. The same experiment has been performed for 300-ps delays after excitation (Fig. 9; only normalized dependencies are shown). Within the accuracy of the measurements, the difference in

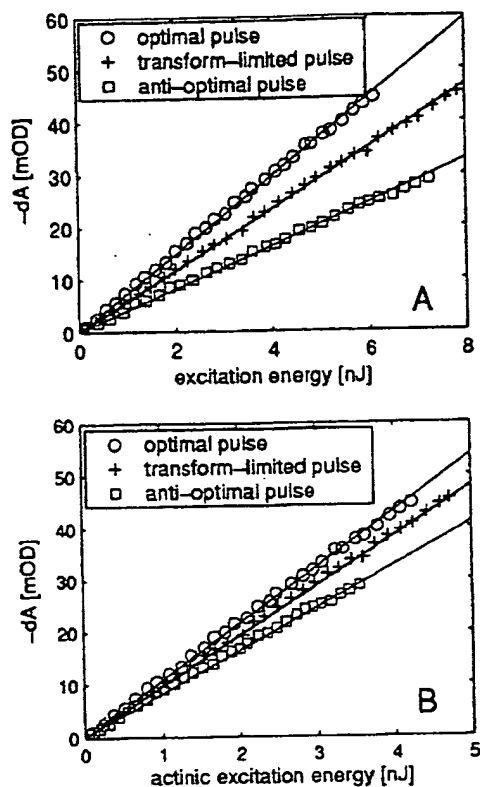


FIG. 8. Bleaching dependencies measured 5 ps after excitation for different excitation pulses (obtained from optimization experiments) in comparison to the transform-limited pulse: (a) measured dependencies and (b) normalized to the spectral overlap factors (see text for details). The lines show a linear fit to the corresponding data.

population obtained for the different excitation pulse shapes is still the same as for the 5-ps delay (30% for optimal–antioptimal pulses and 8% for optimal–transform-limited pulses). Thus, we can conclude that except for radiative and nonradiative decay (T_1 processes) which simply reduce the excited-state population, the difference in population caused by the difference in shaping of the excitation pulses’ temporal profiles has a stationary character.

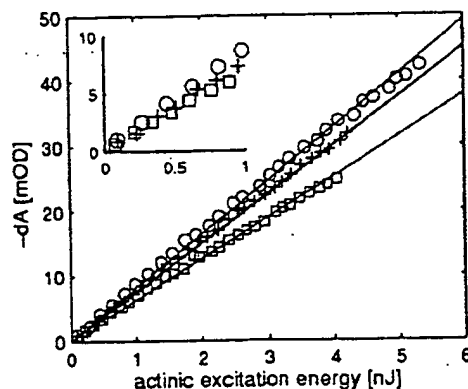


FIG. 9. Bleaching dependencies measured 300 ps after excitation (circles—excitation with optimal pulse, crosses—with transform-limited pulse, boxes—with antioptimal pulse). The inset shows the low excitation range.

Our optimization experiments were performed by keeping the excitation energy at ~ 5 nJ which corresponds to the excitation of 1 molecule per 100 during the laser pulse. However, as it follows from experimental data displayed in Figs. 8 and 9, the difference in the efficiency of population transfer for different excitation pulses is independent of the excitation energy (in the measured range) and is still the same at very low excitations (see inset in Fig. 9) even if only 1 molecule out of 500 absorbs a photon.³⁵ In this case, the probability for an excited molecule to interact with a photon twice during the laser shot is, according to the Poisson statistics, 10^{-3} . Thus, we can conclude that the interaction of the excitation pulse with molecules is essentially a one-photon process and it is not possible to explain the observed effects using a pump-dump scheme based on the simple kinetics equations (the Pauli master equations) approach. The difference in the efficiency of population transfer at very low (one-photon) excitation reflects rather the photon mode properties with respect to the probability of stimulated transitions (the absorption of a photon is also a stimulated process).

D. Role of the phase conditions in the population transfer efficiency

In order to examine the sensitivity of the population transfer to the phase information contained in the excitation pulse (the role of coherence in population transfer), we performed a control experiment using the optimal pulse but with a phase flip (the sign in the data file containing the phase spectrum for the acousto-optic modulator was simply changed). The procedure proposed and realized in Ref. 13 where the phase was shifted by π along its spectrum cannot be applied in a straightforward manner in our experiments due to the coupled changes in the pulse spectrum using our acousto-optic pulse shaper. However, flipping the phase spectrum is straightforward and is actually an equivalent process. This phase-flipped pulse has exactly the same spectrum as the nonflipped optimal pulse, thus the normalizing spectral overlap coefficients (see the Experiment section) for both the optimal and flipped pulses are equal and bleaching dependencies can be compared directly. According to the properties of the Fourier transform, flipping of the phase spectrum leads to the time reversal of the pulse shape. This is clearly demonstrated in the measured FROG trace of such a time-reversed pulse [Fig. 7(b)]. The reversed optimal pulse shows a negative chirp similar to the antioptimal pulse (but with a much stronger magnitude as can be observed in the retrieved profiles). Thus, one can expect that the population transfer for the time-reversed pulse will be effectively suppressed, if the process is phase sensitive, i.e., coherent with respect to the induced polarization.

Indeed, the experiment shows that the time-reversed optimal pulse transfers the population with 5%–6% less efficiency (Fig. 10) as compared to the optimal pulse, demonstrating the sensitivity of the population transfer to the phase information contained within the ~ 600 -fs time window (the pulse duration). However, the difference in bleaching is not as pronounced as, for example, between the antioptimal and optimal pulses. We also performed the same experiment using an antioptimal pulse with a flipped phase. In this case the

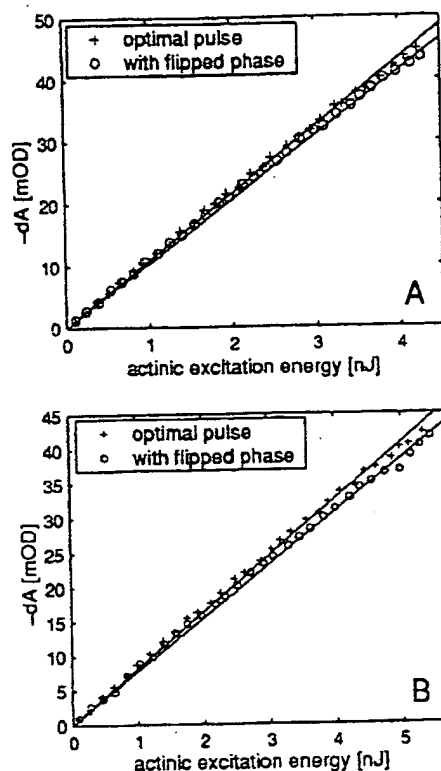


FIG. 10. Bleaching dependencies measured by excitation with the optimal pulse (having positive chirp) and with the time-reversed optimal pulse (having negative chirp) at 5 ps (a) and 300 ps (b) after excitation.

time-reversed antioptimal pulse has a positive chirp with the same magnitude as the antioptimal pulse (data not shown). Surprisingly, the bleaching (and corresponding population transfer) was insensitive to the chirp sign for the antioptimal pulse within the accuracy of the measurements, as demonstrated in Fig. 11. This result can be understood if we compare the absolute magnitudes of the phase shift within the comb of subpulses for the optimal and antioptimal pulses—in the latter case the phase change is significantly smaller [Figs. 7(a) and 7(c); retrieved pulse profiles]. The results obtained for the flipped optimal pulse show that the chirp itself and its sign affect the population transfer, but it is

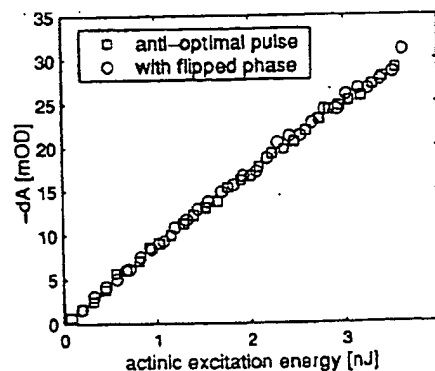


FIG. 11. Bleaching dependence measured by excitation with antioptimal and time-reversed antioptimal pulses (5 ps after excitation).

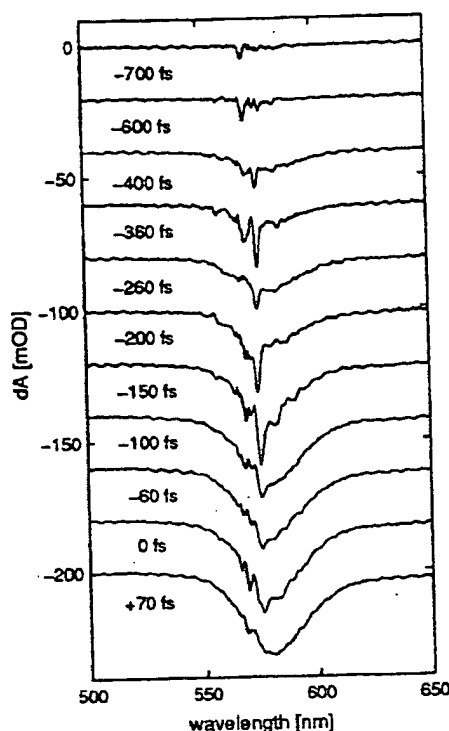


FIG. 12. Differential absorption spectra measured by excitation with the optimal pulse [see Fig. 7(a)] at different delays as indicated. For better viewing, the spectra are shifted by -20 m-OD. The zero delay was defined from the measurement of the cross-correlation function of the probe (white light) and the 23-fs transform-limited pulses centered at 575 nm (see the Experiment section).

not a dominant factor causing the 30% difference in the transfer efficiency. This is in good agreement with the suggestions of Cerullo *et al.*¹⁴ and with the results, obtained in Ref. 31, where the optimal solutions having positive as well as negative chirps, have been found.

In our opinion, the most important reasons causing an enhancement/suppression in the population transfer efficiency are (i) grouping of the excitation pulse into a series of regularly temporally spaced subpulses and (ii) spectral location of the corresponding components in the pulse spectrum with respect to the absorption/emission spectra of the molecule.

E. Pump-probe kinetics with the optimal pulse excitation

Very unusual kinetics of the population transfer have been observed using the optimal pulse for the excitation [Fig. 7(a)]. Figure 12 shows the differential absorption spectra, taken at early delays (as indicated) by excitation with the pulse energy of 5.4 nJ. At "negative" delays the differential absorption spectra display a deep and narrow hole located at ~ 575 nm whose amplitude grows by tuning the delay from -400 fs to -150 fs, and disappears at positive delays. The spectral FWHM of the 575-nm hole, averaged over the spectra recorded in the $[-360, -150]$ -fs delay range, is 2.8 ± 0.4 nm. Note that the main peaks in the spectrum of the optimal pulse (Fig. 6), located at 567 and 573.5 nm, do not

overlap completely with those in the differential absorption spectra (for example, the two well-distinguished holes in the spectra at the -360 delay are located at 569 and 575.5 nm, respectively). Further increase in the delay results in the shape of the differential absorption spectrum approaching that obtained by excitation with a transform-limited pulse, and it becomes stationary from ~ 1.5 ps onward, equivalent to the spectrum shown in Fig. 4(b) (delay of 1.2 ps). No oscillation was observed for positive delays in the pump-probe kinetics driven by the optimal pulse. It is remarkable that the differential absorption spectra at early delays, shown in Fig. 12, are very similar to hole-burning spectra observed usually at very low temperatures³⁶ (note that the so-called nonphotochemical hole-burning spectroscopy is actually a pump-probe technique). The deep hole at 575 nm reflects the lowest bleaching saturation energy and can thus be assigned to the pure electronic transition, to the so-called zero-phonon line. The spectral position of the electronic transition can usually be found as the curve crossing of the stationary absorption and emission spectra whose amplitudes have been normalized. From the measured spectra plotted in Fig. 6 it follows that the pure electronic transition should be located at 579 nm. However, this location corresponds actually to the thermally relaxed transition, whereas the hole at 575 nm observed in the pump-probe spectra (Fig. 12) reflects presumably a "hot" electronic transition. The physical mechanism of this hole formation in the pump-probe spectrum by excitation with a specifically shaped excitation pulse (optimal pulse) is not quite clear yet (some speculation is possible) and requires additional theoretical investigation. However, if we assume that this hole in fact reflects the pure electronic transition, an estimation of the dephasing time for the electronic transition can be made. Fitting the hole shape (located at 575 nm) to the Lorentzian profile (with a fitting correlation coefficient of $R \geq 0.99$) results in a spectral FWHM of 127 ± 30 cm^{-1} , averaged over the spectra recorded in the $[-360, -150]$ -fs delay range. This corresponds to a T_2 dephasing time of 85 ± 20 fs. Unfortunately, there are no published experimental data regarding a direct measurement of T_2 for the R101/MeOH; however, the magnitude of T_2 estimated here seems to be quite reasonable (within a factor of 2) in comparison to the known dephasing times of solvated xanthene dyes [for rhodamine 6G in ethanol the dephasing time was measured to be 30–40 fs (Ref. 37)].

IV. CONCLUDING REMARKS

We have demonstrated experimentally that the population transfer in complex solvated molecules can be controlled at very low excitations. The key result of this study is that the efficiency of population transfer from the ground electronic state to the excited state depends on the time profile of the applied excitation field even at the one-photon excitation level. This automatically creates the possibility for optimizing the population transfer efficiency which we have realized using a feedback-controlled learning algorithm. The temporal profile of the optimal pulse transferring the population with the highest efficiency corresponds to a comb of subpulses spaced by ~ 150 fs, and this spacing matches ex-

actly the beatings observed in the pump-probe kinetics, driven by impulsive excitation. The corresponding spectrum of the optimal pulse consists of a series of peaks with an ~ 6.5 -nm spacing, the positions of which coincide with the maximum of the absorption spectrum. This spectral spacing reflects a comb structure of the optimal pulse in the time domain. In contrast to the optimal pulse, an antioptimal pulse transferring the population with low (minimal) efficiency shows a modulation of the temporal profile with a period of ~ 110 fs, and its spectrum is essentially overlapped with the emission spectrum of the solvated molecules. In addition to the periodic modulation of the pulse shapes, both of these pulses show a clearly resolved chirp—positive for the optimal and negative for the antioptimal pulses. The difference in the efficiency of the population transfer by the excitation with the optimal and antioptimal pulses reaches 30%. Moreover, the population transfer efficiency using optimally tailored pulses is $\sim 10\%$ higher in comparison to the transform-limited pulse, which is not an optimal pulse for the population transfer. The population transfer efficiency can be further augmented by increasing the spectral window over which the pulse shape can be controlled in order to involve higher vibrational states of R101 (in the present work the controllable spectral window was technically limited to 50 nm). Considering the temporal- and spectral features obtained in the optimal/antioptimal pulses we conclude that the physical mechanism responsible for increasing/suppressing of the $S_0 \rightarrow S_1$ population transfer is resonant excitation of the underlying vibrational states by keeping them in a coherent superposition during the excitation. A theoretical analysis of the coherent control of population transfer under weak excitation will be given in a forthcoming paper.

The experimental results obtained here create a straightforward method for the control of excited-state populations of complex molecules in the one-photon limit through the manipulation of the photon mode. The ability to control excited-state populations in this manner avails the control of other photophysical processes in complex systems in which the excited state acts as a doorway state. An important extension of this work will be to affect the light-harvesting efficiency of artificial and natural photosynthetic units. We are capable of manipulating, for example, the population of a donor molecule using specially designed excitation pulses, which in turn would control the efficiency of the energy transfer as well. According to our experimental observations, it will also be possible to carry out this excitation control under extremely low light intensities comparable to the conditions under which the photosynthesis occurs. This latter condition greatly facilitates a correlation of the shaped laser pulses to the equilibrium fluctuations and phase relationships to the microscopic processes governing the natural processes.

ACKNOWLEDGMENTS

This work was supported by the National Sciences and Engineering Research Council of Canada and Photonics Research Ontario. The authors would like to thank V.V. Lozovoy for helpful discussions of the preliminary results.

- ¹T. Brixner and G. Gerber, *ChemPhysChem* 4, 418 (2003).
- ²M. Dantus and V. V. Lozovoy, *Chem. Rev. (Washington, D.C.)* 104, 1813 (2004).
- ³Y. Watanabe, H. Umeda, Y. Ohtsuki, H. Kono, and Y. Fujimura, *Chem. Phys.* 217, 317 (1997).
- ⁴Y. Ohtsuki, M. Sugawara, H. Kono, and Y. Fujimura, *Bull. Chem. Soc. Jpn.* 74, 1167 (2001).
- ⁵M. Shapiro and P. Brumer, *Rep. Prog. Phys.* 66, 859 (2003).
- ⁶R. S. Judson and H. Rabitz, *Phys. Rev. Lett.* 68, 1500 (1992).
- ⁷T. Baumert, T. Brixner, V. Seyfried, M. Strehle, and G. Gerber, *Appl. Phys. B: Lasers Opt.* 65, 779 (1997).
- ⁸A. Assion, T. Baumert, M. Bergt, T. Brixner, B. Kiefer, V. Seyfried, M. Strehle, and G. Gerber, *Science* 282, 919 (1998).
- ⁹T. Brixner, N. H. Damrauer, P. Niklaus, and G. Gerber, *Nature (London)* 414, 57 (2001).
- ¹⁰T. Brixner, N. H. Damrauer, G. Krampert, P. Niklaus, and G. Gerber, *J. Mod. Opt.* 50, 539 (2003).
- ¹¹T. Brixner, N. H. Damrauer, B. Kiefer, and G. Gerber, *J. Chem. Phys.* 118, 3692 (2003).
- ¹²C. J. Bardeen, V. V. Yakovlev, J. A. Squier, and K. R. Wilson, *J. Am. Chem. Soc.* 120, 13023 (1998).
- ¹³J. L. Herek, W. Wohlleben, R. J. Cogdell, D. Zeidler, and M. Moizkus, *Nature (London)* 417, 533 (2002).
- ¹⁴G. Cerullo, C. J. Bardeen, Q. Wang, and C. V. Shank, *Chem. Phys. Lett.* 262, 362 (1996).
- ¹⁵I. Pastirk, E. J. Brown, Q. G. Zhang, and M. Dantus, *J. Chem. Phys.* 108, 4375 (1998).
- ¹⁶V. V. Lozovoy, I. Pastirk, K. A. Walowicz, and M. Dantus, *J. Chem. Phys.* 118, 3187 (2003).
- ¹⁷M. R. Armstrong, P. Plachta, P. A. Ponomarev, and R. J. D. Miller, *Opt. Lett.* 26, 1152 (2001).
- ¹⁸S. A. Kovalenko, A. L. Dobryakov, J. Ruthmann, and N. P. Ermsing, *Phys. Rev. A* 59, 2369 (1999).
- ¹⁹R. Trebino, *Frequency-Resolved Optical Gating: The Measurement of Ultrashort Laser Pulses*, 1st ed. (Kluwer Academic, Amsterdam, 2002).
- ²⁰T. Karstens and K. Kobs, *J. Phys. Chem.* 84, 1871 (1980).
- ²¹The saturation energy density corresponds to the magnitude of the excitation which reduces the absorption coefficient of a thin optical layer by e times (see, e.g., Ref. 22).
- ²²A. Yariv, *Introduction to Optical Electronics* (Holt, Rinehart and Winston, New York, 1971).
- ²³V. I. Prokhorenko, M. V. Melishchuk, and E. A. Tikhonov, *Zh. Tekh. Fiz.* 51, 955 (1981).
- ²⁴V. I. Prokhorenko, *Zh. Tekh. Fiz.* 51, 2603 (1981).
- ²⁵U. Brackmann, *Lambdachrome Laser Dyes* (Lambda Physik GmbH, Goettingen, 1986).
- ²⁶L. V. Dao, J. Lumin. 106, 243 (2004).
- ²⁷H. L. Fragnito, J.-Y. Bigot, P. C. Becker, and C. V. Shank, *Chem. Phys. Lett.* 160, 101 (1989).
- ²⁸S. Mukamel, *Principles of Nonlinear Optical Spectroscopy*, 1st ed. (Oxford University Press, New York, 1995).
- ²⁹V. I. Prokhorenko, A. Nagy, and R. J. D. Miller, 2004 Cross Border Workshop on Laser Science: From Nonlinear Optics to Biophotonics, Ottawa, ON, Canada, 5–8 May 2004 (unpublished).
- ³⁰A. Yabushita, T. Fuji, and T. Kobayashi, *Chem. Phys. Lett.* 398, 495 (2004).
- ³¹C. J. Bardeen, V. V. Yakovlev, K. R. Wilson, S. D. Carpenter, P. M. Weber, and W. S. Warren, *Chem. Phys. Lett.* 280, 151 (1997).
- ³²Note that in this work Ref. 31 only the spectral position, amplitude, spectral width, magnitude, and sign of the linear and quadratic chirp in the excitation pulse were controlled.
- ³³K. Blum, *Density Matrix Theory and Applications* (Plenum, New York, 1981).
- ³⁴C. J. Bardeen, Q. Wang, and C. V. Shank, *Phys. Rev. Lett.* 75, 3410 (1995).
- ³⁵The actinic (absorbed) energy of 0.5 nJ (see inset in Fig. 9) corresponds to the photon density of 8×10^{12} photons/cm² for our experimental conditions. The concentration of molecules in the solvent can be calculated using the extinction coefficient for R101 $\epsilon = 9.5 \times 10^4$ l/mol cm (Ref. 25) to be 1.9×10^{17} cm⁻³. For a path length of 0.02 cm a ratio of excited to nonexcited molecules $8 \times 10^{12} / (1.9 \times 10^{17} \times 0.02)$ is $\sim 1:500$.
- ³⁶J. M. Hayes and G. J. Small, *J. Lumin.* 18/19, 219 (1979).
- ³⁷M. Cowan and R. J. D. Miller (unpublished).

Use of coherent control for selective two-photon fluorescence microscopy in live organisms

Jennifer P. Ogilvie

*Laboratoire d'Optique et Biosciences, Centre National de la Recherche Scientifique Unité Mixte de Recherche 7645
– Institut National de la Santé et de la Recherche Médicale U696 – Ecole Polytechnique, 91128 Palaiseau Cedex,
France*

*and
Department of Physics/Biophysics Research Division, University of Michigan, Ann Arbor, MI 48109
jogilvie@umich.edu*

Delphine Débarre, Xavier Solinas, Jean-Louis Martin, Emmanuel Beaurepaire and
Manuel Joffre

*Laboratoire d'Optique et Biosciences, Centre National de la Recherche Scientifique Unité Mixte de Recherche 7645
– Institut National de la Santé et de la Recherche Médicale U696 – Ecole Polytechnique, 91128 Palaiseau Cedex,
France*

manuel.joffre@polytechnique.fr

Abstract: We demonstrate selective fluorescence excitation of specific molecular species in live organisms by using coherent control of two-photon excitation. We have acquired quasi-simultaneous images in live fluorescently-labeled *Drosophila* embryos by rapid switching between appropriate pulse shapes. Linear combinations of these images demonstrate that a high degree of fluorophore selectivity is attainable through phase-shaping. Broadband phase-shaped excitation opens up new possibilities for single-laser, multiplex, *in-vivo* fluorescence microscopy.

©2006 Optical Society of America

OCIS codes: (320.5540) Pulse shaping; (180.2520) Fluorescence microscopy; (190.4180) Multiphoton processes

References and links

1. K. A. Walowicz, I. Pastirk, V. V. Lozovoy, M. Dantus, "Multiphoton intrapulse interference. I. Control of multiphoton processes in condensed phases," *J. Phys. Chem. A* **106**, 9369-9373 (2002).
2. V. V. Lozovoy, I. Pastirk, K. A. Walowicz, M. Dantus, "Multiphoton intrapulse interference. II. Control of two- and three-photon laser induced fluorescence with shaped pulses," *J. Chem. Phys.* **118**, 3187-3196 (2003).
3. J. Chen, H. Kawano, Y. Nabekawa, H. Mizuno, A. Miyawaki, T. Tanabe, F. Kannari, K. Midorikawa, "Selective excitation between two-photon and three-photon fluorescence with engineered cost functions," *Opt. Express* **12**, 3408-3414 (2004).
4. J. P. Ogilvie, K. Kubarych, A. Alexandrou, M. Joffre, "Fourier transform measurement of two-photon excitation spectra: Applications to microscopy and optimal control," *Opt. Lett.* **30**, 911-913 (2005).
5. A. Assion, T. Baumert, M. Bergt, T. Brixner, B. Kiefer, V. Seyfried, M. Strehle, G. Gerber, "Control of chemical reactions by feedback-optimized phase-shaped femtosecond laser pulses," *Science* **282**, 919-922 (1998).
6. N. Dudovich, D. Oron, Y. Silberberg, "Single-pulse coherently controlled nonlinear Raman spectroscopy and microscopy," *Nature* **418**, 512-514 (2002).
7. I. Pastirk, J. M. Dela Cruz, K. A. Walowicz, V. V. Lozovoy, M. Dantus, "Selective two-photon microscopy with shaped femtosecond pulses," *Opt. Express* **11**, 1695-1701 (2003).
8. J. M. Dela Cruz, I. Pastirk, V. V. Lozovoy, K. A. Walowicz, M. Dantus, "Multiphoton intrapulse interference 3: Probing microscopic chemical environments," *J. Phys. Chem. A* **108**, 53-58 (2004).
9. J. M. Dela Cruz, I. Pastirk, M. Comstock, V. V. Lozovoy, M. Dantus, "Use of coherent control methods through scattering biological tissue to achieve functional imaging," *Proc. Natl. Acad. Sci.* **101**, 16996-17001 (2004).
10. D. Meshulach, Y. Silberberg, "Coherent quantum control of two-photon transitions by a femtosecond laser pulse," *Nature* **396**, 239-242 (1998).

11. R. S. Judson, H. Rabitz, "Teaching lasers to control molecules," *Phys. Rev. Lett.* **68**, 1500-1503 (1992).
12. M. Comstock, V. V. Lozovoy, I. Pastirk, M. Dannus, "Multiphoton intrapulse interference 6; binary phase shaping," *Opt. Express* **12**, 1061-1066 (2004).
13. M. A. Dugan, J. X. Tull, W. S. Warren, "High-resolution acousto-optic shaping of unamplified and amplified femtosecond laser pulses," *J. Opt. Soc. Am. B* **14**, 2348-2358 (1997).
14. E. Frumker, D. Oron, D. Mandelik, Y. Silberberg, "Femtosecond pulse-shape modulation at kilohertz rates," *Opt. Lett.* **29**, 890-892 (2004).
15. E. Frumker, E. Tal, Y. Silberberg, S. Majer, "Femtosecond pulse-shape modulation at nanosecond rates", *Opt. Lett.* **30**, 2796-2798 (2005).
16. F. Vertuise, V. Laude, Z. Cheng, C. Spielmann, P. Tournois, "Amplitude and phase control of ultrashort pulses by use of an acousto-optic programmable dispersive filter: Pulse compression and shaping," *Opt. Lett.* **25**, 575-577 (2000).
17. D. P. Kiehart, C. G. Galbraith, K. A. Edwards, W. L. Rickoll, R. A. Montague, "Multiple forces contribute to cell sheet morphogenesis for dorsal closure in drosophila," *J. Cell Biol.* **149**, 471-490 (2000).
18. E. Wieschaus, C. Nusslein-Volhard, "Drosophila: A practical approach", Oxford, Oxford University Press (1998).
19. I. Davis, "Visualizing fluorescence in drosophila - optical detection in thick specimens". In *Protein localization by fluorescence microscopy: A practical approach*, Edited by Oxford University Press, 133-162 (2000).
20. W. Zipfel, R. M. Williams, R. Christie, A. Y. Nikitin, B. T. Hyman, W. W. Webb, "Live tissue intrinsic emission microscopy using multiphoton-excited native fluorescence and second harmonic generation," *Proc. Natl. Acad. Sci.* **100**, 7075-7080 (2003).
21. C. Xu, W. Zipfel, J. B. Shear, R. M. Williams, W. W. Webb, "Multiphoton fluorescence excitation: New spectral windows for biological nonlinear microscopy," *Proc. Natl. Acad. Sci.* **93**, 10763-10768 (1996).
22. E. Spiess, F. Bestvater, A. Heckel-Pompey, K. Toth, M. Hacker, G. Stobrawa, T. Feurer, C. Wotzlaw, U. Berchner-Pfannschmidt, T. Porwol, et al., "Two-photon excitation and emission spectra of the green fluorescent protein variants eCFP, eGFP and eYFP," *J. of Microscopy* **217**, 200-204 (2005).
23. P. Tournois: "Acousto-optic programmable dispersive filter for adaptive compensation of group delay time dispersion in laser systems," *Opt. Comm.* **140**, 245-249 (1997).
24. R. L. Fork, O. E. Martinez, J. P. Gordon, "Negative dispersion using pairs of prisms," *Opt. Lett.* **9**, 150 (1984).
25. A. C. Millard, D. N. Fittinghoff, J. A. Squier, M. Muller, A. L. Gaeta, "Using GaAsP photodiodes to characterize ultrashort pulses under high numerical aperture focusing in microscopy," *J. of Microscopy* **193**, 179-181 (1999).
26. W. Supatto, D. Débarre, B. Moullia, E. Brouzés, J.-L. Martin, E. Farge, E. Beaupaire, "In vivo modulation of morphogenetic movements in drosophila embryos with femtosecond laser pulses," *Proc. Natl. Acad. Sci.* **102**, 1047-1052 (2005).
27. W. R. Zipfel, Williams, R. M., W. W. Webb, "Nonlinear magic: Multiphoton microscopy in the biosciences," *Nat. Biotech.* **21**, 1369-1377 (2003).
28. J. K. Ranka, R. S. Windeler, A. J. Stentz, "Visible continuum generation in air-silica microstructure optical fibers with anomalous dispersion at 800 nm," *Opt. Lett.* **25**, 25-27 (2000).
29. S. Huang, A. A. Heikal, W. W. Webb, "Two-photon fluorescence spectroscopy and microscopy of NAD(P)H and flavoprotein," *Biophys. J.* **82**, 2811-2825 (2002).

The growing field of coherent control has demonstrated precise manipulation of nonlinear excitation through pulse-shaping methods. These methods tailor the spectral phase and/or amplitude of laser pulses to optimize a particular pathway while suppressing undesirable outcomes. Among the successes of this field have been the control of multiphoton excited fluorescence [1-4], and the branching ratios of chemical reactions [5]. Coherent control methods have recently found applications in nonlinear microscopy, where shaping of the spectral phase has been used to enhance image contrast in coherent anti-Stokes Raman scattering microscopy [6]. Selective multiphoton microscopy has also been demonstrated through the selective excitation of different fluorescent probes [7], as well as through the pH-dependent excitation of a dye, thus probing its local chemical environment [7,8]. Although imaging of biological organisms using this approach has not previously been reported, it has been shown that spectrally tailored pulses maintain their spectral phase-shaping after propagation through scattering media [9], allaying fears that they cannot be used for imaging within complex samples.

In this work we show that spectral phase-shaping of broadband laser pulses can be used to selectively excite the two-photon fluorescence of distinct chromophores in live *Drosophila* embryos labeled with enhanced green fluorescent protein (eGFP). This is achieved using a laser-scanning microscope and an acousto-optic pulse shaper allowing fast switching between two appropriate pulse shapes. We thus demonstrate the quasi-simultaneous acquisition of two images of the embryo under excitation conditions enhancing respectively the eGFP fluorescence and the endogenous fluorescence.

Coherent control of 2-Photon Excited Fluorescence (2PEF) can be easily understood in terms of the Second Harmonic (SH) spectrum of the exciting field [1,4,10]. Let us call $E(t)$ the electric field associated with the shaped pulse, and $E^{(2)}(t)=E(t)^2$ the SH field. In the frequency domain, these fields read respectively $E(\omega)=|E(\omega)|\exp[i\varphi(\omega)]$ and $E^{(2)}(\omega)$, where $\varphi(\omega)$ is the spectral phase. The SH spectrum is given by

$$|E^{(2)}(\omega)|^2 \propto \left| \int_{-\infty}^{\infty} |E(\omega')| |E(\omega - \omega')| \exp[i\{\varphi(\omega') + \varphi(\omega - \omega')\}] d\omega' \right|^2 \quad (1)$$

When there is no resonant intermediate level – a typical case in MPM – the chromophore is effectively driven by the SH field, so that 2PEF is simply proportional to the overlap integral between $|E^{(2)}(\omega)|^2$ and the two-photon excitation spectrum of the chromophore [1,4]. Chromophores with different excitation spectra can then be selectively addressed by shaping the SH spectrum so as to enhance the target 2PEF signal. To find the optimal spectral phase for a particular application, genetic learning-loop algorithms have often been employed [3,11,12]. Here, with knowledge of the two-photon excitation spectrum of the fluorophore of interest, we simply tune the SH spectrum for selective two-photon fluorescence excitation using a sinusoidal spectral phase [1,2], given by $\varphi(\omega)=A \sin(\gamma(\omega-\omega_0)-\delta)$, where ω_0 is the pulse center frequency and the parameters γ and δ determine the target harmonic frequency. Frequencies ω such that the spectral phase is antisymmetric with respect to $\omega/2$ will yield a vanishing phase factor in Eq. (1), and hence a constructive interference at ω , resulting in an effective excitation of this frequency component identical to that corresponding to a transform-limited pulse – a unique feature of phase shaping as opposed to amplitude shaping. In contrast, the SH spectrum will vanish for other frequency values due to destructive interferences. This process, known as multiphoton intrapulse interference [2], allows selective excitation of the chromophore of interest with a narrowband SH spectrum, the target frequency being controlled through the spectral phase of the shaped pulses.

Compared to the straightforward tuning of a narrowband laser pulse, one of the major advantages of shaping a broadband pulse as described above is the potential for rapid switching between different pulse shapes. However, most experiments to date have been based on liquid-crystal pulse shapers, with switching times limited to tens of milliseconds [7,8]. While various methods have been demonstrated to increase the switching frequency of such pulse shapers [13-15], we chose in this study to use a different technology, based on an acousto-optic programmable dispersive filter known as the Dazzler pulse shaper [16]. This device allows switching between two different pulse shapes at a high rate (10 kHz in our experiment), enabling the quasi-simultaneous acquisition of two images corresponding to pulse shapes chosen to alternately optimize the excitation of eGFP and endogenous fluorescence.

To demonstrate the ability to acquire images associated with selective excitation of the fluorescence, we chose to image live eGFP-labelled *Drosophila* embryos, namely the sGMCA transgenic *Drosophila* line [17], expressing eGFP fused with actin-binding moesin fragments. This line exhibits fluorescence labeling of the cytoskeleton and provides a fluorescent outline of cell shape [17]. Embryos were collected and selected during cellularization (just before gastrulation [18]), dechorionated, and glued to a coverslip [19]. Embryos were mounted in Phosphate Buffered Saline (PBS), covered with a coverslip to produce an observation cell of $300 \pm 25 \mu\text{m}$ thickness, and observed at room temperature. At cellularization, cells (and eGFP fluorescence) are confined to a band just beneath the vitelline membrane that surrounds the

embryo. The interior of the embryo (yolk) contains no eGFP, but fluoresces due to endogenous species. This strain therefore provided an ideal live system with spatially separated regions of endogenous and eGFP fluorescence that could be readily compared. We first measured the 2PEF yield as a function of excitation wavelength using a femtosecond Titanium:sapphire oscillator (Coherent), delivering 150 fs pulses with a spectral width of 7 nm at a central wavelength of 800 nm, and tunable in the 700-950 nm range. The relative excitation spectrum of eGFP and embryo endogenous fluorescence, shown in Fig. 1(A), was obtained by acquiring images of the whole embryo using a 20x, 0.8 NA objective (Olympus) and dividing the signal measured in the outer region of the embryo (containing eGFP) by the yolk 2PEF signal. These data confirm that, near 820 nm, the excitation spectrum of eGFP increases towards longer wavelengths, while endogenous fluorescence, which arises from fluorophores with emission spectra similar to that of NADH, shows the opposite trend [20-22].

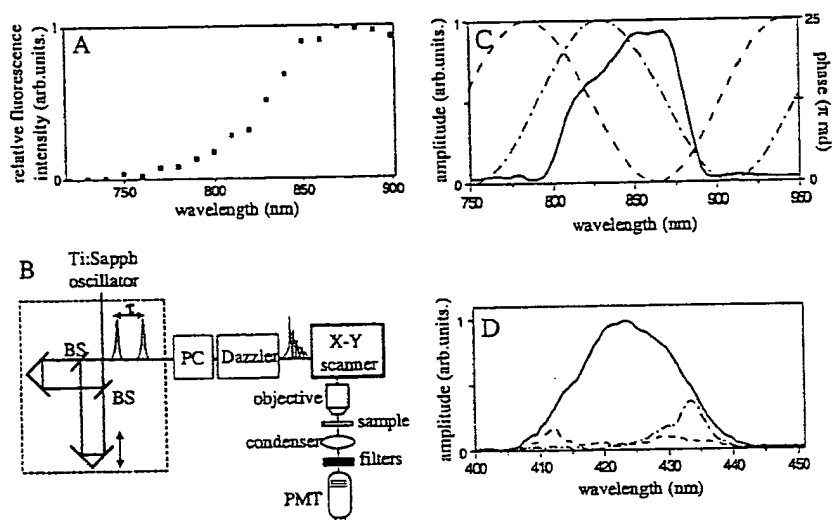


Fig. 1. (a) 2PEF ratio of eGFP/yolk, as measured with a narrow-band (b) Experimental setup. BS: beamsplitter, PC: prism compressor, PMT: photomultiplier tube. The interferometer, shown within the dashed box, was used only for characterizing the shaped pulses and was otherwise bypassed. (c) Spectral amplitude (solid line) for the pulses used in the experiments, as well as the applied sinusoidal phase for the red (dash-dot) and blue (dotted) phase-shaped pulses. (d) Corresponding SH spectra for the TL (solid), red-shaped (dash-dot) and blue-shaped (dotted) pulses. The TL amplitude has been reduced by a factor of two for easier comparison with the other spectra. The applied phases for the red and blue-shaped pulses were sinusoidal as defined in the text, with parameters $A = 25\pi$ rad, $\gamma = 0.09$ rad/THz for both pulses. The offset values used for the red and blue-tuned pulses were $\delta = -1.85$ rad and $\delta = -0.1$ rad respectively.

The coherent-control imaging experimental setup is shown in Fig. 1(b). The laser source was a broadband (~20 fs), homebuilt Ti:sapphire oscillator (300 mW, 100 MHz, center wavelength 820 nm). Before reaching the microscope, the laser pulses were phase-shaped using an acousto-optic programmable pulse shaper (Dazzler, Fastlite) [16,23], inserted into the beam path. We precompensated the microscope dispersion with a combination of the Dazzler and a fused-silica prism compressor [24], which we optimized via second-order autocorrelations in a GaAsP two-photon photodiode at the sample position [25]. Imaging was performed using a custom-built scanning microscope incorporating galvanometer mirrors (GSI Lumonics), an Olympus LMPLAN IR 20X, 0.4 numerical aperture objective and a photon-counting photomultiplier tube (PMT) (Electron Tubes PC25) [26]. The excitation power was 12 mW at the sample. The fluorescence signal was detected in the forward direction, after removing through spectral filtering (Chroma E700SP) the transmitted fundamental light:

Using the Dazzler, we generated two phase-shaped pulses with SH spectra tuned towards respectively low- and high- frequencies, in order to enhance the excitation of respectively the endogenous and eGFP fluorescences. These two pulses, obtained by choosing appropriate values of the δ parameter, will be hereafter referred to as the red-shaped and blue-shaped pulses. Using the interferometer shown in Fig. 1(b), we first characterized the fundamental (Fig. 1(c)) and SH spectra (Fig. 1(d)) of the pulses through linear and nonlinear Fourier-transform spectroscopy as described previously [4]. Figure 1(c) also shows the sinusoidal spectral phase corresponding to the two pulse shapes, which produced the SH spectra shown in Fig. 1(d). We also performed the imaging with transform-limited (TL) pulses (solid line in Fig. 1(d)).

The use of the Dazzler with a 100 MHz femtosecond oscillator requires special care due to the continuous drift between the acoustic waveform propagating in the acousto-optic crystal and the femtosecond pulse train. This drift causes spectral amplitude clipping for pulses that are diffracted when the acoustic waveform is not entirely present inside the crystal. Furthermore, even when the acoustic waveform is entirely inside the crystal, successive femtosecond pulses will be diffracted at different longitudinal positions, and will consequently encounter different amounts of dispersion due to the difference in group velocity dispersion between the ordinary and extraordinary axis. In order to avoid this effect, pulses corresponding to a well-defined position of the acoustic waveform in the crystal must be selected. This can be achieved either at the detection level or at the laser level using a modulator. For simplicity, the former method was implemented here by gating the fluorescence photon counts using a TTL signal synchronized with respect to the Dazzler waveform trigger. With the femtosecond oscillator as a 100-MHz clock, it was possible to select the start and stop position of the gating signal using home-made electronics based on a Complex Programmable Logic Device (M4A3-128/64-55, Lattice Semiconductor Corporation). In order to ensure a good compromise between a large fluorescence signal and a homogenous distribution of pulse shapes, we used a gating width corresponding to 300 oscillator pulses, i.e. 6% of the total number of pulses delivered by the oscillator for each acoustic waveform. Note that a similar gating procedure was used for recording the data shown in Fig. 1(C) and 1(D) so that the characterized spectra correspond to those actually used in the imaging experiment.

Figure 2 shows fluorescence images of a live eGFP labeled *Drosophila* embryo recorded with different phase-shaped pulses, where Fig. 2(a) and 2(b) are the images obtained quasi-simultaneously using blue- and red-shaped pulses respectively. A perfect synchronization at the pixel level was obtained between these two images by alternating the acoustic waveform sent into the Dazzler at 10 kHz. Figure 2(c) shows the image obtained using transform limited pulses which excite the membrane-labelled eGFP, as well as significant endogenous fluorescence in the yolk and vitelline membrane. This should be compared with the blue-shaped pulse, which produces higher fluorescence from the yolk (Fig. 2(a)). Conversely, the red-shaped pulse shows significantly reduced yolk fluorescence and enhanced fluorescence from the eGFP-labelled cytoskeleton (Fig. 2(b)). This difference is readily apparent in Fig. 3, which displays the fluorescence profile along a line (position shown in Fig. 2(c)) through the embryo. The efficiency of the chromophore selection can be described by the contrast factor

$$\Gamma = \frac{R_{blue} - R_{red}}{R_{blue} + R_{red}} \quad (2)$$

where R_{blue} and R_{red} are ratios of emission between the yolk and eGFP regions for blue-shaped and red-shaped pulses respectively. From the graph shown in Fig. 3, we obtain a contrast $\Gamma = 0.35$, in good agreement with the expected value $\Gamma = 0.39$ obtained from the

excitation spectrum shown in Fig. 1(a), assuming switching between 412 and 435-nm SH excitation wavelengths.

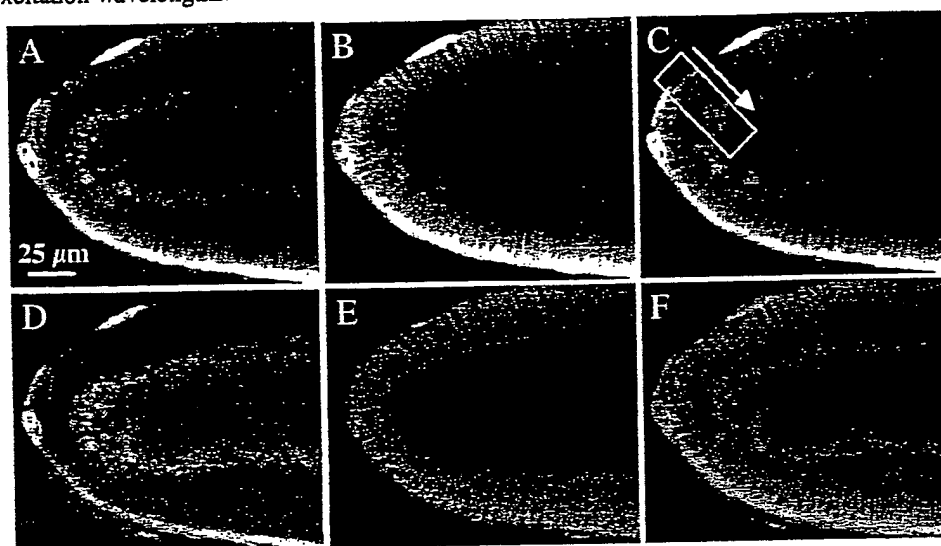


Fig. 2. 2PEF images of an eGFP labeled *Drosophila* embryo. (a) Blue-tuned excitation. (b) Red-tuned excitation. (c) Transform limited pulse. These three images are normalized to the fluorescence signal of the vitelline membrane. (d) Linear combination of A and B to isolate the eGFP fluorescence. (e) Linear combination of A and B to isolate the yolk fluorescence. (f) Composite image of C and D to illustrate the good separation between eGFP and yolk fluorescence.

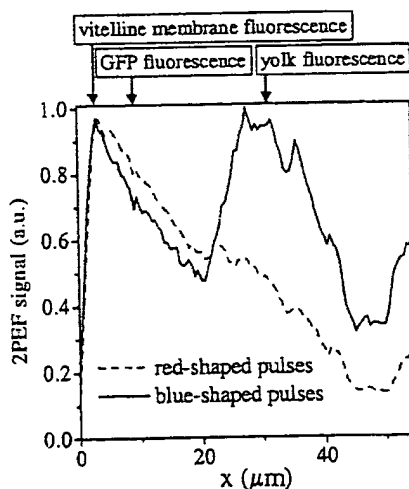


Fig. 3. 2PEF signal profiles for the shaped pulses through the section indicated in Fig. 2(C), showing significantly different signal levels in the eGFP and yolk.

As a side-effect of enhanced selectivity, we observe that the fluorescence yield in the case of the shaped pulses is about 8 to 17% of that for a TL pulse, due to the smaller overlap between the SH spectra shown in Fig. 1(d) and the chromophore absorption spectra. However we note that amplitude shaping resulting in the same SH spectral width would have resulted in a much greater reduction in two-photon excitation efficiency because fewer spectral components would then contribute to chromophore excitation. In general, an appropriate choice for the

spectral phase results from a compromise between optimizing the contrast factor Γ and matching the spectral width of the SH spectrum with that of the chromophore absorption spectrum.

A unique feature of a quasi-simultaneous acquisition of images associated with two different pulse shapes is that it enables the computation of linear combinations of the two images, owing to the perfect correspondence between pixels of identical coordinates. Such a procedure permits the removal of the inevitable crosstalk ($\Gamma < 1$) resulting from the overlap between the excitation spectra of the imaged species. This method is demonstrated in Fig. 2(d) and 2(e), which are linear combinations of the quasi-simultaneously acquired blue and red-shaped images shown in Fig. 2(a) and (b). The coefficients used in the linear combination were determined by selecting two areas of the embryo image in the yolk and in the cell layer region and assuming that the 2PEF signal originated from the endogenous and eGFP fluorescence respectively. Fig. 2(f) is a superposition of the images in Fig. 2(D) and (E), coloured to indicate the respective contributions. This picture clearly illustrates the ability to distinguish eGFP from endogenous fluorescence contributions using phase-shaped laser pulses.

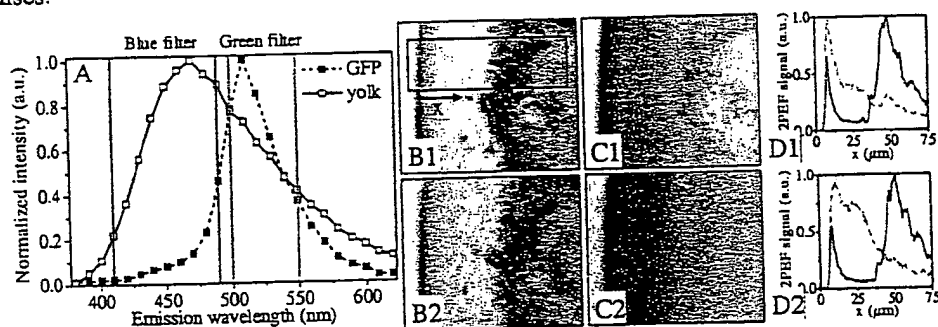


Fig. 4. A) 2PEF spectra of yolk and eGFP measured in vivo under 820-nm excitation by recording the descanned epifluorescence filtered using a 15-nm tunable interferential filter (S-60, Schott). Also shown are the wavelength ranges selected by the emission filters. B1) 2PEF images using blue-filter for TL and B2) blue-shaped pulses. C1) 2PEF images using green-filter for TL and C2) red-shaped (right) pulses. D1) X-profile for TL and D2) shaped pulses with filters at location indicated in B1.

A common approach to separating several types of fluorophores is to spectrally filter their fluorescence emissions. This becomes difficult if there is considerable overlap in the emission spectra, and is accompanied by significant loss of fluorescence signal and poor selectivity. In the case of eGFP and yolk fluorescence, the spectral overlap is large, as shown in Fig. 4(a). We therefore explored how the combined use of shaped pulses and filters could enhance the selectivity achievable with spectral filters alone. Figures 4(b1) and 4(b2) show images that have been spectrally filtered with the blue filter indicated in Fig. 4(a). Figure 4(b1) used TL excitation, while Fig. 4(b2) was taken with the blue-shaped pulses. Similarly, images that were recorded with the green filter are shown in Fig. 4(c1) and Fig. 4(c2), where TL excitation and red-shaped pulses were used respectively. Figures 4(d1) and 4(d2) show the profile, along the box indicated in Fig. 4(b), for the TL and shaped excitation respectively, allowing a comparison of the selectivity provided by using emission filters alone, or a combination of emission filters and phase-shaping. In the filters-only case, the blue filter is quite effective at removing the eGFP fluorescence. However, the green filter does not completely select the eGFP signal, leaving a significant amount of yolk fluorescence. When the filters are combined with phase-shaping, the images show a significant enhancement of the contrasts obtained with the two spectral filters by nearly a factor of 3. This enhancement demonstrates that a combination of phase-shaping and spectral filtering results in better selectivity than spectral filtering alone. This will be true in all cases where emission spectra overlap significantly but excitation spectra are more distinct, and provides an additional

degree of freedom beyond emission filtering for achieving selectivity. As an illustrating example, distinguishing between CFP (Cyan Fluorescent Protein) and NADH through spectral filtering of the 2PEF signal would be particularly difficult due to their very similar emission spectra [20,22]. However, the excitation spectra of these two species present significant differences [22,27], which suggests that pulse shaping would be an efficient tool for their selective imaging.

Phase-only shaping may also have advantages for multiplex fluorescence imaging of fluorophores with significantly different 2PEF cross-sections. In this case, optimizing the excitation conditions can be challenging because different exposure times are necessary to achieve comparable image quality for the different fluorophores. This often requires sacrificing excess signal from the higher cross-section emitter. Phase-shaping can address this problem by choosing the appropriate relative number of red or blue shaped pulses to balance the emission levels, thus more efficiently using the excitation light and avoiding unnecessary illumination of the sample that could lead to photodamage.

The use of a programmable, rapid pulse-shaper allows flexibility in determining optimum phase-shaping for specific imaging conditions. However, once the optimum spectral phase has been determined, the pulse-shaper could easily be replaced by a static phase-mask that provides the required spectral phase shape. This method would have the benefit of using all the oscillator pulses, resulting in shorter acquisition times than the 7 mn required for each of the images shown in Fig. 2(a) and 2(b). Such an approach would be directly analogous and complementary to spectral filtering of the emission. Rapid switching between different static phase masks for multiplex imaging could be achieved by a scanning mirror [14] or an acousto-optic beam deflector. Our current implementation permits selective excitation over the bandwidth of the laser source (~100 nm) with a single laser source. Extending this range is desirable to access a broader range of fluorophores, and may be possible through phase-shaping of continua generated by a photonic crystal fiber [28]. This would remove the need for multiple laser sources while providing access to a wide range of fluorophores that could be rapidly and selectively excited. This possibility is particularly attractive for ratiometric imaging [29]. A broader spectral range will also be of great practical interest for the important application of imaging transgenic animals. Fast shaping approaches will allow simultaneous addressing of a collection of fluorophores such as fluorescent proteins-based constructs (CFP, YFP, cameleons, etc.) as well as endogenous species such as NADH.

In conclusion we have demonstrated the use of spectral phase-shaping for selective two-photon fluorescence imaging of live eGFP labeled *Drosophila* embryos. Employing a fast switching pulse-shaper, we obtained quasi-simultaneous images corresponding to pulse shapes optimized to selectively excite eGFP or endogenous fluorescence. Linear combinations of these images demonstrated that a high degree of selectivity is attainable through phase-shaping. When used in combination with spectral filtering of the emission, we found that phase-shaping improved selectivity between eGFP and endogenous fluorescence by a factor of ~3. Phase-shaping provides an additional dimension towards improving the selectivity and extending the multiplex capabilities of fluorescence microscopy.

Acknowledgments

We thank Emmanuel Farge and Willy Supatto for providing us with the transgenic eGFP labeled *Drosophila* strain and for many discussions. We also thank Kevin Kubarych, Richard Herzog and Thomas Oksenhendler for numerous discussions of the operation of the Dazzler pulse-shaper, as well as Antigoni Alexandrou and Adeline Bonvalet for useful discussions about the experiment. This work was supported by the Délégation Générale pour l'Armement.

Chemical Imaging by Single Pulse Interferometric Coherent Anti-Stokes Raman Scattering Microscopy

Sang-Hyun Lim, Allison G. Caster, Olivier Nicolet, and Stephen R. Leone*

Departments of Chemistry and Physics, University of California at Berkeley and Lawrence Berkeley National Laboratory, Berkeley, California 94720

Received: December 23, 2005

A single pulse interferometric coherent anti-Stokes Raman (CARS) spectroscopy method is used to obtain broadband CARS spectra and microscopy images of liquid and polymer samples. The pump, Stokes, and probe pulses are all selected inside a single broadband ultrafast pulse by a phase- and polarization-controlled pulse shaping technique and used to generate two spectral interference CARS signals simultaneously. The normalized difference of these two signals provides an amplified background-free broadband resonant CARS spectrum over the 400–1500 cm^{-1} range with 35 cm^{-1} spectral resolution. Chemically selective microscopy images of multicomponent polymer and liquid samples are investigated with this new CARS method. Multiplex CARS spectra at 10 000 spatial points are measured within a few minutes, and used to construct chemically selective microscopy images with a spatial resolution of 400 nm. The spectral bandwidth limits, sensitivity, homodyne amplification advantages, spatial resolution, depolarization, chromatic aberration, and chemical imaging aspects of this new technique are discussed in detail.

I. Introduction

Coherent anti-Stokes Raman scattering (CARS) microscopy is a promising chemically selective microscopy technique that uses the vibrational response of the sample molecules themselves as a contrast mechanism, eliminating the need for sample labeling such as fluorescent dyes.^{1–3} Moreover, the method allows three-dimensional imaging and has a higher spatial resolution than one- or even two-photon fluorescence due to the nature of the coherent three-photon process.^{3,4}

The nonresonant CARS signal is the biggest problem in CARS microscopy because it can obscure the desired resonant CARS signal.^{1,5} This background is generated by the electronic response of the sample and is independent of the signal frequency.^{1,6,7} It is more problematic in multiplex CARS experiments, because a broadband ultrafast pulse (a shorter pulse in the time domain) is required, and the shorter the pulse duration, the stronger the nonresonant signals become.^{1,2,8} On the other hand, it is very desirable to cover a broad CARS spectral window for spectral analysis.⁹ The so-called “Raman fingerprint region” spans from 800 to 1800 cm^{-1} for most organic molecules.¹⁰ If one wishes to cover the entire fingerprint window in the previously reported multiplex CARS techniques that use synchronized narrow bandwidth pump and probe pulses together with broad bandwidth Stokes pulses,^{2,5} the Stokes pulse needs to have a bandwidth of more than 1000 cm^{-1} . A pulse having this amount of bandwidth generates a huge nonresonant background, which will completely dominate the relatively weak resonant signals.^{11,12}

Recently, several groups demonstrated the possibility of extracting resonant CARS signals via interferometry (in both the time and spectral domain).^{13–15} Since the resonant and nonresonant signals are coherent and have different responses to the phases of the pump, Stokes, and probe light fields,

interferometry can be used to extract the pure resonant signals.^{13,15} In this approach, one can also amplify the CARS signals via a homodyne amplification mechanism, since the detected signal is the cross term between the resonant signal and a local oscillator.^{8,13}

Silberberg and co-workers pioneered single-pulse multiplex CARS methods with a pulse shaping technique.^{7,11,16–19} This approach greatly simplifies the experimental setup, eliminates the problem of timing jitter between the two pulses, and enables control of the relative phases and polarizations of the resonant and nonresonant CARS signals. With a polarization- and phase-controlled technique, they showed that it is possible to obtain a background-free CARS spectrum.¹⁹

Recently, we combined the interferometric¹³ and polarization/phase control¹⁹ methods to demonstrate a method of single pulse interferometric CARS spectroscopy.¹² We use the pulse shaping technique to generate CARS signals and control the relative phase between the resonant and nonresonant signals to implement a double quadrature spectral interferometry (DQSI).^{13,20} This technique utilizing the internal nonresonant signal as a local oscillator. This new technique can extract the imaginary and real parts of the background-free resonant CARS spectrum in a single experimental measurement.¹² It not only retrieves the imaginary part of the CARS signal, but also amplifies it significantly, allowing a substantial sensitivity improvement.¹² In this report, we present a more thorough analysis of this technique, quantify the sensitivity, and apply it to obtain chemically selective microscopy images of liquid and polymer samples. Detailed analyses of the CARS signal generation, the double quadrature spectral interferometry (DQSI) method, the experimental setup, homodyne amplification advantages, and chemical imaging aspects are presented. Several issues such as spectral bandwidth limits, signal sensitivity, spatial resolution, sample depolarization, and chromatic aberration are also discussed.

* Address correspondence to this author. E-mail: srlone@berkeley.edu

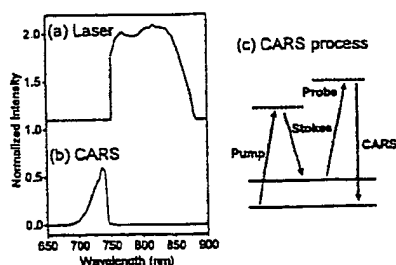


Figure 1. Normalized spectra of (a) the laser pulse and (b) CARS signal generated by the transform-limited (TL) pulse. (c) Energy level diagram of the CARS process.

II. Double Quadrature Spectral Interferometric Coherent Anti-Stokes Raman Scattering (DQSI-CARS) Spectroscopy

In this section, a systematic analysis of the single pulse multiplex CARS signal generation and the double quadrature spectral interferometric CARS (DQSI-CARS) technique is considered. The method is developed to show how a background-free resonant CARS spectrum can be extracted in a single experimental measurement. Briefly, we excite a sample with a single phase/polarization-controlled broadband laser pulse to generate spectral interferometric signal traces along two different polarization directions at the same time. The normalized difference spectrum from the two signals results in the background-free broadband multiplex CARS spectrum, providing vibrational information equivalent to that of spontaneous Raman scattering.

Figure 1a shows the spectrum of the laser pulse used in this experiment. Note that the bandwidth of the laser is more than 120 nm ($\sim 1800 \text{ cm}^{-1}$). The wavelengths of the laser shorter than 750 nm are cut off by a wide variable slit placed after the spatial light modulator inside a pulse shaper. Figure 1b shows the spectrum of the CARS signal from toluene (the sum of both the resonant and nonresonant signals) acquired through a short wave pass filter (to reject the laser pulses) with a transform-limited (TL) pulse.¹¹ All possible combinations of wavelengths within the bandwidth can be used in principle as the pump, Stokes, and probe pulses (as shown in Figure 1c) to generate the CARS signal, which has a smooth spectral shape with monotonically decreasing intensity at shorter wavelengths (Figure 1b).^{11,19} This spectral shape is due to the fact that there are fewer possible frequency combinations of pump, Stokes, and probe pulses to generate the shorter wavelength CARS signals.

With single pulse excitation, the resonant and nonresonant CARS signals can be described by^{6,7}

$$P_R(\omega) \propto \int_0^\infty d\Omega \chi_R(\Omega) E(\omega - \Omega) A(\Omega) \quad (1)$$

$$P_{NR}(\omega) \propto \int_0^\infty d\Omega \chi_{NR}(\Omega) E(\omega - \Omega) A(\Omega) \quad (2)$$

where

$$A(\Omega) = \int_0^\infty d\omega' E^*(\omega') E(\Omega + \omega') \quad (3)$$

$$\chi_R(\Omega) \equiv \alpha_R \sum_k \frac{a_k}{(\Omega_k - \Omega) + i\Gamma_k} \quad (4)$$

$$\chi_{NR}(\Omega) \equiv \alpha_{NR}/\Omega \quad (5)$$

P_R and P_{NR} are the third order vibrationally resonant and nonresonant transient polarizations, respectively. E is the laser

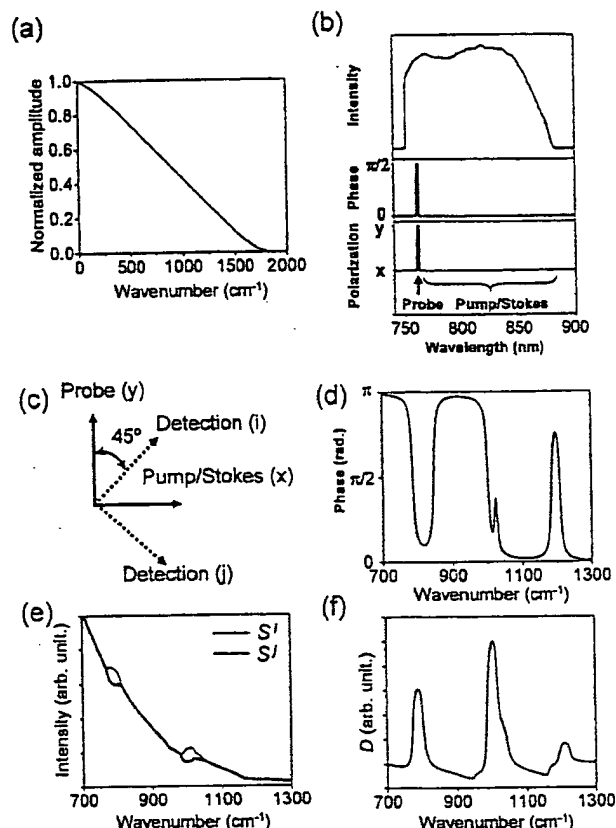


Figure 2. (a) Simulated amplitude spectrum of the coherent vibrational excitation, $A(\Omega)$, with a transform-limited pulse. (b) Intensity, phase, and polarization of the shaped laser pulse used in DQSI-CARS. (c) Polarization directions of pump/Stokes (x), probe (y), and detections (i and j). (d) Phase spectrum calculated for toluene. (e) Simulations of the two signal spectra (S' and S'') for toluene with eqs 1–5, and 11. (f) The normalized difference spectrum (D) according to eq 13 from the two simulated signal traces in part e.

field, and Ω and ω are the frequencies of the coherent vibrational excitation and CARS signals, respectively. χ_R is the vibrationally resonant third-order susceptibility, and a_k , Ω_k , and Γ_k are the relative intensity, energy, and line width of vibrational mode k , respectively. χ_{NR} is the vibrationally nonresonant susceptibility, which generates the nonresonant CARS signals. α_R and α_{NR} are the amplitude coefficients of the resonant and nonresonant susceptibilities, respectively, responsible for the wavelength independent factors such as concentration, electronic polarizability, etc. Note that α_{NR}/α_R determines the relative intensity ratio between the nonresonant and resonant CARS signals. $A(\Omega)$ corresponds to the coherent vibrational excitation generated by the pump and Stokes pulses.⁷ The calculated spectrum of $A(\Omega)$ with a TL pulse, in Figure 2a, has monotonically decreasing intensities versus higher vibrational frequency of the resulting CARS signals. This quantity will determine both the CARS spectral window and peak intensity distribution since the spectral distributions of the resonant vibrational CARS signals are a convolution of $A(\Omega)$, the probe electric field, and the third-order vibrational susceptibility (χ_R) as shown in eq 1.⁷

To obtain a multiplex CARS signal, it is necessary to separate out a spectrally narrow probe pulse.¹⁹ We select the probe pulse by the phase/polarization mask shown in Figure 2b. The probe width is chosen to be two pixels, which corresponds to 30 cm^{-1} bandwidth. The polarization directions of the pump/Stokes pulses and the probe pulse are along the x- and y-directions, respectively (Figure 2c). For simplicity, we begin with an

assumption that the line width of the probe (selected by the phase and polarization-mask shown in Figure 2b) is spectrally much narrower than the vibrational line width (Γ_R). Consider the case where the phase of the probe pulse is set to $\pi/2$. Then, the electric fields of the laser along x - and y -polarization directions become

$$E^y(\omega) \approx E_{Pr} \delta(\omega - \omega_{Pr}) \exp(i\pi/2) = iE_{Pr} \delta(\omega - \omega_{Pr}) \quad (6)$$

$$E^x(\omega) = E(\omega) - E^y(\omega) \approx E(\omega) \quad (7)$$

where E^y and E^x are the electric fields of the laser pulse along the y - and x -polarization directions. E is the amplitude of the total electric field, i.e., $E = |\vec{E}| = |E^x \hat{x} + E^y \hat{y}|$, where \hat{x} and \hat{y} are the unit vectors along x and y directions, respectively. δ is the delta function, ω_{Pr} is the frequency of the probe pulse, and E_{Pr} is the field intensity at the frequency of the probe pulse (ω_{Pr}), respectively. Note that E_{Pr} is a constant, not a function of frequency. Also note that most of the laser pulse energy is in the x -direction (eq 7).

The resulting resonant CARS signals along x - and y -directions are described by

$$P_R^x(\omega) = \int_0^\infty d\Omega \chi_R(\Omega) E(\omega - \Omega) A(\Omega)$$

$$P_R^y(\omega) = \int_0^\infty d\Omega \chi_R(\Omega) i\delta(\omega - \Omega - \omega_{Pr}) E_{Pr} A(\Omega) = i\chi_R(\Omega) E_{Pr} A(\omega - \omega_{Pr}) \quad (8)$$

Since the nonresonant signal with a short pulse laser used in this experiment (pulse duration ~ 10 fs) is orders of magnitude larger than the resonant signal and polarized along the x -direction, the total transient polarizations along the x - and y -polarization directions become

$$P^x(\omega) = P_{NR}(\omega) + P_R^x(\omega) \approx P_{NR}(\omega)$$

$$P^y(\omega) \approx P_R^y = i\chi_R(\omega - \omega_{Pr}) E_{Pr} A(\omega - \omega_{Pr}) \quad (9)$$

As one can see in eq 9, the spectrally resolved resonant CARS signals (P^y) can be separated from the nonresonant signals (P^x) by the polarization directions. The y -polarized signal, i.e., the spectrally resolved resonant CARS signal, is what one wishes to measure in the experiment. Note that P^x is a real quantity, and P^y is a complex one (χ_R is a complex function while χ_{NR} is a real one).

One can selectively detect the spectrally resolved resonant signals by eliminating the nonresonant signals (P^x) with a polarizer, which was demonstrated by Silberberg and co-workers.¹⁹ We adopt a different approach here.¹² If the CARS signals are detected along a polarization direction other than the x -polarization direction (Figure 2c), the resulting signals are a coherent sum of the nonresonant (P^x) and resonant signals (P^y). The x - and y -polarized CARS signals are coherent and have characteristic phase relationships with respect to the phases of the pump/Stokes and probe laser fields. As mentioned above, the x -polarized signal is mostly the nonresonant signal and has a flat phase function over all signal frequencies. Note that even the resonant component of the CARS signal along the x -polarization direction (P_R^x) has a smooth, almost flat phase function, since there is no spectrally narrow probe pulse in this polarization direction. Therefore we can use this signal as a local oscillator. In contrast, the y -polarized signal (P^y) is the spectrally resolved resonant CARS signal. It has a π phase shift at every vibrational resonance frequency, resulting in a nonflat phase

spectrum over the signal frequencies. Figure 2d shows such a phase spectrum calculated for toluene. The spontaneous Raman spectrum of toluene is used for the relative peak intensities and vibrational peak positions in the simulation of Figure 2d, as described further below. When the x - and y -polarized signals are added together in a polarization direction other than the x - and y -axes, the detected signal has a modulated interference pattern at every vibrational resonance frequency since constructive and destructive interferences occur at each vibrational resonance, where the resonant signal has a π phase shift. We can also control the interference pattern by controlling the relative phase between the pump/Stokes and probe pulses. Thus the spectral interferometry uses the nonresonant signal as a phase-controllable local oscillator. We developed this new double quadrature spectral interferometry (DQSI) technique¹² to extract the imaginary part of the amplified resonant signals, since this technique can be performed in a single data acquisition without scanning the spatial light modulator (SLM). Next we show the case where the imaginary part of $\chi_R(\omega)$ is extracted; one can also obtain the real part by using a different probe phase, as demonstrated previously, and is not discussed here.¹²

Consider the signals along the $\pm 45^\circ$ polarization directions relative to the x -axis (i - and j -directions shown in Figure 2c). The transient third-order polarizations along these polarization directions are

$$P^i(\omega) = \frac{P^x(\omega) + P_R^y(\omega)}{\sqrt{2}}$$

$$P^j(\omega) = \frac{P^x(\omega) - P_R^y(\omega)}{\sqrt{2}} \quad (10)$$

The detected signal photons along the i - and j -polarization directions become

$$S^i(\omega) = |P^i(\omega)|^2 = \frac{1}{2}|P^x(\omega)|^2 + \frac{1}{2}|P_R^y(\omega)|^2 + \frac{1}{2}P^x(\omega)(P_R^y(\omega) + P^{y*}(\omega))$$

$$S^j(\omega) = |P^j(\omega)|^2 = \frac{1}{2}|P^x(\omega)|^2 + \frac{1}{2}|P_R^y(\omega)|^2 - \frac{1}{2}P^x(\omega)(P_R^y(\omega) + P^{y*}(\omega)) \quad (11)$$

Figure 2e shows numerical simulations of S^i and S^j for toluene. Details of this simulation will be discussed in section IV.

The difference between these two signal traces leads to

$$S^j(\omega) - S^i(\omega) = -P^x(\omega)(P_R^y(\omega) + P^{y*}(\omega))$$

$$= -P^x(\omega)A(\omega - \omega_{Pr})E_{Pr}\{i\chi_R(\omega - \omega_{Pr}) - i\chi_R^*(\omega - \omega_{Pr})\}$$

$$= 2P^x(\omega)A(\omega - \omega_{Pr})E_{Pr} \text{Im}[\chi(\omega - \omega_{Pr})] \quad (12)$$

As one can see in the result of eq 12, $S^j - S^i$ contains the imaginary part of the resonant CARS signal (i.e., $A(\omega - \omega_{Pr})E_{Pr} \text{Im}[\chi(\omega - \omega_{Pr})]$) multiplied by P^x , which is the local oscillator (nonresonant CARS signal) that has orders of magnitude larger amplitude. Thus the resonant signal is amplified and the imaginary part of the third-order vibrational susceptibility can be obtained.

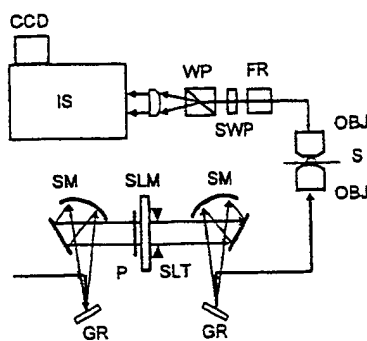


Figure 3. Experimental setup: GR, grating; SM, spherical mirror; P, polarizer; SLM, dual bank liquid crystal spatial light modulator; SLT, slit; OBJ, microscope objective; S, sample on the XY piezo stage; FR, Fresnel rhomb (achromatic half wave plate); SWP, sharp edge short wave pass filter; WP, Wollaston prism; and IS, imaging spectrometer.

The absolute amplitude of the nonamplified resonant signal can also be obtained by the following normalized difference

$$D(\omega) = \frac{S'(\omega) - S''(\omega)}{\sqrt{S'(\omega) + S''(\omega)}} = \frac{2P^x(\omega)A(\omega - \omega_{pr})E_{pr}\text{Im}[\chi(\omega - \omega_{pr})]}{\sqrt{|P^x(\omega)|^2 + |P^y(\omega)|^2}} \approx \frac{2P^x(\omega)A(\omega - \omega_{pr})E_{pr}\text{Im}[\chi(\omega - \omega_{pr})]}{P^x(\omega)} = 2A(\omega - \omega_{pr})E_{pr}\text{Im}[\chi(\omega - \omega_{pr})] \quad (13)$$

The unit of this new scale (D) is $\sqrt{\text{counts}}$, which corresponds to the field amplitude of the signal. Figure 2f shows the normalized difference spectrum (D in eq 13) from the two simulated traces in Figure 2e.

Two approximations have been used to derive eq 13. The first is that the bandwidth of the probe pulse is much narrower than the line width of the vibrational peak, and the second is that the nonresonant signals are much larger than the resonant signals. In section IV, we will investigate the validity of these two approximations and show how the experimental line shape can be affected if they are no longer valid.

III. Experimental Section

CARS signals are generated with a broadband Ti:Sapphire oscillator (MTS, KM Lasers). The repetition rate of the laser is 90 MHz. The oscillator is optimized to have the broadest bandwidth (~ 120 nm as shown in Figure 1a) by carefully adjusting the prism pairs inside the cavity. Figure 3 shows the experimental setup. The pulse is controlled by an all reflective 4f pulse shaper, using a 128 pixel dual bank liquid crystal spatial light modulator (LC-SLM256, CRI). The pulse shaper is configured to control both the phase and polarization of the individual frequency pixels at the Fourier plane by removing the exit polarizer. The 120 nm bandwidth (~ 1800 cm^{-1}) of the laser spectrum is encompassed by the pulse shaper. To block the wavelengths outside the controlled part of the pulse, a wide variable slit is installed after the SLM. The shaped pulse is focused into the sample and the signal is collected, using two high N.A. water immersion IR objectives (1.2 and 1.0 N.A., respectively, Olympus). All the signals with various phase matching angles inside the wide focusing angle ($\sim 128^\circ$ with the 1.2 N.A. water objective) are generated and collected within the tight focusing geometry. Note that the phase matching

conditions for the resonant CARS signal and the local oscillator (nonresonant signals) are exactly the same since they are both generated from the same laser pulse. Comparing the laser spectrum before the focusing objective and after the collecting objective, we do not find any significant transmission irregularity of the microscope objectives used here. The collected signal is rotated by 45° with respect to the x -direction by an achromatic half wave plate (Fresnel Rhomb, CVI) and filtered by a sharp edge short wave pass filter (740ASEP, Omega Optical). The i - and j -polarization signals (as shown in Figure 2c) are separated spatially by a Wollaston prism (CVI), and the two vertically displaced signal beams are coupled to an imaging spectrometer (750si, Chromex) and imaged onto a two-dimensional CCD (DV401-FI, Andor) as two horizontal lines.

The chirp structure of the pulse at the sample position is characterized with the multiple intrapulse interference phase scan (MIIPS) method developed by Dantus and co-workers.²¹ Briefly, a cosine phase mask is applied on the SLM and the second harmonic generation (SHG) spectra from a BBO crystal at the sample position are measured while scanning the phase offset of the cosine phase mask. This results in two-dimensional plots having multiple lines, where the TL pulse shows evenly spaced parallel straight lines. A 10 μm thick BBO crystal (Casix) is used to generate the SHG spectra at the sample position on top of a 180 μm thick glass coverslip and water (between the glass coverslip and the focusing objective). A 0.54 N.A. dry objective collects the SHG signals and a fiber-coupled spectrometer (FL2000USB, Ocean Optics) is used to measure the SHG spectra. A phase mask having a phase modulation given by

$$\phi(\omega) = \alpha \cos(\gamma(\omega - \omega_0) - \delta) \quad (14)$$

is applied on the SLM, where α is set to 2π , and $2\pi/(1800$ cm^{-1}) is used for γ . γ is chosen to have a one cycle of the cosine phase curve over the full spectrum of the laser. ω_0 is the center frequency of the laser spectrum. The second harmonic generation spectra are taken while the phase offset (δ) is scanned from 0 to 4π .

Panels a and b of Figure 4 show the MIIPS plots of transform-limited (Figure 4a) and chirped (Figure 4b) pulses, respectively. The TL pulse shows evenly spaced parallel lines in the MIIPS plot (Figure 4a). Any deviation from this pattern can be related to the phase structure of the uncompressed pulse.²¹ The MIIPS of an uncompressed pulse shows that the neighboring lines are not equally spaced, nor are they parallel to each other (Figure 4b). The different spacing between the nearby lines corresponds to the quadratic phase modulation (ω^2 term), and the different linear slopes of these lines relates to the cubic phase modulation (ω^3 term) of the chirp structure. Higher order chirp structure can also be analyzed by considering the differing higher order curvatures between the neighboring lines in the MIIPS plot.

The MIIPS technique is reliable, easy to use, and gives more information about the pulse phase characteristics than conventional techniques such as SHG autocorrelation or frequency-resolved optical gating (FROG).²² In microscopy, MIIPS is a preferred pulse characterization technique since the noncollinear FROG is very difficult to set up with a high N.A. microscope objective. The pulse for CARS microscopy needs to be compressed not only in the linear but also in higher order chirp terms. We find that it is important to compress the pulse at least up to the cubic chirp (ω^3 term) to generate the optimum CARS signal.

Another problem encountered during the implementation of the DQSI-CARS is the different spectral responses of the spectrometer between P- and S-polarized signals. This is due

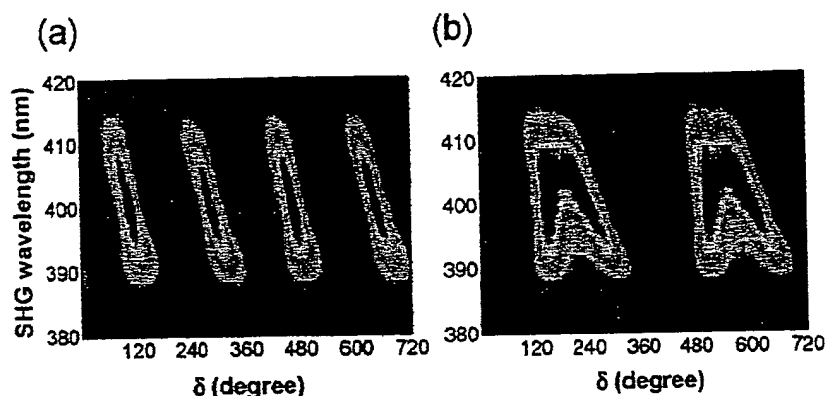


Figure 4. Experimental MIIPS plots of (a) transform-limited (TL) and (b) uncompressed pulses measured at the sample position of the microscope. Note that a TL pulse shows equally spaced parallel lines in panel a. The spacing and different slopes between the lines correspond to the quadratic (ω^2) and cubic (ω^3) phase modulations of the laser pulse, respectively.

to the different reflective response of the grating used in the spectrometer, and we find that it also depends on the optical coupling of the signals to the spectrometer, which can change with different experiments. These effects are calibrated by acquiring CARS signals (S^i and S^j) with the TL pulse as references. Since the S^i and S^j should be exactly the same in this case, normalization of each CCD trace with the CARS reference (the signal with TL pulse) compensates for the different polarization response of the spectrometer. This procedure has to be done only once with each sample.

A CCD exposure time of 10 ms is used here for all the CARS data in both the spectroscopy and microscopy experiments. The time of 10 ms is chosen as representative of the desirable scan time per spatial location (pixel) in a microscopy image, since this is the fastest scan speed of the CCD used here. In the CARS spectroscopy of solvents and solutions, an average laser power of 40 mW before the focusing objective is used. With this power level, we estimate that the power density at the focus is approximately 10^{12} W/cm² per pulse assuming a diffraction-limited spot size and 10 fs pulse duration. For microscopy experiments with liquid and polymer samples, the laser power is reduced to 3 mW to prevent sample damage during scanning of the sample.

Spectroscopy experiments are performed with a small drop of the sample sandwiched between two microscope coverslips. The two signal traces (S^i and S^j) are measured and processed according to eq 13 in real time.

In the microscopy experiments, S^i and S^j are acquired with a so-called "multi-track mode" of a two-dimensional CCD. We integrate (bin) the vertical pixels into two different regions corresponding to S^i and S^j . This mode of the CCD operation allows two vertically displaced signal traces to be measured in a fast single readout process. The CCD is cleared after each 10 ms data acquisition, and the data are transferred to a computer and processed in real time. The readout time for a single multitrack scan is also about 10 ms. The sample is scanned by an XY piezo stage (P-733.2CL, PI) synchronized with the CCD acquisition. In this report, all the images consist of 100 pixels \times 100 pixels with 0.2 and 0.4 μ m step sizes for the amide/PDMS and PS/PMMA images, respectively. The raw data consist of a three-dimensional matrix of CARS spectra at each two-dimensional (2D) spatial point times the number of points in the 2D scans, and the signal traces (S^i and S^j) are also saved for further analysis. The total experiment time for an image with 100 \times 100 pixels is about 3.5 min with 10 ms CCD exposure time for each pixel. This includes the CCD exposure time, readout time, and data-processing time. With the laser

repetition rate of 90 MHz, the number of laser pulses used for the CARS spectral measurement of a single spatial spot is 9×10^5 with the 10 ms CCD exposure.

A poly(dimethylsiloxane) (PDMS) pattern is made by a soft lithographic technique, using a TEM copper grid as a template.²³ A TEM grid (SPI) is attached to a clean glass substrate with a drop of methanol and dried. A 10:1 mixture (weight percent) of the elastomer base and curing agent from a PDMS elastomer kit (Sylgard 184, Dow Corning) is poured onto the TEM grid on top of the glass substrate. After curing in an oven at 80 °C for about 1 h, the PDMS elastomer pattern (mould of the TEM grid) is peeled off with tweezers. A drop of *N,N*-dimethylformamide (Aldrich) is sandwiched between the PDMS pattern and a microscope coverslip. Polystyrene (PS) and poly(methyl methacrylate) (PMMA) samples are purchased from Aldrich and used as received. A 1:1 mixture (weight percent) of polymer powders is dissolved in chloroform. A PS/PMMA film is prepared by spin-casting a PS/PMMA solution on a glass coverslip at 600 rpm until the chloroform is dried out. The sample thickness is around 2 μ m, which is measured at a razor scratch of the film with an atomic force microscope (AFM).

IV. Results and Discussion

Panels a and b of Figure 5 are experimental signal traces of S^i and S^j for toluene liquid and the corresponding DQSI-CARS spectrum processed according to eq 13. One can see that the experiments match the simulations (Figure 2e,f) reasonably well. We calculated the traces in Figure 2e,f using the *E*-fields of the entire shaped laser pulses along the *i*- and *j*-directions separately using eqs 1–5, 11, and 13. In this way, signal traces can be simulated without any approximation. The spontaneous Raman spectrum of toluene is used to obtain the values of α_k , Ω_k , and Γ_k for four different vibrational peaks (resonances at 788, 1001, 1028, and 1210 cm⁻¹, with relative peak intensities, α_k , of 5, 10, 2.5, and 2, respectively). $\Gamma = 10$ cm⁻¹ is used for the line width of all four vibrational peaks. However, the probe spectral width is taken to be 30 cm⁻¹ in the simulation, which corresponds to the two pixel width of the probe selected by the SLM. A value of $\alpha_{NR}/\alpha_R = 500$ is used, as discussed further below. This value is chosen to match the experimental interference modulation of the 788 cm⁻¹ peak.

As one can see in the simulation in Figure 2f, the resulting DQSI-CARS spectrum has a line shape of the predicted imaginary part of χ_R , but convoluted with the probe pulse shape corresponding to the bandwidth of two pixels (30 cm⁻¹) in the SLM. So the failure of the first approximation (narrow probe

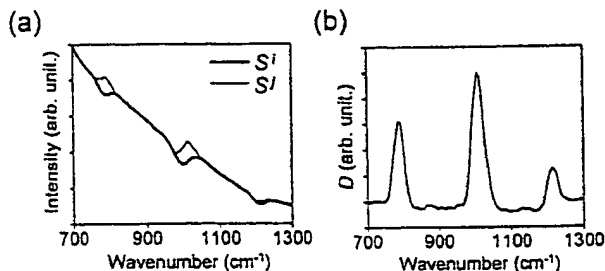


Figure 5. (a) Experimental two-signal spectra (S^I and S^J) and (b) the normalized difference spectrum (D) for toluene.

approximation) leads only to a broadening of the spectral line widths of the vibrational peaks.

The only unknown parameter in the simulations of Figure 2e,f is the relative amplitude ratio of the nonresonant and resonant third-order susceptibilities (α_{NR}/α_R). This value can be estimated by comparing the modulated interference depth of the simulation (Figure 2e) and the experiment (Figure 5a). The experimental interference modulation depth at 788 cm^{-1} for toluene is $\sim 10\%$ in the normalized difference of $(S^J - S^I)/(S^J + S^I)$ and $\alpha_{NR}/\alpha_R = 500$ is found to generate this amount of modulation within 10% error. This ratio validates the second approximation ($P_{NR} \gg P_R$). We investigate the effect of this approximation below by simulating several CARS line shapes with different α_{NR}/α_R values and comparing simulation results with the experiment.

With a broadband pulse like the one used in this experiment, the nonresonant signal is at least an order of magnitude greater than the resonant signal in most condensed phase samples.¹¹ We use the x -polarized signals (P^x) as a local oscillator to perform spectral interferometry. The local oscillator, however, is not only from the nonresonant signal.¹¹ It also contains broadband resonant CARS signals (P_R^x in eq 8) from any possible pump, Stokes, and probe pulse wavelength combinations within the pump/Stokes region of the laser spectrum (Figure 2b). This resonant CARS signal (P_R^x) has a smooth spectral shape because there is no sharp phase or polarization structure in the laser pulse. This signal (P_R^x), however, will change the phase relationship in the interferometry. If we take this effect into account, the local oscillator becomes (P^x)

$$\begin{aligned} P^x(\omega) &= P_{NR}^x(\omega) + P_R^x(\omega) \\ &= \alpha_{NR} \int_0^\infty d\Omega/\Omega E^x(\omega - \Omega) A(\Omega) + \\ &\quad \alpha_R \int_0^\infty d\Omega \sum_k \frac{a_k}{(\Omega_k - \Omega) + i\Gamma_k} E^x(\omega - \Omega) A(\Omega) \\ &\equiv |P^x| \exp(i\phi_{LO}(\omega)) \end{aligned} \quad (15)$$

Here we use eqs 1–5 without any assumptions. Note that P_{NR}^x is a real quantity, and P_R^x is a complex one since it contains an integration of the complex Lorentzian line shape function. In the time domain, it can also be understood such that P_R^x contains the effect of vibrational decoherence, which is manifested as a complex Lorentzian function in the frequency domain. Also note that the phase spectrum of P_R^x is smooth and mostly flat because there are no sharp phase features in E^x and $A(\Omega)$. Thus, the local oscillator (P^x) becomes a complex quantity having a smooth phase spectrum ($\phi_{LO}(\omega)$) instead of a zero phase value. The ratio of α_{NR}/α_R determines how much the phase of the local oscillator is shifted from zero in the

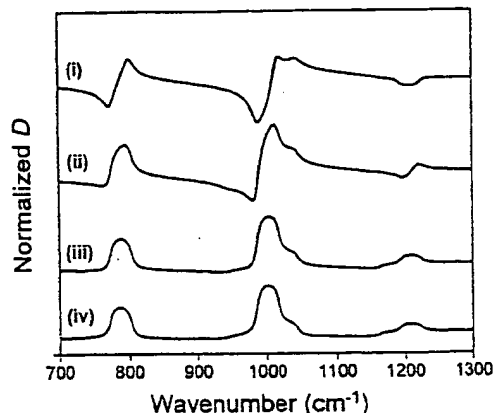


Figure 6. Effect of the resonant CARS signal generated from the pump/Stokes region of the pulse. The toluene vibrational spectrum is used in the simulation. (i) $\alpha_{NR}/\alpha_R = 0$, (ii) $\alpha_{NR}/\alpha_R = 100$, (iii) $\alpha_{NR}/\alpha_R = 500$, and (iv) $\alpha_{NR}/\alpha_R = 10000$. The experimental observations with toluene correspond best to the simulation of (iii).

simulation. In the case of $\alpha_{NR} \gg \alpha_R$, P^x becomes P_{NR}^x , and $\phi_{LO}(\omega) = 0$. This is the assumption we used previously.

However, if there is a significant amount of P_R^x in P^x (i.e., $\alpha_{NR} \gg \alpha_R$ is no longer valid), the interferometry will be modified by the sample-dependent P_R^x (thus $\phi_{LO}(\omega)$, too). We can simulate this effect by comparing the calculations of different α_{NR}/α_R values. Figure 6 shows the simulated CARS spectra for four different α_{NR}/α_R values using the toluene spectra as a model. One can see that the nonpure local oscillator will distort the DQSI-CARS spectral shape in the case of (i) $\{\alpha_{NR}/\alpha_R = 0, \text{ resonant signal only}\}$ and even up to (ii) $\{\alpha_{NR}/\alpha_R = 100\}$. By comparing the interference modulation depth in the simulated S^I and S^J traces with a given α_{NR}/α_R value, one can simulate the experimental α_{NR}/α_R ratio for the sample. In most samples, we find that this ratio is large enough to generate a reasonable spectral shape. In toluene, the ratio between the nonresonant and resonant signals is one of the smallest among condensed phase samples ($\alpha_{NR}/\alpha_R \sim 500$, (iii)), but this is still large enough to generate a reasonable spectral line shape compared to the almost pure nonresonant local oscillator case ($\alpha_{NR}/\alpha_R \sim 10\,000$, (iv)). In the case of biological samples, the ratio of α_{NR}/α_R will be at least an order of magnitude larger than that for toluene, so the interferometric technique can be applied to most materials and biological imaging problems.

Next we explain that even if there is a significant amount of relative broadband resonant signal (P_R^x) in the local oscillator, the resulting DQSI-CARS spectral peak shape becomes a mixture of imaginary and real parts of a Lorentzian line shape function i and ii in Figure 6. By replacing eq 9 with eq 15, one can show that eq 12 leads to

$$S^J(\omega) - S^I(\omega) = 2|P^x(\omega)|A(\omega - \omega_{PT})E_{PT}\{\text{Im}[\chi_R(\omega - \omega_{PT})] \cos\phi_{LO}(\omega) - \text{Re}[\chi_R(\omega - \omega_{PT})] \sin\phi_{LO}(\omega)\} \quad (16)$$

So if the local oscillator is contaminated by P_R^x , it will distort the CARS line shape to be a mixture of imaginary and real parts of a Lorentzian function. We can correct this distortion by adjusting the probe phase to cancel the effect of $\phi_{LO}(\omega)$ or use the distorted spectrum as a contrast mechanism to be interpreted by a numerical fitting process.²

Thus far we described the theoretical aspects of the interferometric CARS technique. Next we show experimental results and discuss several aspects in both the spectroscopy and microscopy imaging with this technique.

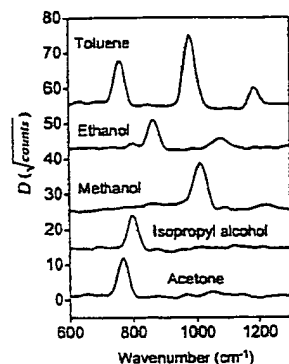


Figure 7. DQSI-CARS spectra of common lab solvents. Each trace is displaced vertically for clarity. Note that the data are taken with the microscope set up with 10 ms CCD exposure time.

Figure 7 shows the experimental DQSI-CARS spectra of several common lab solvents taken with a CCD exposure time of 10 ms. The spectra are processed from the two simultaneously measured signals (S^i and S^j) according to eq 13. The currently accessible CARS window is from 400 to 1500 cm^{-1} , although the signal decreases rapidly beyond 1200 cm^{-1} . The lower limit comes from rejection of the signal by the short wave pass filters used to block the laser. The higher limit is from the limited bandwidth of the laser spectrum. Although we have $\sim 1800 \text{ cm}^{-1}$ of laser bandwidth, the CARS signal intensity at a given frequency is proportional to the available combinations of the pump and Stokes pulse that have frequency differences at the CARS signal frequency. So the signal intensity is proportional to the square of the coherent excitation spectrum $A(\Omega)$ in eq 3. There is, however, another limiting factor. To generate higher frequency signals, two pulses with greater frequency differences have to be focused at the sample. Axial chromatic aberration (ACA) will cause the different color components of the laser pulses to focus at different axial positions, which translates to less spatial overlap between pump and Stokes pulses for the higher frequency CARS signals. We verified the effect of ACA qualitatively by comparing experiments using different microscope objectives with different ACA.

The spectral resolution is $\sim 35 \text{ cm}^{-1}$, which is a little broader than the two pixel width of the SLM (30 cm^{-1}) that defines the probe width (Figure 2b). The vertical scale in Figure 7 is the normalized difference D defined by eq 13. This scale (the units are $\sqrt{\text{counts}}$) corresponds to the field intensity of the nonamplified resonant CARS signal (note that the square of the field is equivalent to the photon counts). For example, the 1001 cm^{-1} peak of the toluene has $\sim 20 \sqrt{\text{counts}}$, so the actual resonant signal has ~ 400 counts in 10 ms. However, the signal-to-noise ratio is enhanced because of the homodyne amplification by the nonresonant signal.¹²

Figure 8 shows the sensitivity achieved thus far by the DQSI-CARS method. The samples are $\sim 1 \text{ M}$ sulfite, phosphate, and nitrite solutions in water, which have an order of magnitude less signal than the solvents shown in Figure 7. We estimate the number of molecules in the excitation volume ($\sim 40 \text{ aL}$) is around 40 attomoles ($\sim 2 \times 10^7$ molecules). The experimental conditions are exactly the same as in Figure 7. The nonamplified resonant CARS signal intensities ($|P_R^j|^2$) for these samples are just a few counts in the 10 ms experiment time, whereas the CCD readout noise is close to the actual peak signal level shown in Figure 8. Note that the signal-to-noise ratio (S/N) in Figure 8 is much greater than would be possible by detecting the nonamplified resonant signals with instrumental noise. Although the scale (D) shows the signal intensities quantitatively (note

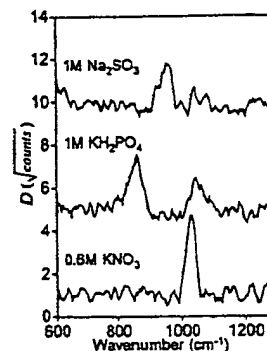


Figure 8. DQSI-CARS spectra of nitrite, phosphate, and sulfite solutions in water. The CCD exposure time is 10 ms. Each trace is displaced vertically for clarity.

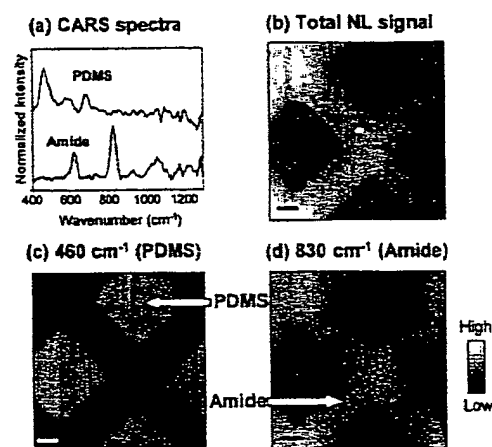


Figure 9. Chemical imaging of amide (*N,N*-dimethylformamide) inside a PDMS (poly(dimethylsiloxane)) template. (a) DQSI-CARS spectra of the amide and PDMS. (b) Image of the total nonlinear (NL) signal integrated over 400–1500 cm^{-1} . (c and d) Images constructed with peaks at (c) 460 cm^{-1} (PDMS) and (d) 830 cm^{-1} (amide), respectively. The scale bar is 2 μm . The pixel size in the image is 200 nm \times 200 nm. Note that these images are constructed from a single experimental scan, where each pixel in the image contains the complete spectrum from 400 to 1500 cm^{-1} .

that vertical traces are displaced for clarity in Figures 7 and 8), the signal-to-noise ratio (S/N) is improved significantly. The background noise here is mostly from the shot noise of the signal traces (S^i and S^j), which is orders of magnitude greater than the resonant signal. We verify this by comparing a theoretical shot noise calculation with the experiment. In a previous publication, we also showed that such samples would be difficult to measure with the original phase- and polarization-controlled CARS technique.¹²

If the sample has distinct CARS marker peak(s), which is the case for the PDMS/*N,N*-dimethylformamide (we refer to this as amide from now on) sample shown in Figure 9, the distinguishing vibrational band can be used for chemical imaging.³ Figure 9a shows the measured DQSI-CARS spectra of PDMS and amide. Here we use the 460 and 830 cm^{-1} peaks as separate markers for PDMS and amide, respectively, because these two peaks are isolated and distinctly characteristic of the two chemicals in the sample. Figure 9b first shows an image with a contrast that we call a "total nonlinear (NL) signal". If we integrate the raw data traces (S^i and S^j) from 400 to 1500 cm^{-1} , this quantity corresponds mostly to the intensity of the nonresonant signal at each spatial position. Since the nonresonant signal depends on the local polarizability, it can be a good

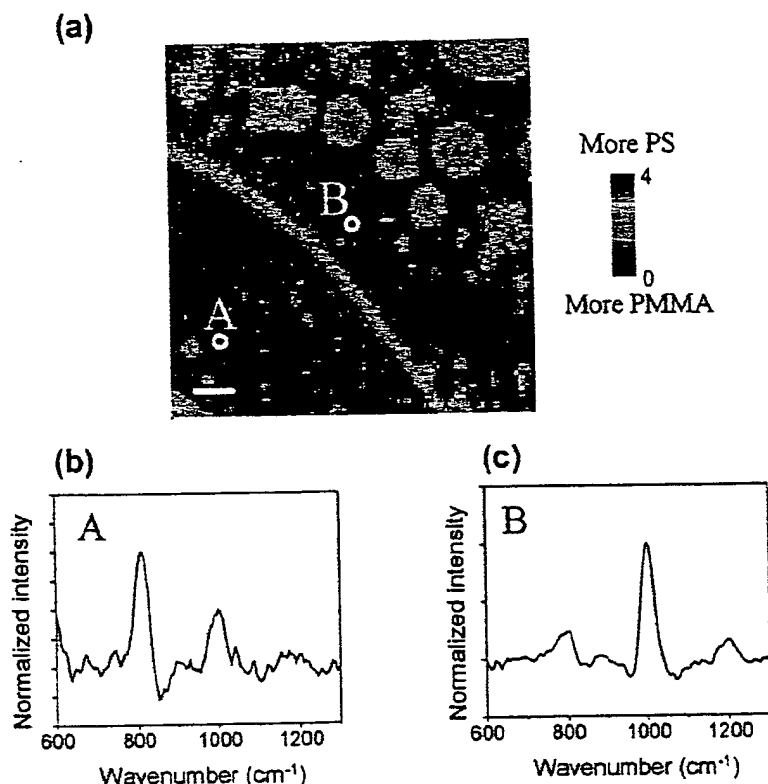


Figure 10. Chemical imaging of a polystyrene (PS)/poly(methyl methacrylate) (PMMA) mixture film. (a) Microscopic image constructed by the relative peak ratio between 1000 and 800 cm^{-1} . The color scale is from the relative peak ratio of 1000 cm^{-1} /800 cm^{-1} . The scale bar is 4 μm . The pixel size in the image is 400 nm \times 400 nm. The DQSI-CARS spectra at (b) location A and (c) location B marked in panel a. (b and c) The two spectra of the actual microscopic data. The image in panel a is constructed with 10 000 such spectral data.

contrast mechanism for polarizability and morphology changes, similar to third harmonic generation (THG) microscopy.²⁴ This gives a better signal-to-noise ratio in the microscopy image due to the orders of magnitude larger nonresonant signal levels than the resonant signals. However, this signal does not permit chemical contrast. We can use this image as a guide (topology and polarizability mapping) for samples with weak signals to find interesting spatial locations and to do longer scan(s) to measure the resonant CARS spectrum. Panels c and d of Figure 9 are the chemical images constructed by the characteristic peaks of the PDMS (460 cm^{-1}) and amide (830 cm^{-1}). All images are scanned with a data acquisition time of 10 ms per pixel. In this case one pixel is 200 nm. We integrate the peak intensity over $\sim 60 \text{ cm}^{-1}$ centered at the peak (note that the current spectral resolution is $\sim 35 \text{ cm}^{-1}$) after removing the background by subtracting a mean value at the two ends of the defined bandwidth of 60 cm^{-1} at each spectral data point. One can see that the contrast is reversed between the two images. In Figure 9c, the brighter contrast corresponds to the concentration of the PDMS, while in Figure 9d it corresponds to the amide. The amide has the same topography of the TEM copper grid and the PDMS has the opposite (negative) shape.

In a sample with chemical species that have overlapping CARS peaks it is not straightforward to apply the single peak imaging method demonstrated above. However, we can use spectral analysis to probe the local chemical identity. Figure 10a shows the chemical image of a spin cast film of a PS/PMMA mixture. We choose this sample for the demonstration, since PS and PMMA are known to phase-separate when cast into a film,²⁵ but both chemicals have peaks at similar positions (800 and 1000 cm^{-1}) in the present CARS window and similar spectral resolution. Thus, the single peak images,

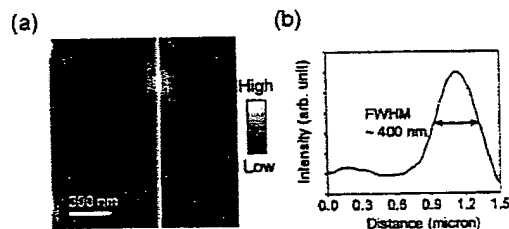


Figure 11. (a) Total nonlinear signal image of a PMMA bead (200 nm diameter). The image size is 1.5 μm \times 1.5 μm . The pixel size in the image is 15 nm \times 15 nm. (b) A line profile plot of the vertical cut-line shown in panel a.

such as in Figure 9c,d, are not appropriate for chemical mapping. Here the relative intensity of the two peaks is used as the contrast mechanism. Again we use a 60 cm^{-1} integration bandwidth centered at 800 and 1000 cm^{-1} and remove background by subtracting a mean value of two points at the ends of the 60 cm^{-1} bandwidth to calculate the peak intensity. In PS, the relative peak ratio (1000 cm^{-1} /800 cm^{-1}) is ~ 4 (Figure 10b), while in PMMA it is ~ 0.5 (Figure 10c). The color code is proportional to this peak ratio and directly related to the local chemical identity. One can see that PS-rich (upper right) and PMMA-rich (lower left) regions are separated nicely and there are some areas exhibiting a mixture and segregation of both chemicals in Figure 10a.

Figure 11a shows the total nonlinear signal image from a PMMA bead (200 nm diameter, Polyscience) attached to a glass coverslip. In Figure 11b, the profile plot of the marked cut-line in Figure 11a is shown. The full width at half-maximum (fwhm) is $\sim 400 \text{ nm}$ and the estimated point spread function has a fwhm of $(400^2 - 100^2)^{1/2} \approx 390 \text{ nm}$ assuming Gaussian distributions

of the PMMA bead signals and beam profiles.⁴ This spatial resolution is worse than a theoretical estimate of 230 nm, which is calculated for a 1.2 N.A., three-photon process and a diffraction-limited spot size from 800 nm wavelength. This discrepancy between the experimental and theoretical spatial resolutions can be attributed to various chromatic and achromatic aberrations, especially due to the broad bandwidth of the laser spectrum used in this paper. In other CARS reports, better spatial resolutions (<300 nm) have been demonstrated.^{3,4}

Depolarization of signals by a scattering sample is a problem in any polarization-based technique. In Silberberg's original polarization and phase-controlled CARS method,¹⁹ if a small amount of the signal is depolarized, the weak resonant signal is dominated by the leakage of an orders-of-magnitude larger nonresonant background. The shot noise from this background can easily obscure the resonant signal. In DQSI-CARS, the depolarization will also distort the spectral line shape and the baseline. Nevertheless, the shot noise from the local oscillator is already included in the resulting spectra (the function D , eq 13) and makes no change in the S/N ratio. The effect is similar to a nonpure local oscillator, i.e., distortion of the line shape. Therefore, DQSI-CARS is more tolerant to sample depolarization than the original polarization and phase-controlled CARS method.

There are some remaining issues to be solved, not just in our technique but also in a general multiplex CARS experiment.²⁵ First, the axial chromatic aberration (ACA) of the microscope objective can be a significant problem.⁹ We have tested several objectives and find that one IR objective (1.2 N.A. water immersion microscope objective, Olympus) has the least ACA within the present bandwidth of the laser. This is verified by looking at the relative intensities of the high-frequency vibrational peaks to the lower frequency ones. If one has significant ACA at the focus, it will show up as weaker relative signal intensities in the higher vibrational frequency peaks. If one wishes to use an objective with a significant ACA (for example, a special objective having a long working distance), the ACA has to be compensated before the microscope setup.⁹ Second, the bandwidth of the laser is still not broad enough to cover the entire fingerprint region. We can detect vibrational peaks from 400 to 1500 cm^{-1} , but the signal intensity decreases rapidly beyond 1200 cm^{-1} . The use of an oscillator with negatively chirped mirrors instead of prism pairs can provide much larger bandwidth, which covers the entire CARS vibrational spectral range,²⁶ but issues such as ACA and pulse compression with this large bandwidth have to be solved first.

Currently the sensitivity limit is that shown for the samples in Figure 8 with 10 ms experiment time. The sensitivity can be improved further by several approaches. First, if the available laser power is high enough, one can focus the laser pulse to a line, not a spot,²⁷ then image the entire line of spectra to a CCD to collect a significantly greater signal with a given time. Adopting this concept to DQSI-CARS can improve the sensitivity significantly. Second, the nonresonant signal will be greater with excitation by a broader bandwidth laser. With a larger local oscillator field, the amplification of the resonant signal will be enhanced. However, the pulse dispersion and ACA by a microscope objective has to be carefully corrected for such a pulse.

Here we demonstrated chemically selective microscopy by two simple methods: peak intensity and peak ratio imaging. A full spectral analysis with a known Raman spectrum will be more informative for chemical selectivity than single peak analysis. Even if there are no known Raman spectroscopic data,

or if complicated chemical identities at a spatial location make the assignment difficult, a linear discrimination analysis can be applied to classify the similarity between spatial positions.²⁸

V. Conclusion

In this paper, we demonstrated a number of results with a new interferometric CARS spectroscopy technique, which can extract a background free vibrational CARS spectrum with single laser pulses and amplify the resonant CARS signals via a homodyne mixing with the nonresonant signal as the local oscillator. It has a simple and very stable experimental setup. We verify chemically selective microscopy using the vibrational spectrum itself as the contrast mechanism. This new technique enhances the signal sensitivity significantly and removes the nonresonant background problem in CARS microscopy. It can be readily applied to most microscopic samples in material and biological studies.

Acknowledgment. The authors gratefully acknowledge the Department of Energy (Contract No. DE-AC02-05CH11231) for the instrumentation used in this research and the National Science Foundation, Division of Materials Research, for support of personnel. A.G.C. acknowledges support of a National Science Foundation Graduate Research Fellowship. O.N. acknowledges support of the Swiss National Science Foundation.

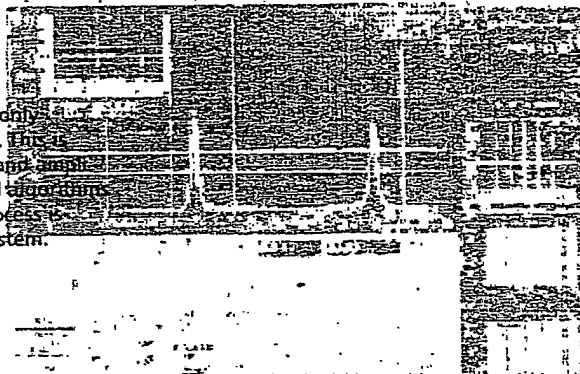
References and Notes

- (1) Cheng, J. X.; Xie, X. S. *J. Phys. Chem. B* 2004, 108, 827.
- (2) Muller, M.; Schins, J. M. *J. Phys. Chem. B* 2002, 106, 3715.
- (3) Potma, E. O.; Xie, X. S.; Muntean, L.; Preusser, J.; Jones, D.; Ye, J.; Leone, S. R.; Hinsberg, W. D.; Schade, W. *J. Phys. Chem. B* 2004, 108, 1296.
- (4) Zumbusch, A.; Holtom, G. R.; Xie, X. S. *Phys. Rev. Lett.* 1999, 82, 4142.
- (5) Cheng, J. X.; Volkmer, A.; Book, L. D.; Xie, X. S. *J. Phys. Chem. B* 2002, 106, 8493.
- (6) Levenson, M. D.; Kano, S. S. *Introduction to Nonlinear Spectroscopy*; Academic Press: San Diego, CA, 1988.
- (7) Dudovich, N.; Oron, D.; Silberberg, Y. *J. Chem. Phys.* 2003, 118, 9208.
- (8) Wurpel, G. W. H.; Schins, J. M.; Muller, M. *J. Phys. Chem. B* 2004, 108, 3400.
- (9) Kee, T. W.; Cicerone, M. T. *Opt. Lett.* 2004, 29, 2701.
- (10) Lin-Vien, D.; Colthup, N. B.; Fateley, W. G.; Grasselli, J. G. *The Handbook of Infrared and Raman Characteristic Frequencies of Organic Molecules*; Academic Press: San Diego, CA, 1991.
- (11) Oron, D.; Dudovich, N.; Silberberg, Y. *Phys. Rev. Lett.* 2002, 89, 273001.
- (12) Lim, S.-H.; Caster, A. G.; Leone, S. R. *Phys. Rev. A* 2005, 72, 041803.
- (13) Evans, C. L.; Potma, E. O.; Xie, X. S. *Opt. Lett.* 2004, 29, 2923.
- (14) Marks, D. L.; Vinegoni, C.; Bredfeldt, J. S.; Boppert, S. A. *Appl. Phys. Lett.* 2004, 85, 5787.
- (15) Marks, D. L.; Boppert, S. A. *Phys. Rev. Lett.* 2004, 92, 123905.
- (16) Dudovich, N.; Oron, D.; Silberberg, Y. *Nature* 2002, 418, 523.
- (17) Oron, D.; Dudovich, N.; Yelin, D.; Silberberg, Y. *Phys. Rev. Lett.* 2002, 88, 063004.
- (18) Oron, D.; Dudovich, N.; Yelin, D.; Silberberg, Y. *Phys. Rev. A* 2002, 65, 043408.
- (19) Oron, D.; Dudovich, N.; Silberberg, Y. *Phys. Rev. Lett.* 2003, 90, 213902.
- (20) Lepetit, L.; Cheriaux, G.; Joffe, M. *J. Opt. Soc. Am. B* 1995, 12, 2467.
- (21) Lozovoy, V. V.; Pastirk, I.; Dantus, M. *Opt. Lett.* 2004, 29, 775.
- (22) Delong, K. W.; Trebino, R.; Hunter, J.; White, W. E. *J. Opt. Soc. Am. B* 1994, 11, 2206.
- (23) Xia, Y.; Whitesides, G. M. *Annu. Rev. Mater. Sci.* 1998, 28, 153.
- (24) Oron, D.; Yelin, D.; Tal, E.; Raz, S.; Fachima, R.; Silberberg, Y. *J. Struct. Biol.* 2003, 147, 3.
- (25) Johnson, W. C.; Wang, J.; Chen, Z. *J. Chem. Phys. B* 2005, 109, 6280.
- (26) Ventec, Nanolayers Inc.
- (27) Oron, D.; Silberberg, Y. *J. Opt. Soc. Am. B* 2004, 21, 1964.
- (28) Schut, T. C. B.; Wolhuis, R.; Caspers, P. J.; Puppels, G. J. *J. Raman Spectrosc.* 2002, 33, 580.

Pulse Shaping with the MIIPS-Process

Jürgen Kolendä, Christian Mäus, Coherent (Deutschland)-GmbH, Dieburg, Germany

The full potential offered by ultra-short laser pulses can only be effectively used when the pulses can be manipulated. This is achieved by analysing them and optimising their phase and amplitude through a closed loop. Until recently, the setup and components were still at an experimental stage, but now a stable process is available that enables applications with a commercial system.



The manipulation of the phase and intensity of ultra-short laser pulses (pulse shaping) is becoming increasingly important in various fields of ultra-short pulse spectroscopy as well as material processing, for example, in order to produce higher harmonics or to further increase the peak power, respectively.

At the same time, the control of molecular reaction kinetics has become a widespread process in biophysics and biochemistry. With this technique, the phase-corrected laser pulses are used to drive molecules into defined target conditions. As the required quantum-mechanical descriptions are generally either very complex or are unknown for the individual process, the signal gained from the experiment is used in a feedback loop that optimises the pulse shape in accordance with the result [1,2].

Pulse shaping

Ultra-short pulses can reach extremely high peak intensities (amplified $>10^{18}$ W/cm²) and thus provide the opportunity to tread completely new paths in scientific and commercial applications. Nevertheless, the shorter the pulse, the more difficult it is to handle. Due to dispersion effects, broadband laser pulses generally lose their shape when they pass through optical components so that they are often already temporally dilated when they reach the sample under investigation [3]. As time periods in the fs-range cannot be directly modulated, the Fourier Transform is

used to represent the relationship between the time and the frequency domain; the temporal shape of a pulse can be manipulated by changing the phase function and the amplitude of the frequency components. A pulse is considered to be Fourier limited when the phases of the spectral components are constant across the complete spectral range. At the same time, this means that the pulse is temporally as short as can be permitted by the given bandwidth.

To fully utilise the complete potential of a pulse, it is thus necessary to exactly measure and, where necessary, correct the phases of the spectral pulse components. Pulse forming is usually achieved through the use of prisms, gratings and negative dispersion mirrors, but also active elements such as acousto-optic modulators or liquid crystal arrays (e.g. [4]). The latter permit the systematic manipulation of the phases and, consequently, the generation of special pulse forms (figure 1). When amplified pulses are the objects of manipulation,

the high intensities can quickly damage the pulse shaping components when the amplifier output is used directly. In addition, in most cases, power is lost through the limited transmission (usually $<50\%$) of the optical setups that are necessary. These problems can be avoided by placing the pulse shaping in front of the amplifier stage. As long as the downstream amplifier is operated at saturation, the losses will not affect the output power of the amplifier [5].

In conventional pulse shaping setups, measuring devices such as FROG [6] or SPIDER [7] are used for spectral analysis. These provide the feedback that sets the active pulse shaping components. These are complex measuring processes that usually require two copies of the same pulse to be generated – and at least an interferometer and a doubling unit have to be used. Genetic algorithms determine from the measurement data the direction and order of magnitude of the correction that is then transposed by the pulse shaping elements. Existing concepts, consequently, require at least two sophisticated optical components, a phase analyzer and a pulse shaper, to perform the measurement procedure and shape the pulse.

The optical components that form and detect the pulses have, until now, usually been developed or put together by the researchers themselves. An alternative is provided by a technology called "Multiphoton Intrapulse Interference Phase Scan", in short MIIPS,

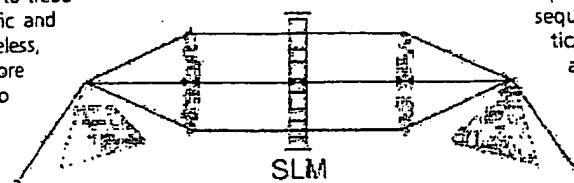


Figure 1: Typical setup of a pulse shaper with a SLM (Spatial Light Modulator). The various frequency components of the pulse are separated through a dispersive element and collimated through a lens. The characteristics of certain frequencies can be selectively manipulated through the individual pixels of the SLM. Following this, the pulse is brought back together again

developed by Prof. Marcos Dantus and his team at the Michigan State University [8].

The MIIPS process

MIIPS is based on a direct measurement at a single beam, making it insensitive to interferences. The phase information is directly taken from the frequency doubled spectrum (SHG spectrum) of the pulse being investigated. For analysis, a pulse shaping unit is used to impress a known reference function $f(\omega)$ onto the spectral phase of a pulse to at least compensate for local interferences of the phase through the unknown phase function of the pulse $\Phi(\omega)$. The sum of the reference function and the original phase function of the pulse is indicated through:

$$\varphi(\omega) = \Phi(\omega) + f(\omega) \quad (1)$$

The local intensity of the signal at the doubled frequency 2ω is the outcome of the square of an integral of all of the possible frequency combinations that occur in the pulse between the frequencies $\omega + \Omega$ and $\omega - \Omega$ with the respective positive and negative deviation Ω from the frequency being considered as ω :

$$S^{(2)}(2\omega) \propto \left| \int E(\omega + \Omega) E(\omega - \Omega) e^{i[\varphi(\omega + \Omega) - \varphi(\omega - \Omega)]} d\Omega \right|^2 \quad (2)$$

The phase exponent of the mixed signal within the pulse is consequently $\varphi(\omega + \Omega) - \varphi(\omega - \Omega)$. The SHG signal is at its strongest the nearer that this phase exponent tends towards 0 (Fourier limited pulse). In this case, the oscillating part of the integral above Ω ceases. As the phase function is continuous, the composite term can be written as a Taylor series:

$$\begin{aligned} \varphi(\omega + \Omega) - \varphi(\omega - \Omega) \\ = 2\varphi(\omega) + \varphi''(\omega)\Omega^2 + \dots + \frac{2}{(2n)!} \varphi^{(2n)}(\omega)\Omega^{2n} \end{aligned} \quad (3)$$

for which, at first approximation, the higher order terms can be disregarded. The SHG signal consequently reaches a local maximum, when $\varphi''(\omega)$ tends towards 0. From (1) the following results for this case:

$$\varphi''(\omega) = -f''(\omega) \quad (4)$$

To determine the phase deviation across the complete spectrum, the reference function is extended by a variable parameter δ that is continuously scanned. In this way, for each frequency ω a $\delta_m(\omega)$ can be determined with which the SHG signal can reach its maximum. The original phase position within the pulse can, therefore, be determined for the complete spectrum through the two-time integration of $-f''(\omega, \delta_m(\omega))$.

As reference a sinus function of the form $a \sin(\gamma\omega - \delta)$ is usually used, whereby the phase variable δ is scanned across 4π . The sinus function is particularly suitable for this as it limits the phase shift applied by the pulse shaper, however, in principle other functions can also be used. For each δ a SHG spectrum is taken. The three-dimensional representation of the SHG-intensity in accordance with the pulse frequency and the scan parameter δ in figure 3 shows a number of so-called MIIPS-traces. The parameters of the maximum SHG intensity can be read from these traces. The $\delta_m(\omega)$ of two neighbouring MIIPS-traces is used for the analysis and calculation of the phase correction, which increases the accuracy. In the same way, the accuracy of the process increases as the phase deviation to be corrected decreases [9]. For this reason, the process is frequently repeated, whereby the sum of the previously determined correction functions is used as the starting point of the next run or for the final correction through the pulse shaper. This in general lowers the phase deviation across the complete area of the spectrum used to less than 0.1 rad.

The MIIPS system

In the commercial MIIPS implementation "Silhouette", the pulse shaper box consists of a zero-dispersion pulse stretcher (4f-setup), a liquid crystal spatial light modulator (SLM) as well as a spectrometer. This is fiber coupled to the sampling head that primarily consists of a thin doubling crystal

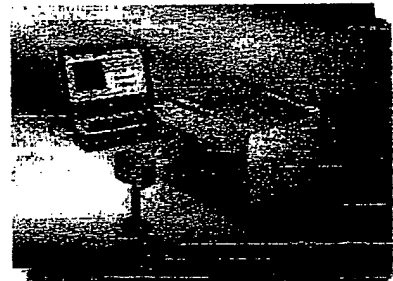


Figure 2: Actual implementation: The Silhouette MIIPS system

that enables broadband phase matching. The measured signals are transmitted through the fiber to the spectrometer in the pulse shaper box. A USB port is provided to enable the connection of a laptop computer for the evaluation of the spectrum, control of the liquid crystal SLM and output of the pulse data. An additional liquid crystal array enables the amplitude of the individual frequency components to be directly manipulated. The shaper box is generally installed directly after the oscillator whereas the small flexible sampling head can be installed at any point within an experimental setup. This is the position at which the phase components are to be compensated, for example at the exact position of the sample being examined. As standard, the system can be adjusted for two different bandwidths. The 128 pixel liquid crystal arrays can modulate spectral regions of 100 nm or 200 nm. The total loss in average power is less than 30%.

Pulse shaping behind the ultra-short pulse oscillator

The first example is the direct shaping of pulses behind an ultra-short pulse oscillator. The oscillator (in this case a Micra-5) has a variable bandwidth between 30 nm and 100 nm and an average power of approx. 400 mW. The repetition rate can be varied between 76 MHz and 82 MHz. The use of pulse shaping and prism compensation enables a pulse duration of

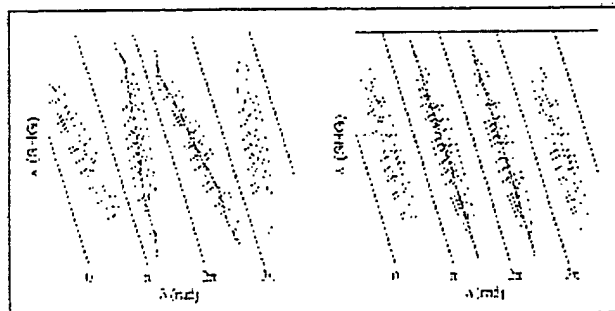


Figure 3: MIIPS trace of an uncompensated pulse (left). The trace of a perfectly compensated pulse shows, with a sinus reference function, straight parallel lines at the distance π (right). Linear chirp changes the distance of the lines to each other, square chirp portions change the angle, and high order interference causes curvatures to be introduced. Fundamental information about the characteristics of the phase within a pulse can be immediately read from the MIIPS trace

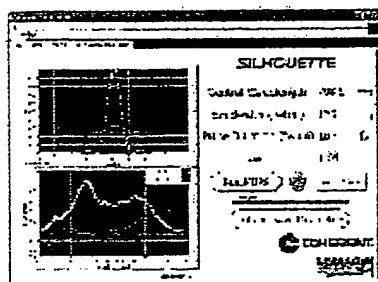


Figure 4: Compressed pulse from a Micra-5 fs oscillator near to the transform limit. The pulse duration measured here is 10.4 fs



Figure 5: Pulse manipulation of a Micra oscillator for CARS - spectroscopy. The results are two coherent pulses with almost identical bandwidth and intensity, but a spectral separation of approx. 88 nm

10.4 fs to be reached, instead of 16 fs if only prism compensation is used (figure 4). In addition, the system enables (any) two components to be selected from the spectrum of the laser, as shown in figure 5. In this way an oscillator is simulated that emits two colours at the same time, in this case 770 nm and 855 nm. Spectral behaviour of this kind is required for a variety of applications, for example in CARS (Coherent Anti-Stokes Raman Scattering) spectroscopy.

Pulse shaping in an amplifier system

In the second example, the Silhouette is inserted between the oscillator and amplifier in a short pulse system similar to that shown figure 6. The oscillator in this setup is, once again, the Micra system described above. The amplifier used in this case is a Legend USP HE, a purely regenerative amplifier with more than 3 mJ pulse energy at 1 kHz repetition rate. Two experiments were carried out; firstly only phase correction was used to optimally compress the bandwidth directly emitted from the amplifier of typically 28-32 nm so as to obtain and specify a pulse

duration of <30 fs (<35 fs without Silhouette). The second experiment addressed the "gain narrowing" in the active medium (Ti:Sapphire), i.e. the spectral constriction through the amplification process. This limits the amplified bandwidth and, in turn, the achievable pulse duration. Through the selective reduction of the amplitude of the central spectral components by at 800 nm before seeding, the attainable bandwidth from the amplifier could be considerably increased. A (transmitted) bandwidth of >51 nm was generated, compressable to 26.3 fs by phase optimisation (figure 7). This improved the complete oscillator/amplifier system and shortened the pulse duration by approx. 25% without affecting the output energy.

The MIIPS-process enables the performance of almost any commercially available or purpose-built laser system with a pulse duration of less than 60 fs to be improved or optimised. Particularly important for the user is that the commercial implementation of the system guarantees constant pulse duration and bandwidth limited pulses at the push of a button - reproducible every day, without time-consuming procedures to optimise the dispersion compensation within the individual components of the laser system.

Literature

- [1] A. Assion, T. Baumert, M. Bergt, T. Brämer, B. Kiefer, V. Seyfried, M. Strehle, G. Gerber, Control of Chemical Reactions by Feedback-Optimized Phase-Shaped Femtosecond Laser Pulses, *Science* 30, Vol. 282, No. 5390, pp. 919-922, Oktober 1998
- [2] A.M. Weiner, Femtosecond pulse shaping using spatial light modulators, *Review of Scientific Instruments*, Volume 71, Issue 5, pp. 1929-1960, Mai 2000

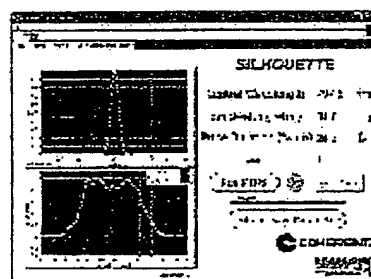


Figure 7: Pulse manipulation enables the pulse duration to be shortened by approx. 25%, almost at the transform limit and with minimum phase error

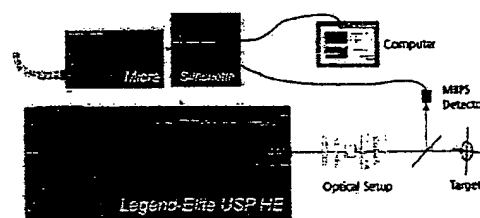


Figure 6: Setup for phase manipulation. The Silhouette pulse shaper is placed between the seed laser (Micra) and amplifier (Legend-Elite). The pulse length can be optimised either directly behind the amplifier or behind the optical setup directly at the experiment

- [3] S. Butcher, B. Resan, A. Fry, J. MacKay, Multiphoton approach shapes ultrafast pulses, *optics.org* article 24896, May 2006
- [4] F. Lindner, G. Paulus, F. Grasbon, A. Dreischuh, H. Walther, Dispersion Control in a 100 kHz-Repetition-Rate 35-fs Ti:Sapphire Regenerative Amplifier System, *IEEE Journal of Quantum Electronics*, Vol. 38, No. 11, 1465, November 2002
- [5] I. Pastirk, B. Resan, A. Fry, J. MacKay, M. Dantus, No loss spectral phase correction and arbitrary phase shaping of regeneratively amplified femtosecond pulses using MIIPS, *Optics Express*, Vol. 14, No. 20, 9537-9543, October 2006
- [6] S. Aktürk, R. Trebino, S. Gu, M. Kimmel, FROG für extrem kurze und relativ lange Ultrakurzpulse, *Photonik* 2/2005, S. 54
- [7] A. Monmayrant, S. Gorza, P. Wasylczyk, I. Walmsley, Jenseits der Beugungsmuster: SPIDER - die Anatomie ultrakurzer Laserpulse, *Photonik* 6/2006, S. 44
- [8] M. Dantus, V. Lozovoy, I. Pastirk, Analogous to a femtosecond Wheatstone bridge, the MIIPS system can perform pulse characterization and compensation rapidly and efficiently, *spies's oemagazine*, 15-17, September 2003
- [9] B. Xu, J.M. Gunn, J.M. Dela Cruz, V.V. Lozovoy, M. Dantus, Quantitative investigation of the multiphoton intrapulse interference phase scan method for simultaneous phase measurement and compensation of femtosecond laser pulses, *JOSA B* 23 No.4, 750-759, April 2006

Author contact:

Dr. Jürgen Kolenda
Marktentwicklung Kurz-
pulsverstärker D, A, Benelux
Coherent (Dtl.) GmbH
Dieselstr. 5b
64807 Dieburg
Germany
Tel. +49/6071/968-204
Fax +49/6071/968-499
eMail: juergen.kolenda@coherent.com
Internet: www.coherent.de

Christian Maus
European Sales
Support Manager
Coherent (Dtl.) GmbH
Dieselstr. 5b
64807 Dieburg
Germany
Tel. +49/6071/968-211
Fax +49/6071/968-499
eMail: christian.maus@coherent.com
Internet: www.coherent.de

Multiphoton approach shapes ultrafast pulses

A new method of phase and amplitude control delivers near-transform limited pulses, even after passing through complex beam delivery systems such as multiphoton excitation microscopes. **Steve Butcher** and colleagues from Coherent explain.

Ultrafast laser pulses present unique challenges and offer unique opportunities to study structures and processes in biology, physics and photochemistry. As femtosecond pulsewidths are pushed to ever shorter durations, the performance of the laser system and the overall experiment are often limited by subtle phase and amplitude effects.

Phase errors arise from group velocity dispersion (GVD) induced by virtually every optic within the laser and beam delivery system. Until recently, commercial and user-built tools to counteract these phase delays have been cumbersome to implement and/or limited in their scope of success. Now, a closed-loop method provides complete turnkey control of pulse phase over the entire spectral bandwidth of any ultrafast laser.

This turnkey method can easily be used to correct phase effects from an entire experimental system—including downstream beam delivery optics such as those found in multiphoton excitation (MPE) microscopes. The same pulse measurement and shaping technology can be configured to arbitrarily shape the pulse's amplitude in order to correct for gain narrowing or gain saturation, to produce a shorter transform limit, or to select or block specific wavelength segments. This pulse control method can also be used to produce custom temporal shapes, including double pulses.

The transform limit and GVD

In a mode-locked Ti:sapphire laser oscillator, interference between the longitudinal cavity modes yields a single pulse circulating in the laser cavity. When there is no phase delay between the modes, the result is a so-called transform-limited pulsewidth. Spectral bandwidth and temporal pulsewidth are related through a Fourier transform: a wider spectral bandwidth gives more longitudinal modes that interfere and result in a shorter transform limit (see figure 1).

But in real world ultrafast laser systems, this transform limit is rarely reached. Even if it is reached within the laser, the pulse is chirped (stretched) to some degree by subse-

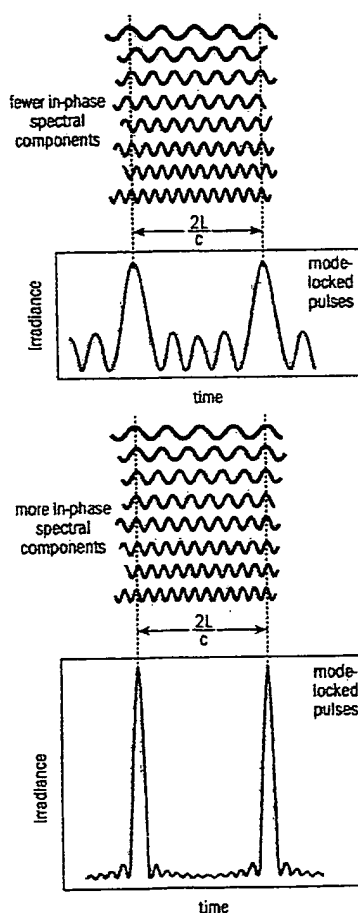


Fig. 1: In a mode-locked laser, the fixed phase relationship between the continuous-wave cavity modes gives rise to interference that causes these modes to collapse to a single pulse circulating around the laser cavity. If this phase relationship is compromised, this leads directly to a pulsewidth that is longer than the transform limit.

quent beam delivery optics before it reaches the interaction zone of the experiment as a result of GVD.

GVD refers to the fact that the velocity of

light in any medium is a function of wavelength. Materials such as glass lenses, multi-layer optical coatings and laser crystals are all dispersive and can impart significant GVD. Most of these materials exhibit positive dispersion where longer wavelengths travel at a higher velocity than shorter wavelengths. For this reason, a high-performance laser oscillator contains some form of optical arrangement that provides negative dispersion in an attempt to counteract intracavity GVD effects.

The problem can be even more complex in a system that includes an amplifier. Here, the oscillator pulse is deliberately chirped by orders of magnitude before it is injected into the amplifier. This avoids high peak-powers that could damage the optics inside of the amplifier. The amplified exit pulse is then re-compressed. Both the stretcher and the compressor usually consist of a pair of matched diffraction gratings. In principle, the compressor perfectly restores the original shape of the pulse. However, in practice, undesirable phase (and amplitude) modifications can occur within the amplifier, where every optic imparts its own specific dispersion profile to the pulse. The end result is that the group velocity delay can have a complex, nonlinear dependence on wavelength.

An amplifier can also affect the amplitude (spectral profile) of an ultrafast pulse due to gain narrowing or gain saturation. Gain narrowing occurs because the amplifier gain is peaked at its centre wavelength. Every time the pulse passes through the Ti:sapphire crystal, the centre is amplified more than the wings of the pulse, making it successively narrower. In addition to modifying the spectral profile, gain narrowing lengthens the pulsewidth that is obtained after re-compression, because of the transform relationship between spectral bandwidth and pulsewidth.

Controlling phase with an SLM

The ideal phase correction tool would be a flexible, programmable method that adjusts phase as a function of wavelength. This can

PULSE SHAPING

be accomplished by using a programmable phase mask in conjunction with a zero dispersion stretcher. This type of stretcher laterally spreads the pulse as a function of wavelength and then recombines it in a way that does not chirp the pulse. In the middle of the stretcher, at the so-called Fourier plane, the beam is parallel (collimated) with a linear mapping of wavelength to lateral displacement (see figure 2).

A linear liquid crystal array, often called a spatial light modulator (SLM), can then be used as a programmable phase mask at this location. Increasing the voltage at any of the SLM pixels retards the phase of light passing through that pixel. For an array with 128 pixels, the spectral bandwidth of the laser pulse is divided into 128 equal segments and the phase of each of these wavelength segments can be arbitrarily changed by adjusting the voltage to that pixel. This type of phase correction tool is normally inserted between the oscillator and the amplifier, so that any losses it introduces have minimal effects on the final system power.

This approach can provide a flexible and rigorous correction of phase distortion but it is potentially very difficult to implement as 128 different voltage values are required. In principle it is possible to use a pulse diagnostic instrument such as a FROG (Frequency Resolved Optical Gating) or SPIDER (Spectral Phase Interferometry for Direct Electric-field Reconstruction) to first measure the phase characteristics of the pulse as a function of wavelength. These parameters are then used to calculate phase correction parameters and then actual voltage values for the liquid crystal array.

But even for a skilled laser operator familiar with these calculations, this process would require two or three manual iterations to get an optimum result: a compressed pulse at < 1.1 times the transform limit. While rigorous and successful, this is not a solution that could be widely used.

Integrated MIIPS

Fortunately, a new method of phase and amplitude characterization has been developed that has led to an integrated, turnkey pulse measurement and correction solution based on a liquid crystal array. This method, pioneered by Marcos Dantus and co-workers at Michigan State University, US, uses a measurement tool called MIIPS (Multiphoton Intrapulse Interference Phase Scan). Using this approach, the researchers have demonstrated pulses of less than 1.001 times the transform limit.

The basic principles of MIIPS are fairly straightforward. Importantly, MIIPS is a single beam technique that does not require an

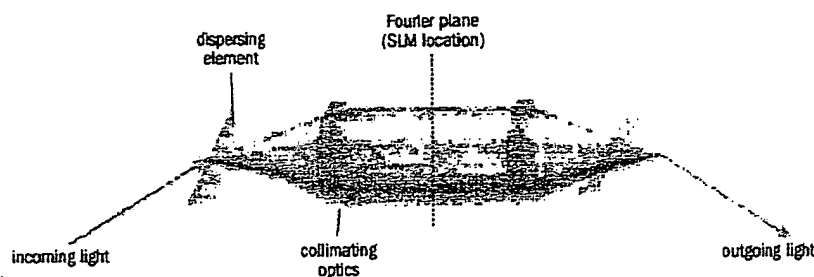


Fig. 2: In a zero-dispersion pulse stretcher, a grating spreads the pulse laterally at the so-called Fourier plane. At this location wavelength maps linearly with X-axis location.

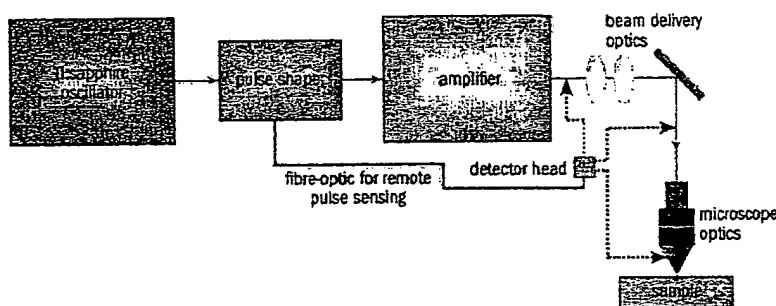


Fig. 3: an integrated approach with a remote fibre-coupled SHG sensor head, enables phase and/or amplitude correction wherever this head is used to sample the ultrafast pulse.

interferometer. Instead, it uses the already described liquid crystal phase mask approach to impose a known (reference) phase delay function on the laterally dispersed ultrafast beam. The overall phase delay of the beam as a function of wavelength is a combination of the existing phase delay due to the laser optics and this applied reference function.

The re-compressed beam is then sampled using a beamsplitter or mirror and directed into a thin nonlinear crystal designed for second harmonic generation (SHG). In practice a 0.05 mm-thick beta barium borate crystal is used to enable broadband phase matching. This is followed by a spectrometer and CCD detector that measures the SHG intensity as a function of wavelength. This approach yields second derivative data about the spectral phase, which is then integrated by the software to retrieve the original spectral phase of the beam.

Coherent has now exclusively licensed this technology and will launch a turnkey phase control system based on this approach at CLEO 2006 in Long Beach, California, US. This new product, called Silhouette, consists of the phase correction box and a separate fibre-coupled detector.

The integrated correction box contains a low-loss, adjustable bandwidth stretcher

and the liquid crystal SLM. The compact detector head contains the thin SHG crystal, which is then fibre-coupled to a spectrometer. System software and a dedicated laptop controller automatically acquire the SHG intensity readings and iteratively adjust the liquid crystal voltages to create the desired phase profile across the laser's spectral bandwidth. The uncorrected and corrected phase information can also be directly accessed by the operator.

For researchers who also want amplitude control as a function of wavelength, a second version will be available in which the single LCD array is replaced with a double array that incorporates a polarizer. Here, each of the 128 elements can also act as a variable amplitude attenuator. The transmitted intensity is controlled by the voltage to the two LCD arrays.

In most instances, the optimum location for the pulse shaping system will be between the oscillator and amplifier (see figure 3). But the fibre-coupled detector head means that it can be inserted at any arbitrary location in the laser system or delivery optics, and the phase and/or amplitude will be re-shaped at that point. In applications where the pulse characteristics of the experimental set-up may change with time, for example in a poorly temperature-controlled environment,

the system can re-sample the phase and/or amplitude and quickly make any necessary corrections.

This approach will allow laser operators with limited expertise to take even a poorly corrected ultrafast laser set-up and do two things. First, phase errors can be corrected to achieve a transform-limited pulse. Second, the spectral profile can be broadened so that this transform limit is even shorter than is possible without pulse-shaping.

For more sophisticated users, the system provides complete access to the uncorrected and corrected phase and amplitude information. In addition, this system can be used to arbitrarily modify the phase and amplitude profile of ultrafast pulses to create some other interesting possibilities. This

includes the ability to switch the wavelength of a broadband pulse to selectively excite one of the multiple fluorophores in a MPE microscope. The user can also create a double pulse profile with the pulse pair closely spaced in time, for coherent studies on fast processes such as wave packet evolution in real-time molecular dynamics. For telecom applications the pulse-shaper enables the generation of a multiwavelength spectrum for WDM or high repetition rate pulse bursts for OTDM.

Conclusion

Ultrafast laser builders and users have long struggled to obtain the elusive transform-limited output pulse with varying degrees of success. Even with highly corrected systems

that approach (i.e. < 1.5 times) the transform limit, the downstream beam delivery optics generally stretch the pulse.

A new integrated approach based on MIIPS allows any commercial or user-built laser system to be interrogated and modified at any point within the entire experimental set-up, including at the focus of an MPE microscope. What's more, the same tool can be used to programme subtle effects into the beam for novel ultrafast experiments.

The authors of this article are Steve Butcher, Bojan Resan, Alan Fry and John MacKay of Coherent, Inc. Steve Butcher is a senior product manager at Coherent. For more information about the new Silhouette product e-mail steve.butcher@coherent.com or see www.coherent.com.

Modified spectrum autointerferometric correlation (MOSAIC) for single-shot pulse characterization

Daniel A. Bender* and Mansoor Sheik-Bahae

Department of Physics and Astronomy, Optical Science and Engineering Program, University of New Mexico, Albuquerque, New Mexico 87131, USA

*Corresponding author: dnbender@unm.edu

Received July 10, 2007; accepted August 10, 2007;

posted August 22, 2007 (Doc. ID 85149); published September 25, 2007

A method for generation of the modified spectrum autointerferometric correlation that allows single-shot pulse characterization is demonstrated. A sensitive graphical representation of the ultrashort pulse phase quality is introduced that delineates the difference between the presence of temporal and spectral phase distortions. Using these schemes, full-field reconstruction of ultrashort laser pulses is obtained in real time using an efficient iterative technique. © 2007 Optical Society of America

OCIS codes: 320.7100, 140.7090.

Detailed characterization of ultrashort laser pulses is vital for many applications. There exist many pulse characterization techniques with varying experimental and/or computational complexity. These range from interferometric autocorrelation (IAC) [1] to full-field reconstruction techniques such as frequency-resolved optical gating (FROG) [2] and spectral shear interferometry for direct electric field reconstruction (SPIDER) [3]. Adaptive pulse characterization techniques such as multiphoton intrapulse interference phase scan (MIIPS) [4] have been successful not only in retrieving the electric field but in compensating the spectral phase to achieve transform-limited pulses. In many applications, full-field reconstruction may not be required, although sensitive real-time information on phase distortions due to the presence of chirp and dispersion is still essential. Modified spectrum autointerferometric correlation (MOSAIC) was developed to address this need using the information contained in an IAC trace and has been shown to be far more sensitive to pulse chirp than a traditional IAC [5]. The new advances in the implementation of MOSAIC are the following.

- (a) Single-shot characterization using a combination of fringe-free (noninterferometric) autocorrelation and second-harmonic spectrum
- (b) A hybrid graphical representation that distinguishes between spectral and temporal phase distortions
- (c) Real-time full-field reconstruction using the above schemes with an efficient sequential search algorithm

Naganuma *et al.* showed that the pulse spectrum and IAC provide a sufficient dataset to uniquely reconstruct the complex electric field, with only a time-direction ambiguity [6]. Retrieval techniques such as phase and intensity from correlation and spectrum only (PICASO) [7] make use of a similar three envelope dataset. The usefulness of MOSAIC was extended by use of homodyne operation and signal averaging [8]. High-fidelity MOSAIC traces were recovered in the presence of extreme noise. This fringe-free averaging technique measures the upper

and lower MOSAIC envelopes with a very high signal-to-noise ratio (SNR) and allows us to clearly distinguish pulses that produce essentially identical IAC traces [9]. The fringe-free MOSAIC technique has recently been used to characterize ultrashort pulses in the mid-IR [10].

The increased SNR found on averaged MOSAIC traces extends the utility of all retrieval techniques using the dataset outlined by Naganuma *et al.* [6]. By combining MOSAIC data with the first-order interferogram and performing additional analysis, the spectral phase of the electric field can be recovered [11]. A number of synthesized pulses of varying complexity were shown to be reconstructed successfully using an iterative method. Retrieval methods using MOSAIC are similar to PICASO but provide the advantages of time-domain signal averaging and straightforward visual chirp interpretation.

The principle of computing a MOSAIC can be described in the frequency domain as follows: a second-order IAC waveform with a fringe frequency Ω is Fourier transformed to generate a spectrum. Spectral filtering is then performed to remove the Ω component and amplify the 2Ω component by a factor of 2. An inverse Fourier transform generates a new time-domain signal known as a fringe-resolved MOSAIC [5]. The upper envelope is replaced by the intensity profile while the lower envelope—identified by two shoulders above the baseline—provides background-free phase information. Examples are shown in Fig. 1 (solid curves). The presence of shoulders is a signature of temporal pulse chirp while a flat baseline is an indication of a flat temporal phase [12].

In the (delay) time-domain analysis, the maximum and minimum envelopes of MOSAIC are given by the intensity autocorrelation, $g(\tau) = \int f(t)f(t+\tau)dt$, and the difference computation, $S_{\min} = g(\tau) - |g_p(\tau)|$, respectively [8]. The amplified 2Ω component of the IAC is expressed as

$$g_p(\tau) = \int f(t)f(t+\tau)e^{2i[\phi(t)-\phi(t+\tau)]}dt, \quad (1)$$

which is also the envelope of the second-harmonic field autocorrelation. The temporal chirp is represented by $\phi(t)$, while $f(t)$ is the intensity of the pulse. The second-harmonic field autocorrelation is related to the second-harmonic spectrum by

$$|g_p(\tau)| = |F^{-1}(|E^2(\Omega)|^2)|, \quad (2)$$

where the second-harmonic power spectrum is represented by $|E^2(\Omega)|^2$ and F^{-1} denotes the inverse Fourier transform operation. For single-shot arrangements, fringe-resolved second-order IAC traces are not practical to produce. The method we present here overcomes this obstacle by making use of the intensity autocorrelation and second-harmonic generation (SHG) spectrum. We call this envelope-MOSAIC or E-MOSAIC, which can be very useful for characterizing ultrashort pulses from low repetition rate (approximately kilohertz) amplified laser systems.

In a proof-of-principle demonstration, E-MOSAIC is compared with MOSAIC in the following experiment. A second-order IAC is produced with mode-locked 85 fs Ti:sapphire laser pulses centered at a wavelength of 825 nm using SHG. An SHG spectrum is collected by blocking the delay arm and routing the frequency-doubled output to an Ocean Optics HR4000 spectrometer with an 8 μm optical fiber. The inverse Fourier transform of the second-harmonic power spectrum is computed over a spectral bandwidth consistent with the total time delay of the intensity autocorrelation. The resulting time-domain trace is normalized to the intensity autocorrelation and subtracted from the intensity autocorrelation to produce S_{\min} [see Fig. 1(a), open circles]. This result is compared with S_{\min} and the intensity autocorrelation obtained from the second-order IAC using the same experimental setup [Fig. 1(a), solid lines]. The excellent agreement between the two approaches validates the fidelity of E-MOSAIC. Next, we deliberately chirp the laser pulse prior to the autocorrelator by passing it through a 2 mm thick ZnSe window and perform the same operations described above. Results presented in Fig. 1(b) again show clear agreement.

Temporal chirp interpretation from a MOSAIC trace is typically straightforward, as evidenced by the appearance of shoulders in the minimum envelope. As Fourier analysis indicates, however, spectral

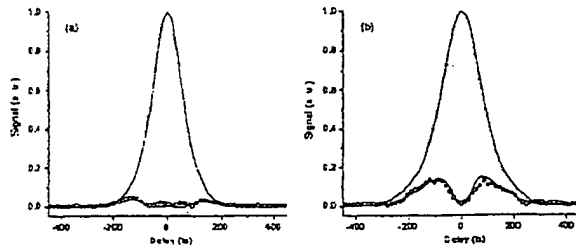


Fig. 1. MOSAIC traces obtained from (a) 85 fs Ti:sapphire laser and (b) intentionally chirping the laser pulse with 2 mm of ZnSe. MOSAIC rendered from an SHG spectral measurement (circles) and a second-order IAC (solid curve).

phase distortion (dispersion) does not necessarily imply temporal phase distortion (chirp). For example, a pulse having a symmetric spectrum and only third-order dispersion (TOD) will exhibit a flat MOSAIC minimum but is not transform limited. Conversely, in the instance of an asymmetric spectrum and flat spectral phase, the MOSAIC trace will exhibit a non-zero minimum envelope while the intensity autocorrelation is bandwidth limited. To accommodate these situations, we introduce an enhanced representation of the MOSAIC trace that is distinctly sensitive to both spectral dispersion and temporal chirp in pulse distortions. The added sensitivity requires the pulse spectrum in addition to second-order IAC. In rapid-scan IAC schemes, this can be obtained by adding a linear detector to the same interferometer [8,11]. This enhanced representation is displayed in the form of a hybrid (H)-MOSAIC. An H-MOSAIC trace is produced by assigning a flat phase across the measured pulse spectrum and computing the transform-limited intensity autocorrelation, $g^{TL}(\tau)$, which is then normalized to $g(\tau)$ at $\tau=0$. The difference between the transform-limited and measured intensity autocorrelation is computed. A symmetric double-hump appears for broadened pulses while a transform-limited pulse is flat. Accounting for symmetry with respect to zero delay, we take the average of both halves in both the difference computation and the measured lower MOSAIC envelope, $g(\tau) - |g_p(\tau)|$. We define the lower envelope of H-MOSAIC as

$$S_{HYB}(\tau) = \begin{cases} g(\tau) - g^{TL}(\tau) & \text{for } \tau < 0 \\ g(\tau) - |g_p(\tau)| & \text{for } \tau \geq 0 \end{cases} \quad (3)$$

The upper envelope of H-MOSAIC is $g(\tau)$. The lower envelope of H-MOSAIC is sensitive to spectral dispersion for $\tau < 0$ and temporal chirp for $\tau \geq 0$. It is important to note the nonorthogonality of the H-MOSAIC peaks, i.e., in general dispersion can give rise to a temporal chirp and vice versa. In Fig. 2 we

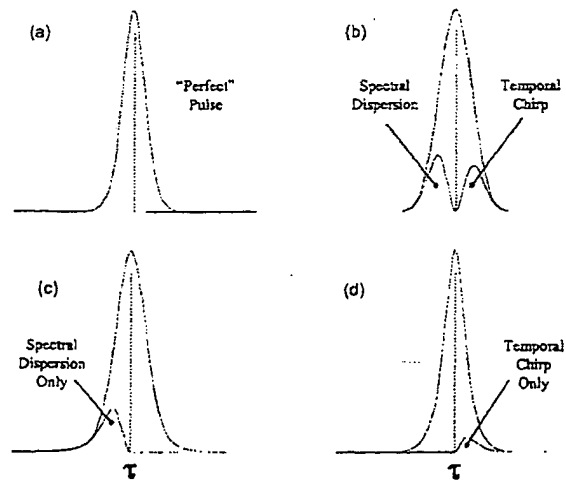


Fig. 2. Simulation of H-MOSAIC for a pulse having a symmetric spectrum with (a) no dispersion, (b) GVD, (c) TOD, and (d) asymmetric spectrum with no dispersion. The dashed line indicates zero delay.

present H-MOSAIC simulations for the special cases of a pulse having a symmetric spectrum with (a) no dispersion, (b) group-velocity dispersion (GVD) only, and (c) TOD only. The pulse distinguished by the trace in (a) can be regarded as the "perfect pulse", symmetric in time and frequency, and without chirp or dispersion. Any small deviation from this symmetry will appear as shoulders in the H-MOSAIC traces. Note that in case (c) when only TOD is present we will have $g(\tau) - |g_p(\tau)| = 0$. Displayed in part (d) of Fig. 2 is an H-MOSAIC produced from an asymmetric spectrum and flat spectral phase. This is transform limited, which leads to $S_{HYB}(\tau) = 0$ for $\tau < 0$ because of the flat spectral phase. We note that there is no new information in H-MOSAIC that is not already present in a MOSAIC trace (or IAC) and spectrum. However, an H-MOSAIC trace extracts and renders such information in an easily identifiable graphical representation.

The H-MOSAIC trace is a visual representation of the dataset used in one-dimensional retrieval schemes. Experimental reconstruction using MOSAIC and the pulse spectrum has been demonstrated using an iterative line minimization technique [11]. In this reconstruction method, all points in the spectral phase are optimized individually at the expense of processing time. We can reduce the processing time $\sim 7\times$ by analyzing phase with a fourth-order Taylor-series expansion and adjusting the coefficients. Our retrieval algorithm is implemented by sequential optimization of the Taylor-series coefficients and works by first optimizing GVD, then TOD and if needed fourth-order dispersion. This sequence accounts for the prominence of the lower-order spectral phase coefficients encountered in realistic pulses and gives direct insight to the order of dispersion on a pulse possessing a Taylor expandable phase.

We use the sequential optimization technique to reconstruct the electric field from the measured pulse spectrum and MOSAIC of Fig. 1(b). An iterative simplex algorithm minimizes the root-mean-square (rms) error, Δ . Minimization of the rms defines convergence of the algorithm. The measured spectrum and retrieved spectral phase from retrieval (R)-MOSAIC are shown in Fig. 3(a). Execution of the sequential reconstruction algorithm using 128 points is accomplished on a laptop computer in less than 1 s with a 1.8 GHz Centrino Duo processor for $\Delta = 0.0072$. This minimum achievable rms error is set by experimental noise and higher-order phase terms not accounted for in the Taylor-series phase expansion.

Further reduction of rms error can be obtained by individual optimization of each point in the spectral phase using a line-search method similar to [11]. Our line-search algorithm is seeded with the sequential reconstruction result and run until a new minimum achievable rms is found. The retrieved phase and re-

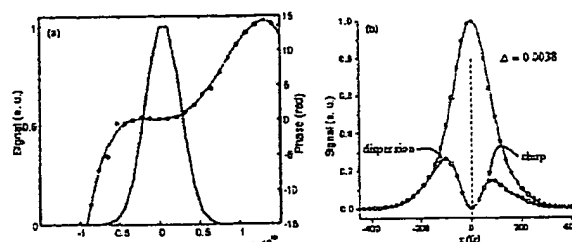


Fig. 3. (a) Measured spectrum (solid curve) and retrieved phase (dashed curve) from the R-MOSAIC algorithm. The retrieved phase from an individual point line search is reproduced (dots). (b) Experimental H-MOSAIC (solid curve) and reconstructed H-MOSAIC (circles) from the phase (dots) and measured spectrum of (a).

constructed H-MOSAIC trace are depicted in Fig. 3(a) (dots) and Fig. 3(b) (circles), respectively. Processing time increases to ~ 30 s, giving a reduction of rms error from 0.0072 to 0.0038. We find this accuracy improvement to be of little practical benefit.

In summary, we have shown that the MOSAIC pulse characterization algorithm can be implemented in a single-shot scheme (provided the SNR is sufficiently high) that we call E-MOSAIC. We determine the location of phase distortions using a selective H-MOSAIC trace. Real-time phase retrieval possessing only time-direction ambiguity was experimentally demonstrated for pulses having spectral dispersion. MOSAIC software is available for free download at <http://www.optics.unm.edu/sbahae/>.

The authors wish to acknowledge helpful discussions with B. Yellampalle and M. Hasselbeck. Support provided through National Science Foundation awards ECS-0100636 and DGE-0114319 (Integrative Graduate) is gratefully acknowledged.

References

1. J.-C. Diels, J. J. Fontaine, I. C. McMichael, and F. Simoni, *Appl. Opt.* **24**, 1270 (1985).
2. D. J. Kane and R. Trebino, *IEEE J. Quantum Electron.* **29**, 571 (1993).
3. C. Iaconis and I. A. Walmsley, *IEEE J. Quantum Electron.* **35**, 501 (1999).
4. V. V. Lozovoy, I. Pastirk, and M. Dantus, *Opt. Lett.* **29**, 775 (2004).
5. T. Hirayama and M. Sheik-Bahae, *Opt. Lett.* **27**, 860 (2002).
6. K. Naganuma, K. Modi, and H. Yamada, *IEEE J. Quantum Electron.* **25**, 1225 (1989).
7. J. W. Nicholson and W. R. Rudolph, *J. Opt. Soc. Am. B* **19**, 330 (2002).
8. D. A. Bender, M. P. Hasselbeck, and M. Sheik-Bahae, *Opt. Lett.* **31**, 122 (2006).
9. J. Chung and A. M. Weiner, *IEEE J. Sel. Top. Quantum Electron.* **7**, 656 (2001).
10. S.-H. Shim, D. B. Strasfeld, and M. T. Zanni, *Opt. Express* **14**, 13120 (2006).
11. B. Yellampalle, R. D. Averitt, and A. J. Taylor, *Opt. Express* **14**, 8890 (2006).
12. M. Sheik-Bahae, *Opt. Lett.* **22**, 399 (1997).

Shaper-assisted collinear SPIDER: fast and simple broadband pulse compression in nonlinear microscopy

Bernhard von Vacano, Tiago Buckup, and Marcus Motzkus

Physikalische Chemie, Philipps-Universität Marburg, Hans-Meerwein Strasse, D-35032 Marburg, Germany

Received October 25, 2006; accepted January 3, 2007;
posted January 25, 2007 (Doc. ID 76409); published April 17, 2007

In situ characterization and control of the phase of broadband femtosecond pulses in microscopy can be achieved with a novel simplified scheme based on spectral shear interferometry for direct electric field reconstruction (SPIDER): the use of a femtosecond pulse shaper eliminates the need for an interferometer setup, allows dispersion-free SPIDER operation and at the same time compression even of complex pulses. Beyond compression, the scheme allows precise phase control at the site of the microscopic experiment. We present the underlying principles, design considerations, and details of the experimental implementation, and show the successful operation of the shaper-assisted collinear (SAC) SPIDER to characterize, compress, and tailor broadband femtosecond pulses *in situ*. The reliability is demonstrated by comparison with independent cross-frequency-resolved optical gating measurement, and improved multiphoton imaging with SAC-SPIDER-compressed pulses is shown. Its simplicity and versatility make SAC-SPIDER an extremely useful tool for next-generation broadband nonlinear microscopy. © 2007 Optical Society of America

OCIS codes: 320.5520, 180.0180, 320.5540, 170.6900.

1. INTRODUCTION

In multiphoton microscopy, high excitation intensities are essential for the efficiency of nonlinear optical processes serving as contrast mechanisms. Intrinsically, this allows high three-dimensional spatial resolution with the signal generation being confined to the focal volume.¹ On the technical side, pulsed laser sources usually have to be employed, with their very advantageous high peak intensities at low average powers, which is utterly desirable for non-destructive imaging. From this point of view, femtosecond lasers are ideally suited for multiphoton microscopy. However, the shorter femtosecond pulses are, and thus the more efficient a nonlinear excitation can be, the more they are susceptible to broadening in time due to the dispersion of optical elements, which introduce distortions in the spectral phase. In conventional femtosecond spectroscopy, dispersive optics are usually avoided for that reason whenever possible. In microscopy though, to realize the highest spatial resolution and imaging quality, elaborate microscope objectives are used, which consist of many dispersive elements. Therefore, to obtain high peak intensities with as short pulses as possible, inevitable distortions of the spectral phase have to be compensated for, for imaging under optimal conditions.² Furthermore, some femtosecond sources, for example, inexpensive and compact fiber-based femtosecond lasers, emit pulses with a spectral phase far from the Fourier-limit case. Only if this can also be accounted for in the compensation of spectral phase distortions, will such a nonlinear microscope reach its full potential.

Typically, the linear dispersion of femtosecond laser

pulses in microscopy has been compensated for by using grating- or prism-based passive compressor schemes,^{3–6} adjusting the compressor to maximize a nonlinear signal from the microscope focus. For even shorter femtosecond pulses, however, higher-order dispersion becomes increasingly important. Additionally, the adjustment of passive compressors is time consuming and the setup is rather inflexible. Very flexible compression of arbitrary phase distortions in the context of microscopy can be achieved by employing femtosecond pulse shaping, typically implemented in a 4f setup.⁷ This allows very rapid and flexible pulse compression, in particular under changing experimental conditions. However, to correct the phase distortions, the appropriate phase to be applied by the pulse shaper has to be found. A simple, yet rather slow approach is to use a nonlinear signal or an autocorrelation trace measured at the site of the microscopic sample as feedback in an optimization, which is typically based on a genetic algorithm learning loop.^{8–10}

A direct approach would be the *in situ* characterization of the femtosecond pulses, and thus the determination of their spectral phase, and applying this inverted phase as a correction in the shaper. There are several schemes that have been applied or have the potential for *in situ* pulse characterization in microscopy. These schemes are all based on collinear beam geometry, which is necessary for use with high numerical aperture microscope objectives. One possibility is collinear frequency-resolved optical gating (FROG), which has been demonstrated under the conditions of microscopy.^{11–13} However, the scanning of the temporal delay during the FROG measurement and nec-

essary iterative reconstruction after the acquisition of the data makes this technique rather slow and prevents a practical use for direct feedback of the retrieved phase for compression. There are other methods also relying on the subsequent scanning of a parameter to measure the spectral phase, which are already based on the presence of a pulse shaper in the experimental setup. One approach is time-domain nonlinear interferometry, where the necessary sequence of pulses with variable delay is generated by pulse shaping.¹⁴ From the obtained interferogram, the spectral phase of the input pulse can be extracted and used for compression. This scheme has not explicitly been demonstrated for microscopy, but should be directly applicable due to its single-beam nature. Another possible approach, equally relying on only a single beam, is the multiphoton intrapulse interference phase scans (MIIPS) technique.¹⁵ Here, the spectral phase of pulses is determined *in situ* by applying subsequently varying reference phase modulations, recording the frequency resolved second-harmonic spectrum, and iterating this correction several times until the phase compensation is sufficient. MIIPS has been demonstrated in microscopy.¹⁶

The techniques mentioned so far are relatively slow and require scanning of at least one parameter. Therefore, they are not capable of a real-time characterization of the spectral phase. This highly desirable capability, even for the measurement of very complex phases, is provided by spectral shear interferometry for direct electric field reconstruction (SPIDER).^{17–19} Consequently, we have recently developed a shaper-assisted collinear (SAC) SPIDER (SAC-SPIDER); a collinear implementation for use in microscopy.²⁰ This novel scheme greatly simplifies the experimental setup by the use of the pulse shaper, and allows precise and very rapid *in situ* total phase control. In this paper, we describe in detail the implementation and operation of SAC-SPIDER, discuss issues of calibration and reproducibility, compare the technique with an *in situ* implementation of the well-known cross-FROG, and demonstrate its great utility for nonlinear microscopy.

2. THEORY AND DESIGN CONSIDERATIONS

A. SPIDER Principle

Spectral interferometry techniques are based on the comparison of two mutually coherent beams. However, these techniques are only sensitive to the relative phase between the two sources. To measure the absolute phase of one of the beams, the phase of the other must be known beforehand. A way out of this tight requirement is to use a self-referencing modification of spectral interferometry, such as the SPIDER method.^{17–19} In the SPIDER method, the unknown test pulse is duplicated and both replicas are upconverted by mixing with a strong chirped reference pulse. The two upconverted replicas interfere and from the interferogram the spectral phase of the unknown pulse can be unambiguously retrieved. The self-referencing in the SPIDER method is achieved by delaying the two replicas against each other by a delay τ before the sum-frequency process. It ensures that each replica will mix with a different single frequency of the chirped reference pulse. The phase reconstruction in the SPIDER

method is a straightforward process known from interferometry²¹ and has been discussed in several publications in the context of SPIDER.^{17,18,22} Very briefly, the interferogram is initially Fourier transformed and one sideband in the time domain centered at delay τ is filtered out. The filter width was found to be not very critical and independent on the signal-to-noise ratio.²³ This sideband is then transformed back to the frequency domain with an inverse fast Fourier transform (FFT). That way, the phase variation of the unknown test pulse is obtained. The phase can then be directly reconstructed by a concatenation or integration process. The delay τ generates a linear term that can be easily measured in the experiment and needs to be subtracted as described in Section 3. If this term is not correctly determined, it will give rise to a quadratic contribution in the reconstructed phase, which cannot be distinguished from such phase terms of unknown pulses.

The phase variation in the frequency domain is sampled with a frequency step given by the spectral shear Ω . That means that the choice of the spectral shear Ω cannot be arbitrary: for Gaussian-shaped pulses, a ratio between the spectral width and the shear of approximately a factor of 4 is enough to reconstruct the phase correctly. Depending on the complexity of the spectra, however, the shear must be chosen to be ~ 20 – 25 times smaller than the spectral bandwidth.²³ On the other hand, the frequency shear Ω is dependent on the amount of delay τ between the replicas and of the group-delay dispersion (GDD) used to generate the chirp of the reference pulse:

$$\Omega = \frac{\tau}{\text{GDD}}. \quad (1)$$

In practice, the amount of delay τ is chosen such that the sideband after the FFT in the phase reconstruction procedure is well separated from the central peak, and that the number of fringes in the interferogram can still be resolved with the given spectrometer resolution. The Whittaker–Kotelnikov–Shannon sampling theorem states that in order to correctly sample the fringes, there must be at least two data points per fringe. The actual sampling rate required will be somewhat higher because of noise and other possible perturbations. It has been shown that a number of at least 20 fringes is enough to reconstruct the phase correctly.¹⁹ Thus, for a given optimal delay τ the spectral shear Ω is fixed. Additionally, the amount of GDD of the reference pulse has to ensure that the instantaneous frequency is approximately constant during the unknown test pulse duration. Of course, even with optimized Ω , τ , and GDD, the maximum relative phase variation that can be measured with spectral interferometry is still limited by the spectral resolution of the spectrometer.

The SPIDER method has, however, the disadvantage that the unknown pulse must be split in two delayed replicas, which adds dispersion. To avoid additional dispersion for the test pulse in an interferometer, a zero additional phase (ZAP) SPIDER has been proposed,²² where the chirped reference pulse is split into a doublet and mixed with an unmodified input pulse. The ZAP-SPIDER has the advantage that the delay between the upcon-

verted replicas is now independent on the frequency shear. Both can be adjusted separately. However, this modified scheme cannot be implemented in a collinear geometry and is more complex to realize experimentally. Very recently, variants of such a SPIDER scheme relying only on an unmodified input pulse have been demonstrated based on spatial²⁴ or collinear time-domain interferograms.²⁵

The choice of the nonlinear process for frequency conversion also plays an important role in the SPIDER method and its variants. In this sense, type-II phase-matched crystals are the best choice for the sum-frequency generation due to their larger phase-matchable bandwidth. Additionally, they are a prerequisite for background-free sum-frequency mixing in collinear beam geometry. It has to be mentioned that SPIDER methods, in general, tolerate even significant variations of the up-conversion efficiency across the pulse spectrum, because the information content of the SPIDER interferogram is within the fringe spacing, and not the amplitude. Therefore, a precise SPIDER measurement can still be performed in cases where the supported upconversion bandwidth is not sufficient for correlation-type measurements.²⁶

B. Basics of SAC-SPIDER

There is a possibility to construct a completely dispersion-free interferometer for the SPIDER setup: a pulse shaper, capable of phase and amplitude modulation, can be used to create double pulses, identical copies of the test pulse, which can then be upconverted by mixing with the chirped reference pulse. For experiments that rely on a shaper anyway (for pulse compression or coherent control)^{27,28}, this means that there is no need to introduce any other element in the beam path. It is only necessary to program the shaper for SPIDER compression.²⁰ To create double pulses with a temporal separation τ , the desired pulse-shaping effect in the time domain is a convolution of the input pulse with two Dirac delta functions at $t + \tau/2$ and $t - \tau/2$ [Fig. 1(a)],

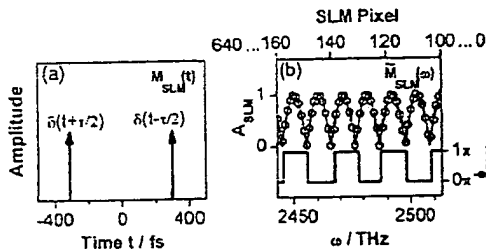


Fig. 1. Creation of double pulses with the femtosecond pulse shaper. (a) Shaping target $M_{SLM}(t)$ in the time domain for the generation of the desired identical copies of the input pulse with a separation $\tau = 600$ fs in this case. (b) Corresponding frequency domain modulation $\tilde{M}_{SLM}(\omega)$ with amplitude $A_{SLM}(\omega)$ and phase $\varphi_{SLM}(\omega)$ as realized by the pixilated SLM in the Fourier plane of the 4f pulse shaper. For clarity, only a section of the 640 pixel range is shown. For the given case ($\tau = 600$ fs), it can be seen that each period is rendered by 18 pixels, which is well above the Nyquist limit (see text).

$$E_{out}(t) = E_{in}(t) \otimes M_{SLM}(t) = \int_{-\infty}^{+\infty} d\tau E_{in}(\tau) \frac{1}{2} \left[\delta\left(t + \frac{\tau}{2}\right) + \delta\left(t - \frac{\tau}{2}\right) \right]. \quad (2)$$

To achieve such a shaping with a 4f pulse shaper,⁷ in the frequency domain the following mask function $\tilde{M}_{SLM}(\omega)$ has to be applied to the input spectrum [Eqs. (3) and (4)],

$$\tilde{E}_{out}(\omega) = \tilde{E}_{in}(\omega) \tilde{M}_{SLM}(\omega), \quad (3)$$

where $\tilde{M}_{SLM}(\omega)$ is given by

$$\begin{aligned} \tilde{M}_{SLM}(\omega) &= FT^{-1} \frac{1}{2} \left\{ \delta\left(t + \frac{\tau}{2}\right) + \delta\left(t - \frac{\tau}{2}\right) \right\} \\ &= \underbrace{abs \left[\cos\left(\frac{\omega\tau}{2}\right) \right]}_{\text{amplitude } A_{SLM}(\omega)} \exp \left\{ i \arg \left[\cos\left(\frac{\omega\tau}{2}\right) \right] \right\}. \end{aligned} \quad (4)$$

For a liquid-crystal spatial light modulator (SLM), this mask function is rendered as a discrete pattern on the pixels [Fig. 1(b)] modulating the input spectrum in phase and amplitude. The modification of the period of the mask function in Eq. (4) (parameter τ) enables the delay between the two replicas to be easily adjusted. Additional phase shaping is possible simply by adding a correction phase $\varphi_{corr}(\omega)$ to $\varphi_{SLM}(\omega)$, leading to a modified mask function $\tilde{M}_{SLM}(\omega)$. The maximum achievable delay τ depends on the number N of pixels illuminated by the spectrum and is limited by the Whittaker–Kotelnikow–Shannon sampling theorem. To create a clean double pulse, each oscillation of the mask function $\tilde{M}_{SLM}(\omega)$ has to be rendered with at least four pixels to ensure that $\tilde{M}_{SLM}(\omega)$ is well defined. This case constitutes the Nyquist limit. Hence, one can approximate that

$$\tau < \frac{\pi N}{2\Delta\omega}, \quad (5)$$

where $\Delta\omega$ is the bandwidth transmitted through N pixels.

The second essential requirement of SAC-SPIDER is collinear sum-frequency mixing under tight focusing conditions. Such sum-frequency generation (SFG) using high numerical aperture objectives, however, is rather easily implemented and even shows advantages over more conventional optical setups: due to the tight-focusing condition, a much broader bandwidth can be phase matched and the effects of walk-off are strongly minimized.^{11,29}

3. EXPERIMENTAL IMPLEMENTATION

The experimental setup is depicted in Fig. 2. The primary laser source used in this study is a standard Ti:sapphire oscillator. It delivers 100 fs pulses with a central wavelength of 795 nm at 80 MHz repetition rate. Of this laser output, 25% are picked off³⁰ and a linear chirp ϕ'' of 37,000 fs² is introduced for SPIDER measurements by a grating stretcher. This provides the intense chirped reference beam for the generation of the spectrally sheared

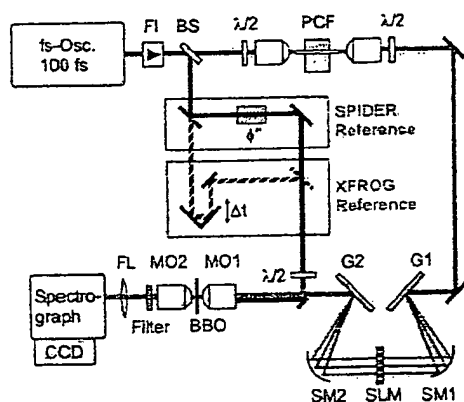


Fig. 2. (Color online) Experimental setup. The femtosecond oscillator output beam is sent through a Faraday isolator (FI) and then split into two parts. Seventy-five percent of the energy is used to generate supercontinuum in a PCF sent into the femtosecond pulse shaper (G1-2, gratings; SM1-2, spherical mirrors; SLM, spatial light modulator with 640 pixels for phase and amplitude modulation). The remaining 25% of oscillator energy is used to provide an orthogonally polarized reference beam, which is chirped (ϕ) for the SPIDER measurement. Both beams are collinearly superimposed and focused (MO1-2, microscope objectives) into a type-II BBO crystal at the position of the sample. The SFG is finally analyzed in a spectrograph (FL, focusing lens). The hatched beam indicates an alternative path for *in situ* XFROG measurements, where the reference beam is not chirped, but delayed by a variable time Δt .

replica. The use of a grating stretcher is by no means necessary or ideal; the introduction of linear chirp can be accomplished much more easily with a simple rod of highly dispersive glass. Finally, the polarization of the reference beam is rotated 90° with a $\lambda/2$ wave plate. The broadband femtosecond pulses to be compressed in this work with SAC-SPIDER stem from nonlinear spectral broadening in a photonic crystal fiber (PCF). This supercontinuum is created by focusing the remaining fundamental laser beam (~ 3 nJ pulse energy) into a polarization maintaining PCF (Crystal Fibre, NL-PM 800, 24 mm). The resulting continuum with 1.2 nJ pulse energy is sent into a 4f pulse shaper, consisting of two gratings (1200 grooves/mm, G1-2) and two spherical mirrors ($f=200$ mm, SM1-2). In the Fourier plane, phase and amplitude of each spectral component can be modulated by a dual mask 640 pixel liquid-crystal SLM with parallel thin-film polarizers. The shaper configuration transmits a spectral range from 750 to 880 nm, yielding shaped 0.3 nJ pulses. After collinearly superimposing the shaper input with the orthogonally polarized reference beam, both are focused with a microscope objective (60 \times ; NA 0.7, MO1) onto a 50 μ m β -barium borate (BBO) (type II). The generated nonlinear signal, together with unconverted excitation light, is recollimated with a second microscope objective (40 \times , NA 0.6, MO2). The desired sum-frequency signal can finally be extracted by a short-pass filter (Schott BG 42), and detected spectrally resolved in a CCD equipped spectrograph ($f=300$ mm). By not applying the GDD in the reference arm and introducing a variable delay Δt instead (shown as hatched beam path in Fig. 2), the setup can immediately be used as an independent *in situ* cross-frequency-resolved optical gating (XFROG) device,

where the unknown pulse is sampled by the 100 fs oscillator pulses and the resulting SFG spectrum is recorded for each Δt .

4. PREPARATIONS FOR SAC-SPIDER OPERATION

A. Creation of Pulse Doublets

In the present study, a spectrum with a bandwidth $\Delta\omega$ of 400 THz was used, which illuminated approximately $N=450$ pixels. According to Eq. (5), the maximum delay τ is therefore ~ 1.75 ps, which allows complete coverage of the usual double-pulse spacing range found in SPIDER literature. To verify the successful creation of pulse doublets, we have applied mask functions $\tilde{M}_{SLM}(\omega)$ for different delays τ and recorded *in situ* frequency resolved cross correlations. Details of the XFROG measurements are given in Section 6, where we use this technique to independently verify the SAC-SPIDER results. The experimental XFROG traces are shown in Fig. 3. In the top row [Fig. 3(a)], a cross correlation of the unshaped input pulse, which is to be characterized and compressed by SAC-SPIDER, can be seen. In this case, no mask function was applied to the shaper. The trace shown thus corresponds to the unknown pulse $E_{in}(t)$. Double pulses have been created with increasing temporal separations τ (200, 800, and 1600 fs). As can be seen in Fig. 3(b), for 200 fs, the resulting pulse is not a well-separated doublet, because the duration of $E_{in}(t)$ still exceeds τ . Therefore, the replicas of $E_{in}(t)$ overlap and yield an interference pattern in the XFROG trace. For $\tau=800$ fs, the pulses are clearly separated. It can be seen that each of the replicas, within the experimental noise of the XFROG implementation, exactly matches the unshaped $E_{in}(t)$. Even twice this temporal separation $\tau=1600$ fs allows the successful creation of double pulses with our pulse-shaping approach, as expected from the estimation based on Eq. (5).

B. Calibration Procedures

Apart from a carefully calibrated pulse shaper and spectrograph, there are three specific calibration steps that

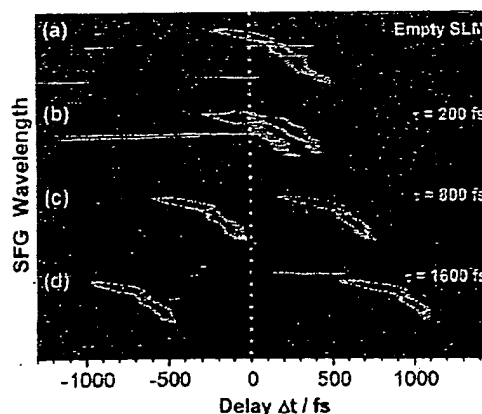


Fig. 3. (Color online) Experimental confirmation of the double-pulse shaping by frequency-resolved cross correlation (XFROG, for details see Section 6). Shown are data sets for an (a) unshaped pulse and doublets with (b) $\tau=200$, (c) 800, and (d) 1600 fs.

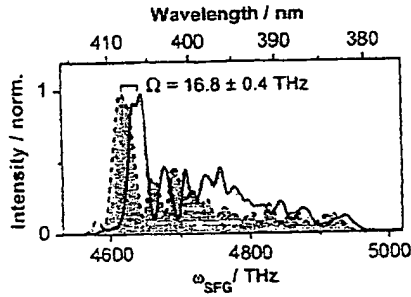


Fig. 4. (Color online) Calibration of the spectral shear with SAC-SPIDER. Shown are two spectra created by sum-frequency mixing of a single test pulse replica delayed by the shaper to 300 fs ($+\tau/2$, solid curve) and -300 fs ($-\tau/2$, dashed curve and shaded area), respectively, with the chirped reference pulse.

have to be performed for successful operation of SAC-SPIDER. First, the measured spectral phase $\phi(\omega)$ is going to be inverted and fed back to the pulse shaper. Therefore, the mapping between the fundamental frequency ω of the pulse to be characterized and the sum frequency $\omega_{\text{SFG}} = \omega + \omega_{\text{ref}}$, where ω_{ref} is the effective mixing frequency of the reference pulse, must be known. With the amplitude modulation capabilities of the pulse shaper, this relation can be very conveniently established, by simply creating a narrow spectral feature at frequency ω' in the supercontinuum and measuring this at a known frequency ω'_{SFG} in the sum-frequency spectrum.

The second calibration requirement is the determination of the spectral shear Ω for the given chirped reference pulse and the temporal separation τ of the test pulse replica. Again, with SAC-SPIDER, this can be achieved in a fully automatic scheme without any changes to the setup. Instead of creating a pulse doublet with a SLM mask function, the test pulse is only shifted in time by $\pm\tau/2$ using the pulse shaper. This is very easily achieved with a phase-only modulation, introducing the spectral phases $\phi_{\text{SLM}}(\omega) = \pm(\omega - \omega_0)\tau/2$ one after the other, and recording the respective sum-frequency spectrum of the delayed pulses. As the pulse at $-\tau/2$ overlaps with a different color of the chirped reference pulse than at $+\tau/2$, the spectral shift of the sum-frequency spectrum immediately gives the shear Ω . To exactly determine Ω , it is necessary to have easily distinguishable spectral features, such as the maximum of a smooth Gaussian spectrum or a sharp dip or peak. If the spectrum of the unknown pulse does not show such a suited spectral feature, the pulse shaper can always create one by amplitude modulation, making the determination of Ω with SAC-SPIDER very easy and straightforward.

An example of two spectra recorded by sum-frequency mixing of two test pulse replicas at $+\tau/2$ and $-\tau/2$ for $\tau = 600$ fs is shown in Fig. 4. The test pulse spectrum is well reproduced for both replicas, only showing some minor deviations in the relative intensities due to the mixing with different parts of the chirped reference pulse. Comparing distinct spectral features of the upconverted replicas, the spectral shear Ω is determined as the average of eight different positions yielding $\Omega = 16.8 \pm 0.4$ THz.

Finally, for the SPIDER measurement of the spectral phase, the temporal separation τ of the double pulses has

to be known precisely. As already stated in Subsection 2.A, the temporal delay between the interfering pulse doublet is directly proportional to the fundamental frequency of the interference fringes. In the SPIDER phase retrieval, the linear contribution of τ to the phase difference between the test pulse replicas has to be subtracted. As discussed in Subsection 2.A, an incorrect value of τ will, in the SPIDER algorithm, lead to an erroneous quadratic contribution in the recovered phase. Additionally, deviations in the spectrometer calibration are known to lead to systematic errors in the recovered phase.³¹ With a simple procedure, already applied in the seminal SPIDER work,¹⁷ these issues can be addressed: it is only necessary to record an interferogram of upconverted replica pulses that are delayed, but not spectrally sheared. Due to the fact that $\Omega = 0$, the interferometric fringes only contain the linear phase term $\omega\tau$ and additional contributions due to residual errors of the spectrometer calibration. This phase difference can now be subtracted from any SPIDER measurement before the final integration step in the algorithm. To obtain the desired interferogram of upconverted, but spectrally not sheared replica, two approaches are viable with SAC-SPIDER. To begin with, due to the collinear nature of SAC-SPIDER, it is possible to simply rotate the nonlinear crystal in the microscope focus for type-I frequency mixing (both beams polarization parallel to the ordinary axis) and blocking the reference beam. Thereby, each of the delayed pulse replicas is frequency doubled yielding the desired interferogram with $\Omega = 0$. Such calibration interferograms are shown in Fig. 5(a) for different values of τ . To obtain the wanted linear phase difference $\omega\tau$, the interferograms are processed in the SPIDER algorithm as described in Subsection 2.A, with-

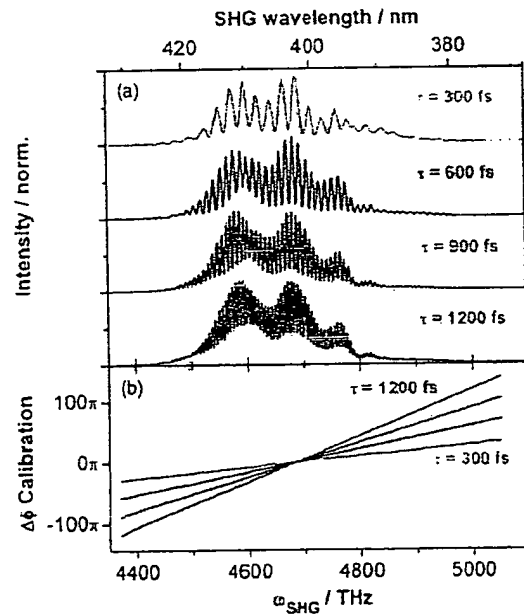


Fig. 5. (Color online) τ calibration. (a) SHG-calibration interferograms for different separations of the test pulse doublet. (b) Phase differences retrieved from the calibration interferograms corresponding to the linear term introduced by τ (see text for details).

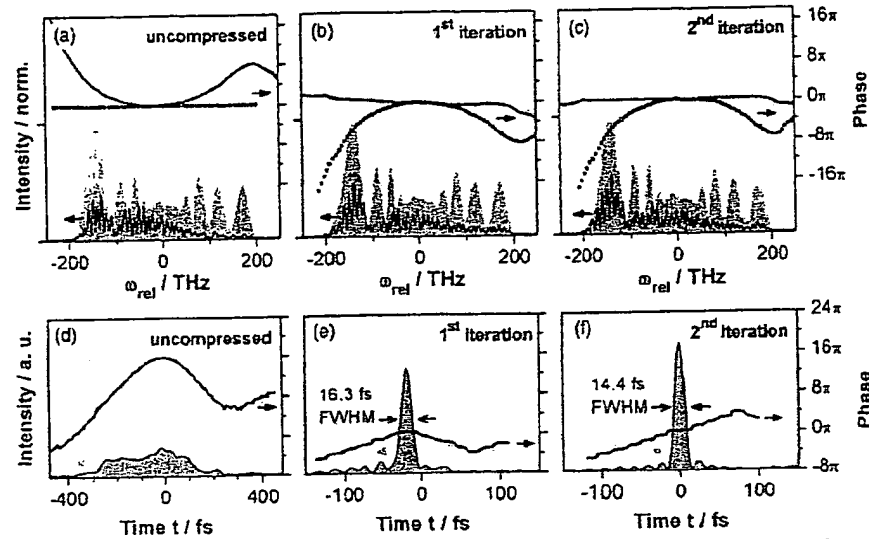


Fig. 6. (Color online) *In situ* pulse compression with SAC SPIDER. Shown are (a)–(c) the pulse spectra, interferograms, and phases in the frequency domain, and (d)–(f) reconstructed temporal pulse profiles and phases. From left to right, the compression sequence can be followed with (a) and (d) the uncompressed case, (b) and (e) the first, and (c) and (f) the second compression iteration. (a)–(c) The spectral phases are shown as thick solid curves, the shaper correction phase $\varphi_{\text{corr}}(\omega)$ as squares, interferograms as thin solid curves, and the fundamental pulse spectrum as the gray shaded area. All frequency domain data are shown relative to the pulse central frequency $\omega_{\text{rel}}=0$. (d)–(f) The temporal pulse intensity is shown as the gray shaded area with a thin contour, the temporal phase as a thick solid curve. Note that the uncompressed pulse in (d) and the compressed pulses in (e) and (f) are shown with different time scales for clarity.

out the last concatenation or integration step. This calibration phase is then stored in the SAC-SPIDER software, and subsequently subtracted prior to concatenation from any phase differences in SPIDER measurements with $\Omega \neq 0$. Note, that the mentioned deviations from a perfect linear phase difference $\omega\tau$ due to spectrometer errors are too small to be discernible in Fig. 5(b), except at the very edges of the second-harmonic generation (SHG) spectrum. However, they have to be taken into account and subtracted with the calibration procedure for a precise SPIDER phase measurement.

The SHG procedure described so far is carried out very easily, but can only be used if the second harmonic of the test pulses lies in the same frequency range as the sum-frequency of the test pulse mixed with the reference pulse, which is evaluated for the SPIDER measurement. Additionally, the intensity of the test pulses needs to be high enough to generate enough SHG signal to detect, because in this calibration step, they are not mixed with a strong reference beam. If this is not the case, a second approach can always be used, which is based on the same sum-frequency mixing process as the SAC-SPIDER measurement. In this approach, the chirped reference beam is filtered to a very narrow spectral portion, which corresponds to a long (picosecond) pulse with approximately constant frequency. Now, the test pulse doublet is mixed in the type-II nonlinear crystal, yielding two upconverted, but spectrally not shifted replicas with $\Omega=0$. In this procedure, the reference interferogram with $\Omega=0$ is always created in the same spectral position where the SPIDER measurement is being performed. Furthermore, a strong reference beam can be used if very weak test pulses are to be characterized. The spectral filtering can be achieved either by a very narrow interference bandpass filter in the reference beam, or conveniently by geometrical filtering

in the Fourier plane, if the chirp of the reference beam is introduced by a grating stretcher, as is the case in our experimental implementation. All the calibration steps can easily be completed within a few minutes, without changes to the experimental setup.

5. SAC-SPIDER OPERATION

A. In situ Phase Measurement and Pulse Compression
With the SAC-SPIDER apparatus carefully calibrated, it can immediately be used for *in situ* pulse compression. As already mentioned in the description of the experimental setup, the microscopic sample is replaced by a thin slab of a nonlinear crystal (BBO). Therefore, all dispersive elements including the focusing microscope objective are taken into account. It is easily possible to include coverslips and even immersion media, depending on the microscopic application. The unknown test pulse in this study is formed by supercontinuum generation in a PCF. Prior to compression, it is stretched in time over more than 450 fs at the site of the nonlinear interaction in the microscope, which can be estimated from the XFROG trace in Fig. 3(a). To characterize this pulse, the first step is to apply a double-pulse forming mask function $\tilde{M}_{SLM}(\omega)$ (see Subsection 2.B). The temporal spacing of the double pulse τ has to be chosen appropriately for the given bandwidth, to achieve a set of experimental parameters τ and Ω that fulfil the SPIDER requirements described in Subsection 2.A. Here, τ was chosen to be 600 fs, which gives a calibrated spectral shear of $\Omega=16.8 \pm 0.4$ THz. This value of Ω is well within the desired range for the bandwidth $\Delta\omega$ of 400 THz. The compression of the test pulse with these parameters is summarized in Fig. 6. Sum-frequency mixing of the test pulse doublet with the chirped reference beam

in the nonlinear crystal gives the SPIDER interferogram of the uncompressed pulse, as can be seen in Fig. 6(a) as a thin solid curve. Comparing the frequency-shifted interferogram with the independently measured spectrum of the test pulse [Fig. 6(a), gray shaded area] confirms that all frequency components are upconverted in the SFG process. From the interferogram, it can already be discerned that the fringe spacing is nonuniform. This corresponds to the spectral phase difference of the spectrally sheared test pulse replica being nonzero. Accordingly, the SPIDER algorithm retrieves a spectral phase [Fig. 6(a), thick solid curve] that is dominated by a quadratic term but also has complex higher-order contributions. This phase measurement is performed with the pulse shaper acting only as dispersionless interferometer, i.e., no additional phase $\varphi_{\text{corr}}(\omega)$ has been applied. $\varphi_{\text{corr}}(\omega)=0$ is depicted in Fig. 6(a) as squares.

The phase information obtained can now directly be used to apply a correction phase $\varphi_{\text{corr}}(\omega)$ in the pulse shaper. Evidently, the necessary correction phase is the sign-inverted measured phase of the unknown test pulse. This correction phase is shown in Fig. 6(b) as squares. By applying the modified mask function $\tilde{M}_{\text{SLM}}(\omega)$ containing the correction, the interferogram changes [Fig. 6(b), thin solid curve]. Accordingly, the reconstructed phase [Fig. 6(b), thick solid curve] is much more flat. Still, there are remaining undulations in the residual phase. This residue can, however, simply be added to $\varphi_{\text{corr}}(\omega)$ in an iterative manner. Thus, in the second iteration step [Fig. 6(c)] the interferogram only shows subtle changes. The retrieved phase is now almost perfectly flat, and compression is successfully achieved. This is confirmed when considering the reverse Fourier transform of the frequency domain data in the time domain to reconstruct the pulse shapes. The uncompressed test pulse [Fig. 6(d)] is stretched in time over more than 450 fs, as expected, and has a mainly quadratic temporal phase in the central part. The first compression step already produces a dramatic effect, as the pulse resulting from the flattened spectral phase has a temporal duration of only 16.3 fs (FWHM). The second iteration corrects for remaining phase distortions and results in a clean 14.4 fs (FWHM) pulse, which is very close (less than 4%) to the calculated Fourier limit of 13.9 fs (FWHM) for this spectrum.

In principle, the combination of SPIDER pulse characterization and pulse shaping is capable of noniterative pulse compression.³² The fact that here the first iteration is not yet giving the optimal compression result can have two reasons. First of all, the assumption that the instantaneous frequency remains constant during the length of the test pulse is not very well fulfilled at the beginning. Uncompressed pulses have several hundred femtosecond durations, while the chirped reference pulse ($\phi'' = 37,000 \text{ fs}^2$) has $\sim 1.5 \text{ ps}$. Such cases of highly chirped test pulses have very recently been thoroughly investigated,³³ and it was found that only a modified retrieval scheme taking into account a chirp-dependent shear will measure the correct phase, while the conventional approach based on the constant frequency assumption will generally underestimate the phase. This is the main reason for the remaining residual phase after the first SAC-SPIDER iteration seen in Fig. 5(b) as a thick solid curve. After this first

iteration, the pulse is short enough to perfectly fulfill the instantaneous frequency requirement; therefore the measured residual phase is correct and the compression succeeds with the second iteration. A second reason why iterations can be necessary in SAC-SPIDER is because of errors in the calibration of Ω . As the measured phase is proportional to Ω^{-1} , a too large shear will underestimate, while a too small Ω will overestimate the measured phase. Iteration, however, makes SAC-SPIDER very robust against even grossly deviating values of Ω . In fact, errors in the estimates of Ω only increase the number of iterations until the residual phase approaches zero. Based on that it becomes clear that Ω was determined precisely for the experiment in Fig. 6, as the first iteration already performs almost all of the compression.

B. Measurement Time and Retrieval of Complex Phases

The complete compression in Fig. 6 was performed very rapidly in less than 2 s. The phase measurement itself in SAC-SPIDER is only limited by the acquisition time of the CCD camera and the time needed to perform the SPIDER algorithm. This is a general property of SPIDER techniques and has already been demonstrated for real-time measurements.¹⁹ An iteration step for *in situ* compression takes a little bit longer, as now the limiting factor is the rate at which the pulse shaper can be updated. The unit used in this study is equipped with a rather slow serial computer interface, which limits the rate at which mask functions $\tilde{M}_{\text{SLM}}(\omega)$ can be written on the SLM. For the present configuration, run-time measurements determined that the complete cycle of a SAC-SPIDER measurement, phase inversion, and writing of the modified mask function is completed within 780 ms.

The presence of the pulse shaper allows us to easily evaluate the capabilities of the system to characterize pulses with even more complex pulse shapes. On the basis of the correction phase $\varphi_{\text{corr}}(\omega)$, which creates a clean pulse with a flat spectral phase, additional phase modulations $\varphi_{\text{mod}}(\omega)$ can be added. This means that the phase of the mask function $\varphi_{\text{SLM}}(\omega)$ now consists of the phase modulation necessary for the creation of double pulses, the correction phase $\varphi_{\text{corr}}(\omega)$ and $\varphi_{\text{mod}}(\omega)$. In Fig. 7, some

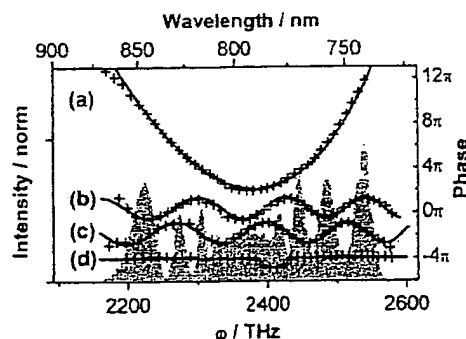


Fig. 7. (Color online) Retrieval of complex phases. In addition to the compressed pulse, arbitrary phase modulations $\varphi_{\text{mod}}(\omega)$ were applied: (a) quadratic phase with 2000 fs^2 , (b) and (c) sinusoidal phases with $\pi/2$ phase offset, (d) rectangular phase indentation. $\varphi_{\text{mod}}(\omega)$ is always shown as a thick solid curve, and the retrieved SAC-SPIDER phases as crosses. For comparison, the pulse spectrum is indicated as the gray shaded area.

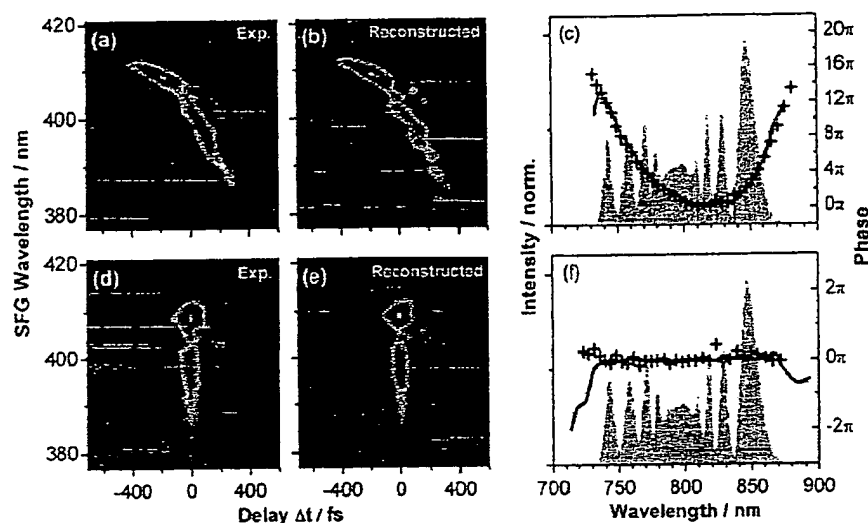


Fig. 8. (Color online) Comparison between SAC-SPIDER and XFROG methods. Both methods retrieved the same phase for (a)–(c) uncompressed and (d)–(f) the compressed supercontinuum pulses. The experimental XFROG traces [(a) and (d)] were reconstructed [(b) and (e), respectively] and the spectral phase was retrieved [crosses in (c) and (f), respectively]. The corresponding phases measured with SAC-SPIDER are shown as solid lines and the test pulse spectrum is indicated as the gray shaded area. Note that the SAC-SPIDER phase shown in (c) is obtained after two iterations (compare Fig. 6).

examples for typical phase modulations $\varphi_{\text{mod}}(\omega)$ are shown, which are frequently used in coherent control.³⁴ In Fig. 7(a), an additional quadratic phase of $\varphi_{\text{mod}}(\omega) = 2000 \text{ fs}^2 (\omega - \omega_0)^2$ (solid curve) was added and successfully retrieved by the SAC-SPIDER (crosses). Similarly, sinusoidal phases of the type $\varphi_{\text{mod}}(\omega) = A \sin(\tau_m \omega + c)$ were added with amplitude $A = \pi$, modulation frequency $\tau_m = 50 \text{ fs}$, and a constant phase offset of $c = 0$ [Fig. 7(b)] and $c = \pi/2$ [Fig. 7(c)]. In both cases, the oscillating phase is nicely retrieved, and the phase shift between Figs. 7(b) and 7(c) is clearly discernible. Sinusoidal phases are highly relevant for applications in nonlinear microscopy, as they can be used for selective multiphoton imaging^{35,36} and for single-beam coherent anti-Stokes Raman scattering microscopy,^{37,38} which allows chemical contrast with a single broadband femtosecond laser and a pulse shaper. Finally, in Fig. 7(d), a phase indent with a “depth” of 0.7π is shown, which is also successfully characterized. Much larger indentation depths, however, can lead to disruptions in the interferograms, which cause the SPIDER algorithm to introduce systematic errors in the reconstructed phase.

Similarly, if the spectrum of the unknown pulse is very much structured and if the spectral intensity drops to zero, the SPIDER phase retrieval loses track of the fringe phase and encounters phase-cycle slip errors, which lead to artificially large linear spectral phases for the spectrum after such a problematic area in the interferogram. This property is common to all SPIDER implementations. SAC-SPIDER, however, allows, in some cases, mitigating phase-cycle slip problems: Due to the creation of the double pulses with the shaper, the relative offset phase between both replicas can be adjusted independently from their temporal separation. This permits very easy shifting of the interference fringes in the SAC-SPIDER interferogram, which can help to overcome problems in the phase reconstruction. If an interference fringe is placed where

there is a sharp dip in the test pulse spectrum, the phase cycle slip can be avoided at this spectral position. Thus, from a series of interferograms recorded with different offset phases, much more robust phase information can be obtained for highly structured pulses.

6. COMPARISON WITH INDEPENDENT XFROG MEASUREMENTS

To independently verify the phase obtained with the SAC-SPIDER, XFROG measurements^{39–41} were performed *in situ*. As the reference pulse, the 100 fs laser oscillator was used. For this purpose, in the SAC-SPIDER setup (Fig. 2, hatched beam path) the reference beam is not chirped as for SPIDER measurements, but can be delayed by Δt using a linear moving stage. Additionally, linear chirp of the reference pulse could be compensated by a pair of gratings. The sum-frequency mixing signal between this reference beam and the beam of the test pulses was detected in the same setup, as described in Section 3. The 100 fs oscillator as the reference pulse that has a much longer duration than the compressed test pulse has to be carefully characterized. This was performed with an *in situ* FROG measurement of the reference pulse under the same experimental conditions, i.e., taking into account all optical dispersive elements.

In Fig. 8, the characterization of the test pulse with the *in situ* XFROG and SAC-SPIDER methods is shown for the uncompressed [Figs. 8(a)–8(c)] and compressed [Figs. 8(d)–8(f)] supercontinuum phase. For both situations, the agreement between the methods is almost perfect: the uncompressed pulse shows a spectral phase with a strong quadratic phase and higher-order contributions, which is correctly identified by SAC-SPIDER [Fig. 8(c), solid curve] and XFROG [Fig. 8(c), crosses]. When the SAC-SPIDER is used to compress the pulse *in situ*, the XFROG also finds a flat spectral phase [Fig. 8(f), crosses] and con-

firms the successful compression. The fact that the reference pulse is not Fourier-transform-limited but has some degree of higher-order phase distortions can be seen in the experimental XFROG traces in Fig. 8: They are, to some extent, smeared out in time. Note that the precise knowledge of these distortions in the reference pulse nevertheless allows a very accurate reconstruction of the test pulse, as can be seen from the very close match of the experimental [Figs. 8(a) and 8(d)] and retrieved [Figs. 8(b) and 8(e)] XFROG traces. However, the procedure to obtain the test pulse phase *in situ* with XFROG is much more time consuming (approaching, including reconstruction, several tens of minutes) and complicated than the original SAC-SPIDER measurement (less than a second).

7. MULTIPHOTON MICROSCOPY APPLICATION EXAMPLE

As shown in the above sections, SAC-SPIDER is a very useful tool for rapid and precise *in situ* compression even of very complex pulses in a nonlinear microscope. To demonstrate how valuable this precise phase control is for multiphoton microscopy, we performed two-photon fluorescence microscopy using our PCF source, and compare images obtained without and with SAC-SPIDER compression. The sample was prepared with a diluted solution of 8 μm monodisperse melamine-formaldehyde-resin microparticles labeled with Rhodamine B (Kisker Biotech) in water, which was placed within a 2×4 mm recess incised in a 100 μm thick Teflon spacer on a microscope slide, and sealed with a coverslip. The sample was mounted on a XYZ-closed loop piezotranslation stage (PI Nanocube), which allows a maximum scanning range of 100 μm in each direction with nanometer resolution. Placing the focal volume exactly inside a microparticle, the two-photon fluorescence spectrum of the labeling dye Rhodamine B could be recorded: In Fig. 9(a), the respective spectra can be seen for uncompressed [solid line, hatched in dark gray

in Fig. 9(a), temporal profile Fig. 6(d)] and compressed pulses [dashed line, hatched in light gray in Fig. 9(a), for temporal profile see Fig. 6(f)]. The integrated intensity of the two-photon fluorescence obtained with compressed pulses is more than 1 order of magnitude larger than for uncompressed pulses. Using the integrated fluorescence signal intensity, imaging of the microparticles could be performed. For each pixel recorded with a step size of 600 nm in the X and Y directions, the shaper first applied an empty mask function for the uncompressed pulses, and then the SAC-SPIDER correction phase for the compressed pulses. In Figs. 9(b) and 9(c), both resulting images are shown on a common normalized intensity scale. As expected, the image obtained with SAC-SPIDER compression has a much higher contrast. Apart from the optimization of the signal level, SAC-SPIDER now immediately allows imprinting additional wanted phase functions [such as the sine modulations shown in Figs. 7(b) and 7(c)], to perform selective multiphoton fluorescence microscopy with shaped pulses.^{35,36}

8. CONCLUSIONS

The SAC-SPIDER method permits full *in situ* phase measurement and control of broadband pulses in the environment of microscopy and microspectroscopy. We have discussed in detail the implementation of this new, to the best of our knowledge, simplified dispersion-free phase characterization method. As an example, we have shown the compression of a broadband supercontinuum from a photonic crystal fiber down to 14.4 fs, and we applied it for the improved multiphoton microscopic imaging of fluorescent microspheres. Successful compression and phase measurement has been verified by comparison with *in situ* XFROG traces. The key feature of SAC-SPIDER is the use of a femtosecond pulse shaper, which completely eliminates the need for an interferometer setup and, at the same time, introduces the possibility to compress complex pulses. The versatility and its straightforward implementation make SAC-SPIDER an extremely useful tool for next-generation broadband nonlinear microscopy, and for microspectroscopy, which can very much profit from precisely tailored femtosecond pulses incorporating coherent control schemes.

ACKNOWLEDGMENTS

Generous support by K.-L. Kompa and the Max-Planck Society, as well as a scholarship from the Fonds der Chemischen Industrie to B. von Vacano, are gratefully appreciated. The authors thank W. Wohlleben for stimulating discussions at the beginning of this project and J. Hauer for his valuable comments. M. Motzkus's e-mail address is motzkus@staff.uni-marburg.de.

REFERENCES AND NOTES

1. W. R. Zipfel, R. M. Williams, and W. W. Webb, "Nonlinear magic: multiphoton microscopy in the biosciences," *Nat. Biotechnol.* **21**, 1369–1377 (2003).
2. J. Squier and M. Muller, "High resolution nonlinear microscopy: a review of sources and methods for achieving optimal imaging," *Rev. Sci. Instrum.* **72**, 2855–2867 (2001).

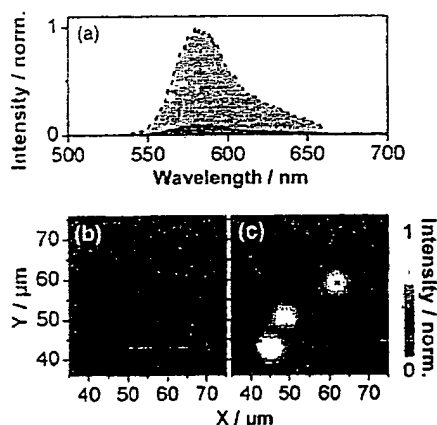


Fig. 9. (Color online) Application example of SAC-SPIDER compressed pulses in two-photon fluorescence microscopy. (a) Two-photon fluorescence spectra measured in a Rhodamine B labeled polymer particle with uncompressed (solid curve, hatched in dark gray) and compressed (dashed curve, hatched in light gray) pulses. Imaging of fluorescent microparticles with (b) uncompressed and (c) compressed pulses. The integrated fluorescence intensity is normalized on the same scale.

3. G. J. Brakenhoff, M. Muller, and J. Squier, "Femtosecond pulse width control in microscopy by two-photon absorption autocorrelation," *J. Microsc.* **179**, 253–260 (1995).
4. C. Soeller and M. B. Cannell, "Construction of a two-photon microscope and optimisation of illumination pulse duration," *Pfluegers Arch.* **432**, 555–561 (1996).
5. R. Wolleschensky, T. Feurer, R. Sauerbrey, and U. Simon, "Characterization and optimization of a laser-scanning microscope in the femtosecond regime," *Appl. Phys. B* **67**, 87–94 (1998).
6. M. Muller, J. Squier, R. Wolleschensky, U. Simon, and G. J. Brakenhoff, "Dispersion precompensation of 15 femtosecond optical pulses for high-numerical-aperture objectives," *J. Microsc.* **191**, 141–150 (1998).
7. A. M. Weiner, "Femtosecond pulse shaping using spatial light modulators," *Rev. Sci. Instrum.* **71**, 1929–1960 (2000).
8. D. Yelin, D. Meshulach, and Y. Silberberg, "Adaptive femtosecond pulse compression," *Opt. Lett.* **22**, 1793–1795 (1997).
9. T. Baumert, T. Brixner, V. Seyfried, M. Strehle, and G. Gerber, "Femtosecond pulse shaping by an evolutionary algorithm with feedback," *Appl. Phys. B* **65**, 779–782 (1997).
10. D. Zeidler, S. Frey, K. L. Kompa, and M. Motzkus, "Evolutionary algorithms and their application to optimal control studies," *Phys. Rev. A* **64**, 023420 (2001).
11. D. N. Fittinghoff, J. A. Squier, C. P. J. Barty, J. N. Sweetser, R. Trebino, and M. Muller, "Collinear type II second-harmonic-generation frequency-resolved optical gating for use with high-numerical-aperture objectives," *Opt. Lett.* **23**, 1046–1048 (1998).
12. I. Amat-Roldan, I. G. Cormack, P. Loza-Alvarez, E. J. Gualda, and D. Artigas, "Ultrashort pulse characterisation with SHG collinear-FROG," *Opt. Express* **12**, 1169–1178 (2004).
13. I. Amat-Roldan, I. G. Cormack, P. Loza-Alvarez, and D. Artigas, "Starch-based second-harmonic-generated collinear frequency-resolved optical gating pulse characterization at the focal plane of a high-numerical-aperture lens," *Opt. Lett.* **29**, 2282–2284 (2004).
14. A. Monmayrant, M. Joffre, T. Oksenhendler, R. Herzog, D. Kaplan, and P. Tourniois, "Time-domain interferometry for direct electric-field reconstruction by use of an acousto-optic programmable filter and a two-photon detector," *Opt. Lett.* **28**, 278–280 (2003).
15. V. V. Lozovoy, I. Pastirk, and M. Dantus, "Multiphoton intrapulse interference. IV. Ultrashort laser pulse spectral phase characterization and compensation," *Opt. Lett.* **29**, 775–777 (2004).
16. B. Xu, J. M. Gunn, J. M. Dela Cruz, V. V. Lozovoy, and M. Dantus, "Quantitative investigation of the multiphoton intrapulse interference phase scan method for simultaneous phase measurement and compensation of femtosecond laser pulses," *J. Opt. Soc. Am. B* **23**, 750–759 (2006).
17. C. Iaconis and I. A. Walmsley, "Spectral phase interferometry for direct electric-field reconstruction of ultrashort optical pulses," *Opt. Lett.* **23**, 792–794 (1998).
18. C. Iaconis and I. A. Walmsley, "Self-referencing spectral interferometry for measuring ultrashort optical pulses," *IEEE J. Quantum Electron.* **35**, 501–509 (1999).
19. T. M. Shuman, M. E. Anderson, J. Bromage, C. Iaconis, L. Waxer, and I. A. Walmsley, "Real-time SPIDER: ultrashort pulse characterization at 20 Hz," *Opt. Express* **5**, 134–143 (1999).
20. B. von Vacano, T. Buckup, and M. Motzkus, "In situ broadband pulse compression for multiphoton microscopy using a shaper-assisted collinear SPIDER," *Opt. Lett.* **31**, 1154–1156 (2006).
21. M. Takeda, H. Ina, and S. Kobayashi, "Fourier-transform method of fringe-pattern analysis for computer-based tomography and interferometry," *J. Opt. Soc. Am.* **72**, 156–160 (1982).
22. P. Baum, S. Lochbrunner, and E. Riedle, "Zero-additional phase SPIDER: full characterization of visible and sub-20-fs ultraviolet pulses," *Opt. Lett.* **29**, 210–212 (2004).
23. M. E. Anderson, L. E. E. de Araujo, E. M. Kosik, and I. A. Walmsley, "The effects of noise on ultrashort-optical-pulse measurement using SPIDER," *Appl. Phys. B* **70**, S85–S93 (2000).
24. E. M. Kosik, A. S. Radunsky, I. A. Walmsley, and C. Dorrer, "Interferometric technique for measuring broadband ultrashort pulses at the sampling limit," *Opt. Lett.* **30**, 326–328 (2005).
25. J. R. Birge, R. Ell, and F. X. Kartner, "Two-dimensional spectral shearing interferometry for few-cycle pulse characterization," *Opt. Lett.* **31**, 2063–2065 (2006).
26. L. Gallmann, D. H. Sutter, N. Matuschek, G. Steinmeyer, and U. Keller, "Techniques for the characterization of sub-10-fs optical pulses: a comparison," *Appl. Phys. B* **70**, S67–S75 (2000).
27. H. Rabitz, R. de Vivie-Riedle, M. Motzkus, and K.-L. Kompa, "Whither the future of controlling quantum phenomena?," *Science* **288**, 824–828 (2000).
28. W. Wohlleben, T. Buckup, J. L. Herek, and M. Motzkus, "Coherent control for spectroscopy and manipulation of biological dynamics," *ChemPhysChem* **6**, 850–857 (2005).
29. D. N. Fittinghoff, A. C. Millard, J. A. Squier, and M. Muller, "Frequency-resolved optical gating measurement of ultrashort pulses passing through a high numerical aperture objective," *IEEE J. Quantum Electron.* **35**, 479–486 (1999).
30. A 3:1 beam splitter was chosen to generate the reference beam to maintain a sufficient power level for the creation of the desired supercontinuum spectrum. An optimal choice might be different for other applications; in our case it ensures high-enough pulse energies of the compressed test pulses *in situ* for microscopy.
31. C. Dorrer, "Influence of the calibration of the detector on spectral interferometry," *J. Opt. Soc. Am. B* **16**, 1160–1168 (1999).
32. J. Thornes, P. Poon, and M. E. Anderson, "Single-iteration compression of femtosecond laser pulses," *J. Opt. Soc. Am. B* **21**, 1387–1390 (2004).
33. J. Wemans, G. Figueira, N. Lopes, and L. Cardoso, "Self-referencing spectral phase interferometry for direct electric-field reconstruction with chirped pulses," *Opt. Lett.* **31**, 2217–2219 (2006).
34. T. Hornung, R. Meier, and M. Motzkus, "Optimal control of molecular states in a learning loop with a parameterization in frequency and time domain," *Chem. Phys. Lett.* **326**, 445–453 (2000).
35. J. M. Dela Cruz, I. Pastirk, V. V. Lozovoy, K. A. Walowicz, and M. Dantus, "Multiphoton intrapulse interference 3: probing microscopic chemical environments," *J. Phys. Chem. A* **108**, 53–58 (2004).
36. J. P. Ogilvie, D. Debarre, X. Solinas, J. L. Martin, E. Beaupaire, and M. Joffre, "Use of coherent control for selective two-photon fluorescence microscopy in live organisms," *Opt. Express* **14**, 759–766 (2006).
37. N. Dudovich, D. Oron, and Y. Silberberg, "Single-pulse coherently controlled nonlinear Raman spectroscopy and microscopy," *Nature* **418**, 512–514 (2002).
38. B. von Vacano, W. Wohlleben, and M. Motzkus, "Actively shaped supercontinuum from a photonic crystal fiber for nonlinear coherent microspectroscopy," *Opt. Lett.* **31**, 413–415 (2006).
39. X. Gu, L. Xu, M. Kimmel, E. Zeek, P. O'Shea, A. P. Shreenath, R. Trebino, and R. S. Windeler, "Frequency-resolved optical gating and single-shot spectral measurements reveal fine structure in microstructure-fiber continuum," *Opt. Lett.* **27**, 1174–1176 (2002).
40. S. Linden, H. Giessen, and J. Kuhl, "XFROG—a new method for amplitude and phase characterization of weak ultrashort pulses," *Phys. Status Solidi B* **206**, 119–124 (1998).
41. S. Linden, J. Kuhl, and H. Giessen, "Amplitude and phase characterization of weak blue ultrashort pulses by downconversion," *Opt. Lett.* **24**, 569–571 (1999).

Generation of 0.5 mJ, few-cycle laser pulses by an adaptive phase modulator

He Wang,¹ Yi Wu,¹ Chengquan Li,¹ Hiroki Mashiko,¹ Steve Gilbertson,¹
and Zenghu Chang^{1*}

¹J. R. Macdonald Laboratory, Department of Physics, Kansas State University,
Manhattan, KS 66506, USA

*Corresponding author: chang@phys.ksu.edu

Abstract: Previously, pulses shorter than 4 fs were generated by compressing white light from gas-filled hollow-core fibers with adaptive phase modulators; however, the energy of the few-cycle pulses was limited to 15 μ J. Here, we report the generation of 550 μ J, 5 fs pulses by using a liquid crystal spatial light modulator in a grating-based 4f system. The high pulse energy was obtained by improving the throughput of the phase modulator and by increasing the input laser energy. When the pulses were used in high harmonic generation, it was found that the harmonic spectra depend strongly on the high order spectral phases of the driving laser fields.

©2008 Optical Society of America

OCIS codes: (320.5540) Pulse Shaping; (320.7100) Ultrafast measurement; (320.7110) Ultrafast Nonlinear optics.

References and links

1. M. Hentschel, R. Kienberger, Ch. Spielmann, G. A. Reider, N. Milosevic, T. Brabec, P. Corkum, U. Heinzmann, M. Drescher, and F. Krausz, "Attosecond metrology," *Nature* **414**, 509-513 (2001).
2. A. Baltuška, Th. Udem, M. Uiberacker, M. Hentschel, E. Goulielmakis, Ch. Gohle, R. Holzwarth, V. S. Yakovlev, A. Scrinzi, T. W. Hänsch, and F. Krausz, "Attosecond control of electronic processes by intense light fields," *Nature* **421**, 611-615 (2003).
3. N. M. Naumova, J. Nees, B. Hou, G. A. Mourou, and I. V. Sokolov, "Isolated attosecond pulses generated by relativistic effects in a wavelength-cubed focal volume," *Opt. Lett.* **29**, 778-780 (2004).
4. G. G. Paulus, F. Grasbon, H. Walther, P. Villaresi, M. Nisoli, S. Stagira, E. Priori, and S. De Silvestri, "Absolute-phase phenomena in photoionization with few-cycle laser pulses," *Nature* **414**, 182-184 (2001).
5. S. Chelkowski, P. B. Corkum, and A. D. Bandrauk, "Femtosecond coulomb explosion imaging of vibrational wave functions," *Phys. Rev. Lett.* **82**, 3416-3419 (1999).
6. U. Morgner, F. X. Kärtner, S. H. Cho, Y. Chen, H. A. Haus, J. G. Fujimoto, and E. P. Ippen, "Sub-two-cycle pulses from a Kerr-lens mode-locked Ti:sapphire laser," *Opt. Lett.* **24**, 411-413 (1999).
7. D. Strickland, and G. Mourou, "Compression of amplified chirped optical pulses," *Opt. Commun.* **56**, 219 (1985).
8. M. Nisoli, S. De Silvestri, and O. Svelto, "Generation of high energy 10 fs pulses by a new pulse compression technique," *Appl. Phys. Lett.* **68**, 2793-2795 (1996).
9. C. P. Hauri, W. Kornelis, F. W. Helbing, A. Couairon, A. Mysyrowicz, J. Biegert, U. Keller, "Generation of intense, carrier-envelope phase-locked few-cycle laser pulses through filamentation," *Appl. Phys. B* **79**, 673-677 (2004).
10. M. Nisoli, S. De Silvestri, O. Svelto, R. Szipöcs, K. Ferencz, Ch. Spielmann, S. Sartania, and F. Krausz, "Compression of high-energy laser pulse below 5 fs," *Opt. Lett.* **22**, 522-524 (1997).
11. B. Schenkel, J. Biegert, U. Keller, C. Vozzi, M. Nisoli, G. Sansone, S. Stagira, S. De Silvestri, and O. Svelto, "Generation of 3.8-fs pulses from adaptive compression of a cascaded hollow fiber supercontinuum," *Opt. Lett.* **28**, 1987-1989 (2003).
12. K. Yamane, Z. Zhang, K. Oka, R. Morita, M. Yamashita, and A. Suguro, "Optical pulse compression to 3.4 fs in the monocycle region by feedback phase compensation," *Opt. Lett.* **28**, 2258-2260 (2004).
13. M. Yamashita, K. Yamane, and R. Morita, "Quasi-automatic phase-control technique for chirp compensation of pulse with over-one-octave bandwidth-generation of few-to mono-cycle optical pulses," *IEEE J. Sel. Top. Quantum Electron.* **12**, 213-222 (2006).
14. A. L. Cavalieri, E. Goulielmakis, B. Horvath, W. Helml, M. Schultze, M. Fieß, V. Pervak, L. Veisz, V. S. Yakovlev, M. Uiberacker, A. Apolonski, F. Krausz and R. Kienberger, "Intense 1.5-cycle near infrared laser waveforms and their use for the generation of ultra-broadband soft-X-ray harmonic continua," *New J. Phys.* **9**, 242 (2007).

15. R. Szpöcs, K. Ferencz, C. Spielmann and F. Krausz, "Chirped multilayer coating for broadband dispersion control in femtosecond lasers," *Opt. Lett.* **19**, 201-203 (1994).
16. G. Steinmeyer, "Femtosecond dispersion compensation with multilayer coatings: towards the optical octave," *Appl. Opt.* **45**, 1484-1490 (2006).
17. M. Schultz, E. Goulielmakis, M. Uiberacker, M. Hofstetter, J. Kim, D. Kim, F. Krausz, and U. Kleinberg, "Powerful 170-attosecond XUV pulses generated with few-cycle laser pulses and broadband multilayer optics," *New J. Phys.* **9**, 243 (2007).
18. H. Mashiko, C. M. Nakamura, C. Li, E. Moon, H. Wang, J. Tackett and Z. Chang, "Carrier-envelope phase stabilized 5.6 fs, 1.2 mJ pulses," *App. Phys. Lett.* **90**, 161114 (2007).
19. K. Yamane, T. Kito, R. Morita, and M. Yamashita, "Experimental and theoretical demonstration of validity and limitations in fringe-resolved autocorrelation measurements for pulses of few optical cycles," *Opt. Express* **12**, 2762-2733 (2004).
20. F. L. Légaré, J. M. Fraser, D. M. Villeneuve, and P. B. Corkum, "Adaptive compression of intense 250-nm-bandwidth laser pulses," *App. Phys. B* **74** [Suppl.], S279-S282 (2002).
21. S. Ghimire, B. Shan, C. Wang and Z. Chang, "High-energy 6.2-fs pulses for attosecond pulse generation," *Laser Phys.* **15**, 838-842 (2005).
22. B. Xu, Y. Coello, V. V. Lozovoy, D. A. Harris, and M. Dantus, "Pulse shaping of octave spanning femtosecond laser pulses," *Opt. Express* **14**, 10939-10944 (2006).
23. B. Xu, J. M. Gunn, J. M. De la Cruz, V. V. Lozovoy, and M. Dantus, "Quantitative investigation of the multiphoton intrapulse interference phase scan method for simultaneous phase measurement and compensation of the femtosecond laser pulses," *J. Opt. Soc. Am. B* **23**, 750-759 (2006).
24. K. Yamane, T. Kito, R. Morita, and M. Yamashita, "2.8-fs transform-limited optical-pulse generation in the monocycle region," in CLEO conference, Lasers and Electro-Optics, 1045-1047 (2004).
25. Z. Cheng, A. Fürbach, S. Sartania, M. Lenzner, Ch. Spielmann, and F. Krausz, "Amplitude and chirp characterization of high-power laser pulses in the 5-fs regime," *Opt. Lett.* **24**, 247-249 (1999).
26. J. Zhou, J. Peatross, M. M. Murnane, and H. C. Kapteyn, "Enhanced high-harmonic generation using 25 fs laser pulses," *Phys. Rev. Lett.* **76**, 752-755 (1996).
27. Z. Chang, A. Rundquist, H. Wang, I. Christov, H. C. Kapteyn, and M. M. Murnane, "Temporal phase control of soft-x-ray harmonics emission," *Phys. Rev. A* **58**, R30 - R33 (1998).
28. H. Mashiko, S. Gilbertson, C. Li, S. D. Khan, M. M. Shaker, E. Moon, and Z. Chang, "Double optical gating of high-order harmonic generation with carrier-envelope phase stabilized lasers," *Phys. Rev. Lett.* **100**, 103906 (2008).

1. Introduction

High energy laser pulses containing a mono-cycle or few-cycle field oscillations are crucial for generating single, isolated attosecond pulses from gases and plasmas, as well as for many other high field physics studies [1-5]. Although pulses as short as 5 fs centered at 800 nm can be generated from Kerr-lens mode-locked Ti:Sapphire oscillators, the pulse energy is only a few nanojoules [6]. When the pulses are amplified to the millijoule level at a kilohertz repetition rate with chirped pulse amplifiers (CPA), they are broadened to more than 10 fs due to gain narrowing of the pulse spectrum [7]. To produce energetic few-cycle and even mono-cycle pulses, the multi-cycle laser pulses from the CPA lasers are sent to nonlinear optical media such as gas-filled hollow-core fibers to broaden the spectral bandwidth so that it covers about one octave range (typically from 500nm to 1000nm) [8, 9]. The positive chirp of the pulses introduced by the nonlinear processes and the material dispersions is then removed by pulse compressors such as chirped mirrors, prism pairs or adaptive phase modulators [10-14].

The most frequently used method to compress white-light pulses from hollow-core fibers or filaments is the chirped mirrors. A chirped mirror consists of multilayer coatings, which allows the different wavelength components of the incident white-light to penetrate and reflect back from different coating depths [15]. By carefully designing the thickness of each layer, the chirped mirror can exhibit negative group delay dispersion (GDD) over the spectral range of the light from the nonlinear medium. Very recently, sub-5 fs pulses with 400 μ J energy measured by second harmonic (SH) and third harmonic autocorrelators were generated by optimizing the chirped mirrors design and by using 23 fs pulses seeding the neon-filled hollow fiber [14]. However, because the negative GDD introduced by a given set of chirped mirrors can only be changed by a discrete amount, it is difficult to accommodate the daily variation of the pulses from the hollow-core fiber or other nonlinear media. As a result, the compressed pulse duration and shape may change from day to day. Furthermore, owing to the interferometric effects at the air/mirror interface and inside the coating structure, GDD ripples are inevitable [16]. Matched pairs of mirrors have been used to overcome this problem to a

certain degree, but not completely. Design and fabrication of chirped mirrors that can compensate high order dispersions is still a challenge. So far, chirped mirrors only compensate GDD and the third order dispersions, while fourth and higher order phase control is important for compressing pulses to a mono-cycle field oscillation.

Compared to chirped mirrors, adaptive phase modulators have high flexibility of phase control. In principle, they can be adjusted to cope with the day to day phase variations of the white-light pulses and to compensate the high order phase errors. In the past, by using a liquid crystal spatial light modulator (SLM), the white light from two cascaded hollow-core fibers was compressed to 3.8 fs with 15 μ J pulse energy [11]. Even shorter pulses, 2.8 fs, were obtained by using the similar phase modulators [12, 13]. Although they are the shortest ones in the visible and infrared wavelength range, the energy of such extremely short pulses is only 0.5 μ J, which is too low for many high field experiments. For example, attosecond pulse generation has been accomplished by using 5 fs laser pulses with more than 300 μ J [17], whose energy is orders of magnitude higher than what the phase modulators have delivered. The low pulse energy is the main obstacle to applying pulses from adaptive phase modulator compressors to strong field physics experiments. In fact, to the best of our knowledge, no such experiments have been done using few-cycle pulses from adaptive compressors. The energy deficiency is the result of the high loss of the phase modulator and the limited input laser energy. In this work, we improved the throughput of the adaptive phase modulator and applied it to a hollow-core fiber with high output energy in order to obtain two-cycle pulses with sub-millijoule energy.

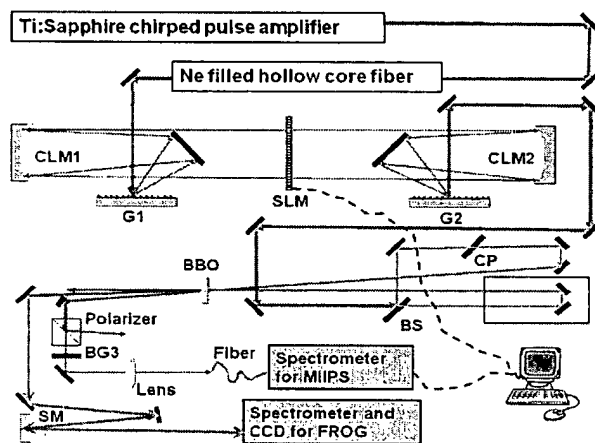


Fig. 1. The adaptive phase modulator. After hollow-core fiber the chirped white-light pulses were sent to the spatial light modulator through gratings (G1, G2) and cylindrical mirrors (CLM1, CLM2). The output beam was directed to the BBO. The central SH beam was used for FROG measurement, and one side SH beam was used as MIIPS feedback signal. The α -BBO polarizer and the BG3 band-pass filter worked together to eliminate the fundamental beam. The MIIPS retrieved phase was applied on SLM to compress the pulse. BS: beam splitter, CP: compensation plate, SM: spherical mirror. The dashed line represents the feedback loop.

2. Experiment and discussion

The home-built phase modulator for pulse compression is shown in Fig. 1. To test the adaptive phase modulator compressor, we used the Kansas Light Source, which is a grating-based CPA Ti:Sapphire laser system operating at 1 kHz repetition rate [18]. More than 2 mJ, 25 fs pulses from the laser were coupled into a 0.9 meter long, 400 μ m inner core diameter hollow fiber filled with 2 bars of neon gas. With such high energy seeding pulses, strong self-phase modulation produced white light whose spectrum covered more than one octave from 500nm to 1000nm, as shown in Fig. 2. The energy of the pulse from the fiber was 1.1 mJ, measured before the collimation mirror. Previously the highest white-light pulse energy used in the phase modulator compression was 0.1 mJ [11]. Thus we gained a factor of more than

ten just from the input side. The energetic pulses from the hollow-core fiber were then collimated and sent into a zero-dispersion 4f system, which consisted of two gratings with a groove density of ~ 230 lines/mm, and two cylindrical mirrors with 50 cm focal length. A 640-pixel liquid crystal SLM was located at the Fourier plane. The broadband laser beam from the hollow-core fiber was angularly dispersed by the first grating. Rather than spherical mirrors, silver-coated cylindrical mirrors were applied to focus each wavelength component to a line on the SLM to avoid damaging the liquid crystal of the SLM by the high energy pulses. The chirp of the pulses was removed by controlling the refraction index on each pixel of the SLM. The second grating recombined the different frequency components into one output beam.

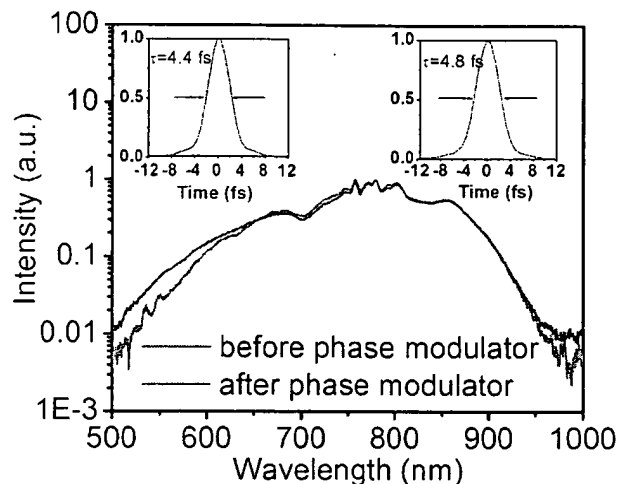


Fig. 2. The white-light spectrum before the phase modulator (blue) and after the phase modulator (red). The inset shows the transform-limited pulses for both spectra.

Previously, low diffraction efficiency of the gratings was the main limiting factor of the overall throughput of the adaptive phase modulator. We used two gratings with protected silver coatings to achieve high diffraction efficiency (average efficiency is $\sim 80\%$) over the bandwidth (500nm-1000nm) of our hollow-core fiber output spectrum. Also, the SLM with broadband anti-reflection coatings on both surfaces provided high transmission of more than 90% in the same wavelength range. To determine the frequency response of the 4f system, the white-light spectrum was measured before and after the phase modulator, as shown in Fig. 2. Although the throughput was somewhat lower at the short wavelength side, the transform limited pulse duration supported by the spectrum of the output pulses was sub-5 fs, which was nearly the same as that of the input. With 1.1 mJ per input pulse, the output pulse energy from the system was 0.55 mJ, which was about 37 times higher than what was demonstrated before. The high throughput, 50%, was the major improvement of our adaptive phase modulator.

One approach to obtain the shortest pulse is to optimize the second harmonic signal by focusing the compressed white-light pulses to a nonlinear crystal. However, it was found that by optimizing the SH signal, neither genetic algorithm nor evolutionary algorithm can compress the pulse with high accuracy [19, 20]. Another approach is to measure the spectral phase of the white light from the fiber and feed the measured value to the phase modulator for correction. For adaptive pulse compression in the near-octave bandwidth and few-cycle regime, accurate retrieval of the spectral phase of the output pulses from the 4f system is crucial. Our laboratory is equipped with a FROG based on second harmonic generation [21].

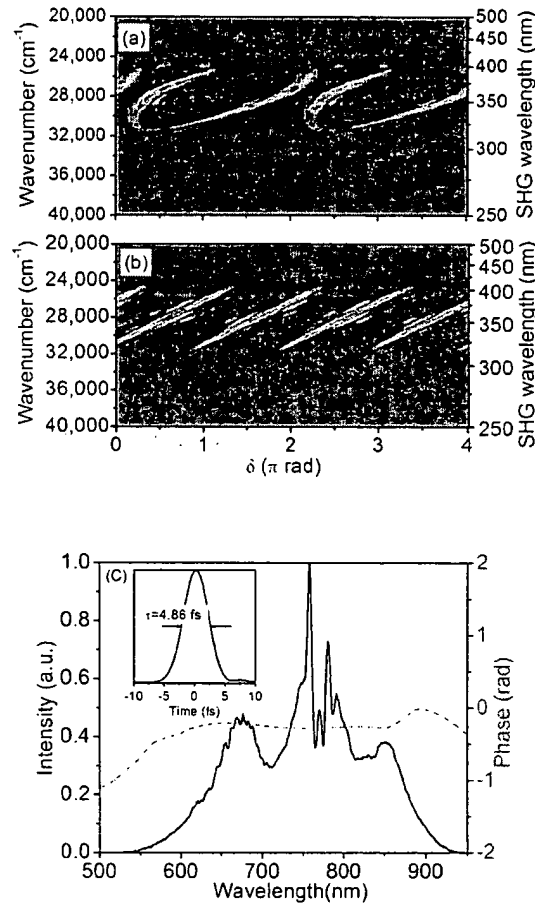


Fig. 3. The MIIPS traces ($\alpha=5$, $\gamma=7$ fs). (a) from the first iteration; (b) from the last iteration; (c) the phase determined by the last iteration and the corresponding pulse duration.

We found that it is difficult to measure the phase of the white-light pulses from the fiber before compression with high accuracy because of the poor signal to noise ratios, especially at the two ends of the spectrum (around ~ 550 nm and around ~ 950 nm). This is because the SH signal is rather low in those regions when the pulses are strongly chirped. As an alternative, the Multiphoton Intrapulse Interference Phase Scan (MIIPS) method was applied [22, 23].

The MIIPS works by modulating the spectral phase of the pulses with the SLM while simultaneously recording the second harmonic (SH) spectra after the 4f system. The applied spectral phase at frequency ω can be expressed as $\Phi(\omega)=\alpha\cos(\gamma\omega-\delta)$, where α and γ are two parameters that need to be chosen properly (In our case $\alpha=5$, $\gamma=7$ fs). By linearly increasing the δ value, one can scan the applied GDD for each frequency ω . When dispersions higher than the second order are ignored, it is found that if the GDD introduced by the phase modulator, $\Phi''(\omega)=\alpha\gamma^2\cos(\gamma\omega-\delta)$, cancels out the GDD of the white light, $\phi''(\omega)$, at a certain frequency ω then a SH signal peak appears at 2ω . After recording all the SH spectra for δ from 0 to 4π , the two dimensional MIIPS trace was constructed as shown in Fig. 3. By searching the peak position δ_p in the MIIPS trace for each SH frequency 2ω , $\phi_1''(\omega)=-\Phi_1''(\omega)=-\alpha\gamma^2\cos(\gamma\omega-\delta_p)$ is retrieved from the MIIPS pattern for the first iteration. $\phi_1''(\omega)$ is an approximate value of $\phi''(\omega)$ since dispersions higher than the second order are ignored. By integrating $\phi_1''(\omega)$ twice, we obtained the phase $\phi_1(\omega)$ from the first iteration. To measure the

phase more precisely, $-\varphi_1(\omega)$ was wrapped and applied on the SLM for the second iteration, which measured the phase difference $\varphi(\omega)-\varphi_1(\omega)$, the second iteration is done in the same way as the first iteration. After about m iterations, the phase correction $\varphi_m(\omega)$ became nearly flat and the retrieved phase $\sum \varphi_m(\omega)$ converges to $\varphi(\omega)$. In our experiments, $m = 8$. The generation of the SH peak increases the signal to noise ratio. At both ends of the fundamental spectrum (600 nm and 900 nm), the SH peak in MIIPS is much stronger than the SH signal in the FROG before the phase was corrected which is the main reason we chose the MIIPS for measuring the initial phase of the white-light pulses.

In our experiments, since the GDD of white light $\varphi''(\omega)$ is large, $\varphi_0''(\omega)=500\text{fs}^2$ was added on the SLM to pre-compensate the phase before the first iteration. The linear component of $\varphi_0(\omega)$ was chosen such that the phase load per pixel was minimized [24]. The first iteration of the MIIPS pattern is shown in Fig. 3(a). The iterations stopped when the retrieved phase accuracy was higher than 0.01 radians per liquid crystal pixel over the whole fundamental spectrum. The MIIPS pattern after the chirp compensation is shown in Fig. 3(b). The evenly spaced parallel SH strip distribution indicates that the residual GDD of the pulses is very small [23]. Since our MIIPS did not resolve the SH peak position clearly below 280nm or above 450nm, there were residual errors on both the short and long wavelength portions of the retrieved phase. The phase $\varphi_m(\omega)$ retrieved from the last iteration is shown in Fig. 3(c). Using this measured phase and the power spectrum at the exit of the 4f system shown in Fig. 2, Fourier transform gave the pulse duration of 4.86 fs, also shown in Fig. 3(c).

The second harmonic signal shown in Fig. 3 was generated in a barium borate (BBO) crystal with a type I phase-matching configuration. A 5 μm thickness thin crystal was used for phase-matching over the broad fundamental spectrum range. The phase matching angle of the crystal was set at 40 degrees to enhance the frequency doubling efficiency around 600 nm of the white light. When the SH was measured by a customized Ocean Optics HR2000+ spectrometer that works in the 200nm to 600nm range, the strong fundamental laser light had to be blocked as to not saturate the detector. The configuration we used for detecting the second harmonic signal is shown in Fig. 1, which is different from what was used in MIIPS in the past [22]. Taking advantage of the fact that the polarization of the second harmonic beam is orthogonal to the fundamental beam for type I phase matching, an α -BBO polarizer was placed after the SH generation BBO crystal to reject most of the fundamental light. A BG3 filter was added to further suppress the fundamental signal. To increase the signal to noise ratio and reduce the integration time of spectrum acquisition, a fused silica UV lens with 5 cm focal length focused the SH signal to an optical fiber that couples the light into the spectrometer. Compared with the prism method that separates SH from the fundamental used in the past with MIIPS, our collinear configuration has higher collection efficiency, which is important for measuring the phase of the weak fundamental at both ends of the spectrum.

After the phase correction by MIIPS, the duration of the compressed pulse was measured by the FROG [21, 25]. Unlike the input pulses, we found that the signal to noise ratio of the FROG pattern obtained with the compressed pulses is good enough for robust phase retrieval. Our MIIPS and FROG shared the same BBO crystal, as shown in Fig. 1. There are three second harmonic beams exiting the BBO crystal. The center one was used by the FROG, while one of the side beams was sent to the MIIPS. It is well known that few-cycle pulses can be easily distorted by dispersion introduced by propagation in air. In such a configuration, the MIIPS and the FROG measured the pulse at the same location, which is critical for few-cycle pulse characterization. The measured and reconstructed FROG patterns are shown in Fig. 4(a) and (b) respectively. The retrieved pulse duration is 5.1 fs as shown in Fig. 4(c), which is slightly longer than what was determined by the MIIPS (4.86 fs). The spectral phase in Fig. 4(d) shows the chirp was well compensated. Also in Fig. 4(d) the retrieved spectrum was compared with the independently measured spectrum. The frequency marginal comparison is shown in Fig. 4(e) to confirm the validity of FROG results. Both methods showed that the pulse duration was around 5 fs, which is shorter than what has been produced from the same hollow-core fiber using commercially available chirped mirrors [18, 21]. For pulse with over one octave spectrum, it is difficult to get perfect FROG traces due the limited phase-matching

bandwidth of the SHG crystal and the spectral response of all the optics in the setup, which explained the difference between the MIIPS results and FROG results.

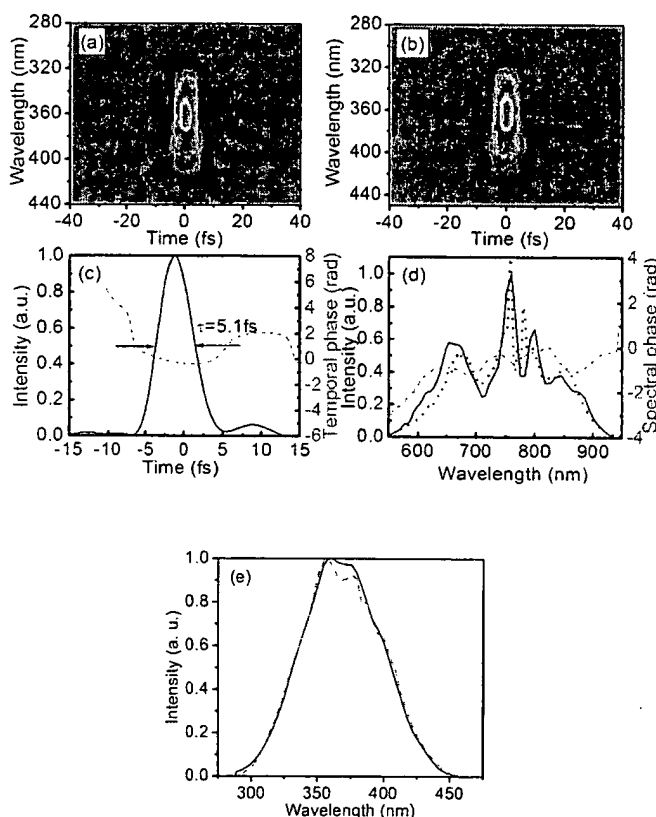


Fig. 4. Characterization of the laser pulse by the FROG. (a) The measured FROG trace. (b) The reconstructed FROG trace. (c) The retrieved pulse shape and phase (dashed curve). (d) The retrieved power spectrum and phase (dashed curve) and independently measured spectrum (dotted curve). (e) The FROG frequency marginal (dotted red curve) and the autoconvolution (solid black curve) of the measured spectrum from hollow-core fiber. The FROG error is 0.5%, and the trace is at 256×256 grids.

The high power of the compressed pulses allowed us to generate high order harmonics. Previously the dependence of high harmonic generation (HHG) spectra on GDD was investigated by using relatively long pulses (30 fs) directly from the CPA system by changing the grating separation [26, 27]. It was found that when the driving laser was positively chirped, the HHG spectra were more discrete and red shifted, whereas for a negatively chirped pump, the HHG spectra became a continuum. We performed coherent control of high harmonic generation with the 0.55 mJ, 5.1 fs pulses by independently changing the GDD and high order spectral phases. Our experiment was carried out with argon gas using a setup described in Ref. 28. The laser beam was focused by a spherical mirror to a gas filled interaction cell with a length of 1.4 mm. The focal length of the mirror was 400 mm. The backing pressure to the gas cell was 30 torr. The gas target was placed approximately 2 mm after the focus to optimize the phase matching for the short trajectory. As seen in Fig. 5(a), when the GDD was scanned, the harmonic peaks shift, like what was discovered with long laser pulses in the past. The spectra also showed an asymmetric dependence on the positive chirp as compared to the negative chirp. We noticed that asymmetry is even stronger for third

order to fifth order phases as shown in Figs. 5(b), 5(c) and 5(d); a coherent control of spectral phase that has not been studied before and deserves further investigation.

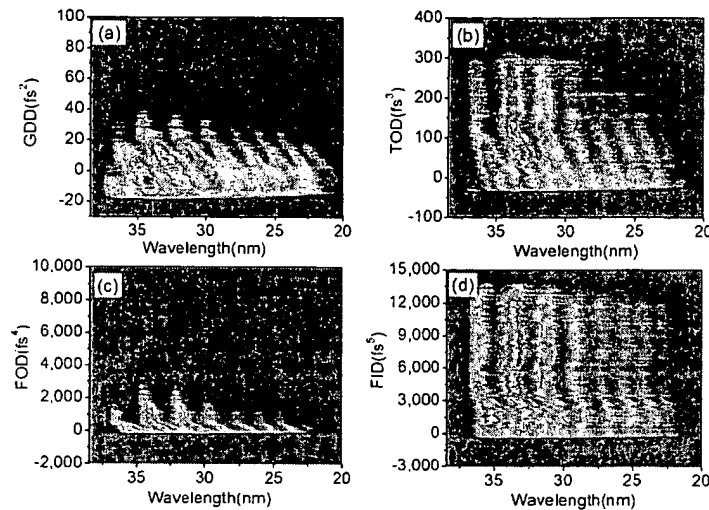


Fig. 5. Dependence of high order harmonic spectra on the high order phases of the driving laser pulses

3. Conclusion:

In conclusion, by improving the throughput of an adaptive phase modulator and by applying it to a high power laser system, we compressed laser pulses to ~ 5 fs at half-millijoule energy levels. As far as we know, this is the highest energy few-cycle pulse ever achieved by adaptive pulse compressors. The Multiphoton Intrapulse Interference Phase Scan method was applied to measure the spectral phase of the pulses after the hollow-core fiber for the first time, which serves as the feedback for the phase correction. The high power, two-cycle pulses were used in high harmonic generation. It was found that the harmonic spectra depended strongly on the high order spectral phases. The phase controllable, millijoule level few-cycle pulses are a new powerful tool for studying single attosecond pulse generation and performing coherent control in new parameter spaces.

Acknowledgments:

We thank Shouyuan Chen for discussion on the MIIPS parameter selection. We also want to thank Michael Chini and Sabih D. Khan for their help with the software. This material is supported by the Chemical Sciences, Geosciences and Biosciences Division, Office of Basic Energy Sciences, Office of Science, U.S. Department of Energy, the NSF under Grant No. 0457269, and by the U. S. Army Research Office under Grant No. W911NF-07-1-0475.